

# Frequency-domain modelling of floating wind turbines



**Richard Lupton**

Department of Engineering  
University of Cambridge

This dissertation is submitted  
for the degree of  
Doctor of Philosophy.

Pembroke College

December 2014



# *Frequency-domain modelling of floating wind turbines*

Richard Lupton

The development of new types of offshore wind turbine on floating platforms requires the development of new approaches to modelling the combined platform-turbine system. In this thesis a linearised frequency-domain approach is developed which gives fast but approximate results: linearised models of the structural dynamics, hydrodynamics, aerodynamics and control system dynamics are brought together to find the overall response of the floating wind turbine to harmonic wind and wave loading.

Initially, a nonlinear flexible multibody dynamics code is developed and verified, which is then used to provide reference nonlinear simulation results. The structural dynamics of a wind turbine on a moving platform are shown to be nonlinear, but for realistic conditions the effects are small.

An approximate analysis of the second-order response of floating cylinders to hydrodynamic loads suggests slow drift motion may be relatively small for floating wind turbines, compared to other floating offshore structures.

The aerodynamic loads are linearised using both harmonic and tangent linearisation approaches; the harmonic linearisation gives improved results when stall occurs. The wake dynamics can also be included. The control system behaviour is linearised using the same method, which works well when the wind speed is far from the rated wind speed; close to the rated wind speed the nonlinearity is stronger, but further improvement should be possible.

These sub-models are combined to give a simple but complete model of a floating wind turbine, with flexible blades and a flexible tower, but neglecting the control system behaviour, wake dynamics and nonlinear hydrodynamic loads. For the OC3-Hywind turbine, the accuracy of the results is assessed by comparison to nonlinear time-domain simulations using the commercial code Bladed. Peak-peak errors of less than 5% are achievable for many harmonic wind and wave inputs, but certain conditions lead to larger errors. The effect of including linearised control system behaviour is demonstrated for a subset of conditions. Overall, the results are promising but more work is needed for practical application.



## Declaration

This dissertation is the result of my own work and includes nothing which is the outcome of work done in collaboration except as declared in the Preface and specified in the text.

It is not substantially the same as any that I have submitted, or, is being concurrently submitted for a degree or diploma or other qualification at the University of Cambridge or any other University or similar institution except as declared in the Preface and specified in the text. I further state that no substantial part of my dissertation has already been submitted, or, is being concurrently submitted for any such degree, diploma or other qualification at the University of Cambridge or any other University of similar institution except as declared in the Preface and specified in the text

It does not exceed the prescribed word limit for the relevant Degree Committee. It contains approximately 37 200 words and 100 figures.

Richard Lupton



## Acknowledgements

I would like to thank my supervisor, Robin Langley, for his excellent guidance during the course of this research.

I am grateful to my colleagues at Garrad Hassan for supporting and funding this work, and in particular to James Nichols for his help before and during this project.

Thanks also to Tore Butlin, Louis Kovalevsky and the other members of the Dynamics and Vibration Research Group for helpful discussions and generally creating a nice place to work.

*For Florence*

# Contents

<b>1</b>	<b>Floating offshore wind turbines</b>	<b>13</b>
1.1	Floating wind turbines . . . . .	13
1.2	Research aims and contributions . . . . .	16
1.3	Components of a floating wind turbine . . . . .	17
1.4	Case study design: OC3-Hywind . . . . .	25
1.5	Time-domain modelling approaches . . . . .	26
1.6	Linearised frequency-domain analysis . . . . .	29
1.7	Conclusions and outline of thesis . . . . .	35
<b>2</b>	<b>Development of a nonlinear multibody dynamics code</b>	<b>37</b>
2.1	Outline of the code . . . . .	38
2.2	Model framework . . . . .	40
2.3	Element library . . . . .	48
2.4	Reduced and linearised systems . . . . .	66
2.5	Time-domain integration . . . . .	68
2.6	Prescribed motion . . . . .	69
2.7	Verification . . . . .	71
<b>3</b>	<b>Linearised structural dynamics</b>	<b>77</b>
3.1	Simplified model . . . . .	79
3.2	Perturbation solution . . . . .	88
3.3	Numerical results . . . . .	92
3.4	Blade dynamics at model scale . . . . .	107
3.5	Linear structural model . . . . .	109
3.6	Conclusions . . . . .	111
<b>4</b>	<b>Linearised hydrodynamics</b>	<b>113</b>
4.1	Frequency-domain hydrodynamic model . . . . .	115
4.2	Scaling of slow drift motions . . . . .	124
4.3	Linearised viscous drag forces . . . . .	134
4.4	Conclusions . . . . .	139

<b>5</b>	<b>Linearised aerodynamics</b>	<b>141</b>
5.1	Blade Element Momentum model . . . . .	142
5.2	Harmonic linearisation of aerodynamic loads . . . . .	152
5.3	Linearised aerodynamic forces with aeroelasticity . . . . .	155
5.4	Linearised wake dynamics . . . . .	161
5.5	Conclusions . . . . .	165
<b>6</b>	<b>Control system dynamics</b>	<b>167</b>
6.1	Wind turbine control systems . . . . .	167
6.2	Harmonic linearisation of torque and pitch control . . . . .	173
6.3	Comparison of linearised and nonlinear results . . . . .	177
6.4	Conclusions . . . . .	183
<b>7</b>	<b>Linearised modelling of floating turbines</b>	<b>185</b>
7.1	Model with fixed rotor speed and pitch angle . . . . .	186
7.2	Results with fixed rotor speed and blade pitch angle . . . . .	193
7.3	Solution including control system behaviour . . . . .	208
7.4	Computational time comparison . . . . .	214
<b>8</b>	<b>Conclusions and future work</b>	<b>217</b>
8.1	Conclusions . . . . .	217
8.2	Future work . . . . .	221
<b>A</b>	<b>Further details of the multibody code</b>	<b>227</b>
A.1	Matrix form of cross product . . . . .	227
A.2	Derivation of beam element mass matrix . . . . .	228
A.3	Derivation of beam element velocity-dependent forces . . . . .	230
A.4	Derivation of beam element applied forces . . . . .	231
<b>B</b>	<b>Further details of flapped-blade equations of motion</b>	<b>233</b>
B.1	Kinematics for platform pitching motion . . . . .	233
B.2	Equation of motion for response to pitching motion . . . . .	237

## Glossary

- barge** a shallow floating platform with a large waterplane area.
- BEM** Blade Element Momentum theory, not to be confused with the Boundary Element Method.
- CFD** Computational Fluid Dynamics.
- FFT** Fast Fourier Transform.
- harmonic linearisation** a linearisation method which produces a linear system with minimal mean-squared error. See p 153.
- heave** vertical platform motion, see p 18.
- MBC** Multi-Blade Coordinate transform.
- NREL** National Renewable Energy Laboratory (USA).
- PID** Proportional-Integral-Derivative.
- pitch** either ‘platform pitch’, a fore-aft platform rotation (see p 18) or ‘blade pitch’, rotation of the blade about its axis to change the angle of attack.
- QTF** Quadratic Transfer Function.
- RAO** Response Amplitude Operator.
- roll** side-side platform rotation, see p 18.
- semisubmersible** a floating platform design with a small waterplane area and sometimes large underwater pontoons.
- spar buoy** a deep floating platform design with small waterplane area.
- surge** fore-aft platform motion, see p 18.
- sway** side-side platform motion, see p 18.
- tangent linearisation** the basic linearisation method which finds the tangent by perturbation about an operating point.
- TLP** Tension-Leg Platform.
- TSR** Tip Speed Ratio =  $\Omega R/U$ , where  $\Omega$  is the rotor speed,  $R$  is the blade radius and  $U$  is the wind speed.
- yaw** rotation of the platform about the vertical axis, see p 18.

Mathematical notation is defined in each chapter as needed.



## *Floating offshore wind turbines*

### 1.1 Floating wind turbines

Interest has been growing recently in floating offshore wind turbines, against a background of rapid growth in wind energy more generally. Between 2000 and 2013, wind energy accounted for 28 % of new electricity generation capacity installed in the EU, and now represents 13 % of the installed generation capacity and 8 % of consumption. Worldwide, the figure is slightly less at 5 % of consumption. In northern Europe, development has been increasingly moving offshore into greater depths, with offshore installations up from 1 % in 2001 to 14 % in 2013 (EWEA 2014b; BP 2014). Figure 1.1 shows that as the easier, shallow sites close to shore have been exploited, the trend is towards building offshore wind farms in greater water depths. This has prompted interest in the development of new designs of wind turbines suitable for deep water, both in the North Sea and in other seas worldwide which, lacking shallow areas, have not so far benefited from offshore wind energy (Henderson and Witcher 2010).

Existing foundation designs for offshore wind turbines are being adapted for greater water depths. However, at sufficient depths new types of wind turbine on floating platforms are expected to become competitive in terms of life cycle cost (Myhr, Bjerkseter, et al. 2014). Other benefits identified by Roddier et al. (2010) include simplified installation and maintenance procedures – the turbine can be assembled in harbour before being towed out for installation – and that a only single hull design is required, as opposed to fixed-bottom turbines where the support structure must be redesigned

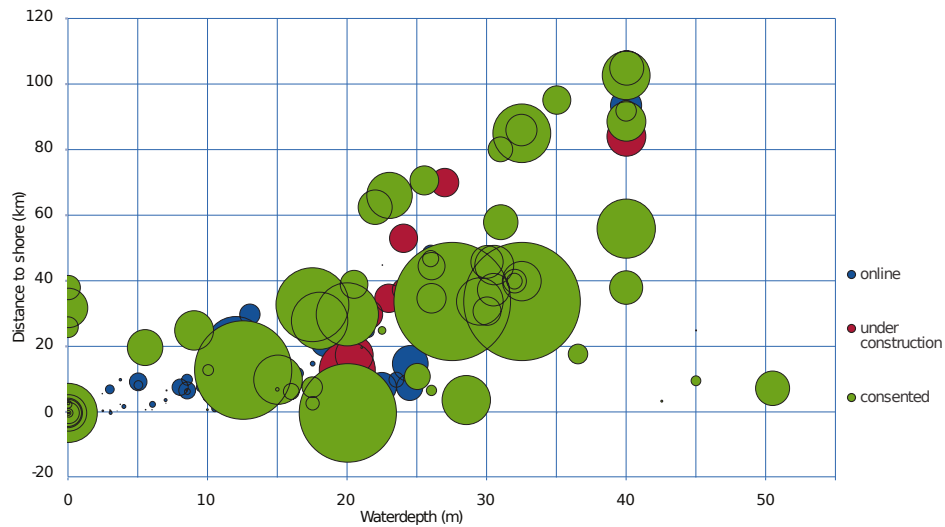


Figure 1.1 – Depth and distance to shore of current and future offshore wind farms. The size of the circle indicates the size of the wind farm. The planned farms show the trend towards being further offshore and in deeper water. Reproduced with permission from EWEA (2014a)

for every location.

The technology used for floating wind turbines draws upon the two established fields of wind energy and offshore engineering. The main types of platform – barge, semisubmersible, Tension-Leg Platform (TLP) and spar buoy – which have been proposed for floating wind turbines are the same as those used for ships and floating offshore gas platforms (Figure 1.2). However, there are also significant differences between the two industries. Compared to offshore oil & gas platforms, wind turbines are generally smaller; mass production at low cost is needed, rather than one-off designs; and the risks of environmental damage and of manned operation are lower.

To date, there are four full-size operational floating wind turbines:

- Hywind was the first multi-megawatt floating wind turbine in the world. The 2.3 MW turbine has been operating in Norway since 2009.
- WindFloat was installed in 2011 off the coast of Portugal with a 2 MW wind turbine.
- A 2 MW turbine on a spar buoy was installed in 2013 off Kabashima

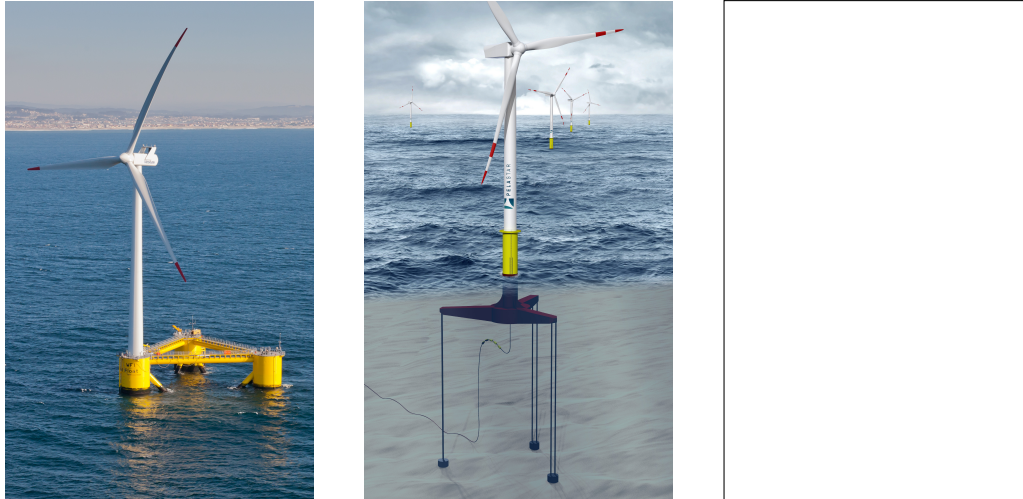


Figure 1.2 – Main types of floating wind turbine platform: from left to right, a semisubmersible (WindFloat\*), tension-leg platform (PelaStar†) and a spar buoy (Hywind‡).

\* photo by Untrakdrover, licenced CC BY-SA.

† photo from Glosten, <http://glosten.com>, with permission.

‡ photo from Statoil, <http://statoil.com>.

Island, Japan.

- Also in Japan in 2013, a 2 MW turbine was installed on a semisubmersible platform off Fukushima.

Others have deployed scale models at sea, including Blue H (2014) with a 3/4-scale platform in 2008 which has since been decommissioned, Sway (2014) with a 1/6-scale prototype since 2012 and VoltturnUS with a 1/8-scale prototype since 2013 (Viselli, Goupee and Dagher 2014). Many other concepts have not made it to the prototype stage, some of which are reviewed by Henderson, Zaaier, et al. (2004).

### 1.1.1 MODELLING APPROACHES

Numerical modelling is an essential part of the design of floating wind turbines. Like the technology of the floating platforms themselves, the modelling tools for floating wind turbines build on the respective approaches of the wind energy and offshore industries.

Wind turbines are complex systems with interactions between the control systems, the structural dynamics of the blades and tower and the aero-

dynamics of the flow around the rotor and the wind loads on the blades. Consequently it is common to use integrated time-domain simulation tools in wind turbine design, and much work has focused on extending these existing simulation tools to model the hydrodynamic loading, mooring lines and platform motion of a floating wind turbine (specific examples are given below).

Although such tools are essential, in some cases faster and more approximate models are needed: to assess initial design concepts, for parametric optimisation, to focus further simulation effort, or for a better understanding of the fundamental behaviour. That the prototypes mentioned above span the full range of platform types shows that this type of broad analysis is still needed. There are a number of approaches to creating simplified models, which can generally be categorised as either simplified nonlinear time-domain methods or linearised frequency-domain methods. Examples of both are reviewed later in this chapter.

## 1.2 Research aims and contributions

Of the modelling approaches mentioned above, it is the frequency-domain approach which is pursued in this thesis. Although frequency-domain analysis is commonly used in the design of ships and offshore platforms, it is uncommon in the wind energy industry. The reason for this, and the main challenge of this approach, is that a linearised model of the system is required. The complexity of the wind turbine system makes this more difficult to obtain, but equally importantly it is more difficult to determine the situations in which the linearised approximation is reasonable. The main contribution of this thesis is to address these twin difficulties in the various sub-domains of a floating wind turbine: structural dynamics, hydrodynamics, aerodynamics, and control system dynamics. Specifically,

- The state of the art in modelling floating wind turbines is reviewed, in particular the use of approximations and linearised analysis.
- Nonlinearity in the structural dynamics of a floating wind turbine is demonstrated, but nonlinear structural effects are shown to be negligible

under reasonable conditions.

- An approximate result is developed for the scaling with platform size of platform motion due to nonlinear hydrodynamic forces. This suggests nonlinearity may be less important for floating wind turbines than other floating structures.
- An improved linearised model of the aerodynamic loads and control system behaviour is developed.
- Finally, a model of a complete floating wind turbine is developed and the results compared to nonlinear time-domain simulations.

If the linearised model is found to be sufficiently accurate, there are several advantages to the frequency-domain approach. Speed has already been mentioned; other advantages include the possibility of directly estimating the statistics of the response, and accounting for uncertainty in the input data. What is ‘sufficiently accurate’ depends on the application: the model might be used for optimisation studies, for estimating fatigue loading over a wide range of environmental conditions, or for focusing further detailed simulation effort, each with different requirements for accuracy.

Overall, the aim is to benchmark the accuracy of the linearisation itself against typical engineering approaches to nonlinear modelling of wind turbines and floating structures. The accuracy of these engineering models themselves is not considered.

The remainder of this chapter introduces some background on the approaches to modelling various sub-domains of a floating wind turbine, before reviewing the literature on modelling of the whole floating wind turbine system.

### 1.3 Components of a floating wind turbine

In this section, for each component of a floating wind turbine the typical modelling approaches used for fixed-bottom turbines or other offshore structures will be reviewed. In particular, new challenges in these areas in the case of floating wind turbines will be highlighted. For more information on wind turbines in general see, for example, Burton et al. (2011). For a

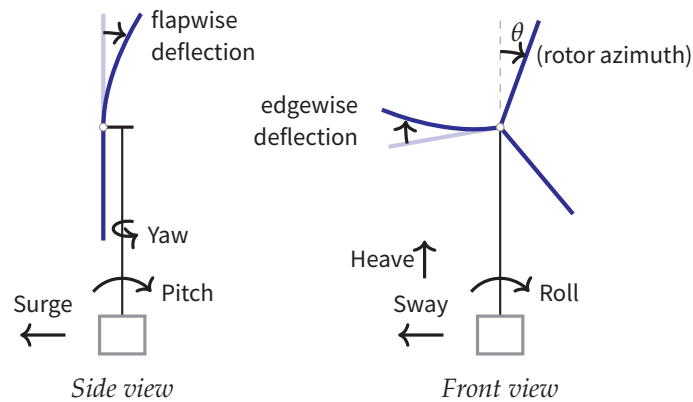


Figure 1.3 – The rigid-body motions of a floating structure are referred to as surge, sway, heave, roll, pitch and yaw as shown.

review of modelling challenges associated with floating wind turbines see Matha, M Schlipf, et al. (2011).

### 1.3.1 PLATFORM MOTION

The rigid-body motions of a floating structure are referred to as surge, sway, heave, roll, pitch and yaw. These terms are illustrated in Figure 1.3 and are used throughout this thesis.

### 1.3.2 THE WIND

The wind varies on timescales ranging from a few seconds to several days. Commonly the variation up to periods of about 10 minutes is referred to as ‘turbulence’ and is modelled as a stationary random process. The longer-term variations are taken to be variations in the statistics of 10-minute samples. Various turbulence models are available which define the power spectral density and spatial coherence of the random processes (Burton et al. 2011, chapter 2).

In addition to the random turbulence, mean wind speeds typically increase with height above the ground, which is known as ‘wind shear’. Wakes from neighbouring turbines or other obstructions can also have a large effect on the air flow.

A similar wind environment is experienced by floating wind turbines

as by other offshore wind turbines. Being surrounded by relatively flat sea, both generally enjoy higher wind speeds, less turbulence and lower wind shear than onshore turbines.

### 1.3.3 AERODYNAMIC LOADS

For ships and offshore structures, relatively simple drag-based models of wind loading are often sufficient (Faltinsen 1993), but for wind turbines more complex models are needed. The most commonly used is the Blade Element Momentum (BEM) method (Burton et al. 2011, chapter 3). Other, more physical approaches, such as vortex models or Computational Fluid Dynamics (CFD), do exist but they are too slow for general use in the modelling of the whole wind turbine system.

In the BEM method, the change in momentum of the air as it flows past the rotor is equated with the lift and drag forces created by the aerofoils on the blades. The lift and drag forces are determined from empirical two-dimensional aerofoil lookup tables, based on the incoming flow speed and direction seen by the aerofoil. An iterative solution is needed because the incoming flow is affected by the blade loading. Since the aerodynamic properties of the blades vary along their span, independent calculations are carried out at multiple points along the blade.

A number of corrections are commonly applied to the basic method, such as a ‘tip loss’ correction for the increased flow through the gaps between blades, and corrections to the aerofoil characteristics to account for the radial flow along the blades caused by the rotation of the rotor. Other corrections may be needed to account for wind shear, yawed flow and tower shadow effects.

There are two main types of dynamic behaviour which are not captured by the standard BEM model: wake dynamics and unsteady aerofoil dynamics. As discussed by Vaal, MOL Hansen and Moan (2014), the wake dynamics reflect the fact that the flow around the rotor responds to changes in the rotor loading on a time scale related to the wind speed and rotor dimensions, typically 5 s to 20 s. The unsteady aerofoil dynamics relate to the relatively short delay between changes to the flow around an aerofoil and the resulting lift and drag forces, with typical time periods of less than

a second. The change from fixed to floating wind turbines is more likely to affect the wake dynamics since the time scales are most similar to the frequencies of platform motion. Various engineering models are available to model these dynamic effects within simulations using the BEM model (Snel and Schepers 1995; Burton et al. 2011, chapter 4). Linearised models of the unsteady aerodynamics have been used for stability analysis (eg MH Hansen 2004), and a linearised model of the wake dynamics has been used in the code TURBU (Engelen and Braam 2004).

Aeroelasticity can be an important effect, in which the aerodynamic loads are affected by the velocity of elastic deflections of the blades or motion of the whole floating platform. Often this is a source of additional damping, sometimes up to 30 % of critical damping (Burton et al. 2011, chapter 5), but instabilities such as flutter can also appear.

Sebastian and Lackner (2013) raised concerns that the greater dynamic motion of the rotor of a floating wind turbine will lead to more complex flow conditions which cannot be adequately modelled by BEM. Vaal, MOL Hansen and Moan (2014), on the other hand, found that at least for up-wind/downwind translation, the motion of the platform is typically slow enough that BEM is adequate. The current general practice in any case is to use a BEM approach.

#### 1.3.4 HYDRODYNAMIC LOADS

Typically, fixed-bottom offshore wind turbines are supported by single columns, known as ‘monopiles’, or occasionally a truss-like ‘jacket’ structure. Structures which are slender in comparison to the wavelength of the incoming waves, such as these, are assumed to be hydrodynamically transparent and can be modelled by the semi-empirical Morison’s equation. This gives the transverse force on a cylindrical strip of length  $ds$  as

$$dF_M = \frac{\rho\pi D^2}{4} ds [C_M \dot{u} - (C_M - 1) \dot{v}] + \frac{\rho D}{2} ds C_D |u - v| (u - v) \quad (1.1)$$

where  $\rho$  is the density of the water,  $D$  is the diameter of the cylinder, and  $u$  is the transverse velocity of the water at the cylinder and  $v$  is the transverse velocity of the cylinder itself. The water velocity may be due to both

waves and currents. The mass and drag coefficients  $C_M$  and  $C_D$  must be determined empirically, and depend on many parameters such as Reynolds number, Keulegan-Carpenter number, mean current speed and surface roughness (Faltinsen 1993, chapter 7). Since Morison's equation is defined in terms of transverse velocities and forces, the loads must be calculated in the local coordinate systems of the individual members of a complex structure, before transformation back to the platform coordinate system. Although Morison's equation applies only to transverse forces, a similar approach has been used to find the axial loads on the large cylinders which make up some floating wind turbine platforms (Philippe, Babarit and Ferrant 2014).

Larger structures, such as ships, oil & gas platforms and larger floating wind turbine platforms, must account for diffraction and radiation effects. In particular, radiation damping is not included in a Morison model but may be significant for large platform motions (Matha, M Schlipf, et al. 2011). Large structures are commonly modelled using potential flow methods, which are a relatively new addition to the modelling of floating wind turbines (Jonkman 2007).

The potential flow problem is usually solved numerically by a panel method. Various external hydrodynamic preprocessor codes exist, so the details are not a concern in the present work (see Chakrabarti 2005, chapter 4). The hydrodynamic loads are found for sinusoidal waves and sinusoidal motion of the platform, both at frequency  $\omega$ , so that the sea surface elevation is  $\eta = \zeta e^{i\omega t}$  and the six rigid-body degrees of freedom of the platform are  $\xi = \bar{\xi} e^{i\omega t}$  (the convention of taking the real part is implied). The results of the hydrodynamic analysis are the frequency-dependent complex  $6 \times 6$  matrices of added mass and damping coefficients  $A(\omega)$  and  $B_h(\omega)$ , and a vector of 6 excitation force coefficients  $X(\omega)$ . The hydrostatic restoring force coefficients  $K_h$  can also be calculated. The hydrodynamic forces and moments  $F_{\text{hydro}} = \bar{F}_{\text{hydro}} e^{i\omega t}$  are then given by

$$\bar{F}_{\text{hydro}}(\omega) = X(\omega)\zeta(\omega) - [-\omega^2 A(\omega) + i\omega B_h(\omega) + K_h] \bar{\xi}(\omega) \quad (1.2)$$

Potential flow is essentially a linearised approach, but it can be extended to calculate second-order nonlinear loads (Pinkster 1980). These are by definition smaller than the first-order loads, but can excite a significant

response when they coincide with the natural frequencies of the structure. The second-order forces occur at the sum and difference frequencies of the incoming waves: the resulting low frequency forces can excite a large resonant motion of the platform on its mooring lines known as ‘slow drift’, while high-frequency second order forces can interact with the natural frequencies of TLPs and with structural vibration modes.

This slow drift motion is known to be important for large moored offshore structures, but it may be less important for floating wind turbines, which are typically smaller structures and are subject to higher levels of loading from the wind. This is discussed further below and in Chapter 4.

Another source of nonlinear loading is viscous drag, which is included in Morison’s equation (1.1) but not in the potential flow solution (1.2). It can be accounted for in a potential flow model by taking only the drag term from Morison’s equation and applying it as an additional force alongside the forces in Equation (1.2) (Jonkman 2007).

#### 1.3.5 MOORING LINE LOADS

There are two main types of mooring lines (Chakrabarti 2005, chapter 8). Catenary lines hang loosely and provide a horizontal restoring force due to the weight of line which rises or falls as the platform moves, but they do not add significant rotational or vertical stiffness. Taut lines directly restrict platform motion and are often made of synthetic rope. Both can be used in complex arrangements, possibly with extra floats and weights to adjust the restoring force, and delta connections at the platform can increase yaw stiffness. Mooring arrangements for floating wind turbines are similar to other floating structures but usually have fewer lines.

The mooring line restoring force is non-linear, in particular for catenary mooring lines where the restoring force is due to the changing geometry of the lines. The dynamics of the mooring lines themselves can also be significant, especially with long lines in deep water, or when the motion of the platform is large (Matha, M Schlipf, et al. 2011). Nonetheless, if the motion of the platform is small, the dynamics of the mooring lines can often be neglected. Jonkman (2009) argues that as the effective inertia of the mooring system is only 2% of the total inertia of the floating wind

turbine it can be neglected, which is in any case a conservative approach. Kallesøe and AM Hansen (2011) agree that using a quasi-static model is conservative; they compared the quasi-static and dynamic approaches for the Hywind turbine, and found that the blade loads were unaffected by the mooring model but the dynamic model predicted lower tower loadings. On the other hand, Hall, Buckham and Crawford (2013) concluded that the fidelity of the mooring line modelling does affect the blade response, but the significance of the mooring line dynamics is strongly dependent on the type of floating platform.

A further possible simplification is to neglect the dynamics and linearise the restoring force, representing the mooring stiffness as a linear stiffness matrix relating to the six platform rigid-body degrees of freedom.

#### 1.3.6 STRUCTURE

Wind turbine blades are long, flexible beams usually made of glass or carbon fibre. They have a cylindrical cross section at the root, where they are attached to the hub, which gradually twists and flattens into an aerofoil profile further out along the blade. This makes them stiffer in the 'edgewise' direction than the 'flapwise' direction, with flapwise referring to bending about the chord of the aerofoils. The internal structure of the blades leads to coupling between torsion and flapwise & edgewise bending.

The blades can usually be 'pitched', that is, rotated about their axis to change the angle of attack of the aerofoils<sup>1</sup>. This terminology can be confusing, since rotation of the floating platform about a side-to-side axis is also referred to as 'pitch'; these are distinguished as 'blade pitch' and 'platform pitch'. When the turbine is operating, the blade pitch angle is usually near 0°, which means the chord lines of the aerofoils are roughly aligned with the rotor plane. When the turbine is shut down, the blades are usually pitched to roughly 90° to reduce the drag on the rotor.

The blades are attached to the 'hub', which is attached to the rotating drive shaft. The generator, gearbox and other equipment are housed in the 'nacelle', which is attached to the top of the tower via a yaw bearing. The

1. Not all wind turbines have pitching blades, but most large offshore turbines do. Other approaches are discussed by, for example, Burton et al. (2011, chapter 3)

tower is usually tubular steel, but steel lattice and tubular concrete towers have been used. The natural frequencies of bending of the tower often turn out to be in a similar range to the aerodynamic forces transmitted from the rotor, so avoiding resonance here is an important design constraint.

As the rotor rotates, the blades rotate through large angles. This can cause difficulties in the use of traditional structural approaches such as the basic finite element method. Instead some type of flexible multibody model is usually used, such as the one described in the next chapter.

### 1.3.7 CONTROL SYSTEM

Most large offshore turbines are variable-speed and variable-pitch; that is, they can vary the pitch angle of their blades as described above, and the generator speed can vary within certain limits. The control system therefore has two main means of influence: the blade pitch angle, which controls the aerodynamic forces, and the generator torque, which balances the aerodynamic torque on the rotor. The main aim of the controller is to maximise power capture while keeping the turbine within safe limits, but there may also be additional goals to balance:

- Improving power quality, that is, reducing short-term variations in power output.
- Reducing tower loads, by controlling the rotor thrust in response to measurements of tower-top acceleration.
- Reducing rotor loads, by cyclically pitching the blades independently of one another.
- For floating turbines, limiting the motion of the platform by controlling rotor thrust.

Typically the controller consists of two Proportional-Integral-Derivative (PID) control loops, one for the blade pitch angle and one for the generator torque. At lower wind speeds, the blade pitch angle is kept constant and the generator torque is varied to maintain the optimum rotor speed, which sets up the optimum aerodynamic conditions for maximum power capture. As the wind speed increases past the point where the maximum rated power of the turbine is being generated, the second control loop starts to

Table 1.1 – Overview of OC3-Hywind platform

Platform diameter	6.5 m to 9.4 m
Platform draft below sea level	120 m
Hub height above sea level	90 m
Number of mooring lines	3
Mooring line attachment depth	70 m
Platform mass	7466 t
Tower mass	250 t
Nacelle mass	240 t
Rotor mass	110 t
Rotor diameter	126 m
Rotor speed	6.9 rpm to 12.1 rpm
Operational wind speeds	$3 \text{ m s}^{-1}$ to $25 \text{ m s}^{-1}$

pitch the blades to capture less of the energy in the wind and maintain constant power (Burton et al. 2011, chapter 8).

For floating wind turbines, generally similar controllers are used but modifications must be made to avoid exciting platform motions (Nielsen, Hanson and Skaare 2006; Larsen and Hanson 2007).

Although the basic control system consists of linear feedback loops, there are several causes of non-linear behaviour which must be considered when building a linearised model of the whole wind turbine system. This will be discussed further in Chapter 6.

## 1.4 Case study design: OC3-Hywind

Although the approaches developed in this thesis are not specific to a particular wind turbine or floating platform design, to demonstrate their application an example design must be chosen. Throughout the thesis the OC3-Hywind floating platform is used for this purpose; this is a published design originally derived from the actual Hywind floating wind turbine (Figure 1.2), which has been widely used in studies of numerical modelling approaches for floating wind turbines. The wind turbine itself is the NREL

5 MW reference wind turbine. Full details are given by Jonkman (2010) and Jonkman, Butterfield, et al. (2009), and the main dimensions and properties of the structure are summarised in Table 1.1.

## 1.5 Time-domain modelling approaches

There is a need for new modelling approaches for floating wind turbines: traditional offshore codes cannot model the complex aerodynamics of the wind turbine, while traditional wind turbine codes typically have not included mooring line models and rigid-body motion of the wind turbine foundation. In the rest of this chapter, the approaches in the literature for modelling floating wind turbines are reviewed. The approaches are divided into the three broad categories which follow. In practice, of course, a range of approaches will coexist, as shown by Cermelli, Roddier and Aubault (2009) who discuss the stages of the design of the WindFloat prototype.

### 1.5.1 FULLY-COUPLED NON-LINEAR SIMULATION CODES

Fully-coupled non-linear time-domain simulation codes are in some sense the state of the art, and aim to model the majority of the important effects simultaneously. Only codes which encompass the dynamics of the wind turbine structure, control system dynamics, aerodynamics and hydrodynamics are included in this category. These codes have been produced either by adding hydrodynamic models to existing wind turbine simulation codes, by adding models of the aerodynamics, turbine structure and control systems to existing codes for floating structures, or by numerically coupling together existing offshore and wind turbine codes. Table 1.2 lists the fully-coupled codes found in the literature. Additional references have been given when the code is later used in further studies.

Although codes which are not fully-coupled are discussed in the next section, some flexibility has been allowed on the coupling of mooring line dynamics: the wind turbine codes FAST, Bladed and HAWC2 do not currently include mooring line dynamics, but are otherwise more similar

Table 1.2 – Fully-coupled non-linear simulation codes.

Code	Selected reference	Notes / other uses
FAST/ADAMS + custom	Withee 2004	Morison's equation loading on TLP.
FAST + TimeFloat	Cermelli, Roddier and Aubault 2009	Used for WindFloat design.
FAST + CHARM3D	Bae and Kim 2014	Used by Bae, Kim, et al. (2011) and Bae and Kim (2013).
SIMO/RIFLEX + HAWC2	Skaare, Hanson, et al. 2006	Used for Hywind design.
SIMO/RIFLEX + AeroDyn	Ormberg, Passano and Luxcey 2011	Used by Bachynski and Moan 2012.
SIMO/RIFLEX	Skaare, Nielsen and Hanson 2014	Stand-alone BEM model added to SIMO/RIFLEX since references above.
DeepC + HAWC2	Karimirad and Moan 2012c	Used to analyse a spar buoy.
3Dfloat	Myhr, Maus and Nygaard 2011	Used to compare a spar buoy and TLP.
DeepLines	Cunff et al. 2013	Mooring software extended for wind.

to the other codes in this section than those in the next section. These are listed in Table 1.3.

Several of these codes are also described in more detail in the review by Cordle (2010).

### 1.5.2 SIMPLIFIED TIME-DOMAIN CODES

To reduce complexity or increase efficiency, some couplings between parts of the model can be neglected, leading to a 'decoupled' code. In the literature codes have been described which neglect one or more of the following:

1. The influence of platform motion on rotor loading.
2. The influence of wind turbine structural dynamics on platform motion.
3. The influence of mooring line dynamics on platform motion.
4. The influence of the control system on platform motion.

Table 1.3 – Codes neglecting mooring line dynamics.

Code	Selected reference	Notes / other uses
FAST + HydroDyn	Jonkman 2009	Widely used, see below. <sup>†</sup>
FAST + hydrodynamics	Philippe, Babarit and Ferrant 2014	Assessing alternative hydrodynamic models.
Bladed	Garrad Hassan 2011	Used by Henderson, Argyriadis, et al. (2010) to assess a TLP.
HAWC2	DTU Wind Energy n.d.	Used by Karimirad and Moan (2012b) to analyse a tension-leg spar. Compared to FAST for a spar by Karimirad (2013).
HAWC2 + WAMSIM	Larsen, Kallesøe and HF Hansen 2011	Used to model Poseidon combined wind-wave platform.
Flex5 TLP	Ramachandran 2012	Extension of Flex5 for TLPs.

<sup>†</sup> Used by NREL researchers and others (Matha 2009; Matha, Fischer, et al. 2009; Jonkman and Matha 2009; Robertson and Jonkman 2011) to analyse various concepts. Used by Sultania and Manuel (2011) for reliability analysis of a spar. Used by Lackner and Rotea (2011) and Si, Karimi and Gao (2014) to investigate tuned mass dampers.

An extreme example of neglecting the coupling in point 1 would be to assume the thrust force is constant, regardless of the motion of the floating platform. In contrast, estimating the rotor thrust force as a drag law based on the *relative* wind speed would approximate this coupling, while the fully-coupled codes listed above model this coupling exactly (within the limits of the BEM model). If the coupling in point 2 is neglected, the platform motion would be solved while assuming the turbine structure is rigid. The dynamic response of the blades, for example, could be found afterwards given the platform motion solution, if required.

In some cases these types of decoupling can be appropriate simplifications, but sometimes the fully-coupled model is required for accurate results. Obvious examples include instabilities in the pitch control system described by Nielsen, Hanson and Skaare (2006) and Larsen and Hanson (2007), and a yaw instability caused by a failed blade (Jonkman 2007); these instabilities would be missed in a decoupled simulation. Bae, Kim, et al. (2011) compared results from a fully-coupled simulation with a decoupled

simulation where the rotor thrust is approximated by a simple drag law, with no accounting for the velocity of the platform, the control system, or the instantaneous position of the platform. They found the uncoupled model over-predicted the platform motions. On the other hand, Karimirad and Moan (2012a) did a similar comparison using a drag law which does account for the velocity of the platform, and concluded that the accuracy was acceptable. Another coupling which might be neglected is the gyroscopic behaviour of the rotor; Fujiwara, Tsubogo and Nihei (2011) modelled these effects but found them to be small for the spar buoy they considered.

Another approach to obtaining a simpler model is to keep full non-linear coupling but reduce the number of degrees of freedom used to describe the model. This approach is often more specific to a particular type of platform. For example, Sandner et al. (2012) developed a reduced-order model of a spar buoy consisting of four rigid bodies, which they used to identify critical load cases (Matha, Sandner and D Schlipf 2012). Table 1.4 lists studies which have used simplified time-domain analysis methods.

## 1.6 Linearised frequency-domain analysis

Rather than using simplified time-domain simulations as described above, another approach to obtaining faster approximate results is to use a linearised model which can be solved efficiently in the frequency domain. This type of approach is widely used for traditional floating offshore structures (Faltinsen 1993). The main difficulties for floating wind turbines are in finding a linearised representation of the model, and assessing the accuracy of this approximation. Various approaches to obtaining linearised models of floating wind turbines have been used and will be discussed in this section.

### 1.6.1 LINEARISED HYDRODYNAMIC FORCES

Linearised approaches to modelling the hydrodynamic forces are already widely used, such as the potential flow forces described by Equation (1.2).

Table 1.4 – Studies using simplified time-domain models.

Code	Selected reference	Notes / other uses
aNySIM + PHATAS	Gueydon, Lindenburg and Savenije 2013	Rigid tower, flexible blades, BEM aerodynamics.
SIMO/RIFLEX + TDHMILL	Karimirad and Moan 2012a	Rigid structure. Variable drag law (relative wind speed). Comparison against HAWC2. Also used by Muliawan et al. (2013).
TimeFloat	Cermelli, Roddier and Aubault 2009	Rigid structure. Constant drag law (relative wind speed).
SESAM	R Zhang et al. 2013	Rigid structure. Constant drag law (relative wind speed).
MOSES	Casale et al. 2010	Rigid structure. Constant rotor thrust.
OrcaFlex	Fulton et al. 2007	Rigid structure. Constant rotor thrust. Bladed used separately for wind turbine analysis.
Reduced-order spar model	Sandner et al. 2012	Four rigid bodies.
Reduced-order TLP model	Ramachandran et al. 2014	
Rigid body model	Wang and Sweetman 2012	Accounts for large rotations.

The second-order slow drift motion (see p 20) is more difficult to include in the linearised analysis. Although the force spectrum can be found, its statistics are non-Gaussian and finding the platform response is not straightforward (Chakrabarti 2005, chapter 5). Therefore it is interesting to know if slow drift motion is as significant for floating wind turbines as it is for other floating structures. This has been investigated recently by Roald et al. (2013) and Bayati et al. (2014), motivated by observations of possible second-order effects in model tests (Coulling et al. 2013). They calculate first- and second-order forces and responses for three specific floating wind turbine designs, a spar buoy, a TLP and a semisubmersible, using the commercial potential flow solver WAMIT (Wamit Inc 2002) together with linearised system matrices calculated by the wind turbine code FAST (Jonkman and Buhl 2005). This issue is revisited in Chapter 4, with the aim of developing a more general result by finding approximate closed-form expressions to estimate the second-order slow drift motion of platforms of different sizes.

Another source of nonlinear loading is viscous drag, which is not included in the potential flow solution (see p 22). Using the method of stochastic linearisation, the viscous loads can be well represented in the linearised model (Langley 1984). Because the viscous force depends on the relative flow velocity seen by the platform, it contributes to the damping matrix as well as the excitation forces. This will also be developed further in Chapter 4.

### 1.6.2 LINEARISED AERODYNAMIC FORCES

The simplest reasonable model of the aerodynamic forces is the actuator disk model (Burton et al. 2011, chapter 3), in which the rotor is considered as a homogeneous energy-extracting disc. The result is an expression for the thrust force  $T$  on the rotor:

$$T = 2\rho A_D U_\infty^2 a(1 - a) \quad (1.3)$$

where  $\rho$  is the density of air,  $A_D$  is the area of the rotor,  $U_\infty$  is the incoming wind speed far from the rotor, and  $a$  is the axial induction factor. This factor describes how much the incoming flow  $U_\infty$  is slowed by the presence of

the rotor: the flow speed at the rotor is  $U_{\text{rotor}} = U_{\infty}(1 - a)$ . The equilibrium value of the axial induction factor is found from the BEM method (see Chapter 5). For a floating wind turbine, the motion of the platform should also be considered. If the height of the rotor is  $h$  above the reference coordinate system origin, the velocity of the rotor in the downwind direction is  $v = \dot{\xi}_1 + h\dot{\xi}_5$ , where the rigid body translational velocities are  $[\dot{\xi}_1 \quad \dot{\xi}_2 \quad \dot{\xi}_3]$ , the rigid body angular velocities are  $[\dot{\xi}_4 \quad \dot{\xi}_5 \quad \dot{\xi}_6]$ , and the wind is assumed to be blowing along the  $x$  axis.

Lee (2005) obtains the linearised aerodynamic forces from the Taylor expansion of Equation (1.3), having replaced  $U_{\infty}$  by  $U_{\infty} - v$  to account for the rotor motion, and assuming that the axial induction factor is constant and that  $v \ll U_{\infty}$ . This gives

$$\begin{aligned} T(U_{\infty} - v) &= T(U_{\infty}) + \frac{\partial T}{\partial U_{\infty}} (-v) + O(v^2) \\ &= 2\rho_a A_D U_{\infty}^2 a(1 - a) - 4\rho_a A_D U_{\infty} [\dot{\xi}_1 + h\dot{\xi}_5] + O(\dot{\xi}^2) \end{aligned}$$

From this the elements of the aerodynamic applied forces and aerodynamic damping matrix may be found. A similar but more empirical approach was used by Fylling and Berthelsen (2011) who assumed the aerodynamic forces ‘to be proportional [to] the relative velocity [...with] a state dependent drag coefficient depending on the operating condition’, and the drag coefficient being ‘tuned’ to produce the correct thrust variations.

Halfpenny (1998) also studied floating wind turbines in the frequency domain, but made use of a BEM model (see p 19) of the aerodynamics rather than the actuator disc used by Lee (2005). In the BEM model, aerodynamic loads are found directly from tables of aerofoil coefficients. Halfpenny describes the linearised aerodynamic forces by ‘gain factors’ which relate the forces to variations in incoming wind speed, tangential blade speed and blade pitch angle. These gain factors are found numerically by perturbing the inputs and calculating the change in aerodynamic forces. Because the aerodynamic forces are linearised at multiple points along the blade, rather than applying to the rotor as a whole, this approach allows loads on individual blades to be described by the linearised model as well as the aggregate rotor loads.

These approaches use a ‘frozen wake’ assumption; that is, they as-

sume that the small perturbations in the linearised model occur sufficiently quickly that the overall flow through the rotor does not have time to respond and the axial induction factor  $a$  is constant. It is possible to relax this assumption by including a linearisation of the wake dynamics (see p 19). According to Engelen and Braam (2004), the frequency domain wind turbine code TURBU includes wake dynamics as a linearised sub-module which is then coupled together with other sub-modules in state-space form, but TURBU has not been adapted for floating wind turbines.

The most common approach to obtaining a linearised model of the floating wind turbine is to use one of the time-domain simulation codes from Section 1.5 that can numerically linearise the system equations. The first step is to solve the non-linear equations to find the equilibrium operating point; then each state of the system is perturbed in turn to find the mass, damping and stiffness matrices. The most widely used tool for this in the literature is FAST, which has been used by Wayman et al. (2006), Tracy (2007), Matha, Fischer, et al. (2009), Philippe, Babarit and Ferrant (2011), Philippe, Babarit and Ferrant (2012), Roald et al. (2013), and Hall, Buckham and Crawford (2014). This approach benefits from the completeness of the time-domain simulation codes, but a possible drawback is the 'black-box' nature of the process, which may make it harder to understand and assess the validity of the linearised model.

Finally, another approach which was used by Brommundt et al. (2012) is to calculate the rotor loads due to turbulent wind in advance, using a model of a fixed-base turbine in a time-domain simulation tool. The spectrum of the rotor loads is then applied in the frequency domain to the floating platform. Although this avoids the need for a linearised aerodynamic model, it neglects the coupling between the platform response and the aerodynamic loads, and does not make clear the relationship between the input and output statistics.

Linearised modelling of the wake dynamics and aerodynamic loads can be improved by the use of stochastic/harmonic linearisation. This is discussed further in Chapter 5.

### 1.6.3 LINEARISED STRUCTURAL DYNAMICS

As with time-domain codes, frequency-domain models can include or neglect structural flexibility. Matha, Fischer, et al. (2009) found that neglecting the flexibility of the structure has a significant effect on the Response Amplitude Operators (RAOs) of a TLP, so it should be included. To date, no frequency-domain analysis of floating wind turbines has included the flexible structure. The frequency domain code TURBU (Engelen and Braam 2004) does include structural flexibility, but does not appear to have been used to model floating wind turbines.

Linearised structural models are widely used for many types of structure, but there are some additional difficulties associated with the analysis of periodic rotating systems. This has been well covered for wind turbines, mostly in the context of stability analysis (see for example MH Hansen 2007), and will be returned to in Chapter 3.

Chapter 2 describes the development of a multibody flexible dynamics code, which can be used to obtain linearised models of the floating turbine structure. Similar results can be obtained from other codes such as FAST and Bladed. In Chapter 7 this will be incorporated into a complete model of a floating wind turbine in the frequency domain.

### 1.6.4 ACCURACY OF LINEARISED MODELS

Understanding the accuracy of the linearised models is as important as obtaining the linearised model in the first place, but is less clearly discussed in the literature. Halfpenny (1998) does discuss the accuracy of his linearised aerodynamic model, and identifies the major difficulty as the nonlinear relationship between angle of attack and the lift and drag forces once the blade has stalled: comparison of measurements with his model's predictions showed approximately 10 % errors in fatigue life for pre-stalled conditions, but in the region of 80 % error when the blades were stalling. Halfpenny uses the assumption of normally-distributed turbulence to consider the expected range of flow speeds: 95 % should be in the range  $\bar{U}(1 \pm 2I_u)$ , where  $\bar{U}$  is the mean wind speed and  $I_u$  is the turbulence intensity. This allows the occurrence of stall under any particular set of

conditions to be predicted, but does not improve the linearisation when it does occur. As a solution he does propose using a weighted linearisation to better account for stall but found it ineffective; this approach is pursued further in Chapter 5.

It is worth noting that the turbines studied by Halfpenny were stall regulated, that is, they rely on the reduced lift forces when the aerofoils are stalled as a means of limiting the aerodynamic torque on the rotor as the wind speed increases. In modern pitch-regulated turbines stall may be less frequent so the associated aerodynamic nonlinearity may be less important. However, stall may still occur, due to variations in the wind speed which occur faster than the control system can respond, or due to spatial variations within the rotor area.

## 1.7 Conclusions and outline of thesis

The novel nature of floating wind turbines means that new analysis tools are needed. The literature on modelling approaches for floating wind turbines has been growing rapidly over the last few years, much of it focusing on development of comprehensive time-domain analysis tools, which have been reviewed above. There is also a need for faster, more approximate methods, which can include simplified time-domain codes and linearised frequency-domain approaches. The frequency-domain approach has the advantage of producing results in forms which give greater insight: the spectrum and statistics of the response are found directly. It is the application of this approach to floating wind turbines which is developed over the following chapters.

Assessing the accuracy of the linearisations used in frequency domain analysis is important but has received relatively little explicit discussion in the literature. This will be addressed where possible throughout the thesis.

Linearisation of the wind turbine structure has been used to analyse stability and resonance problems, but structural dynamics have not yet been included in frequency-domain dynamic analysis of floating wind turbines. As a preliminary step, Chapter 2 presents the development of

a nonlinear flexible multibody simulation code, which forms the basis for benchmark simulations of the wind turbine dynamics and provides a source for later linearised models. The dynamic behaviour of the flexible wind turbine structure is nonlinear when mounted on a moving platform; the importance of this this is discussed in Chapter 3.

For frequency domain analysis, linearisation of hydrodynamic loads is an established approach, but nonlinear second-order forces and viscous drag may need to be considered. In Chapter 4 the hydrodynamic loading is introduced and it is demonstrated that unlike other, larger, floating structures, the nonlinear loads may be less important for floating wind turbines.

Simple linearised models of the rotor aerodynamics have been used in the literature, but more work is needed to improve the accuracy when stall occurs. Linearised models of the wake dynamics have also been used, but not applied to floating wind turbines. Both of these issues are addressed in Chapter 5.

The effect of the control system does not appear to have been included in frequency-domain models of floating wind turbines. A linearised model of the wind turbine control system is developed for this purpose in Chapter 6.

Finally, in Chapter 7 these various sub-problems are brought together to solve the response of a flexible floating wind turbine to wind and wave loading. Overall conclusions and suggestions for future work are given in Chapter 8.

## Chapter 2

### *Development of a nonlinear multibody dynamics code*

This chapter describes the development and validation of a flexible multibody dynamics code called 'mbwind'. The code is used in the following chapters, but the description of the theory and implementation given in this chapter is self-contained.

Multibody dynamics is concerned with modelling the behaviour of systems of interconnected, perhaps flexible, components which may undergo arbitrarily large motions relative to one another. It is therefore a suitable approach to modelling the structure of a wind turbine, where for example the blades can be viewed as flexible components connected together by a hub component, with the combination rotating relative to the tower. Although large rotations between components are properly accounted for, within a flexible component standard methods of structural dynamics which assume small deflections may still be used.

In the context of this thesis, the multibody dynamics code developed in this chapter provides a useful benchmark for more approximate analysis in later chapters, and is a useful tool for the generation of linearised models of the floating wind turbine structure. Although broadly similar codes already exist, creating a new one is helpful for the increased understanding of the author as well as the ability to easily modify the internals of the model in a way that would be more difficult with ready-made software.

The code itself is implemented in Python and is freely available (Lupton 2014b).

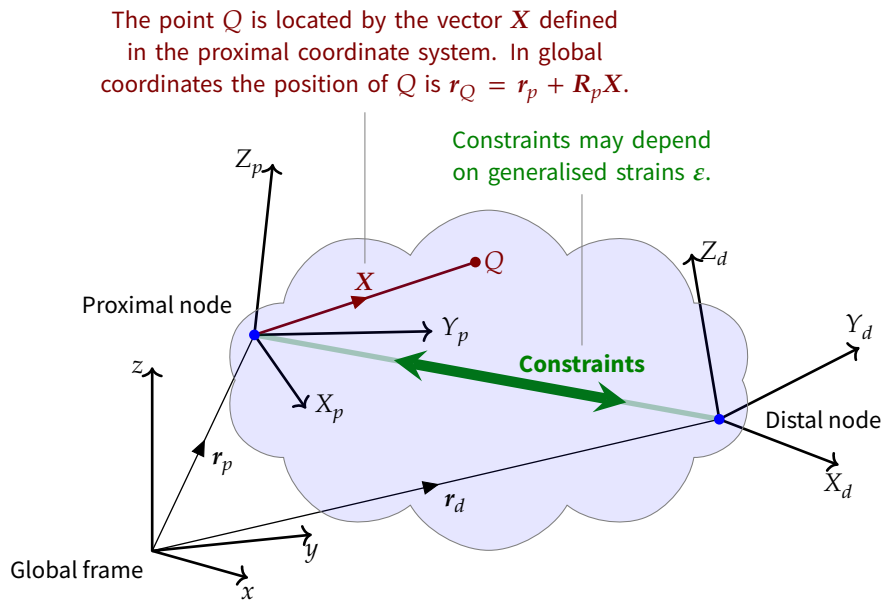


Figure 2.1 – A generic element.

## 2.1 Outline of the code

The dynamic system is described by a set of *nodes* connected by *elements*, in a similar way to a finite element model. From this model the equations of motion can be found in a systematic way. The approach here was originally based on Meijaard (2005), and has the following characteristics.

All elements in the model may be flexible. Examples include:

- a rigid connection between two nodes, which is a special case of a flexible element with no degrees of freedom;
- various types of joint, which possess degrees of freedom describing specific relative motions of two nodes; and
- flexible beam elements, with motions perhaps described by the amplitudes of pre-determined mode shapes

In each case, the degrees of freedom are known as the *generalised strains* of the element.

All elements can rotate through large angles relative to one another. This is important for modelling the rotation of the blades in a wind turbine rotor, for example. At the same time, within an element simplifications can be made by assuming that elastic deflections are small.

Finally, the structure is assumed to be in the form of a tree; that is, there are no closed structural loops. This is true for a typical wind turbine, and has a number of advantages:

- With no structural loops, the motion of all elements can be found explicitly by iteration from the fixed base of the tree to the leaves, without needing to solve nonlinear constraint equations.
- The structure is determinate, meaning that the degrees of freedom can unambiguously be identified as the free parameters of each element.
- Tree-connectivity results in an efficient, banded, structure of the system matrices.

The tree structure provides a convenient naming scheme for the nodes of an element: the node closest to the base of the tree is the *proximal* node, and any other nodes are *distal* nodes. This is illustrated in Figure 2.1.

The positions of the proximal and distal nodes of an element are denoted  $r_p$  and  $r_d$  respectively, and are expressed in the global fixed coordinate system  $xyz$ . For simplicity, it is assumed that the element has exactly one distal node. Elements with no distal nodes do not require kinematic constraints, and elements with multiple distal nodes must repeat the procedure for each node.

The orientation of the nodes are described by  $3 \times 3$  matrices  $R_p$  and  $R_d$ , whose columns are the unit vectors of the coordinate system attached to each node. This is not the minimal representation of the orientation: only three parameters are required to represent an orientation, but the matrix contains nine values. In the present formulation this is not an issue, because the nodal coordinates are not treated as degrees of freedom. Instead the nodal positions, orientations, velocities and accelerations are found recursively from the generalised coordinates, as described below. The generalised coordinates may include rotation parameters if necessary (see for example the hinge joint defined on p 50 and the free joint defined on p 53).

It is useful to have a local element reference frame, and here the frame attached to the proximal node of the element is always used. If the point  $Q$  shown in Figure 2.1 is located relative to the proximal node in the proximal coordinate system as  $X$ , the position of  $Q$  in the global coordinate system

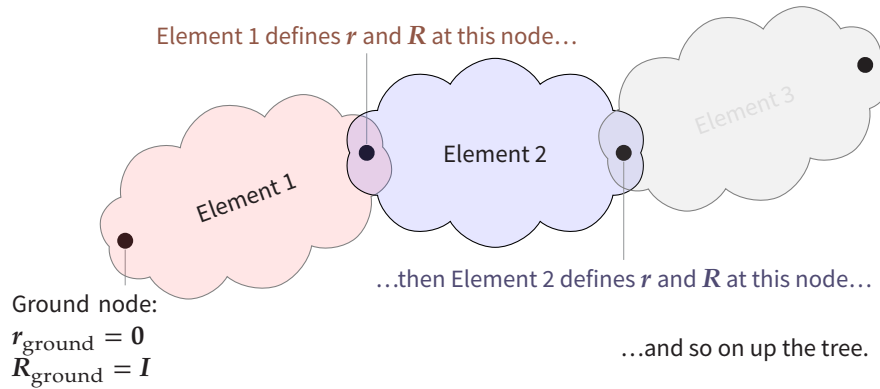


Figure 2.2 – Recursive calculation of element kinematics, starting from the known position of the ground node. Each element calculates the position  $\mathbf{r}$  and orientation  $\mathbf{R}$  of its distal node, as a function of the position and orientation of its proximal node, and the element generalised strains  $\boldsymbol{\varepsilon}$ . Because the elements are considered sequentially, at the time that the element calculations occur, the position and orientation of the proximal node are already known.

is  $\mathbf{r}_Q = \mathbf{r}_p + \mathbf{R}_p \mathbf{X}$ .

## 2.2 Model framework

Each type of element must provide three definitions:

1. The element *constraint equations*, describing the relative position and motion of the nodes of the element;
2. The element *mass matrices*, describing the element's contribution to the inertia of the system; and
3. The means of applying internal or external loading to the element.

Once these are determined for each element, the complete system is assembled from the individual equations for each element. These steps are described in general in this section; Section 2.3 gives the implementation for several specific types of element.

## 2.2.1 ELEMENT KINEMATICS

Because the elements are arranged in a tree structure, the position and orientation of each node can be found by working up the tree from the base towards the leaves (Figure 2.2). Elements must define the motion of their distal node given the motion of their proximal node. In general this transformation will be a function of the generalised strains  $\varepsilon$  of the element:

$$\mathbf{r}_d = F_r(\mathbf{r}_p, \mathbf{R}_p, \varepsilon) \quad (2.1a)$$

$$\mathbf{R}_d = F_R(\mathbf{r}_p, \mathbf{R}_p, \varepsilon) \quad (2.1b)$$

where  $\mathbf{r}_p$ ,  $\mathbf{R}_p$ ,  $\mathbf{r}_d$  and  $\mathbf{R}_d$  are the position and orientation of the nodes as discussed above. Figure 2.2 shows that although for an isolated element  $\mathbf{r}_d$  and  $\mathbf{R}_d$  depend on  $\mathbf{r}_p$ ,  $\mathbf{R}_p$  and  $\varepsilon$ , at the time that the element equations are evaluated in the assembled system  $\mathbf{r}_p$  and  $\mathbf{R}_p$  have already been fixed by the preceding element, and the only unknowns are the generalised strains  $\varepsilon$ . The position and orientation of the first 'ground' node are fixed; if rigid-body motion of the whole system is desired, the free joint element defined on p 53 may be used.

In practice the position and orientation are combined into a single vector,

$$\mathbf{x}_p = \begin{bmatrix} \mathbf{r}_p \\ \mathbf{R}_p^1 \\ \mathbf{R}_p^2 \\ \mathbf{R}_p^3 \end{bmatrix} \quad \mathbf{x}_d = \begin{bmatrix} \mathbf{r}_d \\ \mathbf{R}_d^1 \\ \mathbf{R}_d^2 \\ \mathbf{R}_d^3 \end{bmatrix} \quad (2.2)$$

where  $\mathbf{R}_p^j$  is the  $j$ th column of  $\mathbf{R}_p$ . Similarly the velocity and angular velocity of the nodes are written as:

$$\mathbf{v}_p = \begin{bmatrix} \dot{\mathbf{r}}_p \\ \boldsymbol{\omega}_p \end{bmatrix} \quad \mathbf{v}_d = \begin{bmatrix} \dot{\mathbf{r}}_d \\ \boldsymbol{\omega}_d \end{bmatrix} \quad (2.3)$$

Together the element coordinates and velocities are collected in the vectors

$\hat{\mathbf{q}}^{(e)}$  and  $\dot{\mathbf{q}}^{(e)}$ ,

$$\hat{\mathbf{q}}^{(e)} = \begin{bmatrix} \mathbf{x}_p \\ \mathbf{x}_d \\ \boldsymbol{\varepsilon} \end{bmatrix} \quad \dot{\mathbf{q}}^{(e)} = \begin{bmatrix} \mathbf{v}_p \\ \mathbf{v}_d \\ \dot{\boldsymbol{\varepsilon}} \end{bmatrix} \quad (2.4)$$

The distinction between  $\hat{\mathbf{q}}^{(e)}$  and  $\mathbf{q}^{(e)}$  is due to orientations being represented by the nine elements of the rotation matrix  $\mathbf{R}$  while angular velocities are represented by the three elements of  $\boldsymbol{\omega}$ ; there is not a one-to-one mapping between elements in  $\hat{\mathbf{q}}^{(e)}$  and  $\mathbf{q}^{(e)}$ . The derivatives of  $\hat{\mathbf{q}}^{(e)}$  and  $\mathbf{q}^{(e)}$  are related by

$$\dot{\hat{\mathbf{q}}}^{(e)} = \mathbf{A}(\hat{\mathbf{q}}^{(e)})\dot{\mathbf{q}}^{(e)} \quad (2.5)$$

In particular, this equation relates the derivatives of the unit vectors  $\mathbf{R}_p^i$  and  $\mathbf{R}_d^i$  ( $i = 1, 2, 3$ ) to the angular velocities  $\boldsymbol{\omega}_p$  and  $\boldsymbol{\omega}_d$ . However, because the element kinematics are found recursively by working up the tree, it is not necessary to construct the matrix  $\mathbf{A}$  explicitly.

When deriving the equations of motion for the elements, the velocity and acceleration of an arbitrary point within the element are needed. If the point is identified by the vector  $\mathbf{X}$  in the proximal reference frame, its position in the global reference frame is  $\mathbf{r} = \mathbf{r}_p + \mathbf{R}_p\mathbf{X}$  (Figure 2.1). In general the velocity and acceleration can be written in terms of the element coordinates (2.4) as

$$\dot{\mathbf{r}}(\mathbf{X}) = \mathbf{L}\dot{\mathbf{q}}^{(e)} \quad (2.6a)$$

$$\ddot{\mathbf{r}}(\mathbf{X}) = \mathbf{L}\ddot{\mathbf{q}}^{(e)} + \dot{\mathbf{L}}\dot{\mathbf{q}}^{(e)} \quad (2.6b)$$

where  $\mathbf{L}(\mathbf{X}, \hat{\mathbf{q}}^{(e)})$  is a spatially-varying matrix whose form depends on the type of element.

— *Kinematic constraints*

The positions and orientations of the nodes of an element are not independent; for example a hinge element requires both its nodes to be coincident, with orientations differing only by a rotation about the hinge axis. These requirements form the constraint equations of the element, written in general

as a set of equations

$$\Phi^{(e)}(\hat{q}^{(e)}, t) = \mathbf{0} \quad (2.7)$$

It is simplest to satisfy these constraints during solution of the system if they are differentiated to give constraints on accelerations (Jalón and Bayo 1994, chapter 3). The derivative of Equation (2.7) is

$$\frac{\partial \Phi^{(e)}}{\partial \hat{q}^{(e)}} \dot{\hat{q}}^{(e)} + \frac{\partial \Phi^{(e)}}{\partial t} = \mathbf{0} \quad (2.8)$$

Using Equation (2.5), this can be written as

$$\Phi_q^{(e)} \dot{q}^{(e)} = \mathbf{b}^{(e)} \quad (2.9a)$$

and with further differentiation,

$$\Phi_q^{(e)} \ddot{q}^{(e)} = \mathbf{c}^{(e)} \quad (2.9b)$$

where  $\Phi_q^{(e)}$  is the matrix of partial derivatives of  $\Phi^{(e)}$  with respect to the elements of  $q^{(e)}$ :

$$\Phi_q^{(e)} \equiv \frac{\partial \Phi^{(e)}}{\partial q^{(e)}} = \frac{\partial \Phi^{(e)}}{\partial \hat{q}^{(e)}} A(\hat{q}^{(e)}) \quad (2.10)$$

and

$$\mathbf{b}^{(e)} = -\Phi_t^{(e)} \quad (2.11a)$$

$$\mathbf{c}^{(e)} = -\dot{\Phi}_t^{(e)} - \dot{\Phi}_q^{(e)} \dot{q}^{(e)} \quad (2.11b)$$

where  $\Phi_t$  and  $\dot{\Phi}$  indicate respectively the partial and total derivatives with respect to time. The constraints between the nodes of an element do not depend explicitly on time, so  $\mathbf{b}^{(e)}$  is always zero. This is the case even if the motion of a joint is prescribed as a function of time. The remaining terms appearing in the constraint equations,  $\Phi_q^{(e)}$  and  $\mathbf{c}^{(e)}$ , must be found for each type of element. Generally the approach is to write the acceleration of the distal node in terms of the acceleration of the proximal node, the generalised strain accelerations, and any remaining terms:

$$\dot{v}_d = F_{vv} \dot{v}_p + F_{v\epsilon} \ddot{\epsilon} + F_2 \quad (2.12)$$

This can be written in block matrix form,

$$\begin{bmatrix} \mathbf{F}_{vv} & -\mathbf{I}_6 & \mathbf{F}_{v\epsilon} \end{bmatrix} \begin{bmatrix} \dot{\mathbf{v}}_p \\ \dot{\mathbf{v}}_d \\ \ddot{\boldsymbol{\epsilon}} \end{bmatrix} = -\mathbf{F}_2 \quad (2.13)$$

where  $\mathbf{I}_6$  is the  $6 \times 6$  identity matrix,  $\mathbf{F}_{vv}$  is a  $6 \times 6$  matrix, and if the element has  $N_\epsilon$  degrees of freedom then  $\mathbf{F}_{v\epsilon}$  is a  $6 \times N_\epsilon$  matrix. The required terms of Equation (2.9b) can then be recognised as

$$\boldsymbol{\Phi}_q^{(e)} = \begin{bmatrix} \mathbf{F}_{vv} & -\mathbf{I}_6 & \mathbf{F}_{v\epsilon} \end{bmatrix} \quad \mathbf{c}^{(e)} = -\mathbf{F}_2 \quad (2.14)$$

— *Example: prismatic joint*

As a simple example, consider a prismatic joint which allows a relative displacement of its two nodes a distance  $x$  along the joint axis  $\mathbf{n}$ . Because the joint has no mass, the velocity of an arbitrary point within the element (Equation 2.6) is not needed; only the relative position of the two nodes must be defined. The position and orientation of the distal node are

$$\mathbf{r}_d = \mathbf{r}_p + x\mathbf{n} \quad (2.15a)$$

$$\mathbf{R}_d = \mathbf{R}_p \quad (2.15b)$$

the velocity and angular velocity are

$$\dot{\mathbf{r}}_d = \dot{\mathbf{r}}_p + \dot{x}\mathbf{n} + x\tilde{\boldsymbol{\omega}}_p\mathbf{n} \quad (2.16a)$$

$$\boldsymbol{\omega}_d = \boldsymbol{\omega}_p \quad (2.16b)$$

and the acceleration and angular acceleration are

$$\ddot{\mathbf{r}}_d = \ddot{\mathbf{r}}_p + \ddot{x}\mathbf{n} + 2\dot{x}\tilde{\boldsymbol{\omega}}_p\mathbf{n} + x(\tilde{\boldsymbol{\omega}}_p\tilde{\boldsymbol{\omega}}_p + \dot{\tilde{\boldsymbol{\omega}}}_p)\mathbf{n} \quad (2.17a)$$

$$\dot{\boldsymbol{\omega}}_d = \dot{\boldsymbol{\omega}}_p \quad (2.17b)$$

In these equations, as in the rest of this chapter, the matrix form of the cross product has been used:  $\boldsymbol{\omega}_p \times \mathbf{n} = \tilde{\boldsymbol{\omega}}_p\mathbf{n} = -\tilde{\mathbf{n}}\boldsymbol{\omega}_p$  (see Appendix A.1). In the

form of Equation (2.13), Equations (2.17) become

$$\left[ \begin{array}{cc|cc|c} I & -x\tilde{n} & -I & \mathbf{0} & \mathbf{n} \\ \mathbf{0} & I & \mathbf{0} & -I & \mathbf{0} \end{array} \right] \begin{bmatrix} \dot{v}_p \\ \dot{v}_d \\ \ddot{\varepsilon} \end{bmatrix} = \begin{bmatrix} -2\dot{x}\tilde{\omega}_p \mathbf{n} - x\tilde{\omega}_p \tilde{\omega}_p \mathbf{n} \\ \mathbf{0} \end{bmatrix} \quad (2.18)$$

from which  $F_{vv}$ ,  $F_{v\varepsilon}$  and  $F_2$  can be recognised. This element has only one generalised strain, so  $\varepsilon = [x]$ .

— *Ground node constraints*

The rigid-body motion of the system as a whole must also be defined. The simplest solution is to prevent any motion of the first ‘ground’ node of the system, as shown in Figure 2.2. Acceleration constraints are also required:

$$\ddot{\mathbf{r}}_{\text{ground}} = \mathbf{0} \quad (2.19a)$$

$$\dot{\boldsymbol{\omega}}_{\text{ground}} = \mathbf{0} \quad (2.19b)$$

If rigid body motion of the whole system is desired, this can be modelled by using a free joint element (p 53) between the ground node and the rest of the system.

### 2.2.2 ELEMENT DYNAMICS

The equations of motion for each type of element are found using the principle of virtual power (Jalón and Bayo 1994, chapter 4), which states that the sum of all forces acting on the element multiplied by the corresponding virtual velocities is zero:

$$\dot{W}^* = \int_{\text{element}} \dot{\mathbf{r}}^{*\top} d\mathbf{f}_{\text{total}} = 0 \quad (2.20)$$

Here  $d\mathbf{f}_{\text{total}}$  is the total force acting on an infinitesimal piece of the element, expressed in the global fixed coordinate system, including inertial and applied forces:

$$d\mathbf{f}_{\text{total}} = d\mathbf{f} - \ddot{\mathbf{r}} dm \quad (2.21)$$

The virtual velocity of the piece  $\dot{\mathbf{r}}^*$  is any velocity which is consistent with the velocity constraints (2.9a) considered at a fixed point in time, that is,

such that  $\Phi_q^{(e)} \dot{q}^{*(e)} = \mathbf{0}$  and  $\dot{r}^* = L^{(e)} \dot{q}^{*(e)}$ .

Substituting Equation (2.21) into Equation (2.20) and using Equations (2.6) to express the acceleration in terms of the element generalised coordinates, the equation of motion becomes

$$\dot{q}^{*(e)\top} \int_{\text{element}} L^\top [(L\ddot{q}^{(e)} + \dot{L}\dot{q}^{(e)}) dm - df] = 0 \quad (2.22)$$

— *Lagrange multipliers*

Since the virtual velocities satisfy the constraints  $\Phi_q^{(e)} \dot{q}^{*(e)} = \mathbf{0}$ , if  $\lambda_c^{(e)}$  is a vector of Lagrange multipliers then  $\lambda_c^{(e)\top} \Phi_q^{(e)} \dot{q}^{*(e)}$  must also be zero and may be added to Equation (2.22):

$$\dot{q}^{*(e)\top} \left\{ \int_{\text{element}} L^\top [(L\ddot{q}^{(e)} + \dot{L}\dot{q}^{(e)}) dm - df] + \Phi_q^{(e)\top} \lambda_c^{(e)} \right\} = 0 \quad (2.23)$$

There is a sufficient number of Lagrange multipliers that they may be chosen so the term in braces is always equal to zero, giving the element equation of motion:

$$\int_{\text{element}} L^\top [(L\ddot{q}^{(e)} + \dot{L}\dot{q}^{(e)}) dm - df] + \Phi_q^{(e)\top} \lambda_c^{(e)} = 0 \quad (2.24)$$

These integrals, with respect to the mass and the applied force, must be evaluated for each type of element. In general the result can be written in a form chosen to match the complete system equations found below:

$$\begin{bmatrix} M^{(e)} & \Phi_q^{(e)\top} \end{bmatrix} \begin{bmatrix} \ddot{q}^{(e)} \\ \lambda_c^{(e)} \end{bmatrix} = Q_{\text{applied}}^{(e)} + Q_{\text{reaction}}^{(e)} - g^{(e)} \quad (2.25)$$

where the forces have been divided into applied forces and reaction forces:

$$M^{(e)} = \int_{\text{element}} L^\top L dm \quad (2.26a)$$

$$g^{(e)} = \int_{\text{element}} L^\top \dot{L} \dot{q}^{(e)} dm \quad (2.26b)$$

$$Q_{\text{applied}} = \int_{\text{element}} L^\top df_{\text{applied}} \quad (2.26c)$$

$$Q_{\text{reaction}} = \int_{\text{element}} L^\top df_{\text{reaction}} \quad (2.26d)$$

### 2.2.3 SYSTEM ASSEMBLY

The individual element equations are assembled following a standard finite-element procedure. A table is needed which maps the global nodes of the system to the proximal and distal nodes of each element. Each element's equations of motion are copied to the corresponding place in the global system matrices, summing entries for nodes shared between elements.

The whole-system equations have the same form as the individual element equations (2.25), except the joint reaction forces have cancelled out during the assembly process:

$$\begin{bmatrix} M & \Phi_q^\top \end{bmatrix} \begin{bmatrix} \ddot{q} \\ \lambda_c \end{bmatrix} = Q_{\text{applied}} - g \quad (2.27)$$

The whole-system constraint equations are simply the collection of all the element constraint equations (2.9b), that is,

$$\Phi_q \ddot{q} = c \quad (2.28)$$

Since the constraints have been expressed in terms of the accelerations, the above equations can be combined to give the augmented system equations:

$$\begin{bmatrix} M & \Phi_q^\top \\ \Phi_q & \mathbf{0} \end{bmatrix} \begin{bmatrix} \ddot{q} \\ \lambda_c \end{bmatrix} = \begin{bmatrix} Q_{\text{applied}} - g \\ c \end{bmatrix} \quad (2.29)$$

The ordering of the rows and columns of the system matrix does not affect the equations, and can be chosen for the best computational efficiency. The aim is to concentrate matrix entries as close to the diagonal as possible. If the elements are created from the bottom of the tree upwards, the correct ordering is to add constraints followed by strains and then distal nodes, thus placing the constraint equations and strains between the nodes to which they relate.

### 2.2.4 REACTION FORCES

Once the system equations have been solved and the kinematics of the system are known, the reaction forces at the nodes can be found iteratively by working backwards down the tree structure. For each element, the

reaction force  $\mathbf{R}_F^{(e)}$  and reaction moment  $\mathbf{R}_M^{(e)}$  are defined as acting *on* the element at its proximal node. Equilibrium of forces and moments gives:

$$\mathbf{0} = \mathbf{R}_F^{(e)} + \mathbf{F}_p + \mathbf{F}_d - \mathbf{R}_F^{(e+1)} \quad (2.30)$$

$$\mathbf{0} = \mathbf{R}_M^{(e)} + \mathbf{M}_p + \mathbf{M}_d - \mathbf{R}_M^{(e+1)} + \tilde{\mathbf{x}}_d (\mathbf{F}_d - \mathbf{R}_F^{(e+1)}) \quad (2.31)$$

where  $\mathbf{R}_F^{(e+1)}$  is the reaction force acting on the proximal node of the following element in the tree and  $\mathbf{x}_d = \mathbf{r}_d - \mathbf{r}_p$  is the position of the distal node relative to the proximal node in the global coordinate system. The forces and moments acting on the proximal and distal nodes are due to inertial and applied loads:

$$\begin{bmatrix} \mathbf{F}_p \\ \mathbf{M}_p \\ \mathbf{F}_d \\ \mathbf{M}_d \end{bmatrix} = \mathbf{Q}_{\text{applied}}^{(e)} - \mathbf{M}^{(e)} \begin{bmatrix} \ddot{\mathbf{r}}_p \\ \dot{\boldsymbol{\omega}}_p \\ \ddot{\mathbf{r}}_d \\ \dot{\boldsymbol{\omega}}_d \end{bmatrix} - \mathbf{g}^{(e)} \quad (2.32)$$

From these equations the reaction forces at each node in turn may be found, working backwards down the tree structure.

## 2.3 Element library

In this section concrete definitions will be given for several elements within the framework of Section 2.2. Each element must define:

1. the position of its distal nodes (Equation 2.1),
2. the constraints on the accelerations of its nodes (Equation 2.9b),
3. the inertial forces acting on the element (Equation 2.26), and
4. any applied or internal loads.

For clarity, throughout this section the superscript  $^{(e)}$  is omitted, but it is implied that all variables refer to the individual element. Generally capital bold letters  $\mathbf{X}$  are used to refer to a vector in the proximal coordinate system of an element, as shown in Figure 2.1. The same vector can be expressed in the global coordinate system as  $\mathbf{x} = \mathbf{R}_p \mathbf{X}$ . When the skew matrix form of the cross product (Equation A.1) is used, it can be written equivalently as

$$\mathbf{R}_p \tilde{\mathbf{X}} \mathbf{R}_p^\top = \tilde{\mathbf{x}}.$$

### 2.3.1 RIGID CONNECTION

A rigid connection (Figure 2.3) has no mass and simply allows for an offset and rotation from one node to another, defined by

1. the vector  $\mathbf{X}_c$ , the relative position of the distal node from the proximal node in the proximal coordinate frame, and
2. the transformation matrix  $\mathbf{R}_c$ , the orientation of the distal frame relative to the proximal frame.

The position and orientation of the distal node are:

$$\mathbf{r}_d = \mathbf{r}_p + \mathbf{R}_p \mathbf{X}_c = \mathbf{r}_p + \mathbf{x}_c \quad (2.33a)$$

$$\mathbf{R}_d = \mathbf{R}_p \mathbf{R}_c \quad (2.33b)$$

The velocity and angular velocity of the distal node are

$$\dot{\mathbf{r}}_d = \dot{\mathbf{r}}_p + \boldsymbol{\omega}_p \times \mathbf{x}_c = \dot{\mathbf{r}}_p - \tilde{\mathbf{x}}_c \boldsymbol{\omega}_p \quad (2.34a)$$

$$\boldsymbol{\omega}_d = \boldsymbol{\omega}_p \quad (2.34b)$$

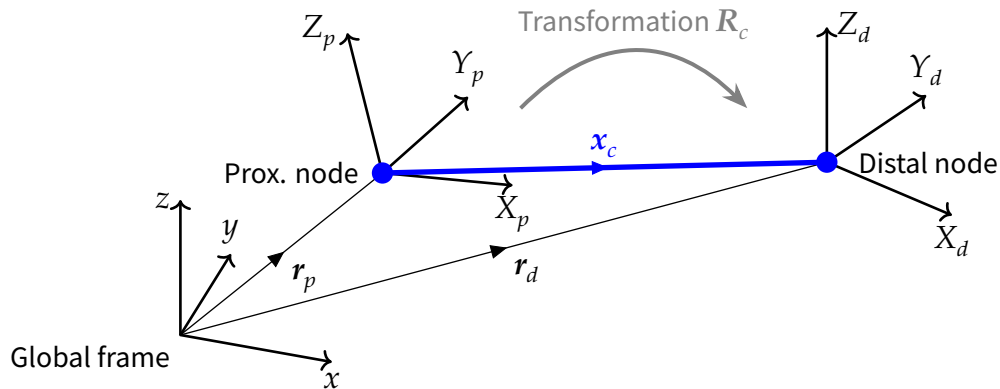


Figure 2.3 – Rigid connection.

making use of the matrix form of the cross product. Differentiation gives the distal linear and angular acceleration,

$$\ddot{\mathbf{r}}_d = \ddot{\mathbf{r}}_p - \tilde{\mathbf{x}}_c \dot{\boldsymbol{\omega}}_p + \tilde{\boldsymbol{\omega}}_p \tilde{\boldsymbol{\omega}}_p \mathbf{x}_c \quad (2.35a)$$

$$\dot{\boldsymbol{\omega}}_d = \dot{\boldsymbol{\omega}}_p \quad (2.35b)$$

Rearranging these in the form of Equation (2.13) gives

$$\left[ \begin{array}{cc|cc} \mathbf{I} & -\tilde{\mathbf{x}}_c & -\mathbf{I} & \mathbf{0} \\ \mathbf{0} & \mathbf{I} & \mathbf{0} & -\mathbf{I} \end{array} \right] \begin{bmatrix} \ddot{\mathbf{r}}_p \\ \dot{\boldsymbol{\omega}}_p \\ \ddot{\mathbf{r}}_d \\ \dot{\boldsymbol{\omega}}_d \end{bmatrix} = \begin{bmatrix} -\tilde{\boldsymbol{\omega}}_p \tilde{\boldsymbol{\omega}}_p \mathbf{x}_c \\ \mathbf{0} \end{bmatrix} \quad (2.36)$$

from which the constraint matrices can be recognised as

$$\mathbf{F}_{vv} = \begin{bmatrix} \mathbf{I} & -\tilde{\mathbf{x}}_c \\ \mathbf{0} & \mathbf{I} \end{bmatrix} \quad (2.37a)$$

$$\mathbf{F}_{v\varepsilon} = \begin{bmatrix} \\ \\ \\ \end{bmatrix} \quad (2.37b)$$

$$\mathbf{F}_2 = \begin{bmatrix} \tilde{\boldsymbol{\omega}}_p \tilde{\boldsymbol{\omega}}_p \mathbf{x}_c \\ \mathbf{0} \end{bmatrix} \quad (2.37c)$$

where  $\mathbf{I}$  and  $\mathbf{O}$  indicate  $3 \times 3$  identity and zero matrices respectively.  $\mathbf{F}_{v\varepsilon}$  is empty as the element has no generalised strains.

### 2.3.2 HINGE JOINT

The hinge joint (Figure 2.4) has a single generalised strain, the angle of rotation about the hinge axis:  $\varepsilon = [\theta]$ . The element parameters are

1. the hinge axis, defined by the unit vector  $\mathbf{N}$ , and
2. an optional transformation matrix  $\mathbf{R}_c$  which defines an additional difference in orientation between the proximal and distal nodes when the rotation angle is zero (not shown in the diagram).

The proximal and distal nodes always have the same position but may differ in orientation.

The hinge axis is defined by the unit vector  $\mathbf{N}$  in the proximal frame, or

$\mathbf{n} = \mathbf{R}_p \mathbf{N}$  in the global frame. The rotation about the hinge axis is given by the transformation matrix  $\mathbf{R}_n$ , found using the Rodriguez formula (Shabana 2013, p 39):

$$\mathbf{R}_n = \mathbf{I} + \tilde{\mathbf{N}} \sin \theta + 2\tilde{\mathbf{N}}\tilde{\mathbf{N}} \sin^2 \frac{\theta}{2} \quad (2.38)$$

In addition, an optional transformation  $\mathbf{R}_c$  is applied to give the orientation of the distal node when the hinge rotation angle is zero. The position and orientation of the distal node are

$$\mathbf{r}_d = \mathbf{r}_p \quad (2.39a)$$

$$\mathbf{R}_d = \mathbf{R}_p \mathbf{R}_n \mathbf{R}_c \quad (2.39b)$$

the velocity and angular velocity are

$$\dot{\mathbf{r}}_d = \dot{\mathbf{r}}_p \quad (2.40a)$$

$$\boldsymbol{\omega}_d = \boldsymbol{\omega}_p + \mathbf{n}\dot{\theta} \quad (2.40b)$$

and the distal linear and angular acceleration are

$$\ddot{\mathbf{r}}_d = \ddot{\mathbf{r}}_p \quad (2.41a)$$

$$\dot{\boldsymbol{\omega}}_d = \dot{\boldsymbol{\omega}}_p + \tilde{\boldsymbol{\omega}}_p \mathbf{n}\dot{\theta} + \mathbf{n}\ddot{\theta} \quad (2.41b)$$

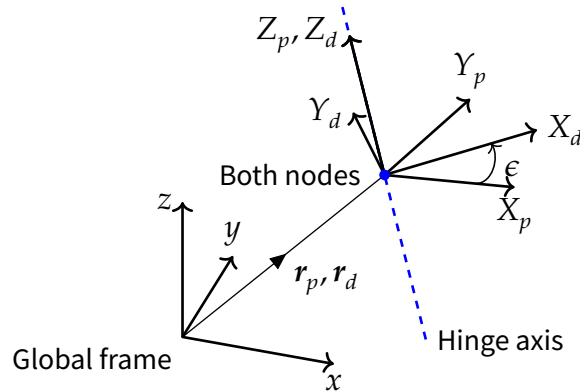


Figure 2.4 – Hinge joint. The hinge axis is shown by the dashed blue line.

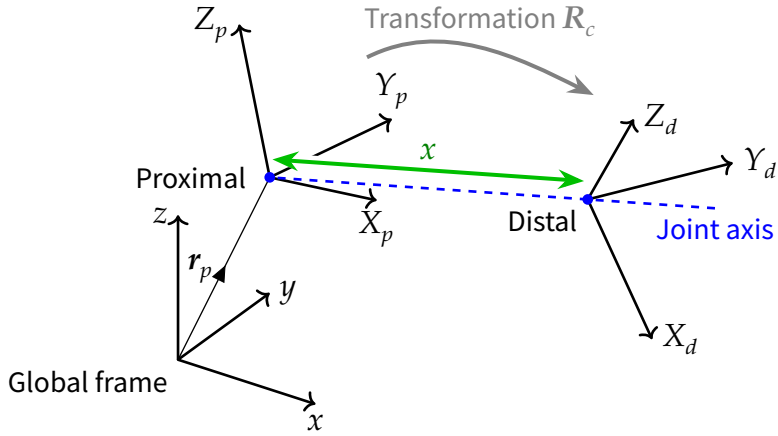


Figure 2.5 – Prismatic joint.

Rearranging these in the form of Equation (2.13) gives

$$\left[ \begin{array}{cc|cc|c} I & \mathbf{0} & -I & \mathbf{0} & \mathbf{0} \\ \mathbf{0} & I & \mathbf{0} & -I & n \end{array} \right] \begin{bmatrix} \ddot{r}_p \\ \dot{\omega}_p \\ \ddot{r}_d \\ \dot{\omega}_d \\ \ddot{\theta} \end{bmatrix} = \begin{bmatrix} \mathbf{0} \\ -\tilde{\omega}_p n \dot{\theta} \end{bmatrix} \quad (2.42)$$

from which the constraint matrices can be recognised as

$$F_{vv} = \begin{bmatrix} I & \mathbf{0} \\ \mathbf{0} & I \end{bmatrix} \quad (2.43a)$$

$$F_{v\varepsilon} = \begin{bmatrix} \mathbf{0} \\ n \end{bmatrix} \quad (2.43b)$$

$$F_2 = \begin{bmatrix} \mathbf{0} \\ \tilde{\omega}_p n \dot{\theta} \end{bmatrix} \quad (2.43c)$$

### 2.3.3 PRISMATIC JOINT

The prismatic joint (Figure 2.5) has a single generalised strain, the displacement along the joint axis:  $\varepsilon = [x]$ . The element parameters are

1. the joint axis, defined by the unit vector  $N$ , and
2. an optional transformation matrix  $R_c$  which defines a constant rotation

between the proximal and distal nodes.

The proximal and distal nodes always have the same relative orientation but may differ in position.

The prismatic joint was used as an example in Section 2.2.1. The constraint matrices are:

$$F_{vv} = \begin{bmatrix} I & \mathbf{0} \\ \mathbf{0} & I \end{bmatrix} \quad (2.44a)$$

$$F_{v\varepsilon} = \begin{bmatrix} \mathbf{n} \\ \mathbf{0} \end{bmatrix} \quad (2.44b)$$

$$F_2 = \begin{bmatrix} 2\dot{x}\tilde{\omega}\mathbf{n} + x\tilde{\omega}\tilde{\omega}\mathbf{n} \\ \mathbf{0} \end{bmatrix} \quad (2.44c)$$

#### 2.3.4 FREE JOINT

The free joint allows motion in six degrees of freedom; its six generalised strains consist of three translations and three Euler angles:

$$\varepsilon = [X \ Y \ Z \ \theta_x \ \theta_y \ \theta_z]^\top = \begin{bmatrix} \varepsilon_X \\ \varepsilon_\theta \end{bmatrix} \quad (2.45)$$

The Euler angles are defined as

1. yaw  $\theta_z$  about the Z axis,
2. pitch  $\theta_y$  about the rotated Y axis, and
3. roll  $\theta_x$  about the twice-rotated X axis.

An optional transformation matrix  $\mathbf{R}_c$  defines an additional constant rotation between the proximal and distal nodes.

The position and orientation of the distal node are:

$$\mathbf{r}_d = \mathbf{r}_p + \mathbf{R}_p \varepsilon_X \quad (2.46a)$$

$$\mathbf{R}_d = \mathbf{R}_p \mathbf{R}_j \mathbf{R}_c \quad (2.46b)$$

where the Euler angles define the rotation matrix

$$\begin{aligned} \mathbf{R}_j &= \text{rotation}_Z(\theta_z) \text{rotation}_Y(\theta_y) \text{rotation}_X(\theta_x) \\ &= \begin{bmatrix} \cos \theta_z & -\sin \theta_z & 0 \\ \sin \theta_z & \cos \theta_z & 0 \\ 0 & 0 & 1 \end{bmatrix} \begin{bmatrix} \cos \theta_y & 0 & \sin \theta_y \\ 0 & 1 & 0 \\ -\sin \theta_y & 0 & \cos \theta_y \end{bmatrix} \begin{bmatrix} 1 & 0 & 0 \\ 0 & \cos \theta_x & -\sin \theta_x \\ 0 & \sin \theta_x & \cos \theta_x \end{bmatrix} \end{aligned} \quad (2.47)$$

The velocity and angular velocity are

$$\dot{\mathbf{r}}_d = \dot{\mathbf{r}}_p + \mathbf{R}_p \dot{\boldsymbol{\varepsilon}}_X + \tilde{\boldsymbol{\omega}}_p \mathbf{R}_p \boldsymbol{\varepsilon}_X \quad (2.48a)$$

$$\boldsymbol{\omega}_d = \boldsymbol{\omega}_p + \mathbf{R}_p \mathbf{G}(\boldsymbol{\varepsilon}) \dot{\boldsymbol{\varepsilon}}_\theta \quad (2.48b)$$

where

$$\mathbf{G}(\boldsymbol{\varepsilon}) = \begin{bmatrix} \cos \theta_y \cos \theta_z & -\sin \theta_z & 0 \\ \cos \theta_y \sin \theta_z & \cos \theta_z & 0 \\ -\sin \theta_y & 0 & 1 \end{bmatrix} \quad (2.49)$$

The acceleration and angular acceleration are

$$\ddot{\mathbf{r}}_d = \ddot{\mathbf{r}}_p + \mathbf{R}_p \ddot{\boldsymbol{\varepsilon}}_X + 2\tilde{\boldsymbol{\omega}}_p \mathbf{R}_p \dot{\boldsymbol{\varepsilon}}_X + (\tilde{\boldsymbol{\omega}}_p \tilde{\boldsymbol{\omega}}_p + \dot{\tilde{\boldsymbol{\omega}}}_p) \mathbf{R}_p \boldsymbol{\varepsilon}_X \quad (2.50a)$$

$$\dot{\boldsymbol{\omega}}_d = \dot{\boldsymbol{\omega}}_p + \mathbf{R}_p \mathbf{G} \ddot{\boldsymbol{\varepsilon}}_\theta + \tilde{\boldsymbol{\omega}}_p \mathbf{R}_p \mathbf{G} \dot{\boldsymbol{\varepsilon}}_\theta + \mathbf{R}_p \dot{\mathbf{G}} \dot{\boldsymbol{\varepsilon}}_\theta \quad (2.50b)$$

where

$$\dot{\mathbf{G}}(\boldsymbol{\varepsilon}, \dot{\boldsymbol{\varepsilon}}) = \begin{bmatrix} -\dot{\theta}_z \sin \theta_z \cos \theta_y & -\dot{\theta}_x \cos \theta_z \sin \theta_y & -\dot{\theta}_y \cos \theta_z \\ +\dot{\theta}_z \cos \theta_z \cos \theta_y & -\dot{\theta}_x \sin \theta_z \sin \theta_y & -\dot{\theta}_y \sin \theta_z \\ 0 & -\dot{\theta}_x \cos \theta_y & 0 \end{bmatrix} \quad (2.51)$$

The constraint matrices are found, in the same way as before, as

$$\mathbf{F}_{vv} = \begin{bmatrix} \mathbf{I} & -\mathbf{R}_p \tilde{\boldsymbol{\varepsilon}}_X \mathbf{R}_p^\top \\ \mathbf{0} & \mathbf{I} \end{bmatrix} \quad (2.52a)$$

$$\mathbf{F}_{v\varepsilon} = \begin{bmatrix} \mathbf{R}_p & \mathbf{0} \\ \mathbf{0} & \mathbf{R}_p \mathbf{G} \end{bmatrix} \quad (2.52b)$$

$$\mathbf{F}_2 = \begin{bmatrix} 2\tilde{\boldsymbol{\omega}}_p \mathbf{R}_p \dot{\boldsymbol{\varepsilon}}_X + \tilde{\boldsymbol{\omega}}_p \tilde{\boldsymbol{\omega}}_p \mathbf{R}_p \boldsymbol{\varepsilon}_X \\ \tilde{\boldsymbol{\omega}}_p \mathbf{R}_p \mathbf{G} \dot{\boldsymbol{\varepsilon}}_\theta + \mathbf{R}_p \dot{\mathbf{G}} \dot{\boldsymbol{\varepsilon}}_\theta \end{bmatrix} \quad (2.52c)$$

## 2.3.5 RIGID BODY

The rigid body element (Figure 2.6) has no degrees of freedom. The element parameters are

1. the mass  $m$ ,
2. the offset  $X_c$  between the proximal node and the centre of mass, and
3. the inertia matrix  $J$ , defined at the proximal node about the proximal coordinate axes.

As the rigid body element has only one node, no kinematic constraints are needed. The inertial loads are found as follows.

If  $X$  is the position of a point P in the body which is fixed relative to the proximal node, then in the global reference frame the position, velocity and acceleration of P are:

$$\mathbf{r} = \mathbf{r}_p + \mathbf{R}_p \mathbf{X} \quad (2.53a)$$

$$\dot{\mathbf{r}} = \dot{\mathbf{r}}_p + \tilde{\omega}_p \mathbf{R}_p \mathbf{X} \quad (2.53b)$$

$$\ddot{\mathbf{r}} = \ddot{\mathbf{r}}_p + (\tilde{\omega}_p \tilde{\omega}_p + \dot{\tilde{\omega}}_p) \mathbf{R}_p \mathbf{X} \quad (2.53c)$$

By making use of Equation (A.7),  $L$  and  $\dot{L}\dot{\mathbf{q}}^{(e)}$  from Equation (2.6) can be found for this element as

$$L = \begin{bmatrix} \mathbf{I} & -\tilde{\mathbf{x}} \end{bmatrix} \quad (2.54a)$$

$$\dot{L}\dot{\mathbf{q}}^{(e)} = \tilde{\omega}_p \tilde{\omega}_p \mathbf{x} \quad (2.54b)$$

From these, the matrices appearing in the equation of motion (2.26) may be found. The symmetric mass matrix is

$$\begin{aligned} \mathbf{M}^{(e)} &= \int \begin{bmatrix} \mathbf{I} & -\tilde{\mathbf{x}} \\ \cdot & -\tilde{\mathbf{x}}\tilde{\mathbf{x}} \end{bmatrix} dm \\ &= \begin{bmatrix} \mathbf{I} & -m\mathbf{R}_p \tilde{\mathbf{X}}_c \mathbf{R}_p^T \\ \cdot & \mathbf{R}_p \mathbf{J} \mathbf{R}_p^T \end{bmatrix} \end{aligned} \quad (2.55)$$

and the quadratic force vector, making use of Equation (A.10), is

$$\begin{aligned} \mathbf{g}^{(e)} &= \int \begin{bmatrix} \tilde{\omega}_p \tilde{\omega}_p \mathbf{x} \\ \tilde{\mathbf{x}} \tilde{\omega}_p \tilde{\omega}_p \mathbf{x} \end{bmatrix} dm \\ &= \begin{bmatrix} m \mathbf{R}_p \tilde{\Omega} \tilde{\Omega} \mathbf{X}_c \\ \mathbf{R}_p \tilde{\Omega} \mathbf{J} \Omega \end{bmatrix} \end{aligned} \quad (2.56)$$

where  $\Omega = \mathbf{R}_p^\top \omega_p$  is the angular velocity in local coordinates. The latter terms represent the centrifugal force and moment on the rigid body.

### 2.3.6 MODAL FINITE-ELEMENT BEAM ELEMENT

Many different implementations of a flexible beam element are possible within the overall multibody framework described so far. For the purposes of this thesis, the beam elements are used to model the flexible parts of the wind turbine structure: the tower and the blades. Since a high level of detail is not required, a simple Euler-Bernoulli finite element model of the beam is used to find the inertia and stiffness of the beam, and a modal reduction is then applied to reduce the required number of degrees of freedom for the element. Although in general wind turbine blades exhibit coupling of bending and torsion, in this thesis the model is applied only to simple blade models for which this coupling can be neglected. On the other hand, wind turbine blades typically have a large range of initial twist angles along the blade which should be accounted for in the model; this is the purpose of the intermediate coordinate systems described below. The derivation of this element is based on Shabana (2012, chapter 7) and Shabana (2013, chapter 6).

The flexible element may be implemented either with or without a distal node. If it is not needed, such as for the blades of a wind turbine, the model is kept simpler by omitting the distal node. If it is needed, such as for the tower of a wind turbine, the element gains an additional node, six additional constraint equations, and additional strains corresponding to the attachment modes which will be described below. In the implementation two versions of the flexible beam element are provided for each of these situations.

The finite elements are assumed to have shape functions which can

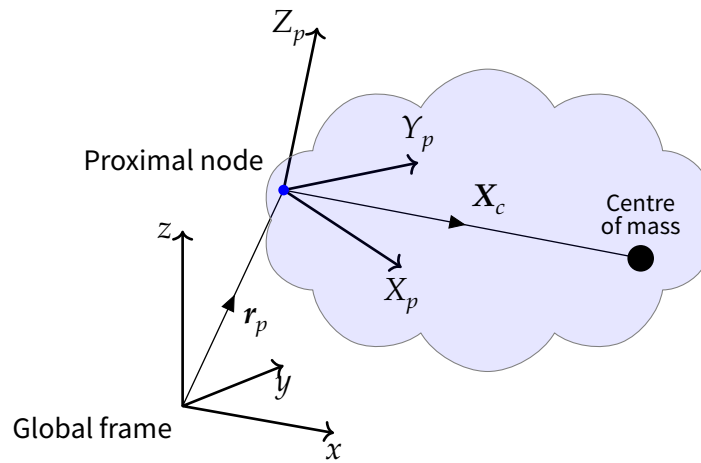


Figure 2.6 – Rigid body element.

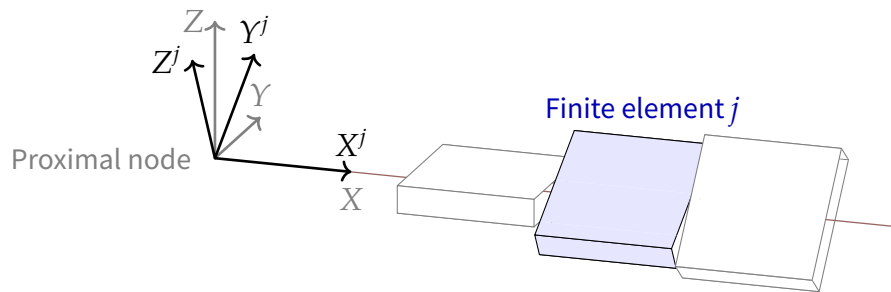


Figure 2.7 – Finite-element beam element. To account for initial rotations, such as due to blade twist, the  $j$ th finite element is defined in the coordinate system  $X^j Y^j Z^j$ , which may be rotated relative to the proximal coordinate system  $XYZ$ .

represent finite rigid-body translations, so that the undeflected position of the finite element can be described by the same shape functions as the elastic deformation of the finite element. On the other hand, simple beam finite elements cannot typically represent arbitrary rigid-body rotations because they are based on small slopes rather than finite rotations. Therefore an additional intermediate coordinate system  $X^jY^jZ^j$  is used to provide the arbitrary orientation of the  $j$ th finite element in its undeflected state, and any further small rotations due to elastic deformation are represented by the finite element shape functions. This is illustrated in Figure 2.7.

Let  $Q$  be a point within this  $j$ th finite element. The position of  $Q$  in the  $X^jY^jZ^j$  coordinate system is  $w^j = \hat{N}^j e^j$ , where  $\hat{N}^j$  are the shape functions and  $e^j$  are the 12 corresponding nodal coordinates of the  $j$ th finite element:

$$e^j = \begin{bmatrix} \xi_1^j \\ \Theta_1^j \\ \xi_2^j \\ \Theta_2^j \end{bmatrix} \quad (2.57)$$

where  $\xi_1^j$  and  $\xi_2^j$  are the positions of each end of the finite element in the intermediate coordinate system, and  $\Theta_1^j$  and  $\Theta_2^j$  are the small rotations about the intermediate coordinate system axes, also at each end of the finite element. The nodal coordinates can be divided into the values in the undeflected state  $e_0^j$  and the elastic deflections  $e_f^j$ :

$$e^j = e_0^j + e_f^j \quad (2.58)$$

The shape functions are

$$\hat{N}^j = \begin{bmatrix} 1-\xi & 0 & 0 & 0 & 0 & 0 \\ 0 & (1-\xi)^2(1+2\xi) & 0 & 0 & 0 & l\xi(1-\xi)^2 \\ 0 & 0 & (1-\xi)^2(1+2\xi) & 0 & -l\xi(1-\xi)^2 & 0 \\ \xi & 0 & 0 & 0 & 0 & 0 \\ 0 & \xi^2(3-2\xi) & 0 & 0 & 0 & -l\xi^2(1-\xi) \\ 0 & 0 & \xi^2(3-2\xi) & 0 & l\xi^2(1-\xi) & 0 \end{bmatrix} \quad (2.59)$$

where  $\xi$  is the non-dimensional length within the element which varies from 0 to 1, and  $l$  is the actual length of the finite element.

The position of  $Q$  in the proximal  $XYZ$  coordinate system is  $X^j = C_X^j w^j$ , where  $C_X^j$  is the transformation matrix from  $X^jY^jZ^j$  to  $XYZ$ . A similar but

opposite relationship transforms the finite element nodal coordinates into the proximal XYZ coordinate system:  $e^j = C_q^j q_n^j$ . The nodal coordinates for finite element  $j$  are a subset of the nodal coordinates of the whole body  $q_n$ , which is expressed by  $q_n^j = B_1^j q_n$  where  $B_1^j$  is a Boolean matrix. All together, these give the position of  $Q$  in the proximal coordinate system in terms of the coordinates of the whole body:

$$\begin{aligned} X^j &= C_X^j \hat{N}^j C_q^j B_1^j q_n \\ &= N^j q_n \end{aligned} \quad (2.60)$$

Similar to Equation (2.58), the nodal coordinates for the whole body consist of the values in the undeformed state  $q_0$  plus the elastic deflections  $\bar{q}_f$ . A set of reference conditions are required which describe how rigid-body motion of the proximal node is related to the rigid-body motion of the finite-element model; here the first node of the finite element model is chosen to be rigidly attached to the proximal node of the multibody model element. These six constraints on the motion of the finite element model are expressed by a matrix  $B_2 = [O \ I]^T$ , leading to

$$\begin{aligned} q_n &= q_0 + \bar{q}_f \\ &= q_0 + B_2 q_f \end{aligned} \quad (2.61)$$

— *Dynamics: inertial loads*

In the global reference frame the position, velocity and acceleration of the point  $Q$  are:

$$r^j = r_p + R_p X^j \quad (2.62a)$$

$$\dot{r}^j = \dot{r}_p + \tilde{\omega}_p R_p X^j + R_p \dot{X}^j \quad (2.62b)$$

$$\ddot{r}^j = \ddot{r}_p + (\tilde{\omega}_p \tilde{\omega}_p + \dot{\tilde{\omega}}_p) R_p X^j + 2\tilde{\omega}_p R_p \dot{X}^j + R_p \ddot{X}^j \quad (2.62c)$$

From Equations (2.60)–(2.61), the velocity of  $Q$  in the proximal reference frame is

$$\dot{X}^j = N^j B_2 \dot{q}_f \quad (2.63)$$

The generalised coordinate velocities for the flexible body consist of the rigid-body motion of the proximal node and the flexible finite element

coordinates:  $\dot{\mathbf{q}}^\top = [\dot{\mathbf{r}}_p^\top \quad \boldsymbol{\omega}_p^\top \quad \dot{\mathbf{q}}_f^\top]^\top$ . By making use of Equation (A.7),  $\mathbf{L}$  and  $\dot{\mathbf{L}}\dot{\mathbf{q}}^{(e)}$  from Equation (2.6) can be found for this element as

$$\mathbf{L}^j = [\mathbf{I} \quad -\mathbf{R}_p \tilde{\mathbf{X}}^j \mathbf{R}_p^\top \quad \mathbf{R}_p \mathbf{N}^j \mathbf{B}_2] \quad (2.64a)$$

$$\dot{\mathbf{L}}^j \dot{\mathbf{q}}^{(e)} = \mathbf{R}_p \tilde{\boldsymbol{\Omega}} \tilde{\mathbf{X}}^j + 2\mathbf{R}_p \tilde{\boldsymbol{\Omega}} \mathbf{N}^j \mathbf{B}_2 \dot{\mathbf{q}}_f \quad (2.64b)$$

where  $\boldsymbol{\Omega} = \mathbf{R}_p^\top \boldsymbol{\omega}_p$  is the angular velocity in local coordinates.

From these, the matrices appearing in the element equation of motion may be found. From Equations (2.26) and (2.64a), the symmetric mass matrix which describes the inertial loads on finite element  $j$  is

$$\mathbf{M}^j = \int T \begin{bmatrix} \mathbf{I} & -\tilde{\mathbf{X}}^j & \mathbf{N}^j \mathbf{B}_2 \\ \cdot & -\tilde{\mathbf{X}}^j \tilde{\mathbf{X}}^j & \tilde{\mathbf{X}}^j \mathbf{N}^j \mathbf{B}_2 \\ \cdot & \cdot & \mathbf{B}_2^\top \mathbf{N}^{j\top} \mathbf{N}^j \mathbf{B}_2 \end{bmatrix} T^\top dm^j \quad (2.65)$$

where  $T$  is a transformation matrix which transforms translational and rotational coordinates from the proximal to the global frame, but leaves the generalised strains unchanged:

$$T = \begin{bmatrix} \mathbf{R}_p & & \\ & \mathbf{R}_p & \\ & & \mathbf{I} \end{bmatrix} \quad (2.66)$$

The mass matrix for the whole flexible multibody element is simply the sum of the individual finite element mass matrices:

$$\mathbf{M}^{(e)} = \sum_j \mathbf{M}^j = T \begin{bmatrix} \mathbf{M}_{rr} & \mathbf{M}_{r\omega} & \mathbf{M}_{rf} \\ \cdot & \mathbf{M}_{\omega\omega} & \mathbf{M}_{\omega f} \\ \cdot & \cdot & \mathbf{M}_{ff} \end{bmatrix} T^\top \quad (2.67)$$

Details of the derivation of the components of the mass matrix are given in Appendix A.2. From Equations (2.26) and (2.64), the velocity-dependent forces on finite element  $j$  are given by:

$$\mathbf{g}^j = \int T \begin{bmatrix} \tilde{\boldsymbol{\Omega}} \tilde{\mathbf{X}}^j + 2\tilde{\boldsymbol{\Omega}} \mathbf{N}^j \mathbf{B}_2 \dot{\mathbf{q}}_f \\ \tilde{\mathbf{X}}^j \tilde{\boldsymbol{\Omega}} \tilde{\mathbf{X}}^j + 2\tilde{\mathbf{X}}^j \tilde{\boldsymbol{\Omega}} \mathbf{N}^j \mathbf{B}_2 \dot{\mathbf{q}}_f \\ \mathbf{B}_2^\top \mathbf{N}^{j\top} \tilde{\boldsymbol{\Omega}} \tilde{\mathbf{X}}^j + 2\mathbf{B}_2^\top \mathbf{N}^{j\top} \tilde{\boldsymbol{\Omega}} \mathbf{N}^j \mathbf{B}_2 \dot{\mathbf{q}}_f \end{bmatrix} dm^j \quad (2.68)$$

The velocity-dependent forces for the whole flexible multibody element

are simply the sum of the individual finite element forces  $\mathbf{g}^j$ :

$$\mathbf{g}^{(e)} = \sum_j \mathbf{g}^j = \mathbf{T} \begin{bmatrix} \mathbf{g}_r \\ \mathbf{g}_\omega \\ \mathbf{g}_f \end{bmatrix} \quad (2.69)$$

As with the mass matrix, details of the derivation of the components of  $\mathbf{g}^{(e)}$  are given in Appendix A.3.

— *Dynamics: external forces*

The generalised forces corresponding to applied loads are found from Equations (2.26) and (2.64a). For an applied point force at  $Q$  this gives

$$\mathbf{Q}_{\text{applied}}^{(e)} = \mathbf{L}^{j\top} \mathbf{R}_p \mathbf{P} = \begin{bmatrix} \mathbf{R}_p \mathbf{P} \\ \mathbf{R}_p \tilde{\mathbf{X}}^j \mathbf{P} \\ \mathbf{B}_2^\top \mathbf{N}^{j\top} \mathbf{P} \end{bmatrix} \quad (2.70)$$

where  $\mathbf{P}$  is the force expressed in the proximal coordinates system.

The generalised forces corresponding to distributed applied loads are also required. The applied force per unit length  $\mathbf{F}$  is defined in the proximal coordinate system. It is interpolated by shape functions  $\bar{\mathbf{N}}$  between nodal values  $\mathbf{F}_n$ , so that in finite element  $j$  the force is  $\mathbf{F}^j(\xi) = \bar{\mathbf{N}}^j(\xi) \mathbf{F}_n$ . From Equations (2.26) and (2.64a), the generalised forces on finite element  $j$  are

$$\mathbf{Q}_{\text{applied}}^j = \mathbf{T} \left( \int \begin{bmatrix} \bar{\mathbf{N}}^j \\ \tilde{\mathbf{X}}^j \bar{\mathbf{N}}^j \\ \mathbf{B}_2^\top \mathbf{N}^{j\top} \bar{\mathbf{N}}^j \end{bmatrix} dx^j \right) \mathbf{F}_n \quad (2.71)$$

As with the inertial loads, the applied load on the whole flexible element is the sum of the load on the individual finite elements:

$$\mathbf{Q}_{\text{applied}}^{(e)} = \sum_j \mathbf{Q}_{\text{applied}}^j = \mathbf{T} \begin{bmatrix} \mathbf{Q}_r \\ \mathbf{Q}_\omega \\ \mathbf{Q}_f \end{bmatrix} \quad (2.72)$$

Details of the components of  $\mathbf{Q}_{\text{applied}}^{(e)}$  are given in Appendix A.4.

— *Finite element sub-model*

The details of the finite element model can be isolated from the main multibody dynamics code. The finite element model must provide the following:

1. The mass  $m$  (Equation A.11)
2. The shape integrals  $S$  and  $S_{kl}$  (Equation A.13 & A.17)
3. The shape integrals for applied loads,  $\bar{S}$  and  $\bar{S}_{kl}$  (Equations A.26 & A.28)
4. The matrix defining the reference conditions  $B_2$

In the present implementation this finite element sub-module is split into a package called 'beamfe' (Lupton 2014a).

— *Elastic forces*

Following Shabana (2013, chapter 6), the virtual power of the elastic forces within one finite element  $j$  is

$$\dot{W}_e^{*j} = \int_{\text{element}} \dot{\boldsymbol{\varepsilon}}^{*\top} \boldsymbol{\sigma} dV^j \quad (2.73)$$

where  $\boldsymbol{\sigma}$  is the stress vector and  $\dot{\boldsymbol{\varepsilon}}^*$  is the vector of virtual strain rates, both applying to finite element  $j$ . The stress and strain are related by the material elastic coefficients as

$$\boldsymbol{\sigma} = \mathbf{E}^j \boldsymbol{\varepsilon} \quad (2.74)$$

where in this case the axial, bending and torsional elastic coefficients are

$$\mathbf{E}^j = \begin{bmatrix} EA & & & \\ & EI_{zz} & & \\ & & EI_{yy} & \\ & & & GJ \end{bmatrix} \quad (2.75)$$

The strain can be written in terms of the generalised elastic coordinates  $\mathbf{q}_f$  which appear in Equation (2.61) as

$$\boldsymbol{\varepsilon} = \mathbf{D}^j \mathbf{q}_f^j \quad (2.76)$$

where  $D^j$  contains the spatial derivatives of the shape functions  $\hat{N}^j$  from Equation (2.60):

$$D^j = \frac{1}{l^2} \begin{bmatrix} l \frac{\partial}{\partial \xi} & & & \\ & \frac{\partial^2}{\partial \xi^2} & & \\ & & \frac{\partial^2}{\partial \xi^2} & \\ & & & l \frac{\partial}{\partial \xi} \end{bmatrix} \hat{N}^j C_q^j B_1^j B_2^j \quad (2.77)$$

Here  $l$  is the length of finite element  $j$ . A fourth row has been added to represent the torsional stiffness, which is linearly interpolated. Substituting Equations (2.74)–(2.76) into Equation (2.73) gives

$$\begin{aligned} \dot{W}_e^{*j} &= \mathbf{q}_f^{j*T} \left[ \int_{\text{element}} D^T E^j D^j dV^j \right] \mathbf{q}_f^j \\ &= \mathbf{q}_f^{j*T} \mathbf{K}_{ff}^j \mathbf{q}_f^j \end{aligned} \quad (2.78)$$

from which the stiffness matrix  $\mathbf{K}_{ff}^j$  can be identified. The complete stiffness matrix for the whole flexible element is given by the sum of the finite element stiffness matrices:

$$\mathbf{K}_{ff}^{(e)} = \sum_j \mathbf{K}_{ff}^j \quad (2.79)$$

In the present model, the stiffness matrix has been calculated allowing for a linear variation in axial, bending and torsional stiffness along the finite element. The results given by Shabana (2013, p 295) are recovered for the case of a uniform beam.

#### — *Stress stiffening*

If the beam is subject to an axial force, the bending stiffness is effectively increased. This commonly arises in wind turbine blades due to the centrifugal force acting on the spinning blades, when it is known as ‘centrifugal stiffening’. Cook, Malkus and Plesha (1989, chapter 14) show that the additional finite element stiffness  $\mathbf{K}_\sigma^j$  is

$$\mathbf{K}_\sigma^j = \int_{\text{element}} \mathbf{G}^T P G dx^j \quad (2.80)$$

where  $P$  is the axial force in finite element  $j$  and  $G$  is a matrix containing the first derivatives of the shape functions  $\hat{N}^j$  from Equation (2.60):

$$G = \frac{1}{l} \frac{\partial}{\partial \xi} \hat{N}^j C_q^j B_1^j B_2^j \quad (2.81)$$

If the axial force is assumed constant within a finite element, this results in the standard stress stiffening matrix given by Cook, Malkus and Plesha (1989, p 434). As with the stiffness matrix (2.79), the additional stiffening matrix for the whole multibody element is

$$K_\sigma^{(e)} = \sum_j K_\sigma^j \quad (2.82)$$

For the specific case of centrifugal stiffening when the finite elements are arranged in sequence from the root to the tip of the blade, the centrifugal force acting on finite element  $k$  is

$$\Delta P^k = \int r \Omega^2 dm^k \quad (2.83)$$

and the average axial force carried by finite element  $j$  is

$$P^j = \frac{1}{2} \Delta P^j + \sum_{k=j+1}^N \Delta P^k \quad (2.84)$$

In practice, since the force is proportional to  $\Omega^2$ ,  $K_\sigma$  need only be calculated once at the start of the simulation.

#### — Modal reduction

The number of coordinates needed to represent the deflection of the finite element model can be greatly decreased by use of a modal reduction. If all nodes of the multibody element are held fixed, free vibration of remaining parts of the element is described by

$$M_{ff}^{(e)} \ddot{q}_f^{(e)} + K_{ff}^{(e)} q_f^{(e)} = \mathbf{0} \quad (2.85)$$

As described by Shabana (2013, chapter 6), a small number of the harmonic solutions to this equation, the normal mode shapes, provide a basis for reducing the number of physical coordinates in the model through the

transformation

$$\mathbf{q}_f^{(e)} = \mathbf{B}_m \mathbf{p}_f^{(e)} \quad (2.86)$$

where the columns of  $\mathbf{B}_m$  are the first  $n_m$  mode shapes, and  $\mathbf{p}_f^{(e)}$  is the vector of modal coordinates. Depending on whether the beam element is modelled with or without a distal node, the normal modes will be the clamped-clamped or clamped-free vibration modes respectively.

If a distal node is required at the end of the beam then an appropriate approach is the Craig-Bampton method (Craig and Bampton 1968; Géradin and Cardona 2001), in which the normal mode shapes are supplemented by a set of ‘attachment modes’  $\mathbf{\Xi}$ :

$$\mathbf{B}_m = [\mathbf{\Xi} \quad \mathbf{\Phi}_m], \quad \mathbf{\Xi} = \begin{bmatrix} \mathbf{I} \\ -\mathbf{K}_{II}^{-1} \mathbf{K}_{IB} \end{bmatrix} \quad (2.87)$$

where  $\mathbf{K}_{II}$  and  $\mathbf{K}_{IB}$  are partitions of the stiffness matrix corresponding to free (I) and boundary (B) finite element nodes. The attachment modes  $\mathbf{\Xi}$  are the deformations corresponding to unit deflection and rotation at each of the boundary nodes of the finite element model.

To apply this transformation to the model, substitute Equation (2.86) into Equation (2.61). This may be achieved in the results above by replacing every occurrence of  $\mathbf{B}_2$  with  $\mathbf{B}_2 \mathbf{B}_m$ . Beyond this, the implementation of the modal multibody element need not be aware of the different types of coordinate – nodal or modal – in use.

#### — Kinematic constraints

The position and orientation of the distal node are

$$\mathbf{r}_d = \mathbf{r}_p + \mathbf{R}_p \mathbf{X}_d \quad (2.88a)$$

$$\mathbf{R}_d = \mathbf{R}_p \mathbf{R}_X \quad (2.88b)$$

where the rotation of the beam at the distal node is expressed approximately by the small rotations  $\mathbf{\Theta}_d$ :

$$\mathbf{R}_X \approx \mathbf{I} + \tilde{\mathbf{\Theta}}_d \quad (2.89)$$

The velocity and angular velocity are

$$\dot{\mathbf{r}}_d = \dot{\mathbf{r}}_p + \tilde{\omega}_p \mathbf{R}_p \mathbf{X}_d + \mathbf{R}_p \dot{\mathbf{X}}_d \quad (2.90a)$$

$$\boldsymbol{\omega}_d = \boldsymbol{\omega}_p + \mathbf{R}_p \dot{\boldsymbol{\Theta}}_d \quad (2.90b)$$

and the acceleration and angular acceleration are

$$\ddot{\mathbf{r}}_d = \ddot{\mathbf{r}}_p + (\tilde{\omega}_p \tilde{\omega}_p + \dot{\tilde{\omega}}_p) \mathbf{R}_p \mathbf{X}_d + 2\tilde{\omega}_p \mathbf{R}_p \dot{\mathbf{X}}_d + \mathbf{R}_p \ddot{\mathbf{X}}_d \quad (2.91a)$$

$$\dot{\boldsymbol{\omega}}_d = \dot{\boldsymbol{\omega}}_p + \tilde{\omega}_p \mathbf{R}_p \dot{\boldsymbol{\Theta}}_d + \mathbf{R}_p \ddot{\boldsymbol{\Theta}}_d \quad (2.91b)$$

From Equations (2.60), (2.61) and (2.86), the motion of the distal node can be expressed in terms of the generalised strains of the element:

$$\dot{\mathbf{X}}_d = \boldsymbol{\Phi}_d^X \dot{\boldsymbol{\varepsilon}} \quad \dot{\boldsymbol{\Theta}}_d = \boldsymbol{\Phi}_d^\Theta \dot{\boldsymbol{\varepsilon}} \quad (2.92)$$

where  $\boldsymbol{\Phi}_d^X = \mathbf{N} \mathbf{B}_2 \mathbf{B}_m$  is the deflection shape function transformed to modal coordinates and evaluated at the distal node, and  $\boldsymbol{\Phi}_d^\Theta$  is the equivalent for the small rotations. Following the same procedure as for the other types of element, the constraint matrices are found as

$$\mathbf{F}_{vv} = \begin{bmatrix} \mathbf{I} & -\mathbf{R}_p \tilde{\mathbf{X}}_d \mathbf{R}_p^\top \\ \mathbf{0} & \mathbf{I} \end{bmatrix} \quad (2.93a)$$

$$\mathbf{F}_{v\varepsilon} = \begin{bmatrix} \mathbf{R}_p \boldsymbol{\Phi}_d^X \\ \mathbf{R}_p \boldsymbol{\Phi}_d^\Theta \end{bmatrix} \quad (2.93b)$$

$$\mathbf{F}_2 = \begin{bmatrix} \tilde{\omega}_p \tilde{\omega}_p \mathbf{R}_p \mathbf{X}_d + 2\tilde{\omega}_p \mathbf{R}_p \dot{\mathbf{X}}_d \\ \tilde{\omega}_p \mathbf{R}_p \dot{\boldsymbol{\Theta}}_d \end{bmatrix} \quad (2.93c)$$

## 2.4 Reduced and linearised systems

It is possible to eliminate the constraint equations and redundant coordinates from the system equations (2.27) to leave the reduced system equations in terms of only the independent coordinates. The independent coordinate velocities are written as  $\dot{\mathbf{z}}$  and are defined by a matrix  $\mathbf{B}$ :

$$\dot{\mathbf{z}} = \mathbf{B} \dot{\mathbf{q}} \quad (2.94)$$

In general there are many possible ways of choosing the set of independent coordinates, but in the present model they are easily chosen as the set of generalised strains of all the elements. In this case  $\mathbf{B}$  is a Boolean matrix which picks out the correct elements from  $\mathbf{q}$ .

Combining Equations (2.9) and (2.94) gives

$$\begin{bmatrix} \Phi_q \\ \mathbf{B} \end{bmatrix} \dot{\mathbf{q}} = \begin{bmatrix} \mathbf{b} \\ \dot{\mathbf{z}} \end{bmatrix} \quad \begin{bmatrix} \Phi_q \\ \mathbf{B} \end{bmatrix} \ddot{\mathbf{q}} = \begin{bmatrix} \mathbf{c} \\ \ddot{\mathbf{z}} \end{bmatrix} \quad (2.95)$$

If the inverse of the left-hand matrix is written as

$$\begin{bmatrix} \Phi_q \\ \mathbf{B} \end{bmatrix}^{-1} = \begin{bmatrix} \mathbf{S} & \mathbf{R} \end{bmatrix} \quad (2.96)$$

then the full set of coordinates  $\dot{\mathbf{q}}$  and  $\ddot{\mathbf{q}}$  are (Jalón and Bayo 1994, chapter 3)

$$\dot{\mathbf{q}} = \mathbf{S}\mathbf{b} + \mathbf{R}\dot{\mathbf{z}} \quad \ddot{\mathbf{q}} = \mathbf{S}\mathbf{c} + \mathbf{R}\ddot{\mathbf{z}} \quad (2.97)$$

To obtain the reduced system equations, substitute Equation (2.97) into Equation (2.27) to give

$$\mathbf{M}(\mathbf{S}\mathbf{c} + \mathbf{R}\ddot{\mathbf{z}}) + \Phi_q^T \lambda_c = \mathbf{Q}_{\text{applied}} - \mathbf{g} \quad (2.98)$$

It can be shown that  $\Phi_q \mathbf{R} = \mathbf{0}$  (Jalón and Bayo 1994, chapter 5), so premultiplying by  $\mathbf{R}^T$  yields the reduced system equations,

$$\bar{\mathbf{M}}\ddot{\mathbf{z}} = \bar{\mathbf{Q}} \quad (2.99)$$

where

$$\bar{\mathbf{M}} = \mathbf{R}^T \mathbf{M} \mathbf{R} \quad (2.100)$$

$$\bar{\mathbf{Q}} = \mathbf{R}^T (\mathbf{Q}_{\text{applied}} - \mathbf{g} - \mathbf{M}\mathbf{S}\mathbf{c}) \quad (2.101)$$

#### 2.4.1 NUMERICAL LINEARISATION

The reduced equations of motion can be linearised about a given operating point  $(z_0, \dot{z}_0, \ddot{z}_0, \mathbf{Q}_0)$  by perturbing the state of the system and calculating the gradient of the forces. The reduced system equations (2.99) may be

written as (Jalón and Bayo 1994, chapter 9)

$$\mathbf{H}(z, \dot{z}, \ddot{z}, \mathbf{Q}) \equiv \mathbf{R}^\top \mathbf{M} \mathbf{R} \ddot{z} - \mathbf{R}^\top (\mathbf{Q} - \mathbf{g} - \mathbf{M} \mathbf{S} c) \quad (2.102)$$

$$\mathbf{H}(z_0, \dot{z}_0, \ddot{z}_0, \mathbf{Q}_0) = \mathbf{0} \quad (2.103)$$

The linearised equations of motion are

$$\mathbf{H}_z \Delta \ddot{z} + \mathbf{H}_{\dot{z}} \Delta \dot{z} + \mathbf{H}_z \Delta z + \mathbf{H}_Q \Delta \mathbf{Q} = \mathbf{0} \quad (2.104)$$

where the partial derivative matrices  $\mathbf{H}_z$  etc. are found numerically. For example,

$$\frac{\partial \mathbf{H}}{\partial z_i} = \frac{1}{2h} [\mathbf{H}(z_0 + \Delta_i, \dot{z}_0, \ddot{z}_0, \mathbf{Q}_0) - \mathbf{H}(z_0 - \Delta_i, \dot{z}_0, \ddot{z}_0, \mathbf{Q}_0)] \quad (2.105)$$

where  $\Delta_i^\top = [0, 0, \dots, 0, h, 0, \dots, 0]$  and  $h$  is the perturbation step size.

#### 2.4.2 EQUILIBRIUM SOLUTION

An equilibrium solution may be found by solving Equation (2.103) with  $\dot{z}_0 = \ddot{z}_0 = \mathbf{0}$ . The equation can be solved for  $z_0$  using a Newton-Raphson or other method.

## 2.5 Time-domain integration

A common use for the multibody model developed so far in this chapter is to integrate the system equations in time to obtain time histories of the system response. There are multiple ways in which this can be achieved. In this section the method used in the present model will be presented; for more discussion of the alternatives see, for example, Shabana (2013).

Only the independent coordinates  $z$  (Equation 2.94) are integrated forward in time. This avoids two difficulties: problems with numerical instability of the acceleration constraints are avoided (Jalón and Bayo 1994; Shabana 2013), and there is no need to use rotation parameters to allow for the integration from nodal angular velocities to nodal orientations. Although if the free joint element is used, its generalised coordinates do

include rotation parameters which will be integrated, there is no need to integrate *nodal* angular velocities.

A standard 4th-order Runge-Kutta integration method (Jones, Oliphant and Peterson 2001; Hairer, Norsett and Wanner 1993) is used to integrate the velocities and accelerations, which are combined into a first-order ODE:

$$\dot{\mathbf{y}} = \begin{bmatrix} \dot{\mathbf{z}}_{\text{other}}(t) \\ \dot{\mathbf{z}}(t) \\ \ddot{\mathbf{z}}(t) \end{bmatrix} \xrightarrow{\text{integrate}} \mathbf{y}(t + \Delta t) = \begin{bmatrix} \mathbf{z}_{\text{other}}(t + \Delta t) \\ \mathbf{z}(t + \Delta t) \\ \dot{\mathbf{z}}(t + \Delta t) \end{bmatrix} \quad (2.106)$$

Space has been left for additional degrees of freedom  $\mathbf{z}_{\text{other}}$  to be integrated alongside the structural equations of motion; this functionality is used in later chapters. The algorithm is shown below and on the following page.

---

**Algorithm 1:** Overall time-domain integration scheme

---

```

begin
  set initial conditions
  while  $t < t_{\text{max}}$  do
    integrate system  $\mathbf{y}$  to time  $t$ , with  $\dot{\mathbf{y}} = \text{systemDerivs}(t, \mathbf{y})$ 
    wrap joint angles to  $[0, 2\pi]$ 
    update kinematics recursively up tree
    solve joint reaction forces recursively down tree
    save outputs
     $t \leftarrow t + \Delta t$ 

```

---

## 2.6 Prescribed motion

It is useful to be able to prescribe the motion of parts of the system. For example, some degrees of freedom – torsion and extension, say – may need to be made rigid, or a constant rotor rotation speed might be prescribed.

There are two situations in which prescribed motion may be applied. The first is during time integration of the system response, when the prescribed acceleration is already known and the relevant rows and columns can be removed from Equation (2.29) before solving for the free accelerations; for this only the acceleration need be provided, as velocities and

---

**Function** systemDerivs( $t, \mathbf{y}$ )    Solution of  $\dot{\mathbf{y}}$  at time  $t$ 


---

```

def systemDerivs ( $t, \mathbf{y}$ ):
     $\begin{bmatrix} z_{\text{other}} \\ \mathbf{z} \\ \dot{\mathbf{z}} \end{bmatrix} \leftarrow \mathbf{y}$ 
    update kinematics recursively up tree using  $\mathbf{z}, \dot{\mathbf{z}}$ 
     $\dot{z}_{\text{other}} \leftarrow \text{otherDerivs}(t, \mathbf{q}, \dot{\mathbf{q}}, z_{\text{other}})$ 
    calculate mass matrix, inertial and external forces
    solve system equations (2.29) for  $\ddot{\mathbf{z}}$ 

     $\dot{\mathbf{y}} \leftarrow \begin{bmatrix} \dot{z}_{\text{other}} \\ \dot{\mathbf{z}} \\ \ddot{\mathbf{z}} \end{bmatrix}$ 
    return  $\dot{\mathbf{y}}$ 

```

---

positions are found by the integrator. The second situation is when the reduced system equations (2.99) are needed, in which case the prescribed motion must be formulated as constraints in the form of Equations (2.9). In this case consistent definitions of both the prescribed velocity and acceleration must be provided.

As an example of the first approach, consider the equations

$$\begin{bmatrix} m_{11} & m_{12} & m_{13} \\ m_{21} & m_{22} & m_{23} \\ m_{31} & m_{32} & m_{33} \end{bmatrix} \begin{bmatrix} \ddot{x}_1 \\ \ddot{x}_2 \\ \ddot{x}_3 \end{bmatrix} = \begin{bmatrix} f_1 \\ f_2 \\ f_3 \end{bmatrix} \quad (2.107)$$

Assume that  $\ddot{x}_2$  is prescribed and the force  $f_2$  is unknown, while  $f_1$  and  $f_3$  are known but  $\ddot{x}_1$  and  $\ddot{x}_3$  are unknown. The prescribed acceleration is removed from the matrix to give two equations,

$$\begin{cases} \begin{bmatrix} m_{11} & m_{13} \\ m_{31} & m_{33} \end{bmatrix} \begin{bmatrix} \ddot{x}_1 \\ \ddot{x}_3 \end{bmatrix} = \begin{bmatrix} f_1 - m_{12}\ddot{x}_2 \\ f_3 - m_{32}\ddot{x}_2 \end{bmatrix} \\ f_2 = m_{21}\ddot{x}_1 + m_{22}\ddot{x}_2 + m_{23}\ddot{x}_3 \end{cases} \quad (2.108)$$

As an example of the second approach, consider a hinge joint prescribed to rotate at constant speed:  $\theta = \Omega t$ . The corresponding constraint equation is  $\Phi(\hat{\mathbf{q}}, t) = \theta - \Omega t = 0$  from which the terms appearing in

Equations (2.9)–(2.11) are

$$\Phi_q = (0, 0, \dots, 1, \dots, 0) \quad \text{corresponding to the position of } \theta \text{ in } q \quad (2.109a)$$

$$b = -\Phi_t = \Omega \quad (2.109b)$$

$$c = -\dot{\Phi}_t - \dot{\Phi}_q \dot{q} = 0 \quad (2.109c)$$

In this way the prescribed motion constraint can be included in Equation (2.96) when finding the reduced system equations.

## 2.7 Verification

The multibody dynamics code described in this chapter has been tested and verified in a number of ways. A set of unit tests aims to test individual functions or modules for correct behaviour in analytically tractable cases. These are backed up by a small set of regression tests, which compare simulation results to previous results after any changes to the code. Finally, results from simulations have been compared against results from the time-domain wind turbine simulation code *Bladed* (Garrad Hassan 2011).

There are currently 98 unit tests, with 100 % of the core code covered by at least one test. Overall 79 % of the code is covered. Some examples of these tests include:

- Testing of book-keeping functions.
- Checking the consistency of the kinematic constraints by numerical differentiation of kinematics under randomised conditions.
- Comparing the reduced mass matrices of assemblies of elements to the results found from hand calculations.
- Checking the reaction forces for known cases, including a single beam with applied loads, a mass with prescribed linear acceleration, and a spinning mass.
- Checking time-domain results for step response of a mass on a spring.
- Comparing the static response of a beam element to textbook results (Reddy 1993).

Details of the tests may be found with the source code, which is freely

available (Lupton 2014b).

Three examples of verification tests are presented below in which results are compared to the wind turbine simulation code Bladed.

### 2.7.1 RESPONSE OF CANTILEVER BLADE TO VARYING LOADING

One test involves comparing the response of a flexible cantilevered blade against results from Bladed. The model contains a single finite-element beam represented by 4 mode shapes, with the beam properties being taken from the National Renewable Energy Laboratory (USA) (NREL) 5 MW turbine (Jonkman, Butterfield, et al. 2009). The drag loading applied to the blade is proportional to the square of the relative wind speed seen by the blade, thereby accounting for aeroelastic effects. The incoming wind speed is ramped from  $0 \text{ m s}^{-1}$  to  $20 \text{ m s}^{-1}$  as shown at the top of Figure 2.8.

The results, shown in the remainder of Figure 2.8, match well with the results from Bladed. In particular, motion of the blade perpendicular to the loading, which is due to the twist of the blade, is captured correctly. The damping, which is due to both the structural damping of the blade and the aerodynamic damping from the drag force, is also similar in both results.

### 2.7.2 CAMPBELL DIAGRAM

A Campbell diagram shows the natural frequencies of the structure as a function of rotor speed. A multibody model of a flexible three-bladed rotor was built, consisting of

1. a hinge, with prescribed motion forcing the rotor to rotate,
2. three rigid offsets representing the roots of the blades, and
3. three modal elements using mode shapes calculated from the FE model.

Note that because the only allowed motion of the rotor is rotation at constant speed, the blades are not coupled to each other in this example; only the flexible beam element natural frequencies and the centrifugal stiffening effect are being tested. The model was linearised for a range of rotor speeds, and the natural frequencies found from the eigenvalues. The results, along with similar results from Bladed, are shown in Figure 2.9. There is good

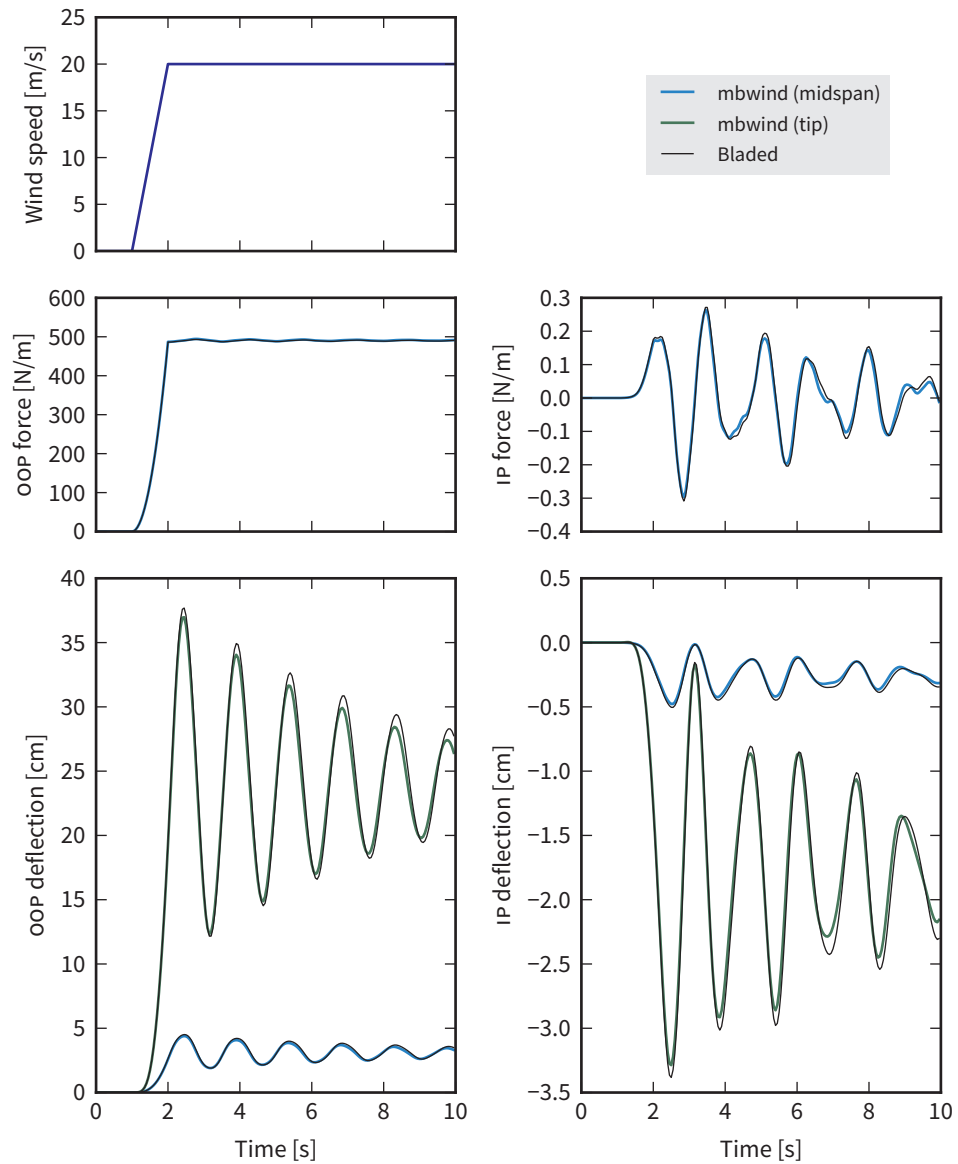


Figure 2.8 – Simulation results for a flexible blade. At top, the ramped wind speed. Middle row: out-of-plane (OOP) and in-plane (IP) drag loading. Bottom row: Deflection of the blade at midspan and at the tip.

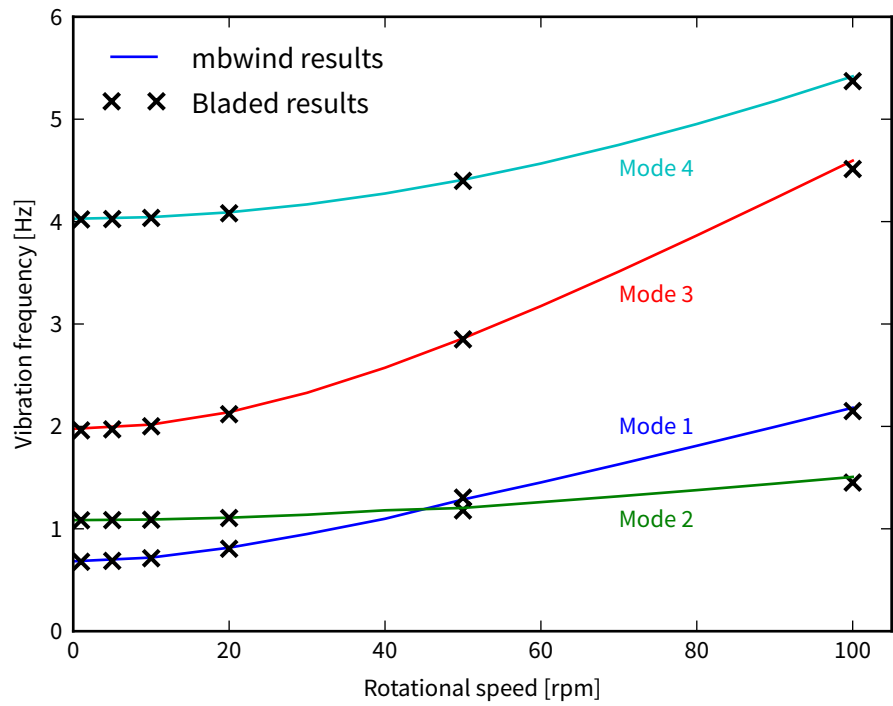


Figure 2.9 – Campbell diagram showing the frequencies of the first two bending modes in the out-of-plane (modes 1 & 3) and in-plane directions (modes 2 & 4).

agreement between the two sets of results, which shows that centrifugal stiffening is being modelled correctly.

### 2.7.3 COUPLED BLADES WITH VARYING LOADING

The previous examples test the flexible blade element in isolation. In this example two coupled flexible beams are modelled. The blade is identical to the first example (Figure 2.8) but instead of being rigidly cantilevered, the base of the blade is attached to a flexible 'tower'. To show a more interesting result, the stiffness of the tower is reduced compared to a real wind turbine tower.

The results, shown in Figure 2.10, match well with the results from Bladed. The match is not exact due to differences in the way the models are implemented in Bladed and the present code, but does demonstrate that coupled flexible elements can be modelled.

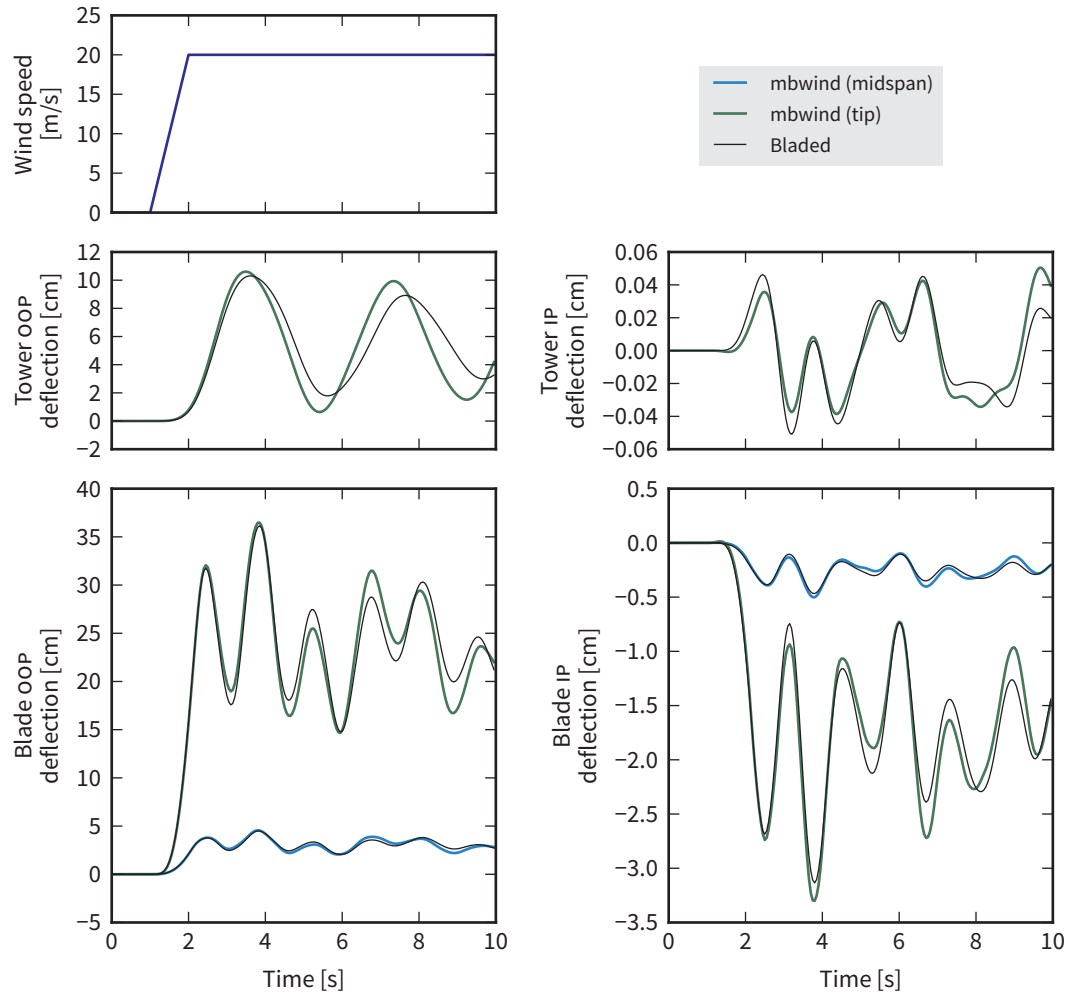


Figure 2.10 – Simulation results for two coupled beams, a ‘blade’ rigidly attached to a ‘tower’. At top, the ramped wind speed. Middle row: out-of-plane (OOP) and in-plane (IP) tower-top deflection. Bottom row: Deflection of the blade at midspan and at the tip.

## Chapter 3

### *Linearised structural dynamics*

The structural dynamics of a floating wind turbine – with flexible blades, in a rotating rotor, on a moving platform – are more complex than in the case of an equivalent fixed-base turbine. Specifically, the acceleration of the platform causes additional loads on the blades, in addition to the gravity and aerodynamic loads a typical wind turbine blade will experience. Steady tilt of the platform can also cause larger periodic gravity and wind loads on the rotor as it rotates. Although the effects may not be dramatic in current designs of floating platforms, which aim to minimise the platform motion so existing commercial turbine designs can be used, a good understanding of the dynamics is needed for development of future optimised integrated designs.

In this chapter the effect of platform motion on the structural dynamics of the blades is investigated by making use of a simplified model of a flexible blade on a moving platform. The platform undergoes prescribed motion in one of 6 degrees of freedom, allowing the effects of platform motion to be studied in isolation from the full dynamics of the floating platform and wind turbine. The aim is to characterise the blade response, identify the conditions leading to the largest blade responses, and assess the importance of nonlinearity in the blade response; nonlinearity is of particular interest when the possibility is considered of using linearised models of the structural dynamics of the floating wind turbine.

Although the multibody dynamics code developed in the previous chapter is capable of simulating the dynamics of the flexible blades on the moving platform, to gain a better understanding of the dynamic behaviour the equations of motion of a simplified model are derived from first prin-

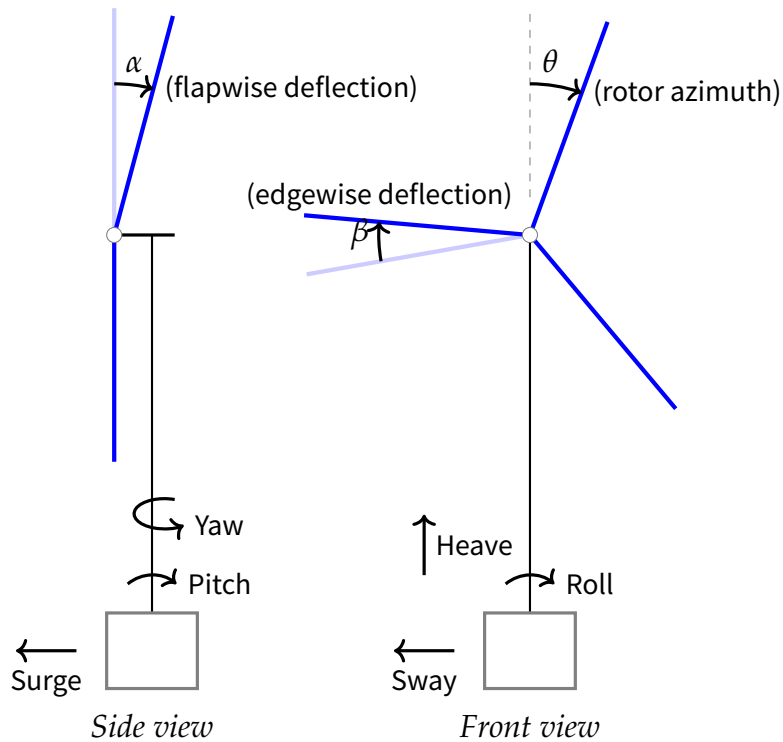


Figure 3.1 – Simplified model of the floating wind turbine, showing types of platform motion.

principles in this chapter. The multibody dynamics code is used to verify the equations.

First, the equations of motion of the simplified model are derived. The solutions are studied both through an approximate analytical perturbation analysis and by direct numerical integration. The blade response is shown to contain harmonics at many frequencies, which is linked to the existence of potentially many resonant conditions. Although the behaviour is non-linear with respect to the amplitude of the platform motion, in practical situations the nonlinearity is found to be small. Finally, the implications of testing at model scale for the effects demonstrated in this chapter are discussed.

Table 3.1 – Blade properties for numerical calculations (NREL 5 MW turbine)

Blade length	63 m
Flapwise natural frequency	0.68 Hz
Edgewise natural frequency	1.08 Hz
First moment of mass $I_1$	363 219 kg m
Second moment of mass $I_2$	11 753 580 kg m <sup>2</sup>

### 3.1 Simplified model

In the simplified model, Figure 3.1, the flexibility of the blades is represented by rigid beams hinged to the hub in the flapwise and edgewise directions; this gives a simple model and still includes centrifugal stiffening effects. The hinge stiffnesses are chosen to reproduce the first flapwise and edgewise natural frequencies of the blade. Only independent flapwise and edgewise motions are considered; note that this ignores the possibility of nonlinear coupling between these two motions. The flexibility of the tower is neglected and the rotor speed is assumed constant.

For numerical calculations, the blade properties and tower height were taken from the OC3-Hywind model (see p 25), as shown in Table 3.1. For simplicity, damping is set at 2 % of critical damping throughout, but it is worth mentioning that for some types of platform motion the damping may be much higher than this: out-of-plane motion of an operational rotor can cause aerodynamic damping of the order of 30 % (Burton et al. 2011). Motion in the plane of the rotor, or when the rotor is not operational, will cause little aerodynamic damping.

#### 3.1.1 AMPLITUDES AND FREQUENCIES OF PLATFORM MOTION

Platform motions in each degree of freedom will be considered independently, for a range of amplitudes and frequencies. The relevant range of frequencies depends on the frequencies of the external wind and wave loading: using the Pierson-Moskowitz or JONSWAP spectra (Chakrabarti 2005), most wave energy lies within the range 0.02 Hz to 0.40 Hz, while using the IEC edition 3 Kaimal wind spectrum (Burton et al. 2011), wind energy lies

below 0.12 Hz. Therefore frequencies up to 0.4 Hz will be considered.

Although most platforms are designed to have natural frequencies away from the main wave spectrum, resonance may still occur. Second-order wave loads can excite large low-frequency resonant motions of the platform, but the frequencies are so low this is unlikely to cause significant inertial loading on the blades. Second-order effects can also cause wave loading above the wave-energy frequency band, potentially exciting resonance of TLPs at higher frequencies. Rotational sampling of turbulence (Burton et al. 2011) causes aerodynamic loads on the platform at multiples of the rotor speed, also potentially leading to higher frequencies of platform motion. However, these effects are not considered further here.

Amplitudes of platform motion up to 21 m and  $19^\circ$ , and rotor speeds up to 20 rpm are considered; current large wind turbines operate at lower rotor speeds than this.

It is important to note that the largest amplitudes of motion will not occur in practice except at the lowest frequencies. Nonetheless for clarity of presentation the results are calculated and plotted for a grid of values which covers all combinations.

### 3.1.2 EQUATIONS OF MOTION – LARGE ROTATIONS

The equations of motion are derived separately for flapwise and edgewise deflection of the blades, leading to two independent one-degree-of-freedom equations. This is an appropriate simplification if the deflections are small. Lagrange's equations are used to find the equations of motion.

As an example, Figure 3.2 shows the model for the particular case of platform pitch motion, which will be used to illustrate the derivation of the equations of motion. In this case there are four coordinates, which are labelled in the figure. The rotor speed  $\dot{\theta}(t)$  and platform pitch angle  $\varphi(t)$  are prescribed. Only flapwise or edgewise deflection is considered at a time, leaving the blade deflection angle  $\alpha(t)$  or  $\beta(t)$  as the only degree of freedom. In the following, two sets of equations are presented corresponding to these two cases.

The first step is to derive the kinetic and potential energies. In terms of the unit vectors and angles shown in Figure 3.2, Appendix B shows that

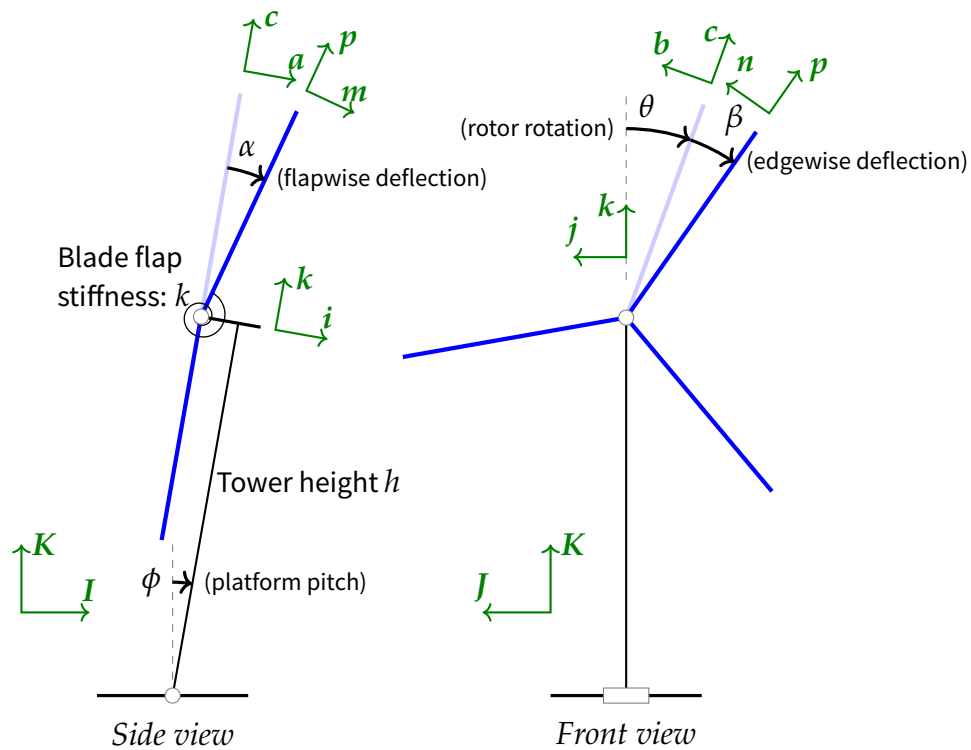


Figure 3.2 – The simplified model of a floating wind turbine showing the flapwise blade response to platform pitching motion. The coordinates are the platform pitch angle  $\phi$ , the rotor azimuth angle  $\theta$ , the blade flapwise deflection  $\alpha$  and the blade edgewise deflection  $\beta$ .

the velocity of a point on the blade at radius  $r$  is given by

$$\dot{\mathbf{r}} = \dot{\varphi} (h + r \cos \alpha \cos \theta) \mathbf{i} - r \dot{\varphi} \sin \alpha \mathbf{k} - r \dot{\theta} \cos \alpha \mathbf{b} + r \dot{\alpha} \mathbf{m} \quad (3.1a)$$

when flapwise deflections are permitted, or

$$\dot{\mathbf{r}} = \dot{\varphi} (h + r \cos \beta \cos \theta - r \sin \beta \sin \theta) \mathbf{i} - r (\dot{\theta} + \dot{\beta}) \mathbf{n} \quad (3.1b)$$

when edgewise deflections are permitted. It is then shown that the kinetic energy  $T$  is given by

$$2T = [Mh^2 + 2hI_1 \cos \alpha \cos \theta + I_2 \cos^2 \alpha \cos^2 \theta + I_2 \sin^2 \alpha] \dot{\varphi}^2 + I_2 \cos^2 \alpha \dot{\theta}^2 + I_2 \dot{\alpha}^2 + 2\dot{\alpha} \dot{\varphi} (hI_1 \cos \alpha + I_2 \cos \theta) + I_2 \dot{\varphi} \dot{\theta} \sin 2\alpha \sin \theta \quad (3.2a)$$

for flapwise deflections, or

$$2T = [Mh^2 + 2hI_1 (\cos \beta \cos \theta - \sin \beta \sin \theta) + I_2 (\cos \beta \cos \theta - \sin \beta \sin \theta)^2] \dot{\varphi}^2 + I_2 [\dot{\theta} + \dot{\beta}]^2 \quad (3.2b)$$

for edgewise deflections, where  $M$  is the blade's mass, and  $I_1$  and  $I_2$  are the first and second moments of mass about the root of the blade. The potential energy is

$$V = \frac{1}{2} k_f \alpha^2 + Mgh \cos \varphi + I_1 g (\cos \alpha \cos \varphi \cos \theta - \sin \alpha \sin \varphi) \quad (3.3a)$$

for flapwise deflections, or

$$V = \frac{1}{2} k_e \beta^2 + Mgh \cos \varphi + I_1 g \cos \varphi (\cos \beta \cos \theta - \sin \beta \sin \theta) \quad (3.3b)$$

for edgewise deflections, where the stiffness of the blade hinge is  $k_f$  and  $k_e$  in the flapwise and edgewise directions respectively. Appendix B shows the application of Lagrange's equation to these energies to find the equations of motion, again using the example of the flapwise response to pitching motion.

For the particular case of harmonic platform motion, with amplitude  $A$  and frequency  $\omega$ , the results are presented below. In total there are 12 equations of motion, for the flapwise and edgewise responses to the 6 types of platform motion (Figure 3.1). The equations were derived in a similar

manner to the example given in the Appendix, but making use of the SymPy symbolic algebra package (SymPy Development Team 2012), and the results are listed below.  $\omega_f = \sqrt{k_f/I_2}$  and  $\omega_e = \sqrt{k_e/I_2}$  are the flapwise and edgewise natural frequencies respectively, and  $\lambda = I_1/I_2$  is the ratio of first and second moments of mass of the blade. The rotor speed  $\Omega$  is assumed constant so  $\theta(t) = \Omega t$ . Note that platform sway motion, as an in-plane translation of the rotor, is similar to heave motion and has not been written out again.

**SURGE**

Flapwise:

$$-A\lambda\omega^2 \sin \omega t \cos \alpha + \Omega^2 \sin \alpha \cos \alpha - g\lambda \sin \alpha \cos \Omega t + \omega_f^2 \alpha + \ddot{\alpha} = 0 \quad (3.4)$$

Edgewise:

$$-g\lambda \sin \Omega t \cos \beta - g\lambda \sin \beta \cos \Omega t + \omega_e^2 \beta + \ddot{\beta} = 0 \quad (3.5)$$

**HEAVE**

Flapwise:

$$A\lambda\omega^2 \sin \omega t \sin \alpha \cos \Omega t + \Omega^2 \sin \alpha \cos \alpha - g\lambda \sin \alpha \cos \Omega t + \omega_f^2 \alpha + \ddot{\alpha} = 0 \quad (3.6)$$

Edgewise:

$$A\lambda\omega^2 \sin \Omega t \sin \omega t \cos \beta + A\lambda\omega^2 \sin \omega t \sin \beta \cos \Omega t - g\lambda \sin \Omega t \cos \beta - g\lambda \sin \beta \cos \Omega t + \omega_e^2 \beta + \ddot{\beta} = 0 \quad (3.7)$$

**ROLL**

Flapwise:

$$\begin{aligned} &A^2 h \lambda \omega^2 \sin \alpha \cos \Omega t \cos^2 \omega t + A^2 \omega^2 \sin \alpha \cos^2 \omega t \cos \alpha \\ &+ 2A\Omega\omega \sin \alpha \cos \omega t \cos \alpha + Ah\lambda\omega^2 \sin \Omega t \sin \omega t \sin \alpha \\ &+ \Omega^2 \sin \alpha \cos \alpha + g\lambda \sin (A \sin \omega t) \sin \Omega t \sin \alpha \\ &- g\lambda \sin \alpha \cos (A \sin \omega t) \cos \Omega t + \omega_f^2 \alpha + \ddot{\alpha} = 0 \quad (3.8) \end{aligned}$$

Edgewise:

$$\begin{aligned}
 & A^2 h \lambda \omega^2 \sin \Omega t \cos^2 \omega t \cos \beta + A^2 h \lambda \omega^2 \sin \beta \cos \Omega t \cos^2 \omega t \\
 & \quad + A h \lambda \omega^2 \sin \Omega t \sin \omega t \sin \beta - A h \lambda \omega^2 \sin \omega t \cos \Omega t \cos \beta \\
 & \quad - A \omega^2 \sin \omega t + g \lambda \sin (A \sin \omega t) \sin \Omega t \sin \beta \\
 & - g \lambda \sin (A \sin \omega t) \cos \Omega t \cos \beta - g \lambda \sin \Omega t \cos (A \sin \omega t) \cos \beta \\
 & \quad - g \lambda \sin \beta \cos (A \sin \omega t) \cos \Omega t + \omega_e^2 \beta + \ddot{\beta} = 0 \quad (3.9)
 \end{aligned}$$

PITCH

Flapwise:

$$\begin{aligned}
 & A^2 h \lambda \omega^2 \sin \alpha \cos \Omega t \cos^2 \omega t + A^2 \omega^2 \sin \alpha \cos^2 \Omega t \cos^2 \omega t \cos \alpha \\
 & \quad - A^2 \omega^2 \sin \alpha \cos^2 \omega t \cos \alpha - 2 A \Omega \omega \sin \Omega t \cos \omega t \cos^2 \alpha \\
 & - A h \lambda \omega^2 \sin \omega t \cos \alpha - A \omega^2 \sin \omega t \cos \Omega t + \Omega^2 \sin \alpha \cos \alpha \\
 & \quad - g \lambda \sin (A \sin \omega t) \cos \alpha - g \lambda \sin \alpha \cos (A \sin \omega t) \cos \Omega t \\
 & \quad \quad \quad + \omega_f^2 \alpha + \ddot{\alpha} = 0 \quad (3.10)
 \end{aligned}$$

Edgewise:

$$\begin{aligned}
 & A^2 h \lambda \omega^2 \sin \Omega t \cos^2 \omega t \cos \beta + A^2 h \lambda \omega^2 \sin \beta \cos \Omega t \cos^2 \omega t \\
 & \quad - A^2 \omega^2 \sin^2 \Omega t \sin \beta \cos^2 \omega t \cos \beta - A^2 \omega^2 \sin \Omega t \sin^2 \beta \cos \Omega t \cos^2 \omega t \\
 & \quad + A^2 \omega^2 \sin \Omega t \cos \Omega t \cos^2 \omega t \cos^2 \beta + A^2 \omega^2 \sin \beta \cos^2 \Omega t \cos^2 \omega t \cos \beta \\
 & \quad - g \lambda \sin \Omega t \cos (A \sin \omega t) \cos \beta - g \lambda \sin \beta \cos (A \sin \omega t) \cos \Omega t \\
 & \quad \quad \quad + \omega_e^2 \beta + \ddot{\beta} = 0 \quad (3.11)
 \end{aligned}$$

YAW

Flapwise:

$$\begin{aligned}
 & A^2 \omega^2 \sin^2 \Omega t \sin \alpha \cos^2 \omega t \cos \alpha - A^2 \omega^2 \sin \alpha \cos^2 \omega t \cos \alpha \\
 & \quad + 2 A \Omega \omega \cos \Omega t \cos \omega t \cos^2 \alpha - A \omega^2 \sin \Omega t \sin \omega t + \Omega^2 \sin \alpha \cos \alpha \\
 & \quad \quad \quad - g \lambda \sin \alpha \cos \Omega t + \omega_f^2 \alpha + \ddot{\alpha} = 0 \quad (3.12)
 \end{aligned}$$

Edgewise:

$$\begin{aligned}
& A^2\omega^2 \sin^2 \Omega t \sin \beta \cos^2 \omega t \cos \beta + A^2\omega^2 \sin \Omega t \sin^2 \beta \cos \Omega t \cos^2 \omega t \\
& - A^2\omega^2 \sin \Omega t \cos \Omega t \cos^2 \omega t \cos^2 \beta - A^2\omega^2 \sin \beta \cos^2 \Omega t \cos^2 \omega t \cos \beta \\
& - g\lambda \sin \Omega t \cos \beta - g\lambda \sin \beta \cos \Omega t \\
& + \omega_e^2 \beta + \ddot{\beta} = 0 \quad (3.13)
\end{aligned}$$

### 3.1.3 EQUATIONS OF MOTION – SMALL ROTATIONS

It is useful to simplify the full equation of motion by assuming small blade deflections and small platform rotations. Specifically, terms are kept to first order in  $\alpha$ ,  $\beta$ , and the platform motions. Again using the case of pitching motion of the platform as an example, Appendix B shows the derivation of the simplified equations of motion. The result is an equation in which individual contributions can be more easily identified:

$$\begin{aligned}
\ddot{\alpha} + \left[ \underbrace{\omega_f^2}_{\text{flap stiffness}} + \underbrace{\Omega^2}_{\text{centrifugal stiffness (rotor)}} + \underbrace{\dot{\varphi}^2 \left( \lambda h \cos \theta + \frac{1}{2} \cos 2\theta - \frac{1}{2} \right)}_{\text{centrifugal stiffness (platform rotation)}} - \underbrace{\lambda g \cos \theta}_{\text{gravity stiffness}} \right] \alpha \\
= \underbrace{\lambda g \varphi}_{\text{out-of-plane gravity load}} + \underbrace{2\dot{\varphi}\Omega \sin \theta}_{\text{Coriolis force}} - \underbrace{\ddot{\varphi} (\lambda h + \cos \theta)}_{\text{platform acceleration force}}
\end{aligned}$$

which after again expanding the constant rotor speed,  $\theta(t) = \Omega t$ , and the harmonic pitching motion,  $\varphi = A \sin \omega t$ , becomes:

$$\begin{aligned}
\ddot{\alpha} + \left( p_f^2 - \lambda g \cos \Omega t \right) \alpha &= \lambda A (g + h\omega^2) \sin \omega t \\
&+ \left( \frac{A\omega}{2} \right) \left[ (\omega + 2\Omega) \sin(\omega + \Omega)t + (\omega - 2\Omega) \sin(\omega - \Omega)t \right] \\
&- \alpha \left( \frac{A\omega}{2} \right)^2 \left\{ 2\lambda h \cos \Omega t + \cos 2\Omega t - \cos 2\omega t - 1 \right. \\
&\quad + \lambda h [\cos(2\omega + \Omega)t + \cos(2\omega - \Omega)t] \\
&\quad \left. + \frac{1}{2} [\cos 2(\omega + \Omega)t + \cos 2(\omega - \Omega)t] \right\} \quad (3.14)
\end{aligned}$$

where all terms containing the platform amplitude  $A$  have been moved to the right-hand side, and the flapwise and edgewise natural frequencies

including centrifugal stiffening are written as

$$p_f = \sqrt{\omega_f^2 + \Omega^2} \quad (3.15a)$$

$$p_e = \omega_e \quad (3.15b)$$

The equation of motion is seen to be nonlinear as the response  $\alpha$  appears on the right-hand side.

Below, the equivalent simplified equations are presented for other types of platform motion. A parametric excitation term due to gravity, visible on the left-hand side of Equation (3.14), has been neglected since  $(p_f^2/\lambda g) \gg 1$  for the blade of the reference wind turbine (the NREL 5 MW). For brevity, the notation is introduced that

$$\sin^+(A \pm B) = \sin(A + B) + \sin(A - B) \quad (3.16a)$$

$$\sin^-(A \pm B) = \sin(A + B) - \sin(A - B) \quad (3.16b)$$

and the equivalent for cos; the terms are written in this expanded form to make the frequency content of the responses explicit. This leads to the following equations:

Surge:

$$\ddot{\alpha} + p_f^2 \alpha = A\lambda\omega^2 \sin \omega t \quad (3.17a)$$

$$\ddot{\beta} + p_e^2 \beta = g\lambda \sin \Omega t \quad (3.17b)$$

Heave:

$$\ddot{\alpha} + p_f^2 \alpha = -\frac{A\lambda}{2} \omega^2 \alpha \sin^-(\omega \pm \Omega)t \quad (3.18a)$$

$$\ddot{\beta} + p_e^2 \beta = \frac{A\lambda}{2} \omega^2 \left[ \cos^-(\omega \pm \Omega)t - \beta \sin^-(\omega \pm \Omega)t \right] + g\lambda \sin \Omega t \quad (3.18b)$$

Roll:

$$\begin{aligned} \ddot{\alpha} + p_f^2 \alpha = & \alpha \left( \frac{A\omega}{2} \right) \left[ -4\Omega \cos \omega t + \lambda(g + h\omega^2) \cos^-(\omega \pm \Omega)t \right] \\ & - \alpha \left( \frac{A\omega}{2} \right)^2 \left[ 2 + 2 \cos 2\omega t + 2h\lambda \cos \Omega t \right] \end{aligned}$$

$$+ h\lambda \cos^+(2\omega \pm \Omega)t \Big] \quad (3.19a)$$

$$\begin{aligned} \ddot{\beta} + p_e^2 \beta &= g\lambda \sin \Omega t + A\omega^2 \sin \omega t \\ &+ \frac{A\lambda}{2} (g + h\omega^2) \left[ \sin^-(\omega \pm \Omega)t + \beta \cos^-(\omega \pm \Omega)t \right] \\ &- \left( \frac{A\omega}{2} \right)^2 h\lambda \left[ \sin^-(2\omega \pm \Omega)t + \beta \cos^+(2\omega \pm \Omega)t \right. \\ &\quad \left. + 2 \sin \Omega t + 2\beta \cos \Omega t \right] \end{aligned} \quad (3.19b)$$

Pitch:

$$\begin{aligned} \ddot{\alpha} + p_f^2 \alpha &= A\lambda (g + h\omega^2) \sin \omega t \\ &+ \left( \frac{A\omega}{2} \right) \left[ (\omega + 2\Omega) \sin(\omega + \Omega)t + (\omega - 2\Omega) \sin(\omega - \Omega)t \right] \\ &- \alpha \left( \frac{A\omega}{2} \right)^2 \left[ 2\lambda h \cos \Omega t + \lambda h \cos^+(2\omega \pm \Omega)t \right. \\ &\quad \left. + \cos 2\Omega t + \frac{1}{2} \cos^+(2\omega \pm 2\Omega)t \right. \\ &\quad \left. - 1 - \cos 2\omega t \right] \end{aligned} \quad (3.20a)$$

$$\begin{aligned} \ddot{\beta} + p_e^2 \beta &= g\lambda \sin(\Omega t) \\ &- \left( \frac{A\omega}{2} \right)^2 \left\{ 2h\lambda [\sin \Omega t + \beta \cos \Omega t] + [\sin 2\Omega t + 2\beta \cos 2\Omega t] \right. \\ &\quad \left. + h\lambda [\sin^-(2\omega \pm \Omega)t + \beta \cos^+(2\omega \pm \Omega)t] \right. \\ &\quad \left. + \frac{1}{2} \sin^-(2\omega \pm 2\Omega)t + \beta \cos^+(2\omega \pm 2\Omega)t \right\} \end{aligned} \quad (3.20b)$$

Yaw:

$$\begin{aligned} \ddot{\alpha} + p_f^2 \alpha &= - \left( \frac{A\omega}{2} \right) \left[ (\omega + 2\Omega) \cos(\omega + \Omega)t - (\omega - 2\Omega) \cos(\omega - \Omega)t \right] \\ &+ \alpha \left( \frac{A\omega}{2} \right)^2 \left[ 1 + \cos 2\Omega t + \cos 2\omega t + \frac{1}{2} \cos^+(2\omega \pm 2\Omega)t \right] \end{aligned} \quad (3.21a)$$

$$\begin{aligned}
\ddot{\beta} + p_e^2 \beta &= g\lambda \sin \Omega t \\
&+ \left( \frac{A\omega}{2} \right)^2 \left[ \frac{1}{2} \sin^-(2\omega \pm 2\Omega)t + \beta \cos^+(2\omega \pm 2\Omega)t \right. \\
&\quad \left. + \sin 2\Omega t + 2\beta \cos 2\Omega t \right]
\end{aligned} \tag{3.21b}$$

## 3.2 Perturbation solution

The equations of motion derived above may be solved numerically, or with further approximation they may be solved analytically. In this section the perturbation method is used to find an approximate solution, which will later be compared to the numerical solution. The simplified versions of the equations of motion (Section 3.1.3) will be used.

The equations of motion for small deflections (3.17)–(3.21) have a general form with a force appearing on the right-hand side of the equation dependent on the current blade deflection:

$$\ddot{x}(t) + p^2 x(t) = f(t) + x(t)g(t) \tag{3.22}$$

where  $x$  is the blade deflection response ( $\alpha$  or  $\beta$ ),  $p$  is the blade's natural frequency including any centrifugal stiffening ( $p_f$  or  $p_e$ ), and  $f(t)$  and  $g(t)$  are the parts of the applied force which are respectively independent of and dependent on  $x(t)$ .

The method of perturbation (Stoker 1950) can provide an approximate solution to a non-linear differential equation. The first step is to expand the response variable in a power series with respect to some parameter, say the amplitude of the platform motion  $A$ :

$$x(t) = x_0(t) + Ax_1(t) + A^2x_2(t) + \dots \tag{3.23}$$

Similarly, the applied forces can be divided into parts by the order of  $A$ , so that  $f(t) = f_0(t) + Af_1(t) + A^2f_2(t) + \dots$  and equivalently for  $g(t)$ . Then, substituting these expansions into Equation (3.23) and equating powers of

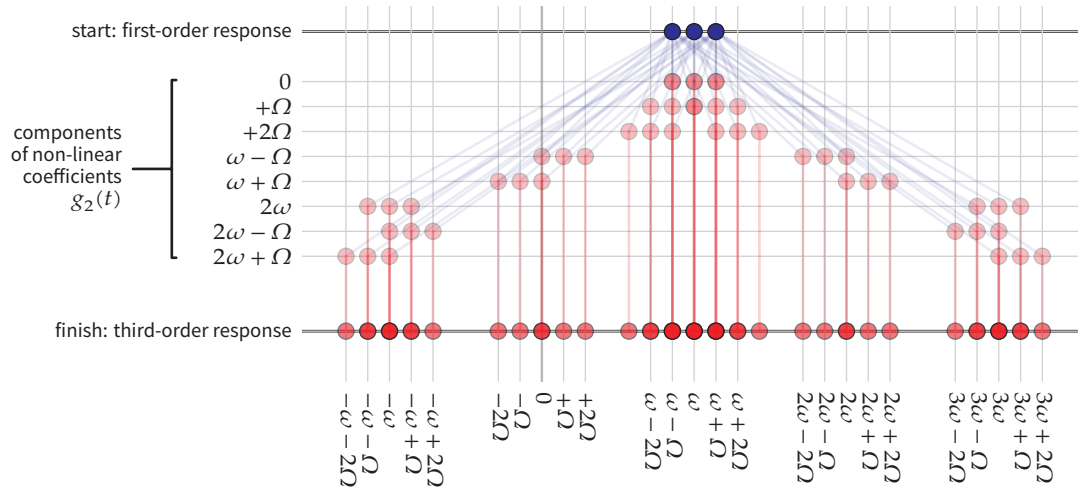


Figure 3.3 – Development of harmonics from 1st- to 3rd-order solution for the case of the flapwise response to platform pitch. The harmonics which make up the 1st-order response are shown in the top row. When multiplied by the non-linear coefficients  $g_2(t)$ , new harmonics at the sum and difference frequencies are created.

A produces a series of linear differential equations:

$$\ddot{x}_0(t) + p^2 x_0(t) = f_0(t) \quad (3.24a)$$

$$\ddot{x}_1(t) + p^2 x_1(t) = f_1(t) + g_1(t)x_0(t) \quad (3.24b)$$

$$\ddot{x}_2(t) + p^2 x_2(t) = f_2(t) + g_2(t)x_0(t) + g_1(t)x_1(t) \quad (3.24c)$$

$$\ddot{x}_3(t) + p^2 x_3(t) = f_3(t) + g_3(t)x_0(t) + g_2(t)x_1(t) + g_1(t)x_2(t) \quad (3.24d)$$

⋮

In this way the original non-linear equation has been transformed into a series of linear differential equations; these can be solved in turn to produce successive approximations to the full non-linear response.

Because the lower-order solution becomes part of the forcing term for the higher-order solutions, when the blade response consists of multiple harmonics these will cascade through the iterations of the method. New harmonics at the sum and difference frequencies of the previous harmonics appear at every step. This qualitative behaviour (illustrated in Figure 3.3) is also expected to be visible in the numerical results: in general the blade response will consist of many harmonics at frequencies of the form  $a\omega + b\Omega$ ,

where  $a$  and  $b$  are positive or negative integers.

In theory, for the power series expansion (3.23) to converge, the perturbation parameter  $A$  must be small. In practice useful qualitative results may be obtained even with larger values of  $A$  but the amplitudes of the harmonics in the perturbation solution will not be accurate.

### 3.2.1 EXAMPLE: FLAPWISE RESPONSE TO PLATFORM PITCH MOTION

The flapwise equation of motion for platform pitch motion will be used to illustrate the method of perturbation. The equation of motion (3.20a) can be written concisely as

$$\ddot{\alpha} + p_f^2 \alpha = A f_1(t) + A^2 g_2(t) \alpha \quad (3.25)$$

Then substitution of a power series (3.23) for  $\alpha$  leads to a series of linear equations like Equations (3.24):

$$\ddot{\alpha}_0 + p_f^2 \alpha_0 = 0 \quad (3.26a)$$

$$\ddot{\alpha}_1 + p_f^2 \alpha_1 = f_1(t) \quad (3.26b)$$

$$\ddot{\alpha}_2 + p_f^2 \alpha_2 = \alpha_0 g_2(t) \quad (3.26c)$$

$$\ddot{\alpha}_3 + p_f^2 \alpha_3 = \alpha_1 g_2(t) \quad (3.26d)$$

⋮

These linear equations can be solved in turn to give successive approximations to the solution of the original non-linear equation.

The zeroth-order equation (3.26a) describes free vibration of the blade at a frequency  $p_f$ . Damping will, although not shown explicitly, cause this free vibration to disappear and in steady-state,

$$\alpha_0 = 0 \quad (3.27)$$

The first-order equation (3.26b), if  $f_1(t)$  is written out in full, becomes

$$\begin{aligned}\ddot{\alpha}_1 + p_f^2 \alpha_1 &= \lambda (g + h\omega^2) \sin \omega t \\ &+ \frac{\omega (\omega + 2\Omega)}{2} \sin(\omega + \Omega)t \\ &+ \frac{\omega (\omega - 2\Omega)}{2} \sin(\omega - \Omega)t\end{aligned}$$

for which the forced vibration solution is

$$\alpha_1 = K_\omega \sin \omega t + K_+ \sin(\omega + \Omega)t + K_- \sin(\omega - \Omega)t \quad (3.28)$$

where

$$\begin{aligned}K_\omega &= \frac{\lambda (g + h\omega^2)}{\omega_f^2 + \Omega^2 - \omega^2} \\ K_+ &= \left(\frac{\omega}{2}\right) \frac{\omega + 2\Omega}{\omega_f^2 - \omega^2 - 2\omega\Omega} \\ K_- &= \left(\frac{\omega}{2}\right) \frac{\omega - 2\Omega}{\omega_f^2 - \omega^2 + 2\omega\Omega}\end{aligned}$$

This shows that the linear part of the solution consists of three harmonics: at the original forcing frequency  $\omega$ , and also at  $\omega \pm \Omega$ . This is due to the equation of motion being periodic in  $\Omega$ . The presence of multiple harmonics in the response of rotating blades is well known; see for example MH Hansen (2007).

Substituting the zeroth-order solution (3.27) into the second-order equation (3.26c) shows that

$$\alpha_2 = 0 \quad (3.29)$$

Substituting the first-order solution (3.28) into the third-order equation (3.26d) gives

$$\begin{aligned}\ddot{\alpha}_3 + p_f^2 \alpha_3 &= -\left(\frac{\omega}{2}\right)^2 \left[ K_\omega \sin \omega t + K_+ \sin(\omega + \Omega)t + K_- \sin(\omega - \Omega)t \right] \times \\ &\times \left[ \lambda h \cos^+(2\omega \pm \Omega)t + \frac{1}{2} \cos^+(2\omega \pm 2\Omega)t \right. \\ &\quad \left. + 2\lambda h \cos \Omega t + \cos 2\Omega t - \cos 2\omega t - 1 \right] \quad (3.30)\end{aligned}$$

The solution for  $\alpha_3$  includes terms at many harmonic combinations of  $\omega$  and  $\Omega$  and is not written out here.

Finally, the total approximate response to third order is

$$\alpha(t) = A\alpha_1(t) + A^3\alpha_3(t) \quad (3.31)$$

The approximate response determined from this procedure will be compared in the next section to the solution of the original nonlinear equations.

### 3.2.2 DAMPING

Damping has a strong influence on the response near resonances, so it is important to include in the approximate results. Explicitly including damping in the perturbation equations, however, is unwieldy due to the need to track phase shifts and damping factors through each iteration. Instead damping is added by modifying the final equations in a similar manner to the ‘correspondence principle of linear viscoelasticity’ (Bland 1960).

In the model, torsional springs at the root of each blade represent the first blade bending mode. If torsional viscous dampers were added in parallel with the torsional springs, the total force would be  $kx + c\dot{x}$ , where  $k$  is the stiffness and  $c$  is the damping. Under harmonic motion,  $x = Xe^{i\omega t}$ , the force is  $(k + ci\omega)Xe^{i\omega t}$ , which is equivalent to a spring of complex stiffness  $k(1 + i2\zeta\omega/\omega_n)$ , where  $\zeta$  is the damping coefficient and  $\omega_n$  is the natural frequency  $\sqrt{k/m}$ . Therefore, to account for viscous damping, it is sufficient to replace every occurrence of the undamped natural frequency  $\omega_n^2$  with

$$\omega_n^2 + i2\zeta\omega\omega_n = \frac{k(1 + i2\zeta\omega/\omega_n)}{m}$$

## 3.3 Numerical results

As an alternative approach, numerical integration of the full equations of motion (Section 3.1.2) was also used to find spectra of the blade response.

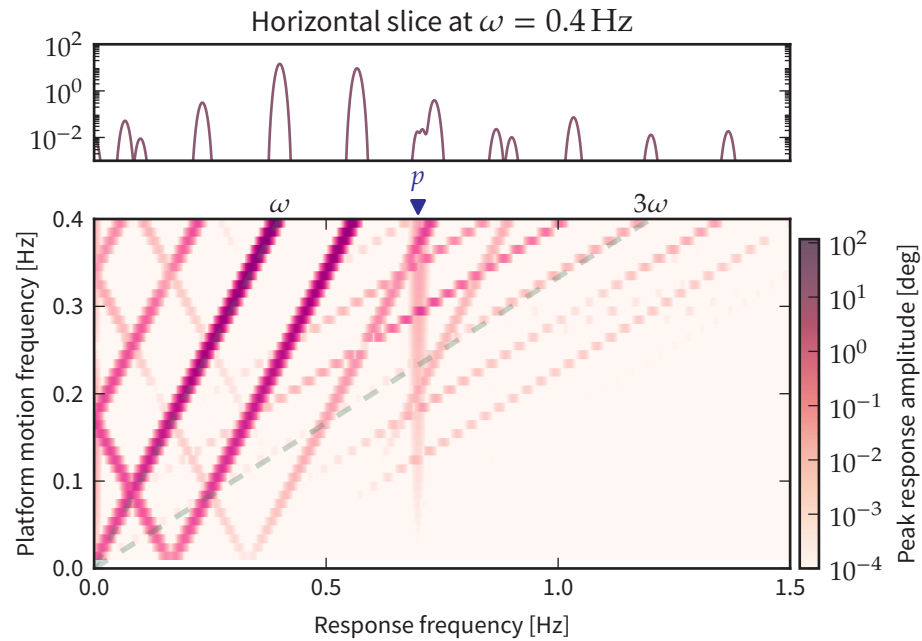


Figure 3.4 – Simulation results showing the many harmonics present in the flapwise blade response to platform pitching motion of  $\pm 11^\circ$ . The rotor speed  $\Omega$  is 10 rpm.  $p$  indicates the blade natural frequency. The lines labelled  $\omega$  and  $3\omega$  show harmonics with frequencies equal to the platform motion frequency and at  $3\times$  the platform motion frequency respectively.

These results will be compared to the analytical perturbation results from the previous section.

Numerical results were calculated for a grid of values of the platform motion frequency  $\omega$ , the rotor speed  $\Omega$  and the platform motion amplitude  $A$ . For each type of motion, the equation was integrated for several periods until initial transients had died away. The spectra were then calculated from the remaining part of the simulation.

Figure 3.4 shows a spectrum of the flapwise blade response for one particular set of conditions, and also the contour plot formed by combining response spectra for many frequencies of platform motion. Clearly the response contains many regularly-spaced harmonics, consistent with the prediction of the perturbation analysis of harmonics with frequencies of the form  $a\omega + b\Omega$ : there are sets of parallel lines, corresponding to different values of  $b$ , and there are multiple sets with different slopes, corresponding to different values of  $a$ .

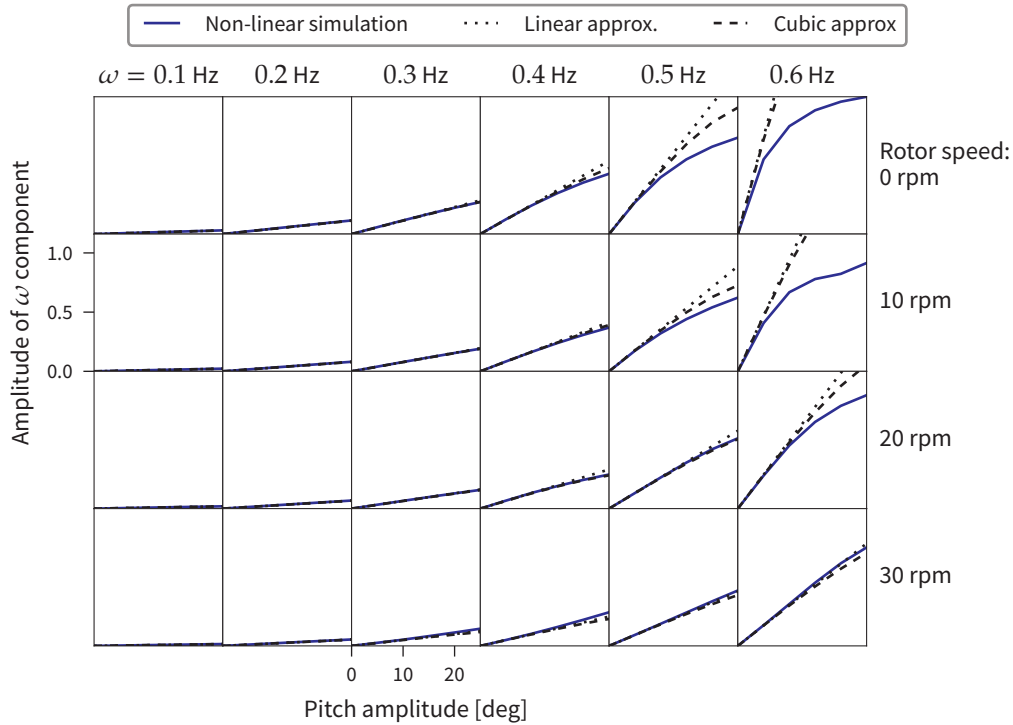


Figure 3.5 – First- and third-order perturbation results for the  $\omega$  component of the flapwise response to platform pitch motion, compared to nonlinear simulation results.

While Figure 3.4 shows the structure of the response, note that the logarithmic scale covers a wide range of amplitudes. Although many harmonics are present, most of them are very small.

### 3.3.1 COMPARISON OF PERTURBATION AND NUMERICAL RESULTS

Figures 3.5–3.7 show a selection of results from the perturbation analysis (Equation 3.31) for various values of the rotor speed  $\Omega$  and platform pitching frequency  $\omega$ . The three figures show the amplitude of three harmonics in the response, at  $\omega$ ,  $\omega - \Omega$  and  $\omega + \Omega$ . The analysis was carried out to third order in the platform motion amplitude, so both first- and third-order estimates of the response are shown. The nonlinear results are also shown for comparison.

For small amplitudes, all the results agree, as expected. For larger amplitudes, generally the nonlinear results increase less quickly than the

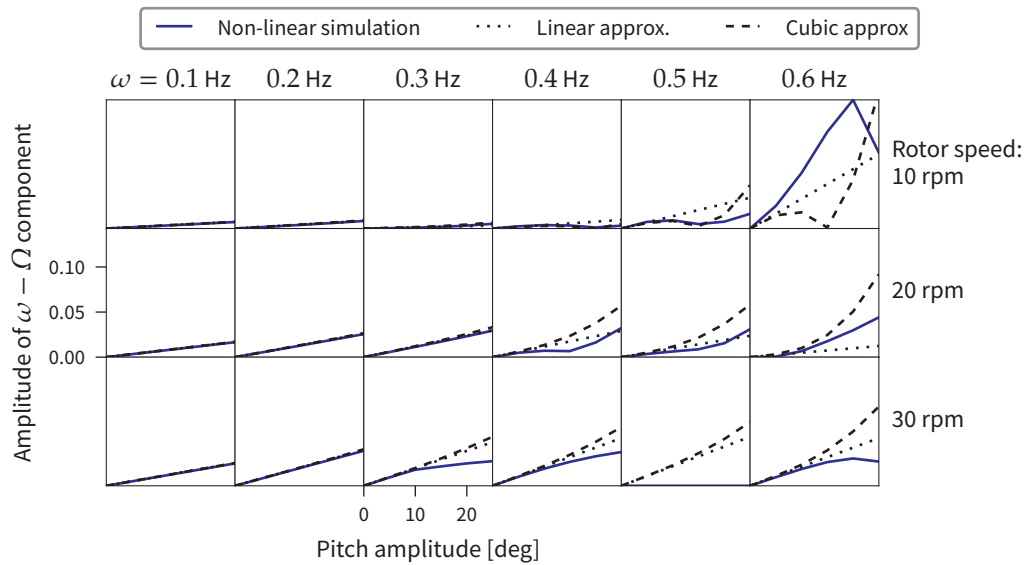


Figure 3.6 – First- and third-order perturbation results for the  $\omega - \Omega$  component of the flapwise response to platform pitch motion, compared to nonlinear simulation results.

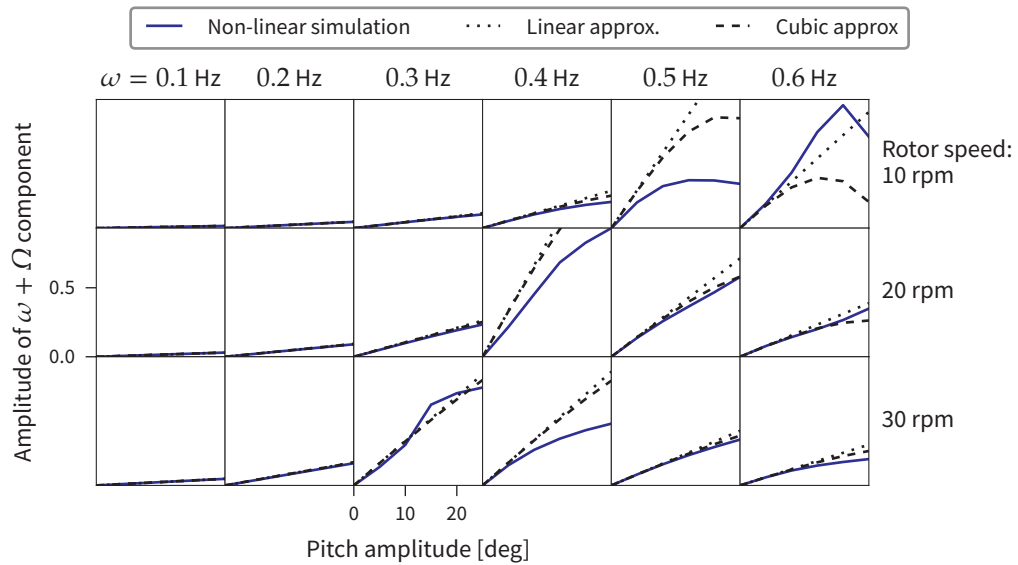


Figure 3.7 – First- and third-order perturbation results for the  $\omega + \Omega$  component of the flapwise response to platform pitch motion, compared to nonlinear simulation results.

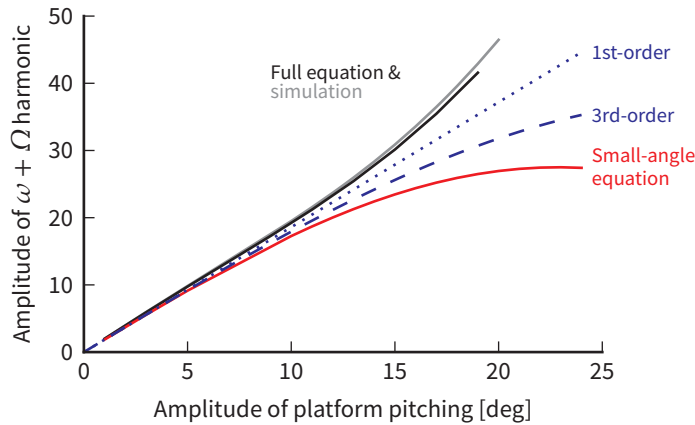


Figure 3.8 – Comparison of small-angle approximate equation, full equation and perturbation results. Part of the error in the perturbation results is due to being based on the small-angle approximate equation of motion, which unsurprisingly does not represent the correct behaviour for large amplitudes. The results shown are the amplitude of the  $\omega + \Omega$  harmonic when  $\omega = 0.58$  Hz and  $\Omega = 15$  rpm.

linear approximation. In some cases the third-order approximation shows the same behaviour, but in others it appears to be worse than the first-order approximation.

Part of the difference between the nonlinear and the perturbation results is due to the use of the approximate small-angle equations of motion, as well as the perturbation approximation itself. This is illustrated in Figure 3.8.

Generally, although the perturbation analysis can give an interesting insight into the blade dynamics, it is not suitable for describing the blade response for large-amplitude motion of the platform. The rest of this section focuses on the numerical results only.

### 3.3.2 VERIFICATION OF NUMERICAL RESULTS

The equations of motion given in Section 3.1.2 were verified by comparing the numerical results presented above to simulation results from the multibody dynamics code ‘mbwind’ (Chapter 2). Simulations were run for a grid of combinations of rotor speeds, platform motion frequencies and amplitudes. In mbwind, the model is represented by a series of rigid bodies and hinges with rotational stiffness (Figure 3.9). In a smaller num-

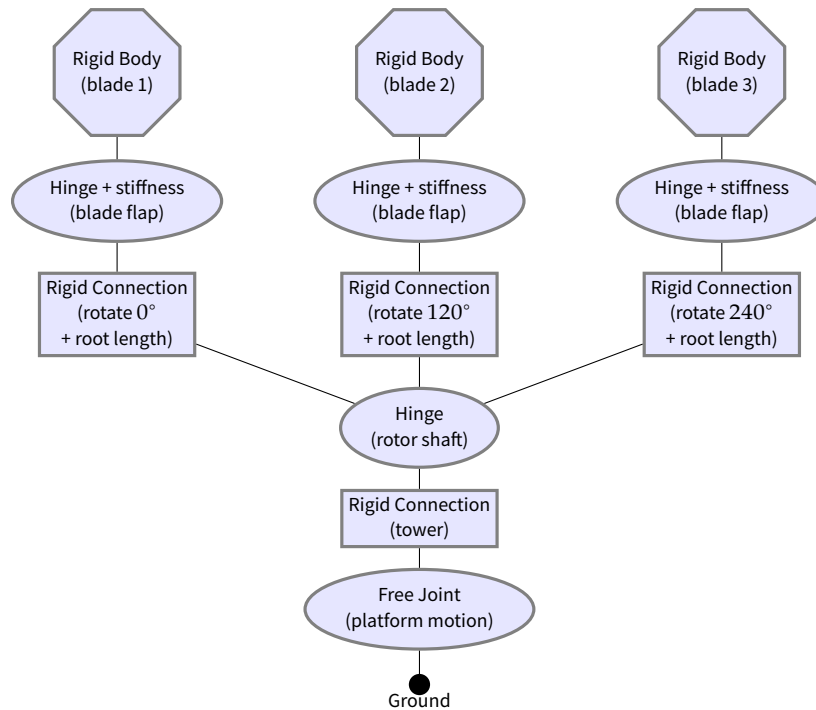


Figure 3.9 – Layout of mbwind numerical model.

ber of cases another time-domain wind turbine simulation code, Bladed (Garrad Hassan 2011), was also used for additional verification. In Bladed the hinged blade is modelled using a one-bladed rotor with a teeter hinge<sup>1</sup>.

Figure 3.10 shows one example of the verification results for the flapwise response to platform pitching motion, for one particular rotor speed. The overall responses are very similar. Figure 3.11 shows the same results as slices along two of the harmonics visible in Figure 3.10, and again there is good agreement.

Although only one set of results is shown here, good agreement was found for both flapwise and edgewise responses to all platform motions.

### 3.3.3 NUMERICAL RESULTS FOR DIFFERENT PLATFORM MOTIONS

Figures 3.12–3.18 present results for both the flapwise and edgewise responses to all types of platform motion. In each case the rotor speed is

1. A teeter hinge is sometimes used in one- and two-bladed wind turbines and allows the blade(s) to rotate freely perpendicular to the axis of rotation of the rotor. It is used here purely because it provides the right geometry for verification.

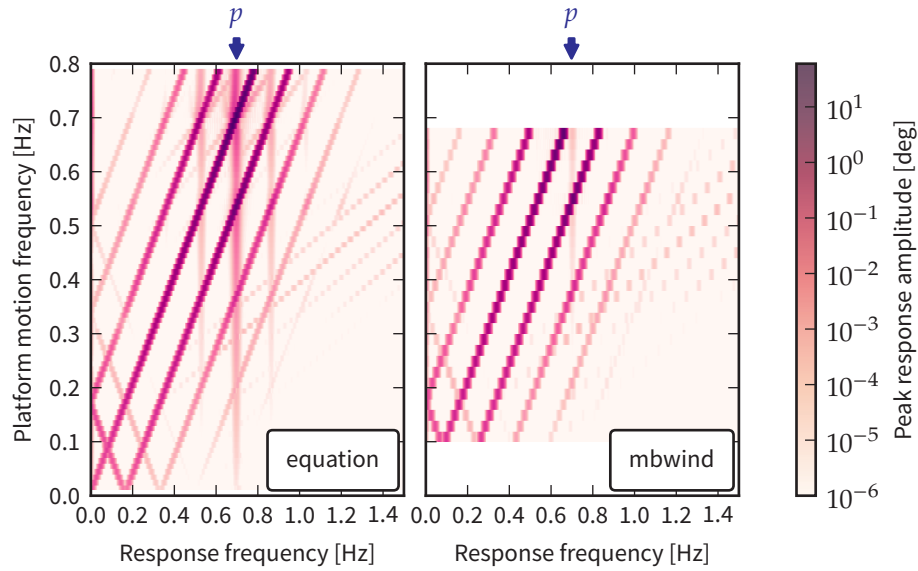


Figure 3.10 – Example verification results, comparing mbwind simulation results with direct solution of equations of motion for the flapwise response to platform pitching motion. The overall behaviour is very similar.  $p$  indicates the natural frequency, and hence the largest responses. Rotor speed  $\Omega = 10$  rpm.

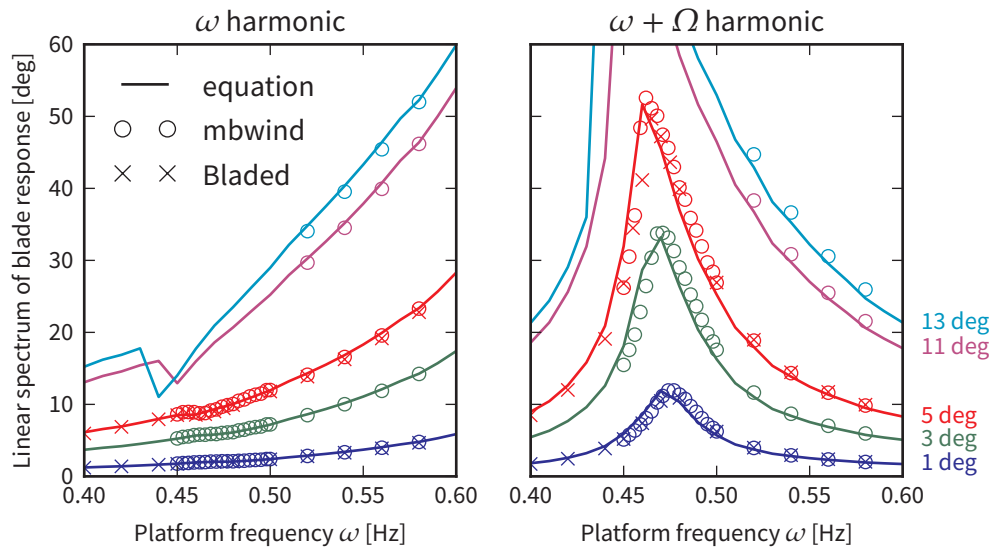


Figure 3.11 – Detail of results shown in Figure 3.10: slices along two response harmonics,  $\omega$  (left) and  $\omega + \Omega$  (right). “Equation” refers to the direct integration of the equations of motion; “mbwind” and “Bladed” are the time-domain simulation results.  $\Omega = 15$  rpm.

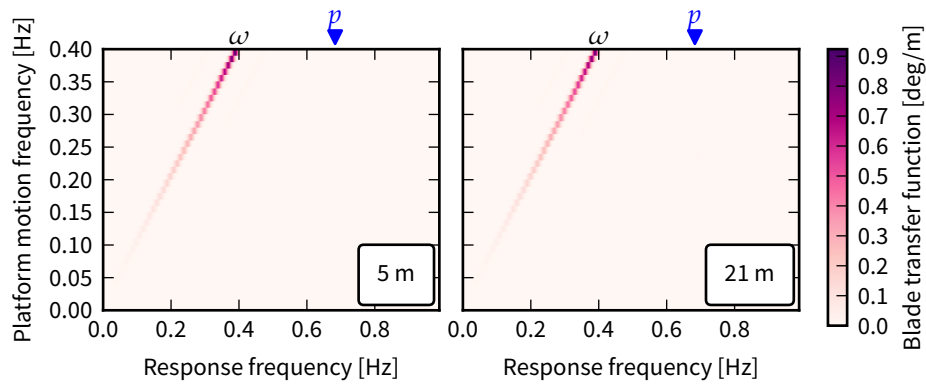


Figure 3.12 – Flapwise response to platform surge motion. The response occurs purely at the forcing frequency  $\omega$ , and is linear.  $p$  indicates the natural frequency.

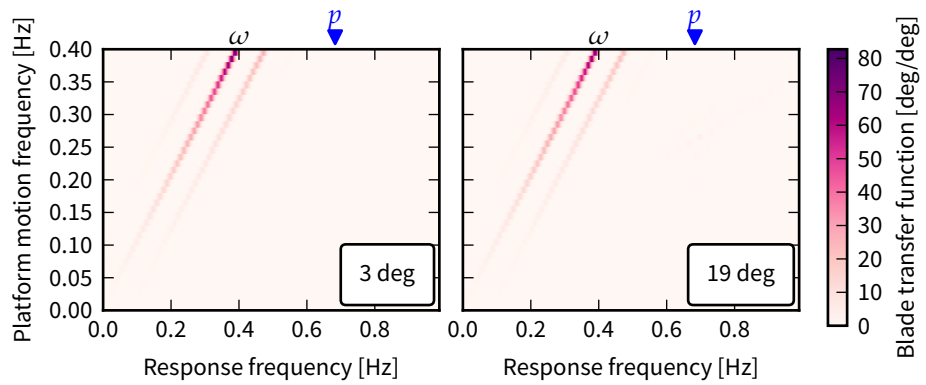


Figure 3.13 – Flapwise response to platform pitch motion. There is some response at  $\omega \pm \Omega$ , but most at the forcing frequency  $\omega$ . All harmonics are linear.

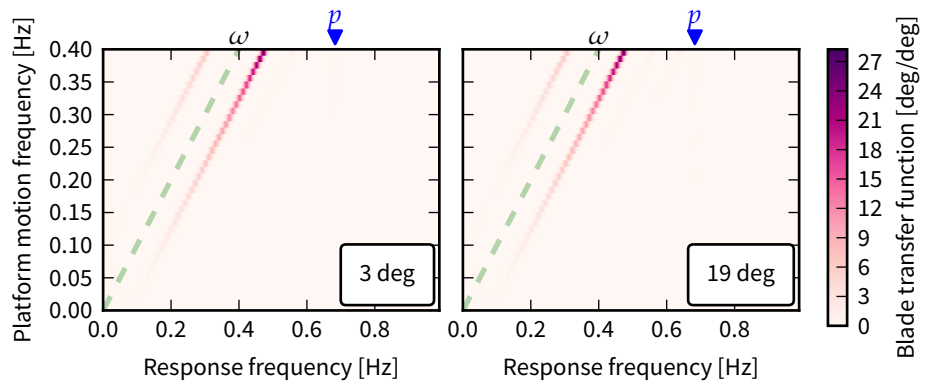


Figure 3.14 – Flapwise response to platform yaw motion. There is no response at the forcing frequency  $\omega$  (shown by the dashed line), only at  $\omega \pm \Omega$ . Both harmonics are linear.

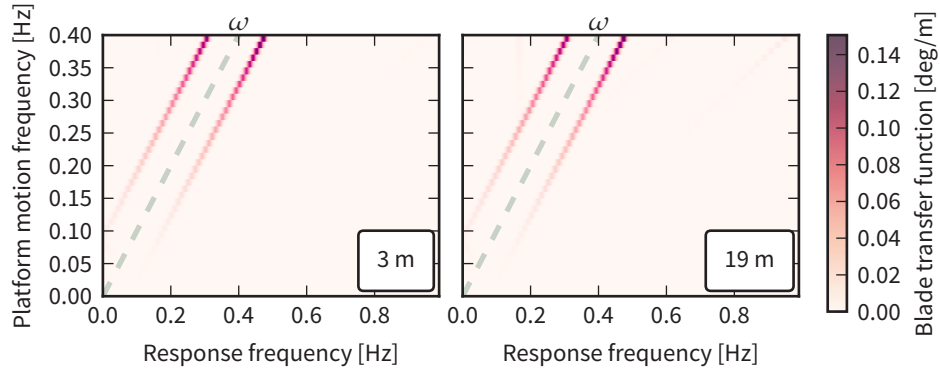


Figure 3.15 – Edgewise response to platform heave motion. There is no response at the forcing frequency  $\omega$  (shown by the dashed line), only at  $\omega \pm \Omega$ . Both harmonics are linear.

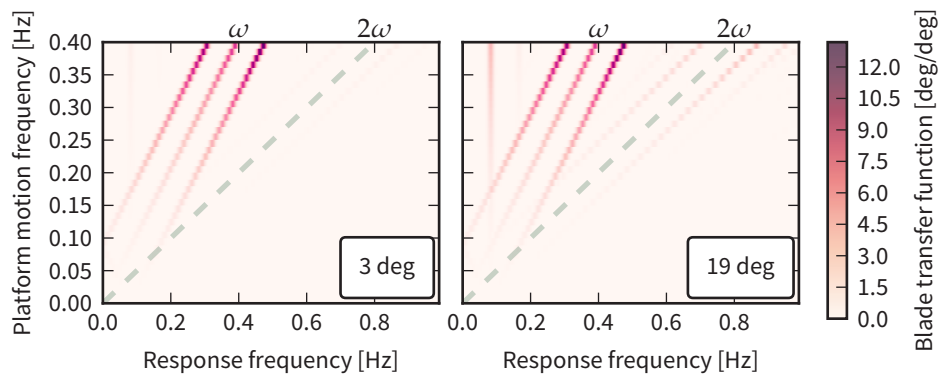


Figure 3.16 – Edgewise response to platform roll motion. There is a linear response at  $\omega$  and  $\omega \pm \Omega$ . Additional nonlinear responses at  $\Omega$  and  $2\omega \pm \Omega$  are visible for larger amplitudes (on either side of the dashed line at  $2\omega$ ).

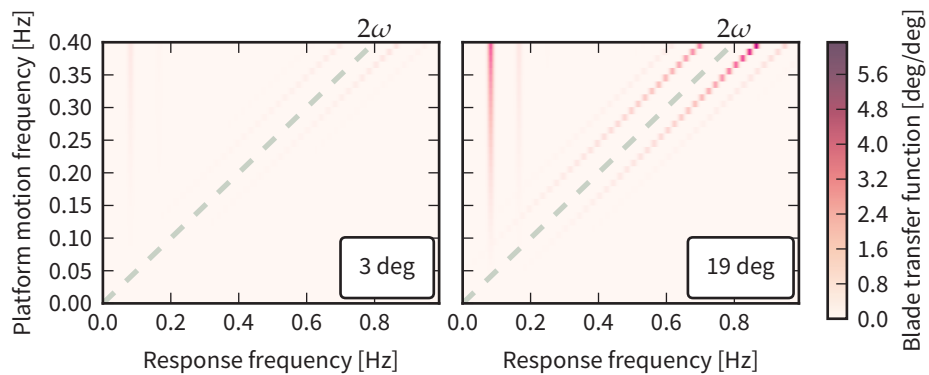


Figure 3.17 – Edgewise response to platform pitch motion. The response is entirely nonlinear, mostly at  $2\omega \pm \Omega$  and  $\Omega$  but also  $2\omega \pm 2\Omega$  and  $2\Omega$ . The dashed guideline shows where the  $2\omega$  harmonic would be.

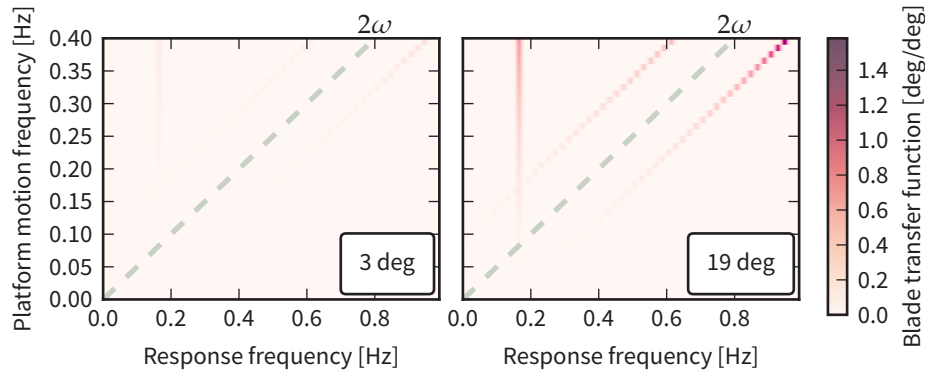


Figure 3.18 – Edgewise response to platform yaw motion. The response is entirely nonlinear, at  $2\omega \pm 2\Omega$  and  $2\Omega$ . The dashed guideline shows where the  $2\omega$  harmonic would be.

5 rpm, which is 0.083 Hz. This determines the horizontal spacing of the harmonics in the figures; the value is arbitrarily chosen to give a clear result.

The plots show transfer functions from platform motion amplitude to blade response, and each plot shows both a large- and a small-amplitude case, giving a simple indication of non-linearity. The natural frequency of the blade is marked by an arrow at the edge of each plot. Note that unlike Figure 3.4, the amplitudes are shown on a linear scale.

The flapwise responses (Figures 3.12–3.14) show that surge motion causes a blade response at frequency  $f = \omega$ , the frequency of the platform motion, while yaw motion causes a blade response at  $\omega \pm \Omega$ . The response to pitch motion contains harmonics at all of these frequencies, which is expected since from the point of view of the rotor centre, pitch is a combined rotation (like yaw) and translation (like surge) motion. By comparing the small- and large-amplitude subplots, it can be seen that these flapwise responses are linear in the amplitude of platform motion.

Platform heave and roll motions both cause linear edgewise blade responses (Figures 3.15 & 3.16). Heave motion causes a response at  $\omega \pm \Omega$ , while roll motion causes a response at both  $\omega \pm \Omega$  and  $\omega$ . Although the two linear harmonics continue to dominate the response to heave motion even at the larger amplitudes, non-linear responses to roll motion are visible on the right of Figure 3.16: these appear at  $\Omega$  and at  $2\omega \pm \Omega$ .

Unlike the result described above, the edgewise responses to platform

Table 3.2 – Summary: frequency content of main responses

Motion	Response	0 + ...		$\omega + \dots$			$2\omega + \dots$				
		$\Omega$	$2\Omega$	$-\Omega$	0	$\Omega$	$-2\Omega$	$-\Omega$	0	$+\Omega$	$+2\Omega$
Surge	flapwise					●					
Pitch	flapwise			●	●	●					
Yaw	flapwise			●		●					
Heave	edgewise			●		●					
Roll	edgewise	●		●	●	●		●		●	
Pitch	edgewise	●	●				●	●		●	●
Yaw	edgewise		●				●				●

pitch and yaw are purely nonlinear (Figures 3.17 & 3.18). This is because the only inertial loading on the blades in these cases is the centrifugal force due to the rotation of the platform in pitch or yaw (as opposed to the centrifugal force due to the rotor rotation). This force is proportional to the squared amplitude of the motion, so the response is purely nonlinear. Yaw motion causes responses at  $2\Omega$  and  $2\omega \pm 2\Omega$ ; these frequencies are also present in the response to pitch motion, along with larger harmonics at  $\Omega$  and  $2\omega \pm \Omega$ .

As noted before, the response to sway motion should be identical to heave, since both are a translational motion in the plane of the rotor.

Some types of platform motion produce no flapwise or edgewise response: surge motion produces no edgewise response, and roll and heave motion produce no flapwise responses. Although if these platform motions are superimposed on a nonzero mean pitch angle then it is possible to excite a blade response, these responses are not shown here.

In summary, the blade response contains harmonics at various frequencies. Table 3.2 shows the most important harmonics present in the response to each type of motion.

### 3.3.4 CONDITIONS LEADING TO LARGE BLADE RESPONSES

The largest blade responses occur for certain combinations of platform motion frequency and rotor speed when a forcing harmonic coincides

with the blade natural frequency. This can be seen in Figures 3.12–3.18 above, where the largest responses are around the natural frequencies, marked by the arrows at the edge of the plots. This is shown more clearly in Figure 3.19 by plotting the total blade response variance against the platform motion frequency and the rotor speed, with resonances expected around the lines  $\omega = (p - b\Omega)/a$ .  $p$  is the natural frequency of the blade, including centrifugal stiffening for flapwise motion.

Of the flapwise responses (Figure 3.19 a-c), surge motion causes the simplest response. Since the only forcing is at the platform frequency  $\omega$  (see also Figure 3.12 above), the response is simply increasing towards the blade natural frequency, located off the top of the plots. For yaw motion, the forcing is at  $\omega \pm \Omega$  (Figure 3.14). Therefore for the same platform frequency and rotor speed, the forcing frequency due to yaw motion is higher than the forcing frequency due to surge motion, and resonance is reached in the top-right corner of Figure 3.19c. Pitching motion is effectively a combination of surging and yawing motions, which is reflected in the results for pitching motion in Figure 3.19b.

The edgewise natural frequency of the blade is higher than the flapwise frequency, so the blade is further from resonance and the edgewise responses in Figure 3.19(d-g) are smaller than the flapwise responses in Figure 3.19(a-c). Additional resonances are visible, excited by higher harmonics in the forcing: for example, at  $2\omega + \Omega$  and  $2\omega + 2\Omega$ , as marked on the plots. These smaller resonances are the only features visible in the edgewise responses to pitch and yaw motion (Figure 3.19 f-g). The responses to heave and roll motion (Figure 3.19 d-e) are larger overall due to forcing around  $\omega$ .

In summary, a general increase in response variance with increasing platform frequency  $\omega$  is observed, as the forcing frequencies approach the blade natural frequencies. For the present reference turbine blade, the frequency of platform motion is always below the natural frequency of the blade, but there may be a risk that in future more flexible blades would lead to a greater response at lower frequencies. In addition, there are particular combinations of  $\omega$  and  $\Omega$  which lead to additional resonances (Table 3.3). These are due to nonlinear harmonics in the inertial forcing coinciding with the blade natural frequency.

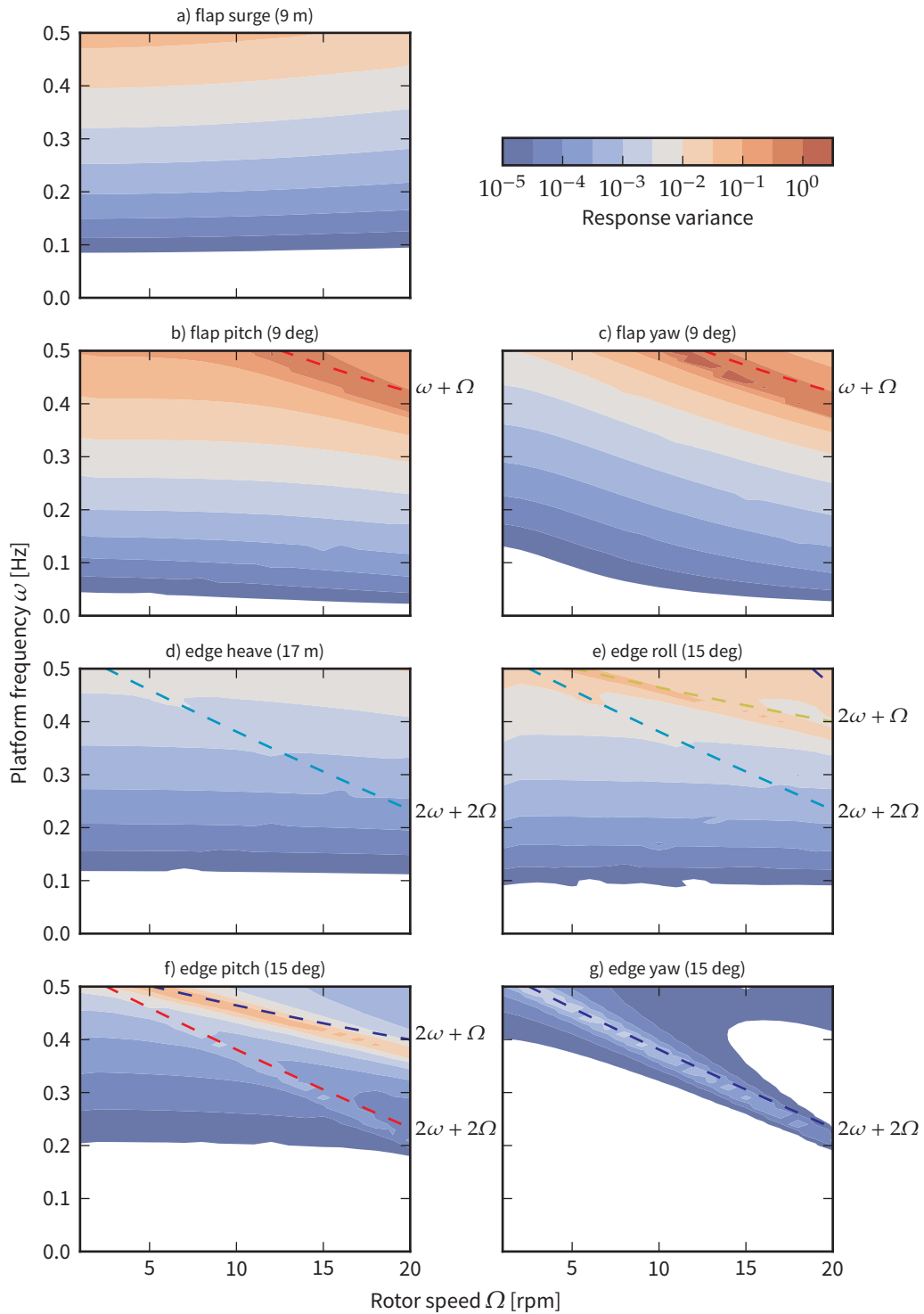


Figure 3.19 – Blade response variance due to different platform motions.

Table 3.3 – Local resonances (up to 0.4 Hz).

Motion	Response	$2\omega+\Omega$	$2\omega+2\Omega$
Heave	edgewise		●
Roll	edgewise	●	●
Pitch	edgewise	●	●
Yaw	edgewise		●

### 3.3.5 LINEARITY OF BLADE RESPONSE

The level of nonlinearity in the blade response to platform motion is important for modelling the whole floating wind turbine system in the frequency domain. In this section the linearity of the blade response results presented above is discussed. ‘Non-linearity’ will be measured as

$$\text{nonlinearity}(A) = \frac{\sigma(A)/A}{\sigma(A_0)/A_0} - 1 \quad (3.32)$$

where  $A$  is the amplitude of the platform motion,  $\sigma(A)$  is the blade response standard deviation at a given amplitude, and  $A_0$  is a small reference amplitude. The nonlinearity is summarised by plotting the ‘critical motion amplitude’ against the platform motion frequency and the rotor speed; the critical motion amplitude is the smallest amplitude for which the nonlinearity (3.32) exceeds a certain value. Figure 3.20 shows plots of the critical motion amplitude for the flapwise response to surge, pitch and yaw, and the edgewise response to heave and roll.

In the majority of conditions the blue colour of the plots indicates that even the largest amplitudes of platform motion considered were not enough to cause significant nonlinear behaviour. In particular, this applies throughout the area where  $\omega < 0.2$  Hz and  $\Omega < 20$  rpm.

There are specific combinations of platform frequency and rotor speed which lead to nonlinear behaviour at moderate or even small amplitudes. These are particularly noticeable in the edgewise responses to heave and roll motion. Note however that as the nonlinearity is defined as the relative change in the transfer function, an area with high nonlinearity may be irrelevant if the response there is small.

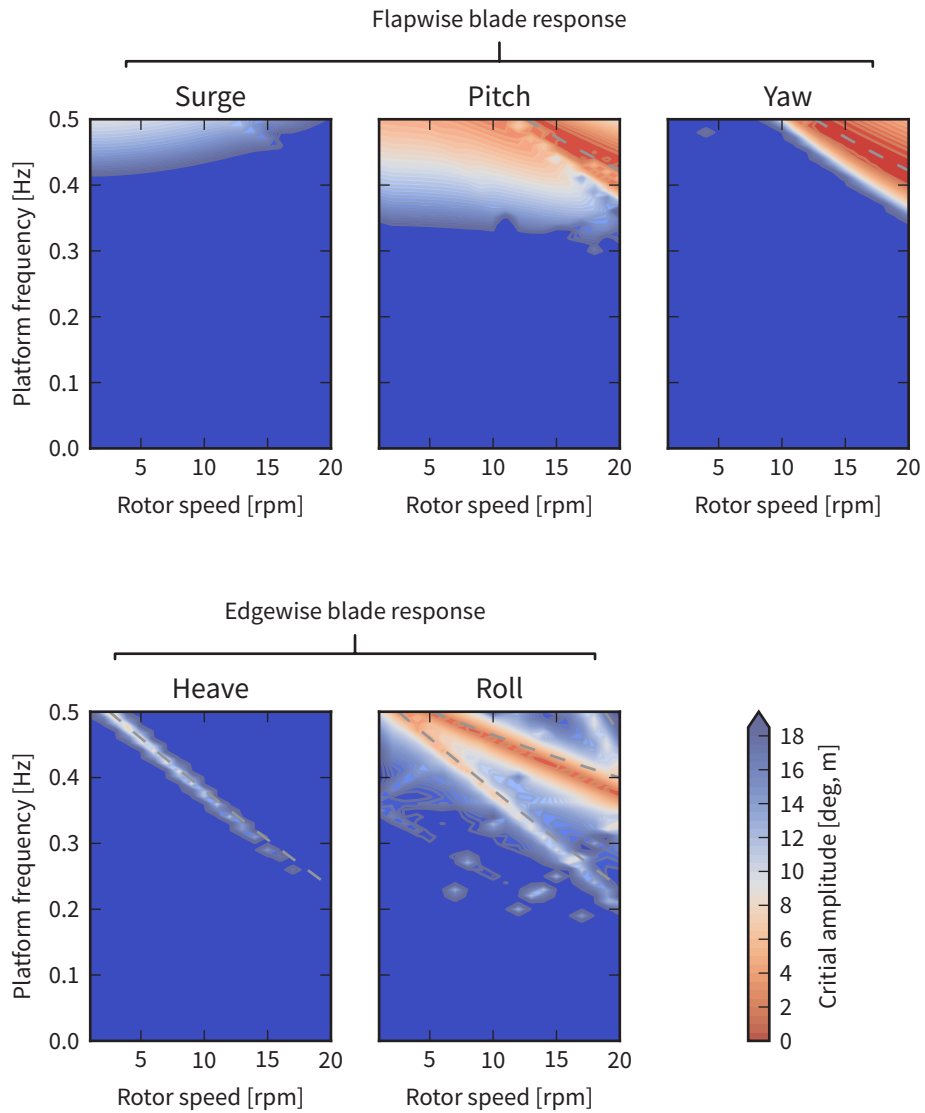


Figure 3.20 – Critical motion amplitude for nonlinearity to exceed 5%.

In the flapwise response to surge and pitch motion, increased nonlinearity is visible at the top of the plots, for higher  $\omega$ . This is due to linear parts of the inertial loads exciting resonance of the hinged blade and leading to large deflections. It is the large deflections which cause the nonlinear response here, and so this shows a limitation of the simplified model rather than an exact result.

The edgewise response to pitch and yaw motion are not included in Figure 3.20 since these responses are purely nonlinear. However, they are both much smaller in magnitude than the other responses.

Finally, it is interesting to note that if in future floating wind turbines are developed which operate at higher rotor speeds, more of these resonances may be excited at lower frequencies of platform motion than shown here.

### 3.4 Blade dynamics at model scale

Model-scale testing is commonly used in the design of offshore structures. Although the complexity of floating wind turbines makes model testing difficult, a few tests have been performed (Roddier et al. 2010; Nielsen, Hanson and Skaare 2006; Goupee et al. 2012). Compromises are usually involved because different effects scale differently: for example, to model the wave loads correctly, the Froude number should be held constant between model and prototype scale, while to model the aerodynamic loads correctly, the Reynolds number should be held constant. Both cannot be achieved simultaneously with a geometrically-similar model, while also keeping the wind and wave forces in proportion (Martin et al. 2014).

In this section, the scaling of the rotor dynamic behaviour described earlier in this chapter is examined. The behaviour is shown to be correct at model scale if the model is geometrically similar and the platform motion frequency, rotor speed and blade natural frequency are all scaled in proportion. To date, this has not been achieved in model tests, which have considered the rotor dynamics out of scope (Goupee et al. 2012).

Table 3.4 – Quantities describing the blade response to platform motion and their dimension: [M]ass, [L]ength and [T]ime.

Quantity	Symbol	Dimension
Blade angular response	$\alpha, \beta$	–
Blade mass	$m$	M
Blade 1st moment of mass	$I_1$	ML
Blade 2nd moment of mass	$I_2$	ML <sup>2</sup>
Blade rotational stiffness	$k$	ML <sup>2</sup> T <sup>-2</sup>
Tower height	$h$	L
Amplitude of platform motion	$A$	L or –
Frequency of platform motion	$\omega$	T <sup>-1</sup>
Rotor speed	$\Omega$	T <sup>-1</sup>
Acceleration due to gravity	$g$	LT <sup>-2</sup>

### 3.4.1 DIMENSIONAL ANALYSIS OF BLADE DYNAMICS

The dynamics of the blade in the simplified model used in this chapter are described by the quantities in Table 3.4. By normalising by a mass scale  $M_0 = m$ , a time scale  $T_0 = 1/\omega$  and a length scale  $L_0 = \sqrt{I_2/m}$ , the non-dimensional blade response is found to depend on six non-dimensional numbers:

$$\left. \begin{array}{l} \alpha \\ \beta \end{array} \right\} = F \left( \frac{g}{L_0 \omega^2}, \frac{I_1}{\sqrt{m I_2}}, \frac{h}{L_0}, \frac{\Omega}{\omega}, \frac{\omega_n}{\omega}, \frac{A}{L_0} \right) \quad (3.33)$$

where  $\omega_n = \sqrt{k/I_2}$ . As written, this applies translational motions of the platform; for rotational motions,  $A$  is already non-dimensional and the last group is not needed. Since the response depends only on these non-dimensional groups, as long as they are held constant between the prototype and model scales then the blade dynamics should be correct.

Assuming geometric similarity, the first three groups are automatically held constant provided that the blade material density is the same at both scales. For the last, the amplitude of the platform motion  $A$  must also be scaled geometrically. Finally, the frequency of platform motion  $\omega$  must be scaled in proportion to the rotor speed  $\Omega$  and the blade natural frequency  $\omega_n$ .

In wave tanks the wave environment is scaled to preserve Froude num-

ber, and to keep the correct ratio of wind- to wave-loading the wind speed should be scaled in the same way. The tip speed ratio<sup>2</sup> of the rotor should also be preserved (Martin et al. 2014). For a scaling factor  $\lambda$ , this leads to the rotor speed scaling as  $\lambda^{-1/2}$ .

For dynamic similarity the natural frequency of the rotor blades should be scaled in proportion to the rotor speed and platform motion frequency. This may be challenging as the model blades must be very light; for example the blades of the 1/50 scale NREL 5MW turbine used by Martin et al. (2014) are 1.23 m long but weigh only 140 g. In practice, model tests have used stiff blades (Goupee et al. 2012) and the blade dynamics have not been considered. This means the ratio  $\omega_n/\omega$  is too high. In Figure 3.19, the response will be towards the bottom of the plot, and nonlinear parts of the response will be underestimated.

Another difficulty may arise if the blades are not simply geometrically scaled. For example the aerodynamic profiles of the blade may be re-designed to deal with the lower Reynolds numbers experienced at model scale (Martin et al. 2014). If the blade dynamics are to be modelled correctly, the moments of mass of the model blade should be preserved.

## 3.5 Linear structural model

Section 3.3.5 showed that the blade dynamics can reasonably be approximated by a linear model. For use in a frequency domain analysis some further work is required, as even though the dependence on the input motion amplitude is linear, the blade response contains multiple frequencies. This is a well known phenomenon and is typically addressed by applying a Multi-Blade Coordinate transform (MBC) or Coleman transformation (MH Hansen 2007), in which the blade deflections are transformed into a non-rotating frame of reference. For example, the flapwise deflection of blade  $k$  is expressed as

$$\alpha_k = a_0 + a_1 \cos \psi_k + b_1 \sin \psi_k \quad (3.34)$$

2. The Tip Speed Ratio (TSR) is  $\Omega R/U$ , where  $\Omega$  is the rotor speed,  $R$  is the rotor radius and  $U$  is the wind speed.

where for a three-bladed rotor  $\psi_k = \Omega t + 2\pi(k - 1)/3$ , and  $a_0$ ,  $a_1$  and  $b_1$  are the ‘multi-blade coordinates’. In this case  $a_0$  represents the average flapwise deflection across all three blades, while  $a_1$  and  $b_1$  represent tilt and yaw motions respectively. Edgewise deflections can be described similarly.

The benefit of this transformation is that if the rotor is isotropic, that is, all three blades are identical, then components of the blade response related to the rotor speed are removed: if the flapwise blade response  $\alpha_k$  contains harmonics at  $\omega$ ,  $\omega - \Omega$  and  $\omega + \Omega$ , then the transformed coordinates  $a_0$ ,  $a_1$  and  $b_1$  contain only one harmonic, at  $\omega$ . This operation can also be viewed as transforming a linear time-periodic system into a linear time-invariant system.

If the rotor is not perfectly isotropic, the MBC transformation will reduce but not eliminate the additional harmonics in the response. In this case the remaining periodicity is often simply neglected, or Floquet analysis can be used (Skjoldan and MH Hansen 2010). For two-bladed rotors the Floquet analysis is always required (Stol, Balas and Bir 2002).

In practice the MBC transformation between the blade-fixed coordinates  $\mathbf{y}$  and the fixed-frame coordinates  $\mathbf{z}$  is achieved via a transformation matrix,

$$\mathbf{y} = \mathbf{B}(t)\mathbf{z} \quad (3.35)$$

where

$$\mathbf{B}(t) = \begin{bmatrix} \mathbf{I}_N & \mathbf{I}_N \cos \psi_1 & \mathbf{I}_N \sin \psi_1 \\ \mathbf{I}_N & \mathbf{I}_N \cos \psi_2 & \mathbf{I}_N \sin \psi_2 \\ \mathbf{I}_N & \mathbf{I}_N \cos \psi_3 & \mathbf{I}_N \sin \psi_3 \end{bmatrix} \quad (3.36)$$

in which  $\mathbf{I}_N$  is an identity matrix of size  $N$ , and  $N$  is the number of degrees of freedom of each blade. After solving the response in terms of the fixed-frame coordinates  $\mathbf{z}$ , the blade response is recovered by the reverse transformation.

## 3.6 Conclusions

In this chapter the structural dynamics of a flexible blade on a moving platform have been studied, making use of a simplified model undergoing prescribed motions. The blade response consists of many harmonics. Of these, the dominant harmonics depend linearly on the amplitude of platform motion. They appear at  $\omega$  and  $\omega \pm \Omega$  in the flapwise response to surge, pitch and yaw motion, and the edgewise response to sway, heave and roll motion. Additional harmonics appear at other combinations of  $\omega$  and  $\Omega$ , which depend nonlinearly on the amplitude of platform motion.

The existence of multiple harmonics means resonance of the blades may be excited in more ways than would be expected from a linear system: there are multiple combinations of values of  $\omega$  and  $\Omega$  which could cause a large blade response.

Although the response does contain nonlinear harmonics, they are small for practical conditions. In particular, the response is linear for  $\omega < 0.2$  Hz and  $\Omega < 20$  rpm; current wind turbines operate at lower rotor speeds than this, and most platform motions with large amplitudes occur at low frequencies. In practice, this means that for the level of accuracy for which a linear structural model is acceptable for a fixed-bottom wind turbine, a linear model should also be acceptable for modelling the dynamics of a wind turbine on a floating platform.



## Chapter 4

### *Linearised hydrodynamics*

In this chapter a frequency-domain model of a flexible floating wind turbine structure with hydrodynamic loading is developed, the importance of nonlinear ‘slow drift motion’ for floating wind turbines is assessed, and techniques for including the nonlinear viscous drag forces in the linearised model are reviewed.

Several types of hydrodynamic loads act on a floating wind turbine, as on any other floating platform: ‘diffraction’ forces due to the acceleration of the waves around the structure, ‘radiation’ forces due to the motion of the platform through the water, and viscous forces due to both waves and platform motion. There may be other effects such as loads due to breaking waves, but they are not considered here. For more background to hydrodynamic loads see the introduction in Section 1.3.4 on p 20, or for example Chakrabarti (2005, chapter 4).

With the exception of the viscous forces, the hydrodynamic loads are often modelled by a linearised potential flow method. Were this to be sufficient, there would be little to add in this chapter on the linearised modelling of floating wind turbine hydrodynamics. However, the nonlinear parts of the hydrodynamic loads – which are not included in the linear potential flow model – are known to be important in some cases for other floating structures. In particular, the slowly-varying loads caused by nonlinear hydrodynamic effects can cause large resonant motion of the floating structure, known as ‘slow drift’. Although slow drift is the focus of this chapter, there are also higher-frequency nonlinear loads which can excite structural vibration modes of the platform (Faltinsen 1993, chapter 5).

To put the second-order low-frequency forces into perspective, when

the turbine is operating the low-frequency aerodynamic forces on the rotor have been shown by Roald et al. (2013) to be much larger than the second-order forces. This does not prevent the second-order forces being of interest: the turbine will routinely shut down in extreme conditions, and may not be operating due to faults in any environmental conditions.

In the first part of this chapter a numerical frequency-domain model is developed of a floating wind turbine with a flexible structure subject to hydrodynamic loading. Given the spectrum of the wave environment, this allows the spectra of the platform rigid-body response and elastic deformations to be found, accounting for both the linear and the second-order hydrodynamic loading. This is an advance over other frequency domain models of floating wind turbines (reviewed in Chapter 1), which have been limited to the rigid-body dynamics of the floating platform.

As an example, the reference floating turbine ‘OC3-Hywind’ defined for the OC3 project (Jonkman 2010) is used. Despite the warnings above about large slow-drift motions, the results for this platform show only very small slow-drift motions. This may not be surprising since the OC3-Hywind platform is a spar buoy with large draft and small water-plane area, but it motivates the main question of this chapter: is slow drift motion as important for floating wind turbines as it is for other types of floating platform? This is of interest because although the spectrum of the second-order forces can be found, in general its statistics are non-Gaussian, so finding the statistics of the platform response is not straightforward. If slow drift motions of floating wind turbines are relatively small, the analysis can be simplified.

Slow drift of floating wind turbines was studied by Lucas (2011), and more recently by Roald et al. (2013), motivated by observations of possible second-order effects in scale model tests. They calculate first- and second-order forces and responses for two specific floating wind turbine designs, a spar buoy and a TLP, using the commercial panel code WAMIT (Wamit Inc 2002) together with linearised system matrices calculated by the wind turbine code FAST (Jonkman and Buhl 2005). Although FAST does not yet account for second-order hydrodynamics, this is being addressed (Duarte, Sarmiento and Jonkman 2014). Bayati et al. (2014) apply the same approach to a semisubmersible platform. The results vary between the different

platforms; in some cases the slow drift response is smaller than the first-order motion, and in some cases it is larger.

A significant difference between floating wind turbines and other floating structures is their smaller scale: some other floating structures can be an order of magnitude larger than floating wind turbine platforms, while ships can be even larger. The next part of this chapter (Section 4.2) aims to determine whether this is the reason that relatively small slow drift motions were found in some cases, by determining how the slow drift response of a floating platform depends on its size. While the studies mentioned above give results for particular platform designs, here we aim to develop a more general result by deriving approximate closed-form expressions to estimate the second-order slow drift motion of platforms of different sizes.

Finally, another source of nonlinear loading is viscous drag, which has a quadratic dependence on the relative flow velocity. There are well-established techniques for including a linearised approximation of the viscous drag forces in a frequency-domain approach; these are discussed in relation to floating wind turbines in Section 4.3 at the end of the chapter.

## 4.1 Frequency-domain model of flexible structure with hydrodynamic loading

The basic form of the frequency domain model is

$$\{-\omega^2\mathbf{M} + i\omega\mathbf{B} + \mathbf{K}\}\bar{\mathbf{q}}(\omega) = \bar{\mathbf{F}}(\omega) \quad (4.1)$$

or equivalently

$$\mathbf{H}^{-1}(\omega)\bar{\mathbf{q}}(\omega) = \bar{\mathbf{F}}(\omega) \quad (4.2)$$

where  $\mathbf{H}$  is the system transfer function matrix, and  $\bar{\mathbf{q}}$  and  $\bar{\mathbf{F}}$  are the complex amplitude of the response and applied force for sinusoidal motion at

frequency  $\omega$ :

$$\mathbf{F} = \bar{\mathbf{F}}(\omega)e^{i\omega t} \quad (4.3a)$$

$$\mathbf{q} = \bar{\mathbf{q}}(\omega)e^{i\omega t} \quad (4.3b)$$

with the convention that the real part is assumed. If the cross-spectral density of the force is  $S_{FF}(\omega)$ , the cross-spectral response of the system response can be found as (Lin 1976, chapter 6):

$$S_{qq}(\omega) = \mathbf{H}(\omega) S_{FF}(\omega) \mathbf{H}^{*\top}(\omega) \quad (4.4)$$

where  $^{*\top}$  indicates the complex conjugate transpose. The response variances can then be calculated as

$$\sigma_{qq}^2 = \int_0^\infty S_{qq}(\omega) d\omega \quad (4.5)$$

These equations are very general. Next, the parts of the equation of motion (4.1) will be defined in more detail in relation to a general floating structure. Then the frequency-domain model is applied to an example floating wind turbine.

#### 4.1.1 EQUATIONS OF MOTION OF A FLOATING STRUCTURE

For a flexible structure with hydrodynamic loading, the mass, damping and stiffness matrices which appear in Equation (4.1) can be written as

$$\mathbf{M} = \mathbf{M}_{\text{struct}} + \mathbf{A}_h(\omega) \quad (4.6a)$$

$$\mathbf{B} = \mathbf{B}_{\text{struct}} + \mathbf{B}_h(\omega) + \mathbf{B}_v \quad (4.6b)$$

$$\mathbf{K} = \mathbf{K}_{\text{struct}} + \mathbf{K}_h + \mathbf{K}_m \quad (4.6c)$$

Here  $\mathbf{A}_h$  and  $\mathbf{B}_h$  are the hydrodynamic added mass and radiation damping matrices;  $\mathbf{B}_v$  is a linearised viscous damping matrix;  $\mathbf{K}_h$  is the hydrostatic stiffness matrix;  $\mathbf{K}_m$  is the linearised mooring line stiffness; and  $\mathbf{M}_{\text{struct}}$ ,  $\mathbf{B}_{\text{struct}}$  and  $\mathbf{K}_{\text{struct}}$  are the structural mass, stiffness and damping matrices. Most commonly the submerged part of the structure will be assumed rigid and the hydrodynamic, hydrostatic and mooring matrices will contain only the terms relating to the six rigid-body degrees of freedom, while the structural system matrices will in general relate to all the degrees of

freedom of the structure.

The applied forces consist of aerodynamic loads on the wind turbine rotor, wave excitation forces, and possibly viscous drag forces. The aerodynamic loads are ignored here but will be reintroduced in the next chapter. The viscous forces will also be ignored for now, but will be discussed later in Section 4.3. Mooring line forces are assumed to be accounted for by the linearised stiffness matrix  $\mathbf{K}_m$  and are not counted as applied forces here. Correct to second order, the wave excitation force in one degree of freedom can be written as the first two terms in a Volterra series. Langley (1987) shows that this can be expressed as

$$F(t) = \int_{-\infty}^{\infty} H_1(\omega)\zeta(\omega)e^{i\omega t} d\omega + \quad (4.7)$$

$$\int_{-\infty}^{\infty} \int_{-\infty}^{\infty} H_2(\omega_1, \omega_2)\zeta(\omega_1)\zeta(\omega_2)e^{i(\omega_1+\omega_2)t} d\omega_1 d\omega_2 \quad (4.8)$$

where  $\zeta(\omega)$ ,  $H_1(\omega)$  and  $H_2(\omega_1, \omega_2)$  are the sea surface elevation, first- and second-order Volterra kernels in the frequency domain. This shows that the wave loading consists of forces at  $\omega$  which are linear in the wave amplitudes, and forces at  $\omega_1 + \omega_2$  which are second order in the wave amplitudes. Because the range of the integrals above is from  $-\infty$  to  $\infty$ , the second-order forces occur at both the sum and difference frequencies of the waves. The difference-frequency forces are of particular interest because they can excite large platform motions. Although in future it may be of interest to include sum-frequency forces they are not considered further at present.

The wave forces are more commonly written in terms of the wave excitation coefficients  $\mathbf{X}(\omega)$  and the Quadratic Transfer Functions (QTFs)  $\mathbf{T}(\omega_1, \omega_2)$ , which are directly related to the formal Volterra kernels  $H_1$  and  $H_2$  (Langley 1987). The spectrum of the first-order forces is

$$\mathbf{S}_{FF}^{(1)}(\omega) = \mathbf{X}(\omega)\mathbf{S}_{\zeta\zeta}(\omega)\mathbf{X}(\omega)^{*T} \quad (4.9)$$

Pinkster (1980) shows that the second-order force spectrum is

$$\mathbf{S}_{FF}^{(2)}(\omega) = 8 \int_0^{\infty} \mathbf{T}(\omega', \omega' + \omega)\mathbf{S}_{\zeta\zeta}(\omega')\mathbf{S}_{\zeta\zeta}(\omega' + \omega)\mathbf{T}(\omega', \omega' + \omega)^{*T} d\omega' \quad (4.10)$$

where  $S_{\zeta\zeta}(\omega)$  is the wave power spectrum.

Calculation of the full QTF matrix  $T(\omega_1, \omega_2)$  can be time consuming, so sometimes an approximation known as Newman's approximation is used (Faltinsen 1993, chapter 5):

$$T(\omega_1, \omega_2) \approx T(\omega_2, \omega_1) \approx \frac{T(\omega_1, \omega_1) + T(\omega_2, \omega_2)}{2} \quad (4.11)$$

This can give satisfactory results because in most cases it is the low frequency forces that are of interest, when  $\omega_1$  is close to  $\omega_2$ .

Although in general the first and second order forces vary with the angle of approach of the waves, throughout this thesis only unidirectional waves are considered.

#### 4.1.2 EQUATIONS OF MOTION FOR A FLOATING WIND TURBINE

The equations above apply to any floating structure. We now consider the application to a floating wind turbine. In particular, as a specific example the OC3-Hywind reference turbine defined by the OC3 project is used (Jonkman 2010).

The structural matrices are found by building a multibody structural model using the framework developed in Chapter 2. The layout of the model is shown in Figure 4.1. All parameters are supplied by the OC3 project (Jonkman 2010). From this multibody model the matrices  $M_{\text{struct}}$ ,  $B_{\text{struct}}$  and  $K_{\text{struct}}$  are found by numerical linearisation as described in Section 2.4 on p 66.

The hydrodynamic coefficients are typically calculated by a numerical panel method code. The details are not presented here, since data is published by the OC3 project for  $A_h(\omega)$ ,  $B_h(\omega)$ ,  $K_h$  and  $X(\omega)$ , as well as the linearised mooring line stiffness  $K_m$ . The diagonals of the QTFs are provided by Lucas (2011); the full matrix  $T(\omega_1, \omega_2)$  is reconstructed using Newman's approximation (Equation 4.11). Viscous drag effects are neglected, but will be reintroduced in Section 4.3.

Figure 4.2 shows an example of the first- and second-order hydrodynamic forces on the platform. They have been calculated for a JONSWAP wave spectrum with a significant wave height of 4 m and a peak period of

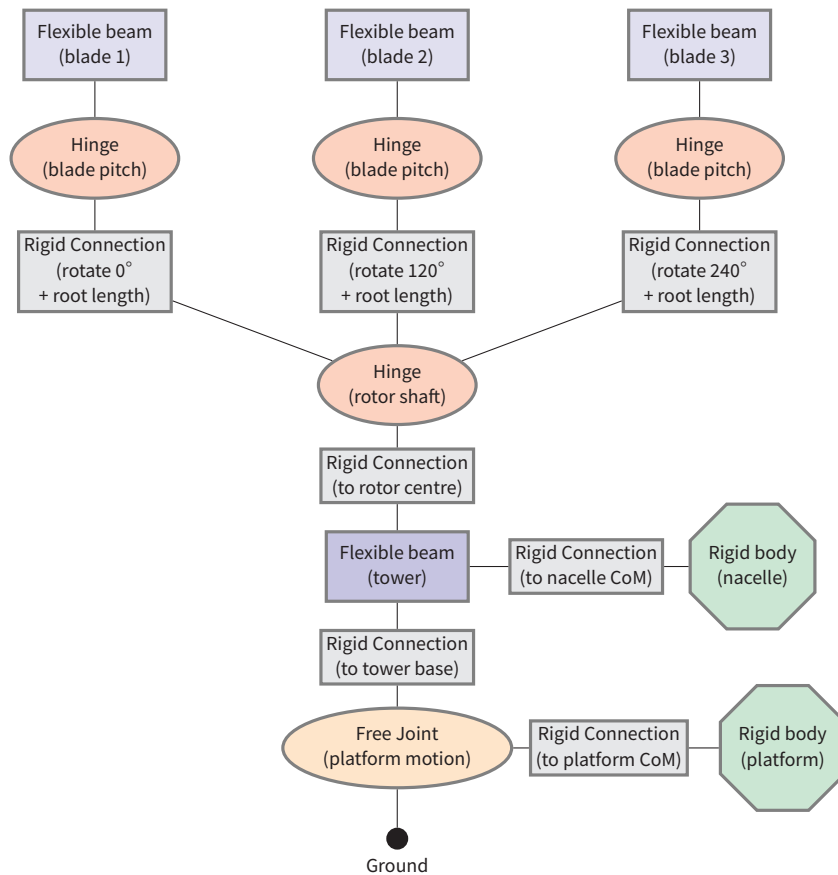


Figure 4.1 – Elements making up the multibody mbwind model of the flexible floating wind turbine. The free joint defines the position and orientation of the platform origin, located at the mean water level. The bottom of the flexible part of the tower, and the centre of mass of the platform, are offset from this origin by rigid connections. The ‘nacelle’ contains the gearbox, bearings and generator at the tower top. ‘Root length’ refers to the radial distance from the rotor axis to the start of the flexible blade.

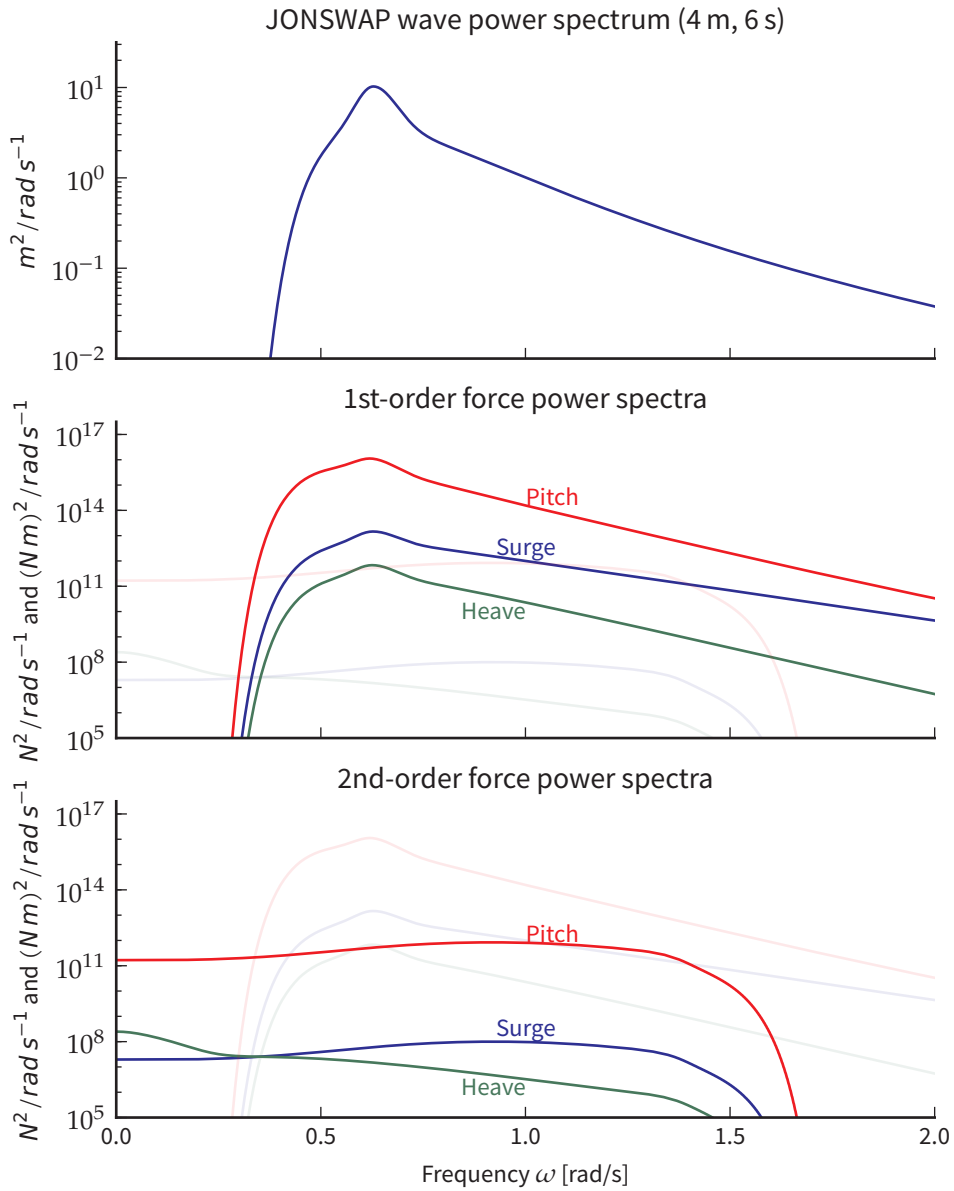


Figure 4.2 – Example of OC3-Hywind platform forces for one wave spectrum. The second-order forces are about  $10^5$  times smaller than the first-order forces in the wave frequency range, but at low frequencies they are the only source of wave loading.

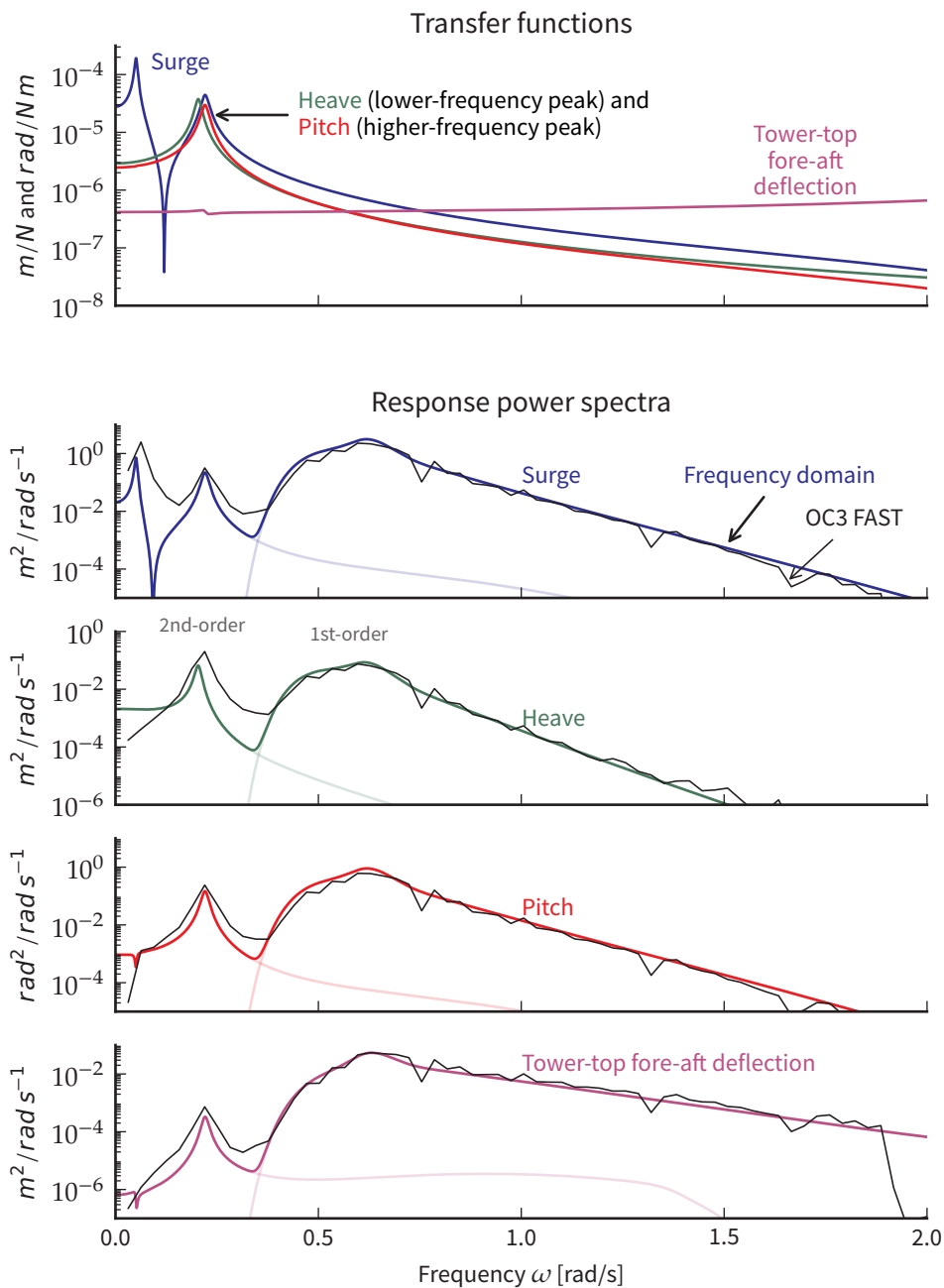


Figure 4.3 – OC3-Hywind platform transfer functions, and responses corresponding to forces shown in Figure 4.2. The response is the sum of the first- and second-order responses, which are also shown individually by faint lines. Published results from FAST simulations are shown by thin black lines.

Table 4.1 – The first 16 OC3-Hywind platform natural frequencies. ‘Bladed’ and ‘FAST’ from OC3 published results, ‘Current’ are the results from the present model.

Mode (frequencies in rad/s)	Bladed	FAST	Current
Platform sway	0.075	0.051	0.051
Platform surge	0.050	0.051	0.051
Platform heave	0.207	0.204	0.204
Platform roll	0.199	0.215	0.221
Platform pitch	0.199	0.215	0.221
Platform yaw	0.767	0.760	0.763
1st tower side-to-side	2.827	2.874	3.131
1st tower fore-aft	2.890	2.973	3.112
1st blade asymmetric flapwise pitch	4.210	4.262	4.260
1st blade asymmetric flapwise yaw	3.990	4.364	4.467
1st blade collective flapwise	4.430	4.461	4.560
1st blade asymmetric edgewise pitch	6.943	6.793	6.991
1st blade asymmetric edgewise yaw		6.870	6.817
2nd blade asymmetric flapwise pitch	11.624	12.144	12.004
2nd blade asymmetric flapwise yaw		12.296	12.541
2nd blade collective flapwise	12.127	12.712	12.615

‘Asymmetric flapwise pitch’ is a mode where the blades move out of the rotor plane with a horizontal axis of symmetry; ‘asymmetric flapwise yaw’ is similar but with a vertical axis of symmetry. In the ‘collective flap’ modes all blades move out of the rotor plane together. The edgewise modes are analogous but with motion in the rotor plane.

6 s. The waves are unidirectional and aligned with the surge axis; because the platform is symmetric, the sway and roll forces are zero.

Some of the platform transfer functions are plotted in the top of Figure 4.3. Peaks at the surge, pitch and heave natural frequencies are visible. The frequencies match well with published results from the OC3 code-comparison project, shown by Table 4.1 and Figure 4.4.

Also shown in Figure 4.3 are the response power spectra for platform motion in surge, heave and pitch, as well as the tower top elastic deflection. Results provided by OC3 from simulations in FAST are shown by the black lines. Generally there is a good match, although the frequency resolution in the FAST results is low, and the dynamic range of the plots is large.

The slow drift motion is visible as the peaks at the left, corresponding to the platform natural frequencies in surge and pitch. In general it is found

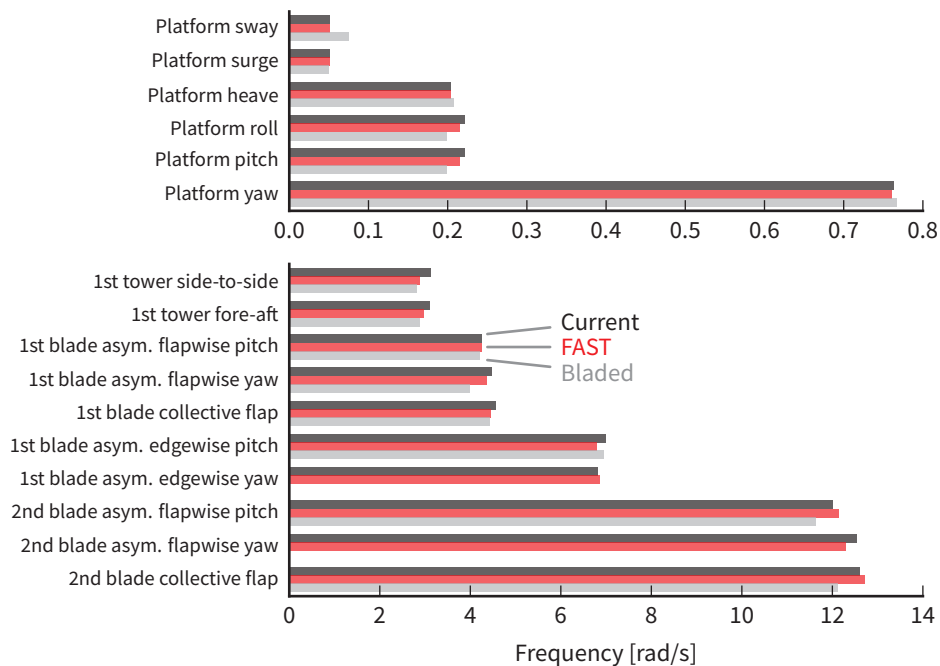


Figure 4.4 – The first 16 OC3-Hywind platform natural frequencies. See Table 4.1 for explanation.

that this low-frequency peak can be large compared to the first-order wave-frequency response, but not in this case. As discussed in the introduction, this is the motivation for the following section which aims to understand if this is due to the smaller scale of floating wind turbines.

## 4.2 Scaling of slow drift motions

As discussed at the start of the chapter, in this section the scaling of slow drift motions with platform size is investigated. Since the aim is to derive simple, approximate results, only surge motion of platforms which are vertical cylinders of various draft and radius is considered. The natural frequency in surge is assumed to be constant as the mass of the platform varies, since it is usually chosen to avoid the main wave forcing frequencies, which are independent of the size of the platform. Damping is also assumed independent of platform size.

### 4.2.1 DERIVATION OF APPROXIMATE RESPONSE

Since for simplicity only the surge degree of freedom of the platform is considered, only the surge component of the second order force is required. The surge component of the spectrum  $S_{FF}^{(2)}(\omega)$  is written  $S^{(2)}(\omega)$ . Aranha and Fernades (1995) show that for small  $\omega$  the spectrum is nearly flat,

$$S^{(2)}(\omega) = S_0 + O(\omega^2) \quad (4.12)$$

In general the slow drift response would be found from Equations (4.4) and (4.5), but because the surge motion is assumed to be lightly damped and the surge natural frequency is small, the slow drift response can be found using the white-noise approximation (Lin 1976):

$$\sigma_x^2 = \frac{\pi S_0}{4\zeta \omega_n^3 M^2} \quad (4.13)$$

where  $\sigma_x$  is the surge response standard deviation,  $S_0$  is the white-noise approximation of the surge force,  $M$  is the platform mass, and  $\zeta$  and  $\omega_n$  are the damping and natural frequency in surge respectively. This is acceptable because the lightly-damped response is mostly determined by the forcing at the resonant frequency which, since the force spectrum is nearly flat, is almost the same as the force spectrum at zero frequency.

The mass of the cylinder is assumed to be equal to its displacement:

$$M = \rho d \pi a^2 \quad (4.14)$$

where  $\rho$  is the density of water,  $d$  is the draft of the cylinder and  $a$  is the radius. Added mass, which depends non-trivially on the shape of the platform, is neglected to give a conservative estimate of the response.

The value of the second-order force spectrum at zero frequency is needed in Equation (4.13). It can be found from Equation (4.10) as

$$\begin{aligned} S_0 = S^{(2)}(0) &= 8 \int_0^\infty S_{\zeta\zeta}^2(\omega') |T_{11}(\omega', \omega')|^2 d\omega' \\ &= 8(\rho g a)^2 I \end{aligned} \quad (4.15)$$

where

$$I = \int_0^\infty S_{\zeta\zeta}^2(\omega) D^2(\omega) d\omega \quad (4.16)$$

in which  $D(\omega)$  is the normalised mean surge force such that  $T_{11}(\omega, \omega) = \rho g a D(\omega)$ . We now introduce approximations for  $D(\omega)$  and  $S_{\zeta\zeta}(\omega)$  which allow this integral to be evaluated analytically.

The ISSC description of the wave spectrum is taken as a starting point (Faltinsen 1993, chapter 2):

$$\frac{S_{\zeta\zeta}(\omega)}{H_s^2 T_m} = \frac{A}{2\pi} \left( \frac{\omega T_m}{2\pi} \right)^{-5} \exp \left( -b^4 \left( \frac{\omega T_m}{2\pi} \right)^{-4} \right) \quad (4.17)$$

where  $A = 0.11$ ,  $b^4 = 0.44$ ,  $H_s$  is the significant wave height and  $T_m$  is the mean wave period, defined in terms of the spectral moments  $m_k = \int_0^\infty \omega^k S(\omega) d\omega$  as  $T_m = 2\pi m_0 / m_1$  and  $H_s = 4\sqrt{m_0}$ . This description of the wave spectrum allows the two parameters  $T_m$  and  $H_s$  to be specified independently. Sometimes a one-parameter wave spectrum is used, in which case the following relationship can be used:

$$T_m = 3.84\sqrt{H_s} \quad (4.18)$$

(Chakrabarti 2005, chapter 3; Faltinsen 1993, chapter 2)

The exact shape of the wave spectrum is not a concern here; rather the aim is to find an approximate but closed-form result. Therefore for analytical convenience the wave spectrum is approximated by a uniform rectangular spectrum of height  $C$  between  $\omega_1$  and  $\omega_2$  (Figure 4.5, left),

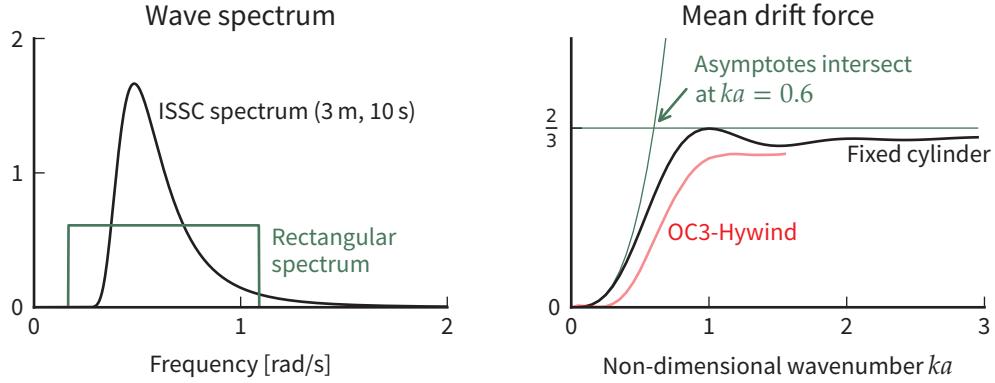


Figure 4.5 – Approximations introduced in deriving the slow drift motion results. On the left, the wave spectrum is approximated by a rectangular spectrum which matches the first three spectral moments. On the right, the mean drift force is approximated by the two asymptotes.

which matches the first 3 spectral moments. It can be shown that

$$\omega_1 = (1 - Kb) \omega_m \quad (4.19a)$$

$$\omega_2 = (1 + Kb) \omega_m \quad (4.19b)$$

$$C = \frac{AH_s^2}{8bK\omega_m} \quad (4.19c)$$

where  $K^2 = 3\sqrt{\pi} - 3\Gamma^2(3/4)$  and the mean wave frequency is  $\omega_m = 2\pi/T_m$ .

For simplicity the mean surge force on a fixed bottom-piercing cylinder is used as an estimate of  $D(\omega)$ , although it is recognised that this is only an approximation of the more complex force on the moving platform. The mean force can then be written as a sum of Bessel and Hankel functions (Drake 2011), but is not in a form which is easily integratable. Instead it is approximated by the two asymptotes shown in the right of Figure 4.5:

$$D(ka) \approx \begin{cases} \frac{2}{3} & \text{for large } ka \\ \frac{5\pi^2}{16} (ka)^3 & \text{for small } ka \end{cases} \quad (4.20)$$

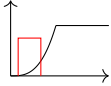
where  $ka$  is the non-dimensional frequency, which in deep water is related to angular frequency  $\omega$  by  $ka = \omega^2 a/g$  (Faltinsen 1993; Eatock Taylor, Hu and Nielsen 1990). The two asymptotes meet when  $ka = 0.6$ , which corresponds to a frequency of  $\omega_x = (0.6g/a)^{1/2}$ . Note that these asymptotes are conservative for all values of  $ka$ , although the underlying assumption

of using the force on a fixed cylinder instead of the true floating cylinder may not always be conservative. As an example of the approximation involved, Figure 4.5 also shows the mean drift force on the OC3-Hywind platform (data from Lucas 2011); in this case the approximation is in fact conservative.

Using Equations (4.19), the integral in Equation (4.16) can be evaluated:

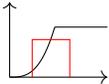
$$I = C^2 \int_{\omega_1}^{\omega_2} D^2(\omega) d\omega \quad (4.21)$$

This integral must be evaluated in two parts, corresponding to the two asymptotes of Equation (4.20); depending on the relative values of the cylinder radius and the wave spectrum mean period, one or both parts are needed. The results are:



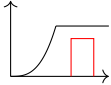
$$I = I_{L2} - I_{L1} \quad (4.22a)$$

$$= 1.70 H_s^4 \omega_m^{11} (a/g)^6$$



$$I = (I_{LX} - I_{L1}) + (I_{H2} - I_{HX}) \quad (4.22b)$$

$$= 1.40 \times 10^{-3} H_s^4 [\omega_m^{-1} - 0.412 \omega_m^{-2} (a/g)^{-1/2} - 3.15 \times 10^{-8} \omega_m^{-13} (a/g)^6]$$



$$I = I_{H2} - I_{H1} \quad (4.22c)$$

$$= 1.18 \times 10^{-3} H_s^4 \omega_m^{-1}$$

where  $I_{L1}$  is the value of the integral evaluated at  $\omega_1$  when this lies within the lower asymptote,  $I_{H1}$  is the corresponding value when  $\omega_1$  lies within the upper asymptote,  $I_{HX}$  is the value for the upper asymptote at  $\omega_X$ , and so on.

Substituting Equations (4.14)–(4.22) into Equation (4.13) results in an expression for the slow drift standard deviation:

$$\sigma_x = \left( g \sqrt{\frac{2}{\pi}} \right) \zeta^{-1/2} \omega_n^{-3/2} d^{-1} H_s^2 F(a, \omega_m) \quad (4.23)$$

where  $F(a, \omega_m) = \frac{\sqrt{I}}{aH_s^2}$  and  $I$  is given in Equation (4.22). This shows that the response depends on various powers of the damping  $\zeta$ , natural frequency  $\omega_n$ , draft  $d$  and significant wave height  $H_s$ , and in a more complicated fash-

Table 4.2 – Scaling of slow drift response  $\sigma_x$  with various parameters in the limits of small and large diameter platforms.

Parameter	Small diameter Low frequency	Large diameter High frequency
Platform radius	$a^2$	$a^{-1}$
Mean wave frequency	$\omega_m^{11/2}$	$\omega_m^{-1/2}$
Damping factor		$\zeta^{-1/2}$
Natural frequency		$\omega_n^{-3/2}$
Significant wave height		$H_s^2$
Platform draft		$d^{-1}$

ion on the platform radius  $a$  and mean wave period  $\omega_m$ , described by the function  $F(a, \omega_m)$ . Table 4.2 lists the results in the limits of very small and very large diameters when only one of the asymptotes of Equation (4.20) applies. The scaling at intermediate diameters can of course be determined from Equations (4.22) and (4.23) but takes a more complicated form.

The force function  $I$  and response function  $F$  are both plotted in the top row of Figure 4.6. Overall, the slow drift force  $I$  increases with the cylinder diameter. The force is reduced for very low-frequency waves, because then the platform is small compared to the wavelength. Looking at the response function  $F$  in the top right of Figure 4.6, different types of behaviour are seen at low and high frequencies. At low frequencies, the response increases with the size of the platform in the same way as the force. At high frequencies, the inertia of the platform becomes more important and the large inertia of large platforms causes the response to reduce as the size of the platform increases.

Typical mean wave frequencies in the North Sea might be roughly  $0.5\text{--}0.8\text{ rad s}^{-1}$ , while in extreme conditions they may be  $0.3\text{--}0.4\text{ rad s}^{-1}$  (Faltinsen 1993). If a typical floating wind turbine is taken to be less than 10 m, then the approximate results predict the slow drift motion will scale as  $a^2$ , thereby supporting the original suggestion that smaller floating structures will experience smaller slow drift motions.

According to Equation (4.23), the draft of the platform also has a significant effect. This seems relevant to the original example of the OC3-Hywind platform, which is a spar buoy with a very deep draft of 120 m. In the

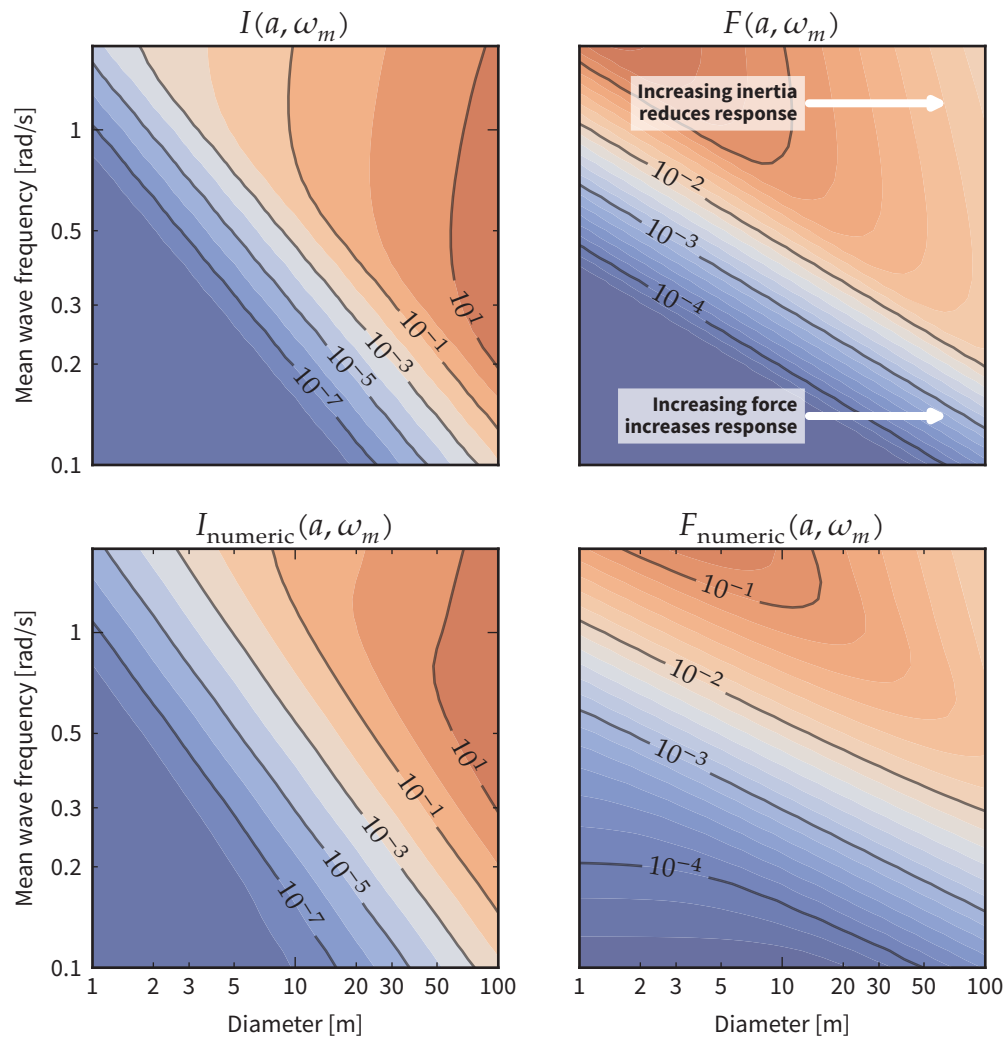


Figure 4.6 – Left: slow drift force integral  $I$ . Right: slow drift response function  $F$ . Top row: analytical results with rectangular spectrum approximation and mean drift force asymptotes. Bottom row: numerical results with ISSC spectrum and mean drift force on fixed cylinder. All scales are logarithmic.

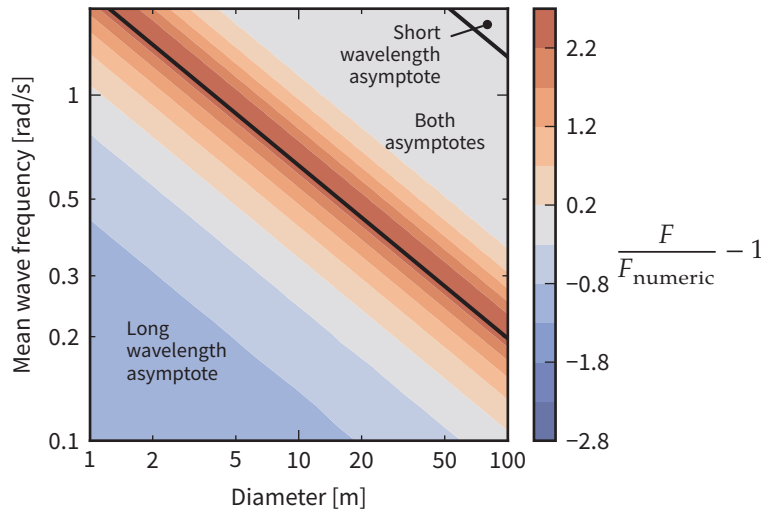


Figure 4.7 – Error due to rectangular spectrum and mean drift force asymptotes. The regions where the long- and short-wavelength asymptotes apply are also shown.

approximate result, the dependence on draft is purely through its effect on the platform inertia. In reality the mean drift force is also affected by draft, but this is not seen in the approximate results because the mean drift force is approximated by the mean drift force on a bottom-piercing fixed cylinder. The difference will be negligible for short waves (high  $\omega_m$ ) but for long waves (low  $\omega_m$ ) the force may be overestimated since part of the wave can pass below the platform.

#### 4.2.2 VALIDITY OF APPROXIMATIONS

In deriving the approximate result of Equation (4.23), seven main assumptions have been made:

1. **Only cylindrical platforms are considered.** Although this is a limitation, many platforms are basically cylindrical.
2. **Only surge motion is allowed.** Allowing motion in other directions should not affect the order of magnitude of slow drift motion. The order of magnitude of coupled surge, sway and yaw motion should be similar to the order of magnitude of the isolated surge motion considered here.
3. **Natural frequency and damping are assumed constant for any size of**

**platform.** This is reasonable in that natural frequencies are usually chosen to be far away from the main wave-frequency forcing, which is independent of platform size.

4. **The natural frequency is assumed to be small and damping is assumed to be light**, where ‘small’ implies that  $S_{FF}^{(2)}(\omega_n) \approx S_{FF}^{(2)}(0)$ .
5. **The mean surge force on the floating platform is approximated by the mean surge force on a fixed bottom-piercing cylinder of the same diameter.** The impact of this and the previous assumption will be illustrated for one particular case in the next section.
6. **The mean surge force on the fixed cylinder is approximated by its two asymptotes.** ...
7. **The wave spectrum is approximated by the rectangular spectrum.** These two can easily be assessed by numerically calculating the integral  $I$  using the original ISSC wave spectrum and the fixed cylinder mean drift force, rather than using the rectangular approximation and the mean drift force asymptotes of Figure 4.5. The results of the latter are shown in the top part of Figure 4.6 and were described above; the results of the former are shown in the bottom part of Figure 4.6. Compared to the numerical solution, the approximations over-predict the response for moderate diameters and wave frequencies. Figure 4.7 shows this more clearly. Since the approximate results are conservative by a factor of 3 or less, the use of the results to estimate the scaling of the slow drift motion is justified.

#### 4.2.3 NUMERICAL RESULTS FOR SLOW DRIFT MOTION

Of the assumptions above, the impact of numbers 3 and 4 can be illustrated by calculating the full transfer function and second-order force spectrum for a particular case where data is available, the OC3-Hywind platform used previously. This platform is a spar buoy and has a diameter of 6.5 m at the waterline, tapering to 9.4 m diameter 12 m below the surface. This causes the actual mass of the platform to be roughly twice the value calculated by Equation (4.14), and this has been corrected for in the results which follow by modifying the estimated platform mass of Equation (4.14) to reflect the actual shape of the platform.

Table 4.3 – Example platform geometries. Damping for UMaine TLP and Sevan FPSO are assumed values.

Platform	Radius [m]	Draft [m]	$\omega_n$ [rad/s]	$\zeta$
OC3-Hywind (Jonkman 2010)	3.25	120.0	0.05	6 %
UMaine TLP (Robertson and Jonkman 2011)	3.25	24.0	0.16	5 %
Sevan FPSO (Y Zhang 2010)	30.00	17.0	0.053	5 %

The slow drift motion standard deviation is found from Equations (4.4) and (4.5), as described in Section 4.1. To be consistent with the approximate results, only the surge degree of freedom is included.

The upper part of Figure 4.8 compares the approximate slow drift standard deviation with the full numerical calculation, for the ISSC spectrum (Equation 4.17) with  $H_s = 1$  m. The difference between the results labelled ‘analytical’ and ‘numerical’ is the same as that discussed above and shown in Figure 4.6: the rectangular approximation of the spectrum and the asymptotic mean drift force. The difference between the ‘numerical’ and ‘full’ curves is due mainly to the fact that the cylinder is not rigidly attached to the sea bed, and also the tapered shape. In this case, the ‘numerical’ results overestimate the slow drift motion by up to a factor of 10, and at worst the ‘analytical’ results overestimate the motion by a additional factor of 4.

The lower part of Figure 4.8 shows the approximate predictions for the three platform geometries listed in Table 4.3. The UMaine TLP has been included as it is the other platform studied by Roald et al. (2013). The Sevan FPSO (Y Zhang 2010) is included as an example of a much larger offshore floating structure. These results illustrate again the prediction of the approximate result that the slow drift motion of the larger structure is indeed larger than the smaller wind turbine platforms.

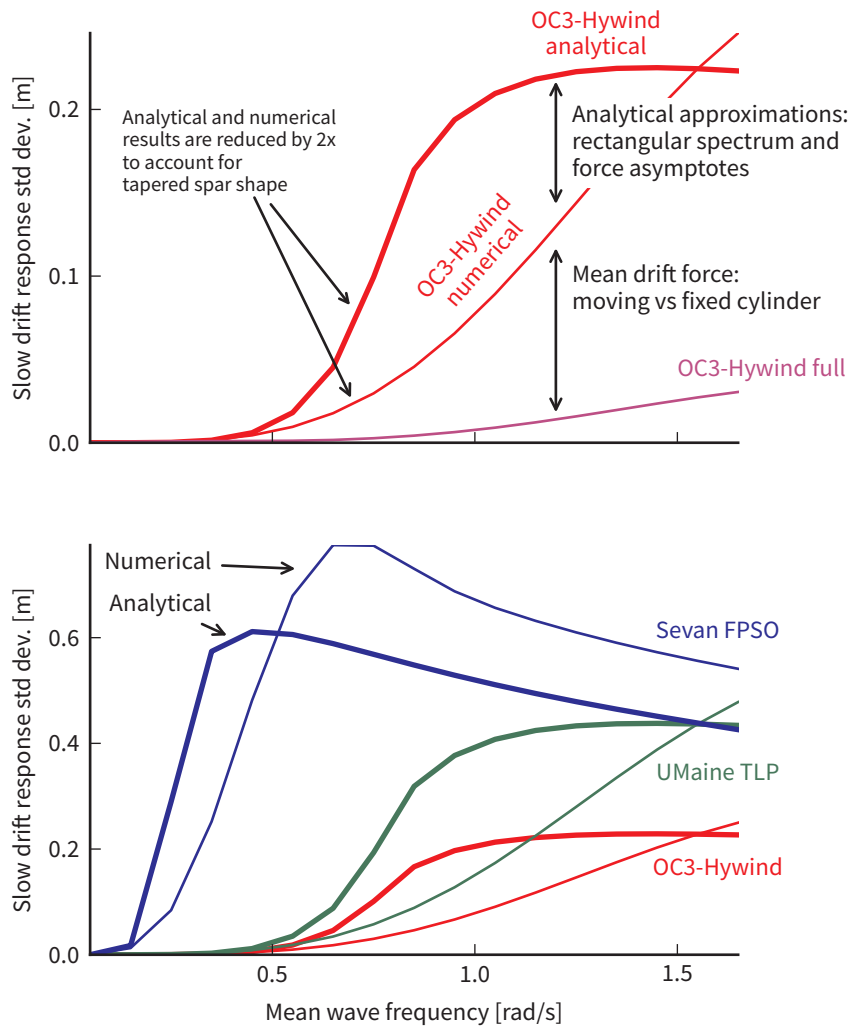


Figure 4.8 – Above: comparison of analytical and numerical results for the simple cylinder with actual numerical results for the OC3-Hywind platform. Below: analytical and numerical results for the three platform geometries listed in Table 4.3.

### 4.3 Linearised viscous drag forces

Viscous drag forces have not been included in the potential flow forces discussed so far in this chapter. Whether they are necessary depends on many parameters, including the Reynolds number, surface roughness and the Keulegan-Carpenter number (Faltinsen 1993). When required, Morison's equation is often used to calculate forces on the cylindrical members of a structure. The full version of Morison's equation was given in Equation (1.1) on p 20, but here we consider only the viscous drag term, assuming the acceleration loads are accounted for by the potential flow method described previously. The force on a strip  $ds$  of the cylindrical member is

$$d\mathbf{F}_{3d} = \frac{1}{2}\rho D ds C_D |\mathbf{u}_n| \mathbf{u}_n \quad (4.24)$$

where  $\rho$  is the water density,  $D$  is the cylinder diameter,  $C_D$  is a drag coefficient, and  $\mathbf{u}_n$  is the relative flow velocity normal to the cylinder. Since the drag force given by this equation is quadratic in the velocity, the viscous drag cannot be directly accounted for in a frequency-domain analysis. In the analysis of offshore structures, an effective approach is to use the method of equivalent linearisation, which defines an equivalent linear system such that the error is minimised in the least squares sense. This approach does not appear to have been applied to the analysis of floating wind turbines, so in this section its application is demonstrated, following the method of Langley (1984). For completeness, the derivation is outlined below following that reference.

Since the drag force is based on the flow normal to the cylinder, it should be linearised in the local reference frame of the cylinder. The normal relative flow velocity is

$$\mathbf{u}_n = (\mathbf{u}_c + \mathbf{u}_v - \mathbf{v}) - [(\mathbf{u}_c + \mathbf{u}_v - \mathbf{v}) \cdot \mathbf{t}] \mathbf{t} \quad (4.25)$$

where  $\mathbf{u}_c$  is the constant fluid velocity due to current,  $\mathbf{u}_v$  is the fluid velocity due to the waves,  $\mathbf{v}$  is the velocity of the structure itself, all evaluated at the location of the strip, and  $\mathbf{t}$  is a unit vector along the axis of the cylinder. Expressed as a two-dimensional velocity in the plane of the strip,

the normal relative flow velocity is

$$\boldsymbol{w} = \begin{bmatrix} \boldsymbol{u}_n \cdot \boldsymbol{n}_1 \\ \boldsymbol{u}_n \cdot \boldsymbol{n}_2 \end{bmatrix} = \begin{bmatrix} (\boldsymbol{u}_c + \boldsymbol{u}_v - \boldsymbol{v}) \cdot \boldsymbol{n}_1 \\ (\boldsymbol{u}_c + \boldsymbol{u}_v - \boldsymbol{v}) \cdot \boldsymbol{n}_2 \end{bmatrix} \quad (4.26)$$

where  $\boldsymbol{n}_1$  and  $\boldsymbol{n}_2$  are arbitrary orthogonal unit vectors perpendicular to the cylinder axis, and  $\boldsymbol{n}_1 \cdot \boldsymbol{t} = \boldsymbol{n}_2 \cdot \boldsymbol{t} = 0$ . The drag force in the plane of the strip is then

$$d\boldsymbol{F} = C\boldsymbol{w}|\boldsymbol{w}| \quad (4.27)$$

where  $C = \frac{1}{2}\rho DC_D ds$ .

The method of equivalent linearisation aims to replace Equation (4.27) with a force of the form

$$d\boldsymbol{F} = C(\boldsymbol{A}\boldsymbol{w}_v + \boldsymbol{b}) \quad (4.28)$$

where  $\boldsymbol{w}$  has been assumed to consist of constant and time-varying parts such that  $\boldsymbol{w} = \boldsymbol{w}_c + \boldsymbol{w}_v$ . The coefficients  $\boldsymbol{A}$  and  $\boldsymbol{b}$  are chosen to minimise the error,

$$\boldsymbol{\varepsilon} = C(\boldsymbol{w}|\boldsymbol{w}| - \boldsymbol{A}\boldsymbol{w}_v - \boldsymbol{b}) \quad (4.29)$$

which implies

$$\frac{\partial E[\boldsymbol{\varepsilon} \cdot \boldsymbol{\varepsilon}]}{\partial A_{ij}} = \frac{\partial E[\boldsymbol{\varepsilon} \cdot \boldsymbol{\varepsilon}]}{\partial b_i} = 0 \quad i, j = 1, 2 \quad (4.30)$$

where the expectation  $E[x]$  is the average value of  $x$ . Langley (1984) shows that the values for  $\boldsymbol{A}$  and  $\boldsymbol{b}$  which minimise the error are

$$\boldsymbol{b} = E[\boldsymbol{w}|\boldsymbol{w}|] \quad (4.31a)$$

$$\boldsymbol{A} = \frac{1}{\sigma_{11}^2 \sigma_{22}^2 - \sigma_{12}^4} E \left[ |\boldsymbol{w}| \begin{pmatrix} w_1 w_{v1} \sigma_{22}^2 - w_1 w_{v2} \sigma_{12}^2 & w_1 w_{v2} \sigma_{11}^2 - w_1 w_{v1} \sigma_{12}^2 \\ w_2 w_{v1} \sigma_{22}^2 - w_2 w_{v2} \sigma_{12}^2 & w_2 w_{v2} \sigma_{11}^2 - w_2 w_{v1} \sigma_{12}^2 \end{pmatrix} \right] \quad (4.31b)$$

where  $\sigma_{ij}^2 = E[w_{vi}w_{vj}]$ , and  $w_i$  and  $w_{vi}$  are components of  $\boldsymbol{w}$  and  $\boldsymbol{w}_v$  respectively.

To evaluate these expectations the statistics of  $\boldsymbol{w}$  must be known.  $\boldsymbol{w}$  depends on both the platform response and the fluid velocity due to the

waves. Usually both are assumed to be Gaussian, which is commonly accepted for the fluid velocity, but depends on the importance of the non-linear forces in the case of the platform response. The solution for the linearised viscous forces must be iterative, since  $A$  and  $b$  depend on the platform response statistics, which depend in turn on the viscous forces. To find  $\sigma_{ij}$ , define transfer functions from wave amplitude to wave fluid velocity  $u_v$  and platform motion  $v$  respectively:

$$u_v = H_u \zeta \qquad v = H_v \zeta \qquad (4.32)$$

At a cylindrical strip located at  $r = (x, y, z)$ , where  $z$  is measured upwards from the sea surface, these transfer functions are defined as

$$H_u = \begin{bmatrix} \omega \\ 0 \\ i\omega \end{bmatrix} e^{kz - ikx} \qquad (4.33)$$

$$H_v = i\omega L^\top H_{RB}(\omega) X(\omega) \qquad (4.34)$$

where the wavenumber is  $k = \omega^2/g$  in deep water, and the waves are assumed to be travelling in the positive  $x$  direction.  $H_{RB}$  is the part of the platform structural response transfer function relating to rigid-body motion (Equation 4.2).  $L^\top = [\mathbf{I} \quad -\tilde{r}]$ , where the matrix form of the cross product is used (Equation A.1).  $X$  is the vector of wave excitation coefficients (Equation 4.9). The normal relative flow velocity transfer function is then

$$\hat{H} = (H_u - H_v) - [(H_u - H_v) \cdot t] t \qquad (4.35)$$

analogous to Equation (4.25), and  $\sigma_{ij}$  can be found from Equations (4.4)–(4.5):

$$\sigma^2 = \int_0^\infty \hat{H} S_{\zeta\zeta} \hat{H}^{*\top} d\omega \qquad (4.36)$$

In general the linearisation must be evaluated numerically. If  $p(w_{v1}, w_{v2})$  is the standard Gaussian joint probability density function of  $w_{v1}$  and  $w_{v2}$ , the expectations which appear in Equation (4.31) can be found using

$$E[f(w_{v1}, w_{v2})] = \int_{-\infty}^\infty \int_{-\infty}^\infty f(w_{v1}, w_{v2}) p(w_{v1}, w_{v2}) dw_{v1} dw_{v2} \qquad (4.37)$$

Finally, the linearised viscous forces from Equation (4.28) must be transformed from the local cylinder reference frame back into the platform

reference frame. Let  $P$  be the transformation matrix  $P = \begin{bmatrix} n_1 & n_2 \end{bmatrix}$ . The force in the platform reference frame is

$$dF_{3d} = P dF \quad (4.38)$$

and from Equation (4.26),

$$w_v = P^T (u_v - v) \quad (4.39)$$

Together with Equation (4.28) this gives

$$dF_{3d} = C [PAP^T (u_v - v) + Pb] \quad (4.40)$$

Since  $v$  depends on the platform velocity, part of the viscous force acts as a damping contribution, which is transformed to a force and moment acting at the origin by the matrix  $L$ . For strip  $k$  the contribution is

$$B_v^k = CLPAP^T \times i\omega L^T \quad (4.41)$$

Similarly there is a contribution to the applied current drag force  $F_c$  and the viscous wave excitation force  $\bar{F}_v$ :

$$F_c^k = CLPb \quad (4.42)$$

$$\bar{F}_v^k = CLPAP^T H_u \zeta \quad (4.43)$$

The total damping and force contributions are simply the sum for all strips.

#### 4.3.1 EXAMPLE DRAG LINEARISATION

Figure 4.9 shows an example of the viscous drag linearisation obtained for the OC3-Hywind platform. The optimum linearisation depends on the range of flow speeds that occur, and is therefore different at the two depths shown.

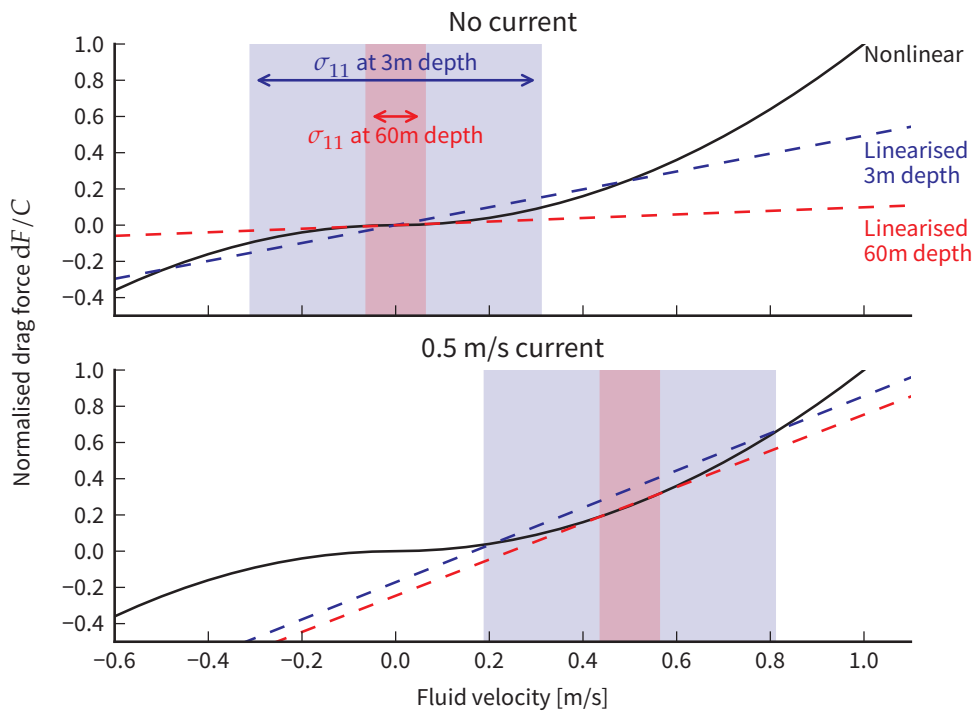


Figure 4.9 – Linearisation of viscous drag force with and without current, at two depths. The waves cause the flow speed to vary; the standard deviation of the variation is shown by the shaded areas. There is more variation in relative flow speed near the surface, so the linearisation adapts to give a greater slope.

## 4.4 Conclusions

In this chapter a frequency-domain model of a flexible floating wind turbine structure with hydrodynamic loading has been developed. The main hydrodynamic loads are already often modelled using a linear approach, and therefore pose no difficulty for a frequency-domain approach.

Two types of nonlinear loading have been considered. The first, the second-order potential flow forces, can in general be included in a frequency-domain model, but with more complexity as the response statistics are then non-Gaussian. However, if the second-order response is small, approximating the response as Gaussian can be sufficient.

A simplified analysis of the scaling of the second-order response with the size of the platform was developed, which predicts the second-order response to decrease for smaller platforms. Since floating wind turbine platforms are generally smaller than other offshore floating structures, the second-order response may indeed be relatively small. More data is needed to determine to what extent the simplified analysis represents actual floating wind turbine platforms.

The second type of nonlinear loading is due to viscous drag forces. These can be linearised using the method of equivalent linearisation, and therefore included approximately in the frequency-domain model. This is a well-established technique for offshore structures, but as it does not appear to have been applied to floating wind turbines, an example for the OC3-Hywind platform is developed to demonstrate the approach.



## Chapter 5

### *Linearised aerodynamics*

This chapter develops improved linearised models of the aerodynamic loads acting on a wind turbine. In the previous chapters it has been possible to justify the use of a linear model because the nonlinear effects are very small (in the case of the structural dynamics) or at least are small enough that the impact on the response statistics may be negligible (in the case of the nonlinear hydrodynamics). However in the aerodynamics nonlinearity is more dominant, and rather than trying to neglect it, this chapter applies more advanced linearisation techniques to try to get the best possible linear representation of the nonlinear behaviour.

As a starting point, the aerodynamic loads are linearised while assuming that the rotor speed and the blade pitch angle are constant. In fact, the control system will vary the rotor speed and blade pitch angle, and a linearised model of the control system is developed in the next chapter. In this chapter, first the Blade Element Momentum (BEM) model for calculating aerodynamic loads is introduced and the implementation verified. The method of harmonic linearisation is then used to linearise the nonlinear aerodynamic forces, including the aeroelastic interactions between the blade vibration and aerodynamic loads. Comparison against nonlinear simulations shows that good results are possible, but the error increases for larger wind speed variations and frequencies. The wake dynamic behaviour is also nonlinear, but less strongly, so when linearised in a similar way it is possible to get a good match with nonlinear simulations.

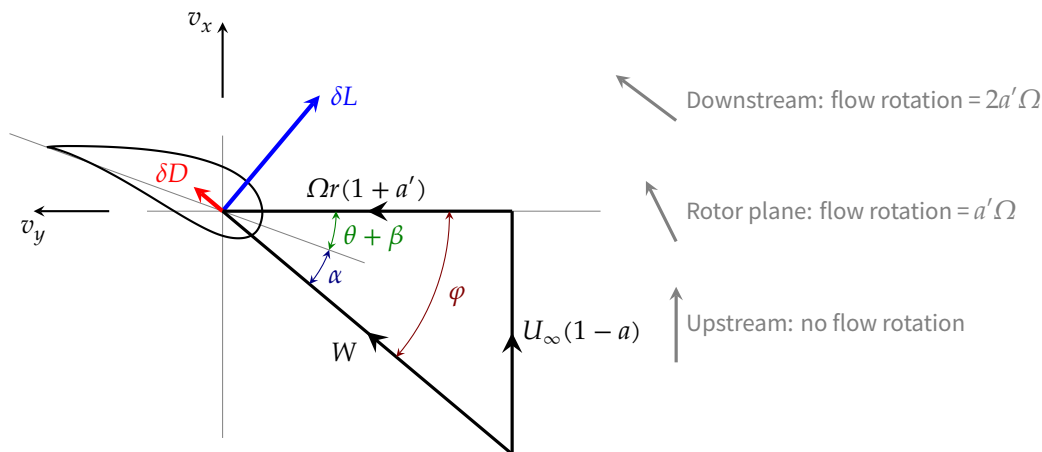
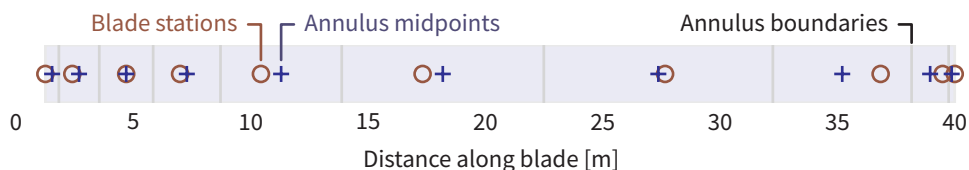


Figure 5.1 – Blade element flow velocities and lift and drag forces. The inflow angle is  $\varphi$ , the total blade rotation is  $\theta + \beta$  due to blade pitch angle and constant twist respectively, leaving the angle of attack  $\alpha$ .

## 5.1 Blade Element Momentum model

The most commonly used approach to modelling the aerodynamic loads of wind turbines is the BEM method<sup>1</sup>, in which the change in momentum of the air as it flows past the rotor is equated with the lift and drag forces created by the aerofoils on the blades. In this section the theory is introduced in the standard manner, following Burton et al. (2011, chapter 3).

A fundamental assumption of the BEM theory is that the rotor can be broken down into concentric annuli which do not interact with each other. This means that the aerodynamic forces are found using a set of completely independent calculations at a series of blade stations spread along the blade:



All quantities in the rest of this section relate to one annulus only.

The lift and drag forces are determined from empirical two-dimensional aerofoil lookup tables, based on the incoming flow speed and direction seen by the aerofoil. Figure 5.1 shows the flow velocities seen by an element of the blade at radius  $r$  when the free-stream wind speed is  $U_\infty$ . Note

1. Not to be confused with the Boundary Element Method

that the use of the symbols  $\alpha$ ,  $\beta$  and  $\theta$  from this chapter onwards is not related to their use in previous chapters. The presence of the rotor affects the incoming wind, so the wind speed and direction at the blade are not the same as in the free stream; the difference is described by the non-dimensional axial induction factor  $a$  and the tangential induction factor  $a'$  as shown in Figure 5.1.

If the blade is moving, due to elastic deflection or motion of the whole floating platform, the relative wind speed seen by the blade will be modified. This will be considered later, but for now is neglected. The resultant velocity at the blade is

$$W = \sqrt{U_\infty^2 (1 - a)^2 + r^2 \Omega^2 (1 + a')^2} \quad (5.1)$$

and the inflow angle  $\varphi$  is defined by either

$$\sin \varphi = \frac{U_\infty (1 - a)}{W} \quad \text{or} \quad \cos \varphi = \frac{r \Omega (1 + a')}{W} \quad (5.2)$$

The blade element is twisted by a constant angle  $\beta$  relative to the root of the blade, and the whole blade is pitched by an angle  $\theta$ , so the angle of attack is given by

$$\alpha = \varphi - \theta - \beta \quad (5.3)$$

It is assumed that the aerodynamic lift and drag forces acting on the blade element can be found from empirical data, namely the lift and drag coefficients  $C_l(\alpha)$  and  $C_d(\alpha)$ . The lift and drag forces on a length  $\delta r$  of the blade are then given by

$$\delta L = \frac{1}{2} \rho W^2 c C_l \delta r \quad \text{and} \quad \delta D = \frac{1}{2} \rho W^2 c C_d \delta r \quad (5.4)$$

where  $\rho$  is the density of air and  $c$  is the chord length. Resolving the forces into the plane of rotor rotation and summing over  $B$  blades gives the thrust and torque on the annulus at radius  $r$ :

$$\delta T = \delta L \cos \varphi + \delta D \sin \varphi = \frac{1}{2} \rho W^2 B c (C_l \cos \varphi + C_d \sin \varphi) \delta r \quad (5.5a)$$

$$\delta Q = r (\delta L \sin \varphi - \delta D \cos \varphi) = \frac{1}{2} \rho W^2 B c r (C_l \sin \varphi - C_d \cos \varphi) \delta r \quad (5.5b)$$

where the positive direction is taken as downstream and clockwise.

The flow through this annulus initially had speed  $U_\infty$  far upstream of the turbine, and far downstream its speed will be  $U_W$ . It can easily be shown that  $U_W = (1 - 2a)U_\infty$  (Burton et al. 2011, chapter 3). The force acting on the air is equal to the rate of change of momentum  $\delta\dot{m}(U_W - U_\infty)$ , where the mass flow rate is  $\delta\dot{m} = \rho \delta A U_\infty (1 - a)$  and  $\delta A$  is the area of the annulus. This gives the thrust on the blades as

$$\delta T = -[\rho \delta A U_\infty (1 - a)] \times [-2a U_\infty] = 2\rho \delta A U_\infty^2 a (1 - a) \quad (5.6a)$$

Similarly the torque can be found from the total rate of change of angular momentum  $-2\delta\dot{m}r^2a'\Omega$  as

$$\delta Q = -[\rho \delta A U_\infty (1 - a)] \times [-2a'\Omega r^2] = 2\rho \delta A U_\infty \Omega r^2 a' (1 - a) \quad (5.6b)$$

Equating Equations (5.5) and (5.6) and rearranging gives

$$\frac{a}{1 - a} = \frac{\sigma_r C_x}{4 \sin^2 \varphi} \quad (5.7a)$$

$$\frac{a'}{1 + a'} = \frac{-\sigma_r C_y}{4 \sin \varphi \cos \varphi} \quad (5.7b)$$

where  $\sigma_r = Bc/2\pi r$  is the chord solidity, and

$$C_x = C_l \cos \varphi + C_d \sin \varphi \quad (5.8a)$$

$$C_y = -C_l \sin \varphi + C_d \cos \varphi \quad (5.8b)$$

Because the inflow angle  $\varphi$  and hence the angle of attack and  $C_l$  and  $C_d$  depend on the induction factors according to Equation (5.2), these equations must be solved iteratively for  $a$  and  $a'$ .

The momentum theory breaks down when the rotor is heavily loaded and the pressure downstream of the rotor is too low. Under these conditions flow separation occurs, but this is not predicted by the momentum-based theory. This can be accounted for by an empirical correction; here the same model as used in Bladed (Garrad Hassan 2011) is used, in which the right-hand side of Equation (5.7a) is multiplied by a factor  $H$ , such that

$$H = \begin{cases} 1 & \text{when } a \leq 0.3539 \\ \frac{4a(1-a)}{0.6+0.61a+0.79a^2} & \text{otherwise} \end{cases} \quad (5.9)$$

In this theory the flow through the annulus is assumed to be uniform, but in practice the rotor consists of a finite number of blades and the flow varies around the annulus. This is often corrected for approximately by a ‘tip loss’ correction (Burton et al. 2011, chapter 3). For simplicity, tip loss is not corrected for here, since for any one annulus it is a constant and does not affect the difficulty of linearising the aerodynamic loads.

### 5.1.1 UNSTEADY AERODYNAMICS

There are two main types of unsteady aerodynamics relevant to floating wind turbines: unsteady aerofoil aerodynamics, and the wake dynamics. The unsteady aerofoil behaviour is relatively high frequency, typically with periods of less than one second (Vaal, MOL Hansen and Moan 2014), and describes the delay between the flow conditions changing and a change in the aerodynamic forces of Equation (5.5). The wake dynamics take place over longer periods related to the wind speed and rotor dimensions, typically 5 s to 20 s, and relate to the delay between a change in rotor loading and the change in flow speed seen at the rotor (Equation 5.6). Both of these effects can be important to model, but here we choose to focus on the wake dynamics: the lower frequencies are more likely to interact with the floating platform dynamics, and in any case the linearisation of unsteady aerofoil aerodynamics has already been further developed in the context of stability analysis (see for example MH Hansen 2004).

The dynamic wake model used by Bladed (Pitt and Peters 1981, reported by Garrad Hassan 2011) is used here, in which an extra inertial thrust is applied to the rotor corresponding to the ‘added mass’ of air which is accelerated when the flow changes. Again, this is applied to each annulus independently. The added mass  $\delta m_a$  of air associated with the annulus is

$$\delta m_a = \frac{8}{3}\rho (R_2^3 - R_1^3) \quad (5.10)$$

where the annulus extends from radius  $R_1$  to  $R_2$ . This expression is based on the standard result for the added mass associated with a solid disc of radius  $R$ , which is  $8\rho R^3/3$ : the added mass of the annulus is estimated as the difference between the added mass of discs of radius  $R_1$  and  $R_2$  respectively. Because the free-stream velocity  $U_\infty$  may be changing, it is

useful to replace the non-dimensional induction factors  $a$  and  $a'$  with the actual induced velocities:

$$u = aU_\infty \quad \text{and} \quad u' = a'\Omega r \quad (5.11)$$

Equation (5.6a) then becomes

$$\delta T = 2\rho \delta A u (U_\infty - u) + \delta m_a \dot{u} \quad (5.12)$$

which when combined with Equation (5.5a) defines the dynamic wake behaviour for one annulus:

$$\dot{u} = \frac{2\rho \delta A (U_\infty - u)}{\delta m_a} \left[ (U_\infty - u) \frac{\sigma_r C_x}{4 \sin^2 \varphi} - u \right] \quad (5.13)$$

The tangential induced velocity  $u'$  can be treated similarly, but the appropriate added mass is not so easily chosen. Approaches include keeping the equilibrium calculation of Equation (5.6b), or setting the time constant relative to the axial induction factor (Engelen and Braam 2004). At the level of detail considered here it makes little difference, and the added mass in the tangential direction is arbitrarily assumed equal to the axial added mass.

### 5.1.2 AEROELASTICITY

If the blade is moving, either due to elastic deflections of the blades and tower or motion of the whole floating platform, the flow conditions seen by the aerofoils will change. Often this leads to additional damping, perhaps up to 30% of critical damping (Burton et al. 2011, chapter 5), but instabilities such as flutter can also develop. If the velocity of the blade in Figure 5.1 is  $(v_x, v_y)$ , Equations (5.1) and (5.2) become

$$W = \sqrt{[U_\infty (1 - a) - v_x]^2 + [r\Omega (1 + a') - v_y]^2} \quad (5.14a)$$

$$\sin \varphi = \frac{U_\infty (1 - a) - v_x}{W} \quad (5.14b)$$

$$\cos \varphi = \frac{r\Omega (1 + a') - v_y}{W} \quad (5.14c)$$

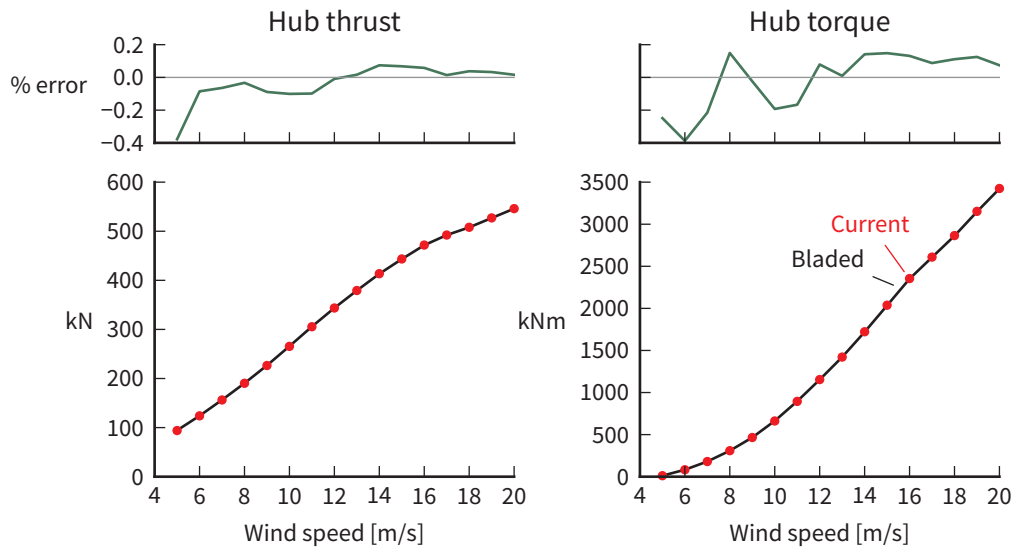


Figure 5.2 – Steady values for rotor thrust (left) and rotor torque (right), compared to Bladed. Model: ‘demo\_a’ sample project supplied with Bladed. Rotor speed: 22 rpm.

and Equations (5.3)–(5.8) are updated accordingly.

### 5.1.3 IMPLEMENTATION AND VERIFICATION

An implementation of the BEM model as described above was developed and tested by a set of unit and regression tests. These include tests of individual parts of the model, as well as overall comparison of the results with results from Bladed. The code is implemented in Python and is freely available (Lupton 2014c); further details of the tests may be found with the source code. In this section a few examples of comparisons against Bladed are presented to demonstrate the working of the code.

The aerodynamic model used by Bladed is more complex than the present implementation. The purpose of this model of the aerodynamics is to assess the accuracy of linearisations; it is sufficient for the underlying nonlinear model to be only approximately correct. Known differences between this model and Bladed include: differences in the details of the dynamic wake model; unsteady aerofoil dynamics are neglected; the aerodynamic pitching moment is neglected. In the results given here neither model includes tip loss corrections.

Table 5.1 – Summary of NREL 5 MW blade aerodynamic parameters

Blade length	61.5 m
Maximum twist	13.3°
Maximum chord	4.65 m
Aerofoil profiles	Cylinder DU21–40 NACA64

Figure 5.2 shows the overall thrust and torque on the rotor calculated from the sum of the contributions defined in Equation (5.5), for a range of steady wind speeds. The wind speed is uniform across the rotor. There is very good agreement between the present results and Bladed. The blade model is from the ‘demo\_a’ project supplied with Bladed.

The following results are based on the blade of the NREL 5 MW reference turbine (see p 25), with a few changes due to limitations of the present model: the centre of mass and neutral axis were moved to the centreline of the blade, and torsional flexibility was neglected. These changes are not thought to be significant in the context of this work. The blade aerodynamic parameters are summarised in Table 5.1; full details of the chord, twist and aerofoil profiles at each blade station are given by Jonkman, Butterfield, et al. (2009).

Figures 5.3 and 5.4 show results for a step change in wind speed from  $5 \text{ m s}^{-1}$  to  $8 \text{ m s}^{-1}$  after 5 s. Both the blade dynamics and wake dynamics are included in these results. There are differences in the time constants associated with the wake dynamics at different points along the blade. However, the overall loading on the blade appears to match well. The blade root loads also match very well, with the exception of the aerodynamic pitching moment  $M_z$ , which is not implemented in the present code.

Since the following sections study the response to harmonic wind speed inputs, Bladed and the present code were also compared in that case. Simulations were run for uniform harmonic wind speed variations of  $1 \text{ m s}^{-1}$  to  $5 \text{ m s}^{-1}$  about mean values of  $8 \text{ m s}^{-1}$  and  $16 \text{ m s}^{-1}$ . Frequencies were chosen to span roughly the range from floating platform natural frequencies to the ‘extreme operating gust’ used in wind turbine design (International Electrotechnical Commission 2005). Simulations were run

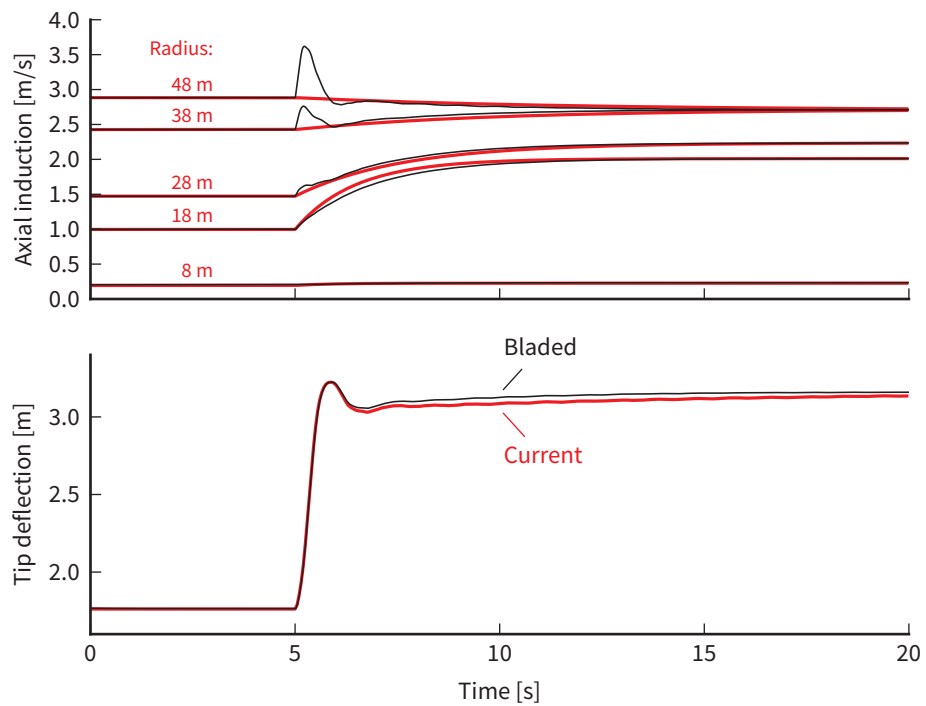


Figure 5.3 – Top: axial induced velocities before and after a step change in wind speed at  $t = 5$  s. Bottom: blade tip deflection. There are some differences in the transient behaviour, especially towards the tip of the blade. Model: NREL 5 MW turbine.

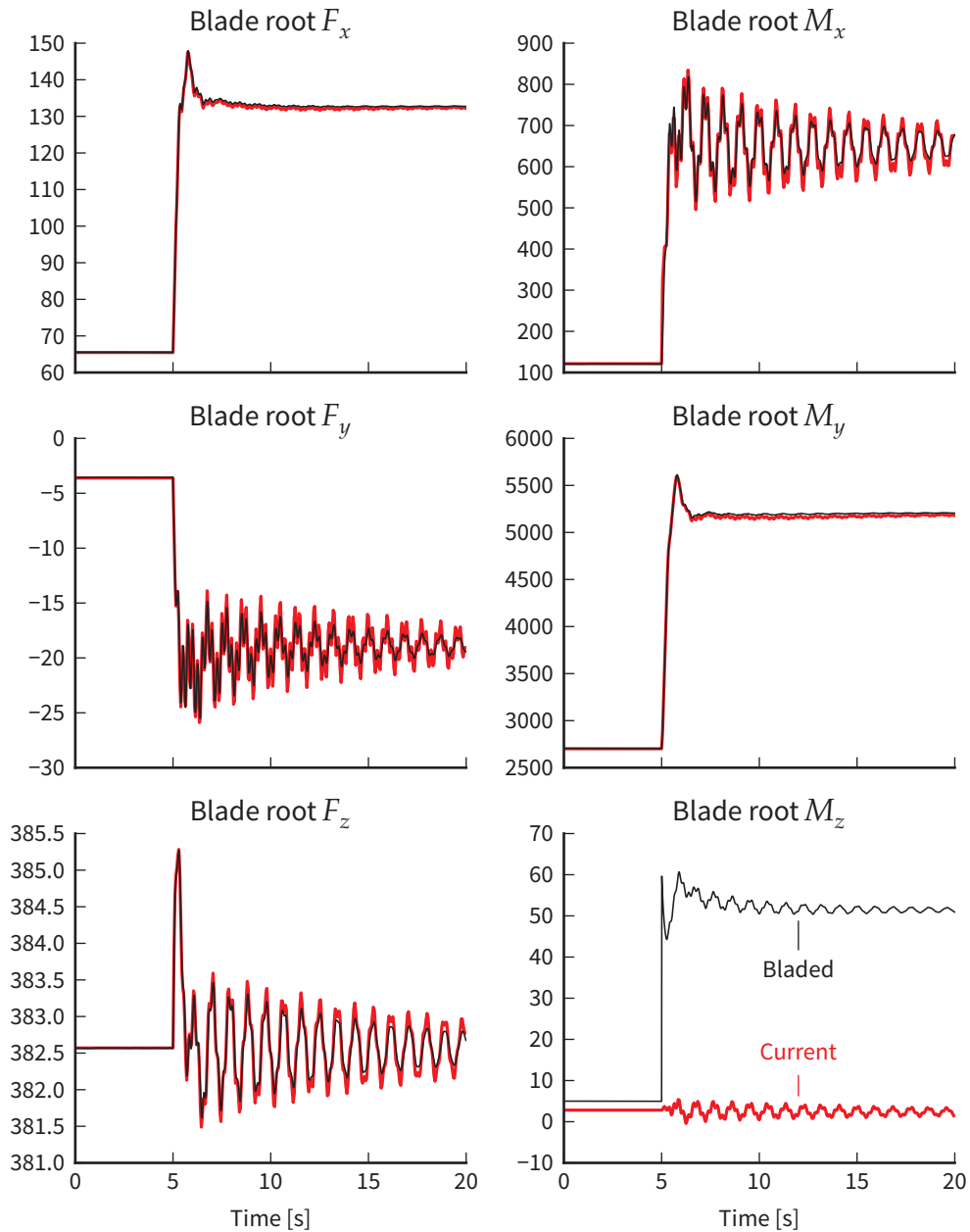


Figure 5.4 – Blade root forces (kN) and moments (kNm), before and after a step change in wind speed at  $t = 5$  s. The  $x$  axis points downwind and the  $z$  axis points towards the tip of the blade. Apart from the pitching moment  $M_z$ , which is not implemented, there is good agreement. Model: NREL 5 MW turbine.

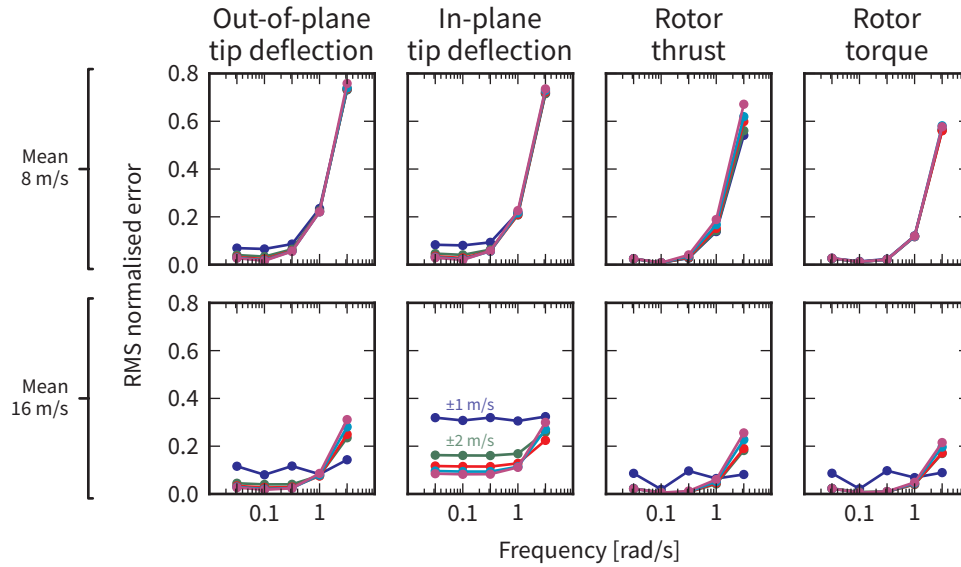


Figure 5.5 – Error between Bladed and present code for harmonic wind speed inputs. Blade dynamics are included, but the induced velocities are assumed constant (wake dynamics are neglected). The error is calculated according to Equation (5.15).

for the minimum of 60 s or 5 cycles, leading to the following parameters:

$0.03 \text{ rad s}^{-1}$	$t_{\max} = 1987 \text{ s}$	$\Delta t = 1 \text{ s}$
$0.10 \text{ rad s}^{-1}$	$t_{\max} = 628 \text{ s}$	$\Delta t = 1 \text{ s}$
$0.32 \text{ rad s}^{-1}$	$t_{\max} = 199 \text{ s}$	$\Delta t = 0.1 \text{ s}$
$1.00 \text{ rad s}^{-1}$	$t_{\max} = 63 \text{ s}$	$\Delta t = 0.1 \text{ s}$
$3.16 \text{ rad s}^{-1}$	$t_{\max} = 60 \text{ s}$	$\Delta t = 0.01 \text{ s}$

This was achieved in Bladed by generating ‘wind files’ containing the harmonic wind speed variation. The present results were obtained using the BEM model described above to calculate the aerodynamic forces, which were applied to the structural model and integrated as described in Chapter 2. The first parts of the simulations are discarded, removing initial transients, and only the final cycle is used. Again, the NREL 5 MW blade was used.

Figure 5.5 shows the comparison between the final results for the tip deflections and the overall rotor thrust and torque. The error is defined as

$$\varepsilon = \frac{\sqrt{\sum (y_i - z_i)^2 / N}}{\sigma_y} \quad (5.15)$$

where  $y_i$  are the Bladed simulation values at time  $t_i$ , and  $z_i$  are the corresponding values being compared. In each case, there is good agreement at low frequencies. The agreement at  $3.16 \text{ rad s}^{-1}$  is less good, in particular as the phase of the results is different between the two codes. This may be due to unsteady aerodynamic calculations in Bladed or differences between the structural dynamic models which are exercised at the higher frequency. In any case, the results are sufficient to show that the present model is sufficiently realistic for the analysis of linearisation techniques in the remainder of this chapter.

## 5.2 Harmonic linearisation of aerodynamic loads

The response of the blades to aerodynamic loads is described by

$$M\ddot{q} + C\dot{q} + Kq = F \quad (5.16)$$

The structural mass matrix  $M$ , damping matrix  $C$  and stiffness matrix  $K$  are obtained from a finite-element beam model such as the one described in Section 2.3.6 on p 56. The aerodynamic forces  $F$  are made up of the distributed lift and drag forces for each annulus, as defined by Equation (5.4). The required modal transformations are included in  $M$ ,  $C$ ,  $K$  and  $F$ . These forces are nonlinear functions of three global variables – the wind speed  $U_\infty$ , the rotor speed  $\Omega$  and the blade pitch angle  $\theta$  – and four variables relating to an individual annulus  $k$  – the induced velocities  $u^k$  and  $u'^k$ , and the in-plane and out-of-plane blade velocities  $v_x^k$  and  $v_y^k$ :

$$F = \sum_k f^k(U_\infty, \Omega, \theta, u^k, u'^k, v_x^k, v_y^k) = \sum_k f^k(\mathbf{x}, \dot{\mathbf{x}}) \quad (5.17)$$

The variables have been gathered into a ‘state vector’  $\mathbf{x}$ , which includes both the known inputs and the unknown response variables:

$$\mathbf{x}^\top = [U_\infty \quad \Omega \quad \theta \quad \mathbf{u}^\top \quad \mathbf{q}^\top] \quad (5.18)$$

where  $\mathbf{u}$  includes the induced velocities for every annulus, and  $\mathbf{q}$  are the modal amplitudes of the flexible blade. It is straightforward to obtain

the required blade velocities  $v_x^k$  and  $v_y^k$  from  $\dot{\mathbf{q}}$ . The specific form of the functions  $f^k$  can be found from the equations presented in the previous section. The forces in each annulus are coupled only through the structural dynamics of the blade; because the blade bending is represented by the linear model on the left-hand side of Equation (5.16), the annuli forces can be considered in isolation and then later superimposed. Therefore in the following only one function  $f^k$  is considered and the superscript is dropped.

To obtain a solution to Equation (5.16) in the frequency domain, the aerodynamic force must be linearised. A common approach is to use the tangent linearisation, in which small perturbations  $h$  about an operating point  $\mathbf{x}_0, \dot{\mathbf{x}}_0$  are applied as inputs to the nonlinear function. The perturbed results are used to calculate the tangent stiffness and damping matrices:

$$[K_f]_{ij} = \frac{f_i(\mathbf{x}_0 + \mathbf{h}_j, \dot{\mathbf{x}}_0) - f_i(\mathbf{x}_0 - \mathbf{h}_j, \dot{\mathbf{x}}_0)}{2h} \quad (5.19a)$$

$$[C_f]_{ij} = \frac{f_i(\mathbf{x}_0, \dot{\mathbf{x}}_0 + \mathbf{h}_j) - f_i(\mathbf{x}_0, \dot{\mathbf{x}}_0 - \mathbf{h}_j)}{2h} \quad (5.19b)$$

where  $[h_j]_k = h$  when  $j = k$ , 0 otherwise. The linearised approximation to  $f(\mathbf{x}, \dot{\mathbf{x}})$  is then

$$f(\mathbf{x}, \dot{\mathbf{x}}) \approx f(\mathbf{x}_0, \dot{\mathbf{x}}_0) + K_f (\mathbf{x} - \mathbf{x}_0) + C_f (\dot{\mathbf{x}} - \dot{\mathbf{x}}_0) \quad (5.20)$$

This approximation is valid as long as  $\mathbf{x}$  and  $\dot{\mathbf{x}}$  remains close to  $\mathbf{x}_0$  and  $\dot{\mathbf{x}}_0$ , or as long as  $f(\mathbf{x}, \dot{\mathbf{x}})$  remains approximately linear. For example, the lift curve of an aerofoil is linearised with a slope of  $2\pi$  for small angles of attack, but this does not capture the behaviour in stall at larger angles of attack.

Another approach is to find an equivalent linear system which is in some sense the optimum approximation to the real function, given the inputs which actually occur. Specifically, the mean-squared error between the nonlinear and linear functions is minimised by this approach (Vidyasagar 1993). Because the optimum linearisation depends on the inputs, there are different approaches for different types of input. In Section 4.3, the use of equivalent linearisation with viscous drag forces was discussed. In that case, the inputs are usually random processes. Here we choose instead to consider harmonic sinusoidal inputs, in which case the approach is known

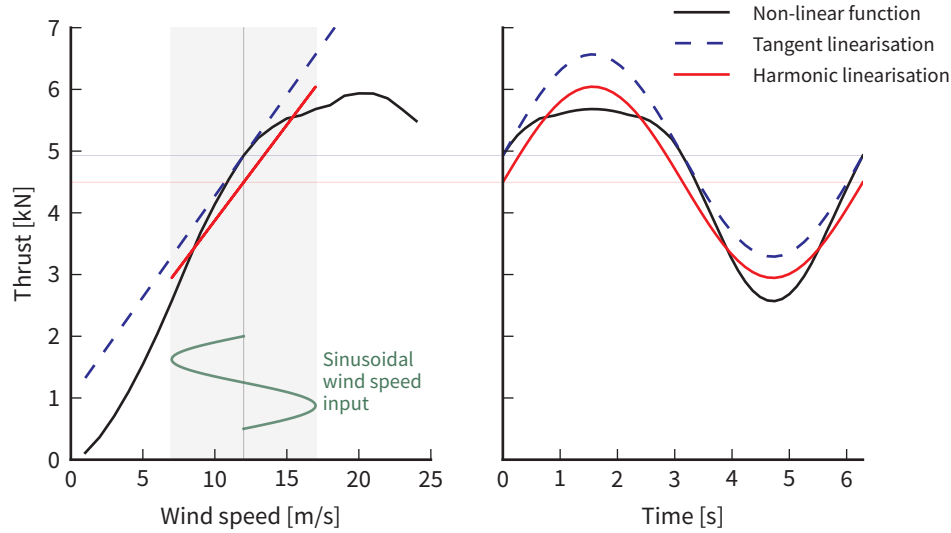


Figure 5.6 – Example of harmonic and tangent linearisations of the thrust on one BEM annulus, with all inputs held constant apart from a sinusoidal wind speed input. Left: thrust as a function of wind speed. Right: harmonic thrust output.

as ‘harmonic linearisation’, but the method can be adapted to suit either type of input. The differences between tangent and harmonic linearisation are illustrated in Figure 5.6. There is a limit to how well a single sinusoid can be made to fit the output of the original nonlinear function, but the harmonic linearisation gives the best possible sinusoid.

The basic assumption of this approach is that the inputs and responses are harmonic at frequency  $\omega$ , so the state vector can be written as

$$\mathbf{x}(t) = \mathbf{x}_0 + \frac{1}{2} (\bar{\mathbf{x}} e^{i\omega t} + \bar{\mathbf{x}}^* e^{-i\omega t}) \quad (5.21)$$

where  $\mathbf{x}_0$  is the mean value of  $\mathbf{x}$ ,  $\bar{\mathbf{x}}$  is a complex vector representing the magnitude and phase of  $\mathbf{x}$ , and  $\bar{\mathbf{x}}^*$  is its complex conjugate. The output of the nonlinear function can be written similarly as

$$\mathbf{f}[\mathbf{x}(t), \dot{\mathbf{x}}(t)] = \mathbf{f}_0 + \frac{1}{2} (\bar{\mathbf{f}} e^{i\omega t} + \bar{\mathbf{f}}^* e^{-i\omega t}) + \boldsymbol{\varepsilon}(t) \quad (5.22)$$

where  $\boldsymbol{\varepsilon}(t)$  represents higher harmonics in  $\mathbf{f}[\mathbf{x}(t), \dot{\mathbf{x}}(t)]$  at frequency  $n\omega$ ,  $n > 1$ , which are neglected. The mean and first harmonic of  $\mathbf{f}$  are (Langley

1988)

$$f_0 = \frac{1}{T} \int_0^T f[x(t), \dot{x}(t)] dt \quad (5.23a)$$

$$\bar{f} = \frac{2}{T} \int_0^T f[x(t), \dot{x}(t)] e^{-i\omega t} dt \quad (5.23b)$$

where  $T = 2\pi/\omega$ . In practice, these can be evaluated efficiently from the first two coefficients of the Fast Fourier Transform of  $f[x(t), \dot{x}(t)]$ .

Returning to the specific case of the aerodynamic loads at one point on the blade, the harmonic force and response, Equations (5.21)–(5.22), can then be substituted into the original equations (5.16)–(5.17) to give

$$Kq_0 = \sum_k f_0^k \quad (5.24a)$$

$$[-\omega^2 M + i\omega C + K] \bar{q} = \sum_k \bar{f}^k \quad (5.24b)$$

where  $q_0$  and  $\bar{q}$  are sub-vectors of  $x_0$  and  $\bar{x}$ , according to Equation (5.18). Together with Equations (5.23), these form a set of complex nonlinear equations which must be solved for  $x_0$  and  $\bar{x}$ .

Note that because the first harmonic of the nonlinear function is found numerically, the dependence of  $\bar{f}^k$  on  $\bar{q}$  is implicit. Compare this to the tangent linearisation described below on p 5.3.2, where the stiffness and damping matrices associated with the nonlinear force can be brought to the left-hand side of the equation.

Different variables can be considered as unknowns in finding the harmonic response. Initially, in the following subsections, the rotor speed and pitch angle are assumed to be constant, and the aerodynamic loads and the wake dynamics are linearised in turn. In an operating wind turbine, however, the rotor speed and pitch angle are actively controlled; this will be addressed in the next chapter.

### 5.3 Linearised aerodynamic forces with aeroelasticity

For now, assume that the rotor speed, blade pitch angle and induced velocities are all known and constant. The state vector of Equation (5.18) is then

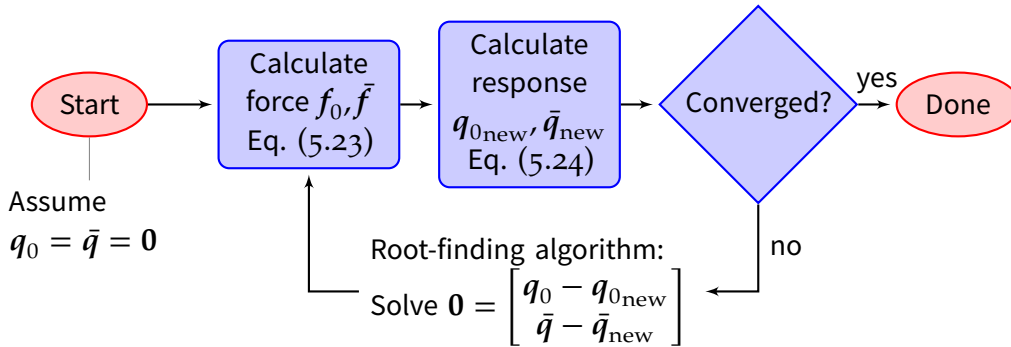
reduced to

$$\mathbf{x} = \begin{bmatrix} U_\infty \\ \mathbf{q} \end{bmatrix} \quad (5.25)$$

while the nonlinear force  $\mathbf{f}(\mathbf{x}, \dot{\mathbf{x}})$  represents the distributed aerodynamic loads along the blade, according to Equation (5.5). A harmonic solution for the blade deflection  $\mathbf{q}$  is sought. In this section three approaches will be compared: an iterative harmonic linearisation, a non-iterative tangent linearisation, and the nonlinear time-integration solution.

### 5.3.1 HARMONIC LINEARISATION

The solution procedure for the harmonic linearisation is broadly as follows:



where the iteration is controlled by a numerical multi-dimensional root-finding algorithm. In this case there is little difficulty in finding the solution since the structural response is linear, but because more difficult problems are solved later using the same framework, a general-purpose numerical solver is used<sup>2</sup>.

Using this procedure, results were calculated for the same grid of mean wind speed, harmonic amplitude and frequency described above on p 148. The results are the mean and harmonic parts of the response modal amplitudes  $(q_0, \bar{q})$  and the aerodynamic distributed force  $(f_0, \bar{f})$ . The tip deflection summarises the response, and may be calculated as

$$\begin{aligned} \delta_0 &= \Phi_d^X q_0 \\ \bar{\delta} &= \Phi_d^X \bar{q} \end{aligned} \quad (5.26)$$

2. The 'hybr' method implemented in SciPy (Jones, Oliphant and Peterson 2001)

where  $\Phi_d^x$  is defined in Equation (2.92) on p 66. The rotor overall thrust and torque can also be calculated numerically from  $f$  as follows. If  $k$  is a unit vector pointing towards the tip of the blade, the total aerodynamic blade force and moment at the rotor centre are

$$\begin{aligned} F_0^{\text{aero}} &= \int f_0(r) dr & M_0^{\text{aero}} &= \int [rk] \times f_0(r) dr \\ \bar{F}^{\text{aero}} &= \int \bar{f}(r) dr & \bar{M}^{\text{aero}} &= \int [rk] \times \bar{f}(r) dr \end{aligned} \quad (5.27)$$

where the integrals represent numerical integration of the values at each annulus evaluated using the trapezium rule. The inertial force and moment on the rotor are given by the beam element mass matrix,

$$\begin{aligned} F_0^{\text{iner}} &= \mathbf{0} & M_0^{\text{iner}} &= \mathbf{0} \\ \bar{F}^{\text{iner}} &= \omega^2 M_{rf} \bar{q} & \bar{M}^{\text{iner}} &= \omega^2 M_{\omega f} \bar{q} \end{aligned} \quad (5.28)$$

where  $M_{rf}$  and  $M_{\omega f}$  are defined by Equations (A.14) and (A.18). The total rotor force and moment are then

$$\begin{aligned} F_0^{\text{rotor}} &= 3F_0^{\text{aero}} & M_0^{\text{rotor}} &= 3M_0^{\text{aero}} \\ \bar{F}^{\text{rotor}} &= 3(\bar{F}^{\text{aero}} + \bar{F}^{\text{iner}}) & \bar{M}^{\text{rotor}} &= 3(\bar{M}^{\text{aero}} + \bar{M}^{\text{iner}}) \end{aligned} \quad (5.29)$$

for a three-bladed rotor.

### 5.3.2 TANGENT LINEARISATION

In the tangent linearisation, Equations (5.23)–(5.24) are replaced by the linear equations

$$Kq_0 = \sum_k f^k(x_0, \mathbf{0}) \quad (5.30a)$$

$$\left[ -\omega^2 M + i\omega C + K - \sum_k (K_q^k + i\omega C_q^k) \right] \bar{q} = \sum_k K_U^k \bar{U} \quad (5.30b)$$

The function and its tangent matrices are evaluated at  $x_0^T = [U_0 \quad \mathbf{0}^T]$ , and the tangent matrices from Equation (5.19) are partitioned as  $K_f = [K_U \quad K_q]$  and  $C_f = [C_U \quad C_q]$  to match the partition of  $x$  in Equation (5.25). In this way, the tangent linearisation does account for linear aeroelasticity.

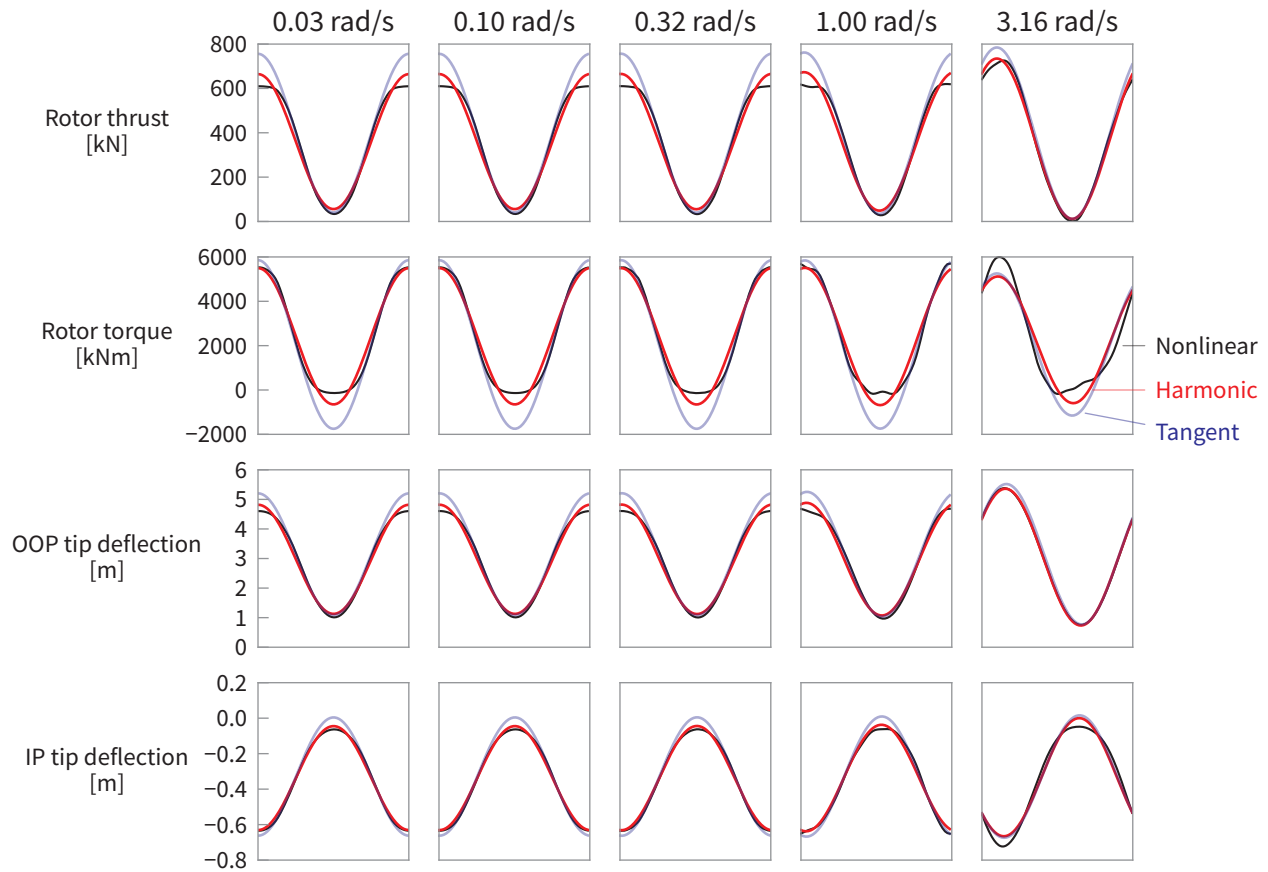


Figure 5.7 – Example linearisation results for rotor loads and blade tip in-plane (IP) and out-of-plane (OOP) deflections, plotted over one cycle of harmonic wind speed input ( $8 \pm 5 \text{ m s}^{-1}$ ). The columns correspond to wind speed variations of different frequencies.

### 5.3.3 RESULTS

In the following results, the harmonic linearisation is compared to the nonlinear reference simulations and a tangent linearisation. The nonlinear results are the same as described on p 148. A set of examples of the harmonic linearisation are shown in Figures 5.7 and 5.8 for a harmonic wind speed input with amplitude  $5 \text{ m s}^{-1}$  about the mean  $8 \text{ m s}^{-1}$ . The same results are plotted in two ways: against time and against the harmonic wind speed. The aerodynamic thrust and torque is noticeably nonlinear, due to the aerofoils stalling during part of the large cyclic variation in wind speed. The deflection responses are also therefore somewhat non-

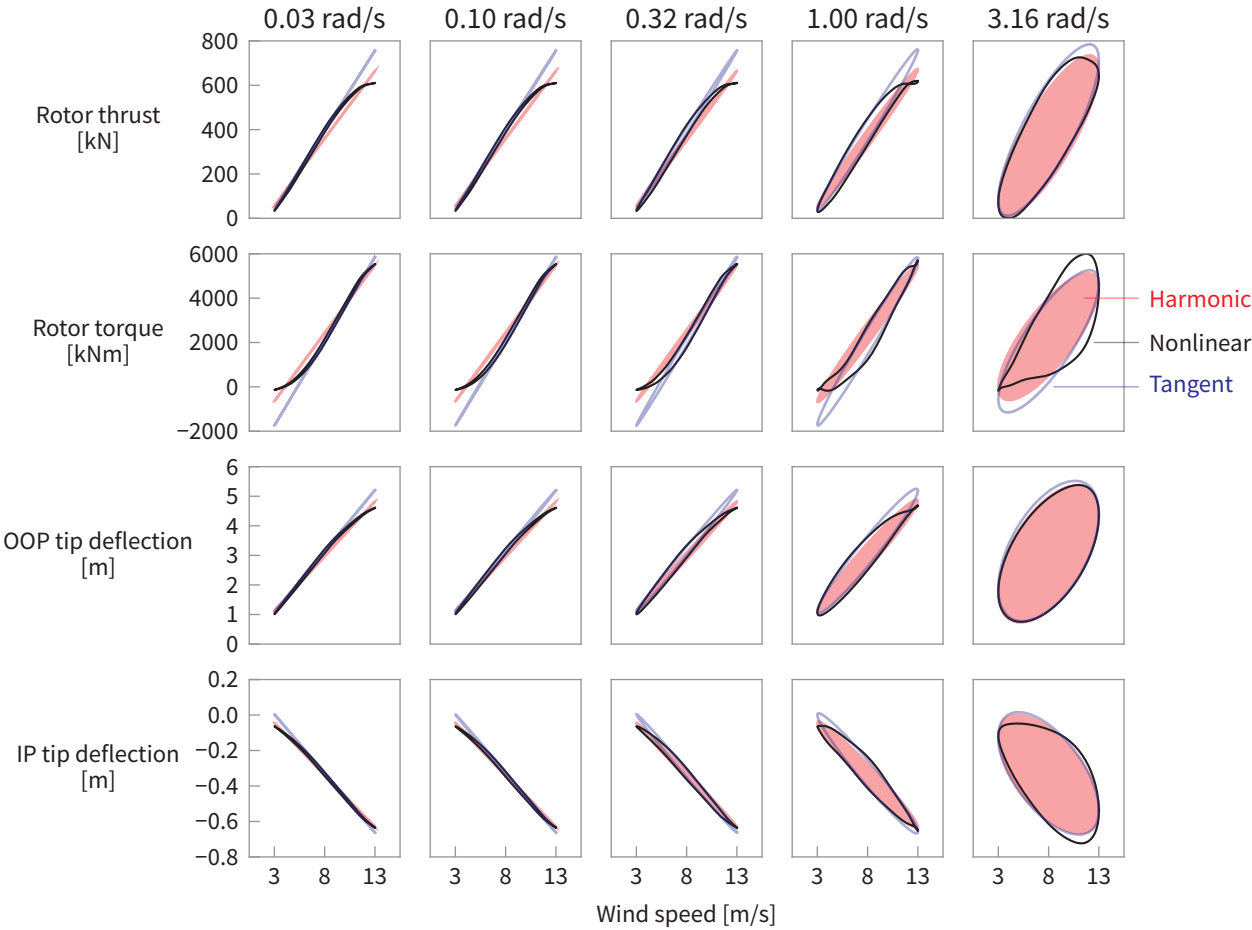


Figure 5.8 – Example linearisation results for rotor loads and blade tip in-plane (IP) and out-of-plane (OOP) deflections, plotted against the harmonic wind speed input ( $8 \pm 5 \text{ m s}^{-1}$ ). The columns correspond to wind speed variations of different frequencies.

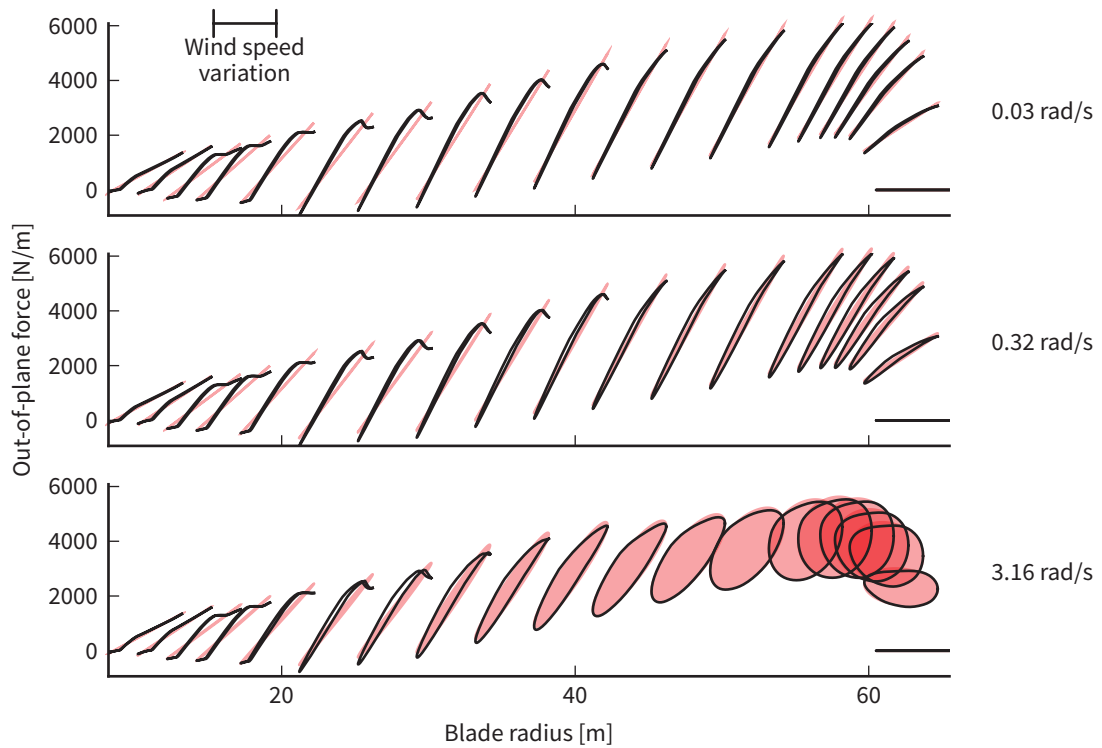


Figure 5.9 – Out-of-plane aerodynamic blade loading at several points along the blade, for three frequencies.

sinusoidal. The harmonic linearisation represents the behaviour reasonably well; the tangent linearisation tends to overestimate the peak thrust.

Figure 5.9 show the distributed blade loads at several points along the blade, which together make up the rotor thrust and torque shown in Figures 5.7 and 5.8. Most of the nonlinear behaviour due to stalling can be seen in the midspan of the blade. The larger loops towards the tip are due to the greater blade bending motions there.

Figures 5.10–5.11 show the error between the linearised results and the nonlinear simulations. The peak-peak error is a simple measure which is relevant whether fatigue or extreme loads are of interest; the error plotted in these figures is the peak-peak error normalised by the Bladed peak-peak value. The same data is also given in Table 5.2. For small wind speed perturbations, both harmonic and tangent linearisations give small errors. The errors of both increase as the size of the wind speed perturbations increases, but the increase is greater for the tangent linearisation. At a mean wind speed of  $8 \text{ m s}^{-1}$ , which is the case shown in Figures 5.7–5.9, the harmonic linearisation is up to 4 times better than the tangent linearisation. At the higher mean wind speed of  $16 \text{ m s}^{-1}$ , the behaviour is more linear. The improvements are less significant, but the error in the rotor torque is still reduced by a factor of 2.

Overall, the maximum error in the harmonic linearisation results is 8.4% of the peak-peak range, and occurs in the rotor torque. If the wind speed variations are below  $3 \text{ m s}^{-1}$ , the maximum error is 3.4%.

The details of these results are specific to the particular blade used in these calculations, but the overall behaviour should be similar in most wind turbines: harmonic linearisation can significantly reduce the error in the calculation of the aerodynamic loads, although clearly it is not perfect. In practice, the results could be better than shown here: the uniform wind speed applied across the whole rotor in these examples is the worst case for rotor loading. Wind speed variations due to rigid body motion of the whole platform may come close to this worst case. Variations in wind speed due to turbulence, on the other hand, have less spatial correlation. Spatial averaging therefore reduces the level of nonlinearity in the overall rotor loading.

## 5.4 Linearised wake dynamics

In the previous subsection the wake dynamics were neglected and the aeroelastic response to wind speed variations was examined; now the wake dynamics are included while neglecting the blade dynamics. Because

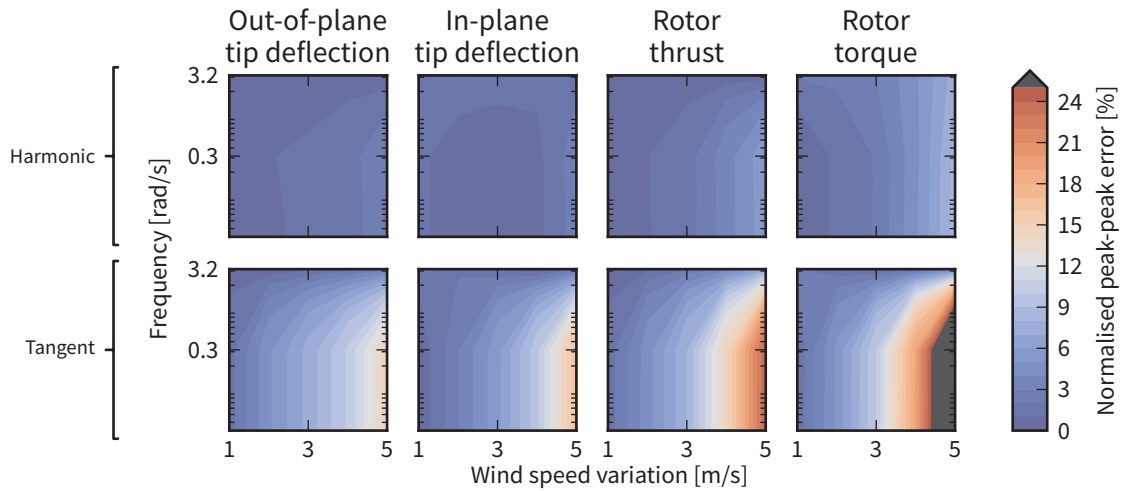


Figure 5.10 – Error between linearised and nonlinear results, for mean wind speed of  $8 \text{ m s}^{-1}$  (below rated). The error is defined as the peak-peak range of the linearised result, normalised by the peak-peak range of the nonlinear result.

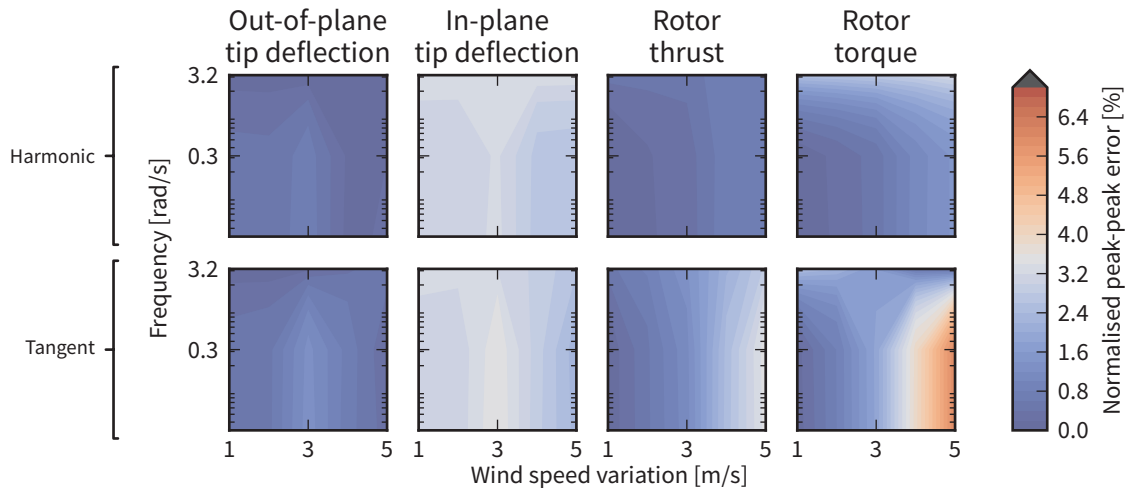


Figure 5.11 – As above, for mean wind speed of  $16 \text{ m s}^{-1}$  (above rated).

Table 5.2 – Error of linearisations, as shown in Figures 5.10–5.11. The maximum error for various amplitudes of wind speed variation  $A$  is shown.

	Out-of-plane defl.	In-plane defl.	Rotor thrust	Rotor torque
Mean wind speed $8 \text{ m s}^{-1}$				
Harmonic:				
$A < 1 \text{ m s}^{-1}$	0.5 %	2.0 %	0.5 %	2.2 %
$A < 2 \text{ m s}^{-1}$	1.0 %	2.1 %	1.0 %	2.6 %
$A < 3 \text{ m s}^{-1}$	1.1 %	2.1 %	1.5 %	3.0 %
$A < 4 \text{ m s}^{-1}$	1.6 %	2.1 %	3.5 %	4.8 %
$A < 5 \text{ m s}^{-1}$	2.8 %	2.6 %	5.7 %	8.4 %
Tangent:				
$A < 1 \text{ m s}^{-1}$	1.6 %	2.3 %	1.4 %	2.1 %
$A < 2 \text{ m s}^{-1}$	4.8 %	3.0 %	4.5 %	5.2 %
$A < 3 \text{ m s}^{-1}$	7.4 %	5.7 %	8.0 %	10.1 %
$A < 4 \text{ m s}^{-1}$	10.1 %	9.7 %	14.4 %	19.3 %
$A < 5 \text{ m s}^{-1}$	14.5 %	16.7 %	24.1 %	34.1 %
Mean wind speed $16 \text{ m s}^{-1}$				
Harmonic:				
$A < 1 \text{ m s}^{-1}$	0.5 %	3.4 %	0.5 %	2.6 %
$A < 2 \text{ m s}^{-1}$	0.5 %	3.4 %	0.5 %	2.7 %
$A < 3 \text{ m s}^{-1}$	0.7 %	3.4 %	0.6 %	2.8 %
$A < 4 \text{ m s}^{-1}$	0.7 %	3.4 %	0.7 %	3.0 %
$A < 5 \text{ m s}^{-1}$	0.7 %	3.4 %	0.8 %	3.3 %
Tangent:				
$A < 1 \text{ m s}^{-1}$	0.5 %	3.4 %	0.5 %	2.5 %
$A < 2 \text{ m s}^{-1}$	0.5 %	3.4 %	0.9 %	2.5 %
$A < 3 \text{ m s}^{-1}$	1.3 %	3.6 %	1.4 %	2.5 %
$A < 4 \text{ m s}^{-1}$	1.3 %	3.6 %	2.5 %	3.9 %
$A < 5 \text{ m s}^{-1}$	1.3 %	3.6 %	3.5 %	6.0 %

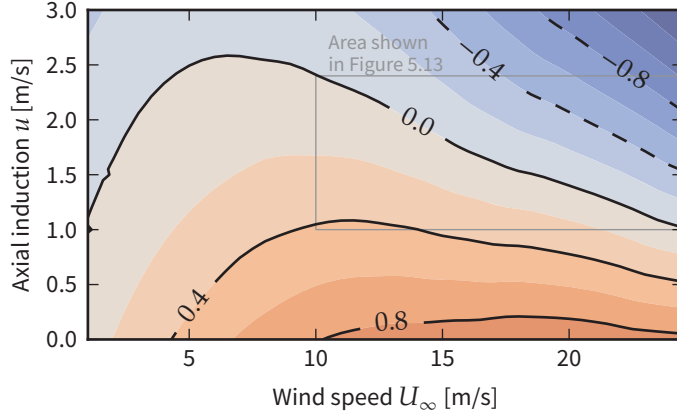


Figure 5.12 – Wake derivative function  $\dot{u}$  for the NREL blade. Rotor speed 9.45 rpm, pitch angle  $0^\circ$ , blade station at 43.7 m.

the aerodynamic calculations in each annulus are independent, only one annulus need be considered at a time. Again, the rotor speed and blade pitch angle are assumed constant, so the state vector of Equation (5.18) is reduced to

$$\mathbf{x} = \begin{bmatrix} U_\infty \\ u \end{bmatrix} \quad (5.31)$$

where  $u$  is the induced axial velocity in the annulus. The induced tangential velocity  $u'$  is neglected for simplicity, but could be included in an analogous manner. The nonlinear function  $f(\mathbf{x}, \dot{\mathbf{x}})$  now represents the wake dynamics:

$$\dot{u} = f(\mathbf{x}) \quad (5.32)$$

This is illustrated in Figure 5.12.

A harmonic steady-state solution is sought for the induced velocity  $u$ . The solution is determined implicitly by the requirements that the induced velocity is harmonic and has constant mean. These requirements are satisfied by solving the nonlinear equations

$$f_0 = 0 \quad (5.33a)$$

$$\bar{f} = i\omega\bar{u} \quad (5.33b)$$

with  $f_0$  and  $\bar{f}$  being calculated according to Equations (5.23). In practice this is achieved using a standard numerical root-finding algorithm as described

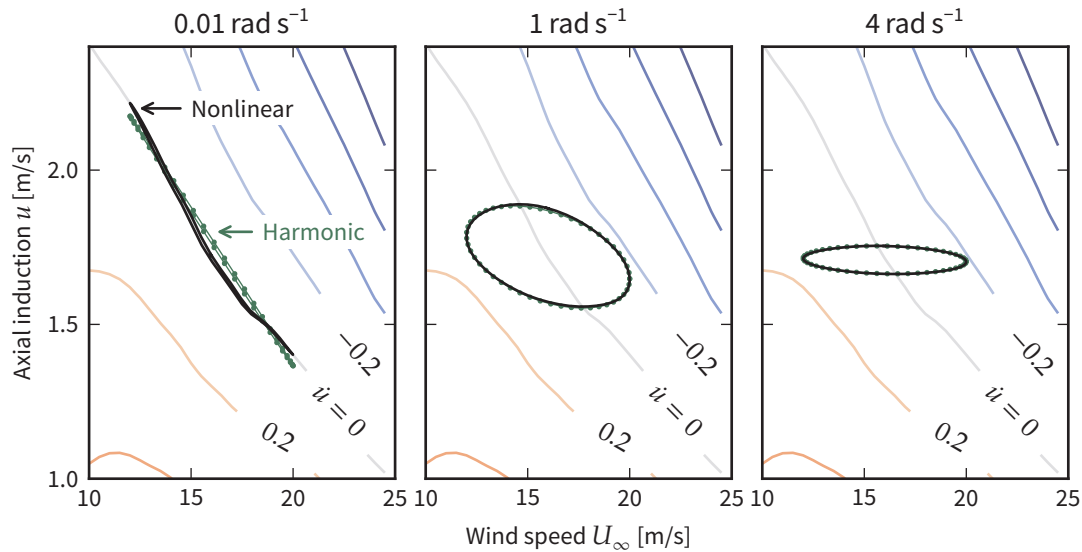


Figure 5.13 – Wake solution for harmonic wind input of  $16 \pm 4 \text{ m s}^{-1}$  at three frequencies.

in the previous section.

As an example, Figure 5.13 shows results for harmonic wind speed inputs at low, medium and high frequencies. At low frequencies the response is quasi-static, following the contour line for  $\dot{u} = 0$ . Since the quasi-static response is nonlinear in wind speed, the linearisation deviates from the nonlinear solution. At higher frequencies, the wake dynamics cause a lag between the change in wind speed and the change in induced velocity, and the nonlinearity in the quasi-static solution is less important.

The ‘frozen wake’ assumption used in the previous section, that  $u$  is constant, corresponds to a horizontal line on these contour plots. While this is reasonable for small variations in wind speed or high frequency variations, these results suggest that the wake dynamics may need to be included in the linearised model.

## 5.5 Conclusions

Having developed an implementation of the BEM method and verified it against Bladed simulations, the accuracy of linearised approaches to calcu-

lating aerodynamic loads can be assessed. Two cases have been studied: in the first, the wake state is held constant and the aeroelastic dynamic solution is found, while in the second the wake dynamics are solved while keeping the blades rigid.

In the aeroelastic case, the nonlinearity is due mainly to stalling of the blade aerofoils. The tangent and harmonic linearisations have been compared to the nonlinear solution. The harmonic linearisation captures this behaviour better than the tangent linearisation, reducing the maximum error by up to 4 times. Both linearisations unsurprisingly perform better when the variations in wind speed are smaller. The maximum error in the harmonic linearisation results is 8.4% of the peak-peak range, and occurs in the rotor torque. If the wind speed variations are below  $3 \text{ m s}^{-1}$ , the error is less than 4%.

The wake dynamics are smoothly nonlinear, and the harmonic linearisation captures the behaviour well, especially at higher frequencies.

All results in this chapter have been found assuming constant rotor speed and blade pitch angle, but in reality the rotor speed and blade pitch angle will vary. In this following chapter a linearised model of the control system is developed to account for this.

## Chapter 6

### *Control system dynamics*

The results in the previous chapter were calculated for constant rotational speed of the rotor, and a constant blade pitch angle. In reality, both of these are actively controlled by the wind turbine controller (see introduction on p 24). In this chapter a linearised model of the controller is developed. Although there are many approaches to control of wind turbines (see for example Burton et al. 2011, chapter 8), here the controller of the NREL 5MW turbine is used, which is representative of typical modern wind turbines (Jonkman, Butterfield, et al. 2009).

#### 6.1 Wind turbine control systems

The overall principle of operation of a variable-speed, variable-pitch wind turbine such as the one used here is shown in Figure 6.1. At low wind speeds, the rotor speed is controlled in proportion to the wind speed, because this sets up the optimum aerodynamic conditions in the rotor to maximise the power captured. This is achieved by controlling the generator torque. At higher wind speeds, once the maximum generator power is being produced, the blades are pitched to reduce the amount of aerodynamic power that is captured. These two control actions are introduced in the following sections in their nonlinear reference implementation, before a linearisation is developed and compared to the reference.

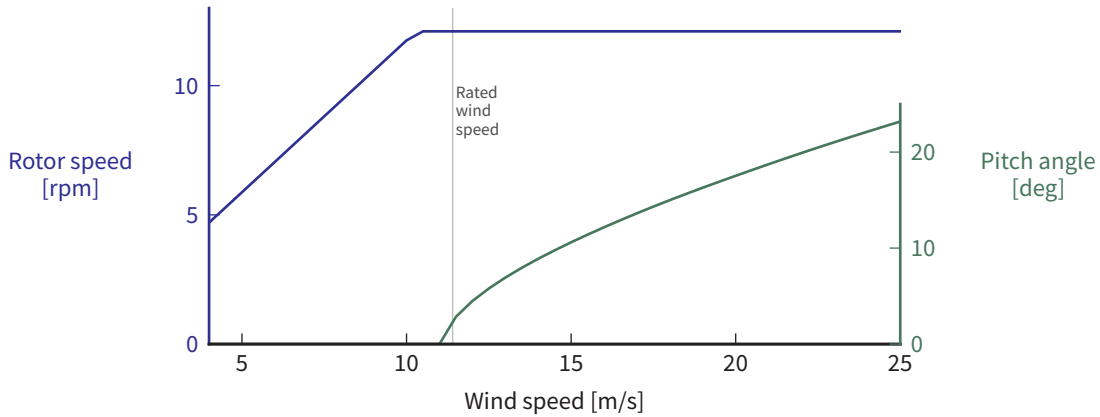


Figure 6.1 – Operation of a variable-speed, variable-pitch wind turbine. Blade pitch angle is defined so that increasing the pitch angle rotates the leading edge of the aerofoil towards the upwind side of the rotor, thus keeping the angle of attack roughly constant as the wind speed increases.

### 6.1.1 TORQUE CONTROLLER

The aim of the torque controller is to maintain the optimum rotor speed which leads to the correct air flow for maximum aerodynamic efficiency. This turns out to be achieved by a quadratic relationship between rotor speed and generator torque (Burton et al. 2011, chapter 8):

$$Q_g = k_{\text{opt}} \Omega_g^2 \quad (6.1)$$

where  $\Omega_g$  is the filtered generator speed. The measured generator speed is passed through a low-pass filter before being used to calculate the generator torque demand. In practice the controller is implemented with a discrete timestep and at time  $t_i$  the filtered generator speed is calculated as

$$[\Omega_g]_i = (1 - \alpha) \Omega_g^{\text{meas}} + \alpha [\Omega_g]_{i-1} \quad (6.2)$$

where  $\Omega_g^{\text{meas}}$  is the measured generator speed,  $\alpha = \exp[-\omega_c(t_i - t_{i-1})]$ , and the filtering is determined by the filter corner frequency  $\omega_c$ . Note that both the generator speed and torque are defined on the generator side of the gearbox, and are related to the rotor speed and torque by the gearbox ratio  $G$ , so if  $\Omega$  is the rotor speed then  $\Omega_g^{\text{meas}} = G\Omega$ .

The optimum quadratic control can only be achieved over a limited

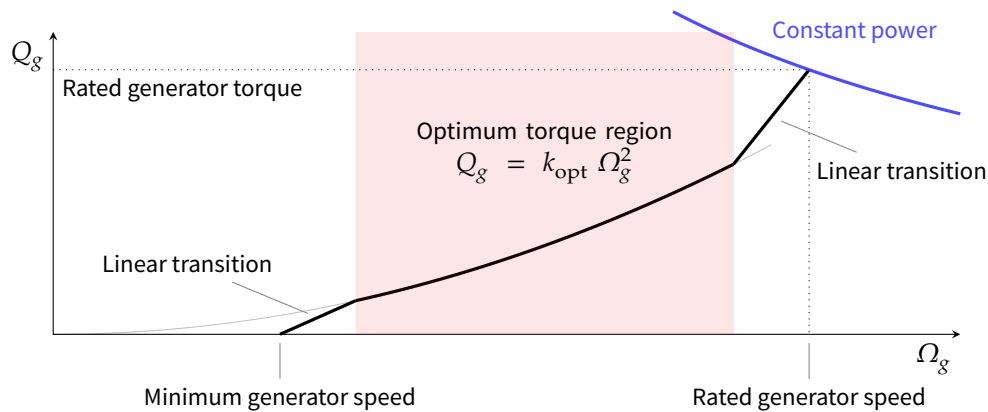


Figure 6.2 – Generator torque control.

range of generator speeds. At the minimum and maximum generator speeds, the torque transitions linearly to zero and the rated generator torque respectively. This is illustrated in Figure 6.2. In reality, there will also be limits on the maximum torque and maximum rate of change of torque, which are applied after finding the desired torque from Figure 6.2.

As the wind speed increases, the generator speed and the generated power also increase. Once the wind speed rises high enough that the rated power is being produced (at the ‘rated wind speed’ of the turbine), the torque controller can no longer regulate the generator speed without exceeding the rated power. At this point the pitch controller, described in the following section, becomes active. The torque controller may then either maintain a constant torque, or aim to achieve constant output power by switching to controlling the torque as  $Q_g = P_{\text{rated}}/\Omega_g$ , as shown in Figure 6.2.

### 6.1.2 PITCH CONTROLLER

The pitch controller is based on a PID controller acting on the error between the generator speed and the nominal rated generator speed:

$$\varepsilon_g = \Omega_g - \Omega_{\text{rated}} \quad (6.3)$$

The same filtered generator speed signal as the torque controller is used (Equation 6.2). The demanded pitch angle is

$$\theta = G_K [K_P \varepsilon_g + K_I I_\varepsilon] \quad (6.4a)$$

$$I_\varepsilon = \int_0^t \varepsilon_g dt \quad (6.4b)$$

$K_P$  and  $K_I$  are the proportional and derivative gains respectively. In general a derivative term  $K_D \dot{\varepsilon}_g$  could be present, but was not used in the example controller. The factor  $G_K$  represents a 'gain schedule', which compensates for the variable sensitivity of the blade loads to changes in pitch angle at different wind speeds. The wind speed over the rotor is difficult to measure accurately, but because there is a monotonic relationship between the wind speed and the pitch angle (Figure 6.1), the pitch angle itself is used to set the gain schedule:

$$G_K = \frac{1}{1 + \theta/\theta_2} \quad (6.5)$$

where  $\theta_2$  is the pitch angle at which the gain should be halved.

In practice, the pitch controller works at discrete timesteps and the integral error at time  $t_i$  is calculated as

$$[I_\varepsilon]_i = [I_\varepsilon]_{i-1} + \varepsilon_g (t_i - t_{i-1}) \quad (6.6)$$

To prevent integrator windup, the integral error must be prevented from decreasing past the value corresponding to the minimum pitch angle. As with the torque controller, in practice the pitch demand from Equation (6.4) will be subject to limits on the value and rate of change.

### 6.1.3 INTERACTION BETWEEN TORQUE AND PITCH CONTROL

When the wind speed varies close to the rated wind speed, both the pitch and torque controllers may be active. To prevent the controllers conflicting, the torque controller is forced into 'constant power' mode whenever the

pitch angle is greater than some minimum value  $\theta_{CP}$ :

$$Q_g = \begin{cases} f(\Omega_g) & \text{when } \theta \leq \theta_{CP} \\ P_{rated}/\Omega_g & \text{otherwise} \end{cases} \quad (6.7)$$

where  $f(\Omega_g)$  is the function shown in Figure 6.2. This deactivates the torque controller when the pitch controller is active; the converse is automatically achieved because when  $\Omega_g < \Omega_{rated}$  then  $\varepsilon_g < 0$  always, forcing the pitch angle to zero. In practice, more complicated arrangements may be used to improve the control behaviour when this boundary is crossed (Burton et al. 2011, chapter 8).

#### 6.1.4 VERIFICATION

The implementation of the nonlinear controllers was verified against a reference implementation of the controller which can be run in Bladed (Jonkman, Butterfield, et al. 2009). Simulations were run in Bladed for the same set of conditions used previously (p 148). In order to test the controller implementation in isolation, the rotor speed and pitch angle at each timestep was taken from the Bladed simulations and fed to the present controller implementation (Equations 6.1–6.6), and the demanded generator torque and pitch angle calculated. This avoids any differences due to differing modelling of the rotor dynamics when verifying the controller.

The results are shown in Figure 6.3; in almost all cases the results agree very well. In the results for the largest amplitude at  $0.1 \text{ rad s}^{-1}$ , some differences are visible in the pitch angle, which in turn causes the relatively large difference in the spikes in torque demand. This is an example of the torque and pitch controllers interacting. When the pitch angle reaches zero there is a sudden drop in generator torque: at this point the pitch controller can do no more to regulate the generator speed, and the torque controller takes over.

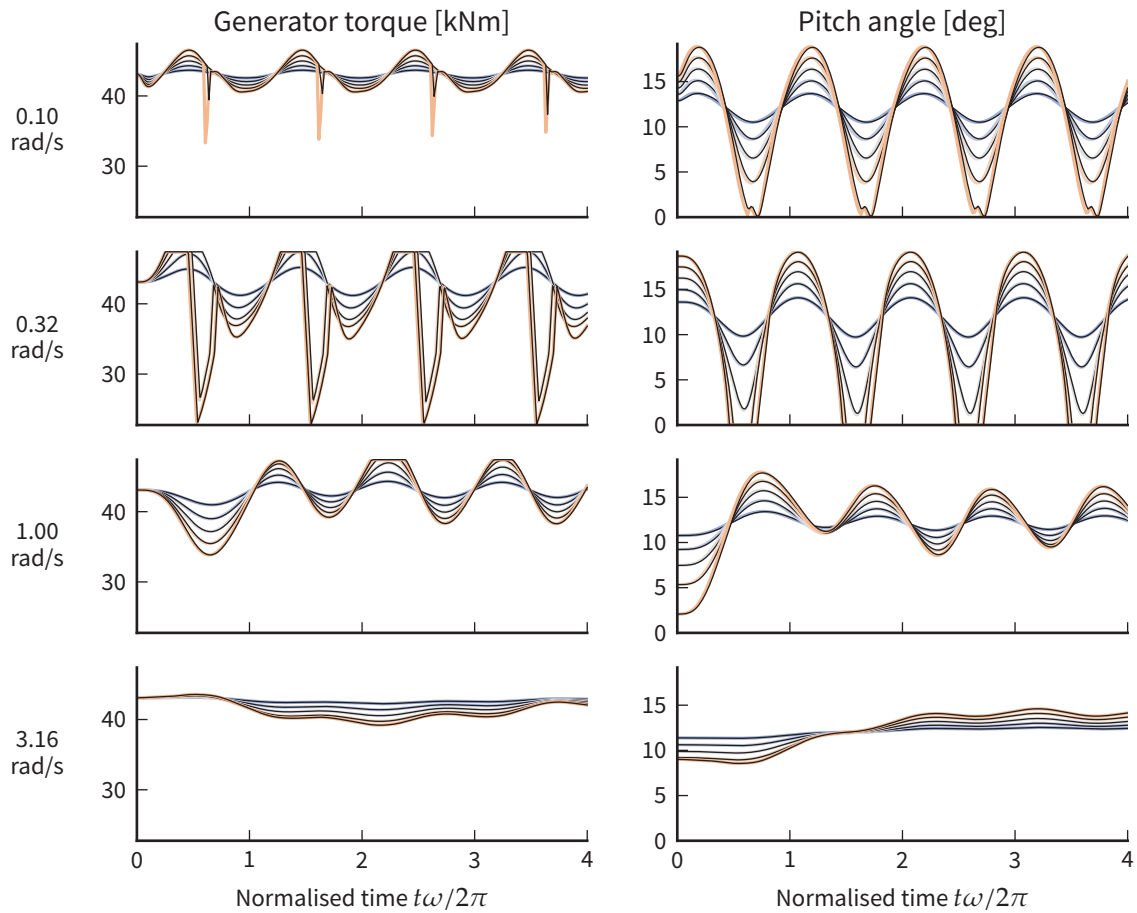


Figure 6.3 – Verification of pitch and torque controller implementation. Bladed simulations (thin black lines) were run with harmonic wind speed inputs: mean wind speed  $16 \text{ m s}^{-1}$ , amplitudes from  $1 \text{ m s}^{-1}$  to  $5 \text{ m s}^{-1}$ , frequencies from  $0.10 \text{ rad s}^{-1}$  to  $3.16 \text{ rad s}^{-1}$ . The rotor speed and pitch angle from the Bladed simulations were fed to the present controller implementation and the pitch and torque demands calculated (thick coloured lines). There is a good match in almost all cases.

## 6.2 Harmonic linearisation of torque and pitch control

Now the behaviour of the torque and pitch controllers will be linearised subject to harmonic wind speed input, following the same approach used in Chapter 5. There are three steps: firstly the torque behaviour shown in Figure 6.2 is linearised in isolation, assuming the rotor speed is known. Secondly, the linearised torque is used to solve for the rotor speed response. This applies to operation below the rated wind speed. Finally, for wind speeds above the rated wind speed, the pitch controller is also active and the pitch angle response is solved simultaneously.

Using the same notation as Section 5.2, both the known inputs and the unknown responses are included the 'state vector'  $\mathbf{x}$ . Here, it contains the wind speed, rotor speed, and pitch controller integral error:

$$\mathbf{x} = \begin{bmatrix} U_{\infty} \\ \Omega \\ I_e \end{bmatrix} \quad (6.8)$$

The wind speed is always treated as a known input. The steps listed above correspond to first assuming  $\mathbf{x}$  is fully known, then solving for unknown harmonic  $\Omega$ , and finally solving for  $\Omega$  and  $I_e$ .

### 6.2.1 HARMONIC LINEARISATION OF GENERATOR TORQUE

The nonlinear function being linearised  $f(\mathbf{x}, \dot{\mathbf{x}})$  is the generator torque function shown in Figure 6.2:

$$Q_g = f(\mathbf{x}, \dot{\mathbf{x}}) \quad (6.9)$$

The controller acts on the low-pass filtered generator speed as described by Equation (6.2). Since the wind speed and rotor speed are both assumed to be harmonic, the filtered generator speed is also harmonic. The mean value and complex amplitude of the filtered speed can be determined from

the harmonic rotor speed  $\Omega$  as

$$(\Omega_g)_0 = G\Omega_0 \quad (6.10a)$$

$$\overline{\Omega_g} = \frac{G\overline{\Omega}}{1 + i\omega/\omega_c} \quad (6.10b)$$

where  $\omega$  is the frequency of the harmonic signals, and  $\omega_c$  is the filter corner frequency from Equation (6.10).

Initially the wind speed  $U_\infty$  and the rotor speed  $\Omega$  are both taken as known inputs. The mean value and complex amplitude of the harmonic generator torque can then be determined numerically:

$$(\mathcal{Q}_g)_0 = \frac{1}{T} \int_0^T f[\mathbf{x}(t), \dot{\mathbf{x}}(t)] dt \quad (6.11a)$$

$$\overline{\mathcal{Q}_g} = \frac{2}{T} \int_0^T f[\mathbf{x}(t), \dot{\mathbf{x}}(t)] e^{-i\omega t} dt \quad (6.11b)$$

See page 153 for more background to these equations.

#### — Results

The accuracy of the linearisation depends on the mean value and the amplitude of the rotor speed, and hence which region of the torque curve is involved. Figure 6.4 compares the nonlinear and linearised generator torques corresponding to various choices of the harmonic wind speed.

Results are shown for harmonic variations in rotor speed at three frequencies. Because of the filtering of the generator speed signal, at high frequencies the torque variations are relatively small and the linearisation performs well. At lower frequencies the nonlinearity is more pronounced, especially around the rated generator speed, but the linearisation still gives a fairly good representation of the generator torque.

### 6.2.2 BELOW RATED: SOLUTION FOR ROTOR SPEED

The rotor speed is not usually known in advance, so now the harmonic rotor speed is sought corresponding to a harmonic wind speed input. To solve for this, the torque controller must be combined with the rotor rotational dynamics and the linearised aerodynamic loads described in the previous chapter. There are now two nonlinear functions to be linearised: the torque

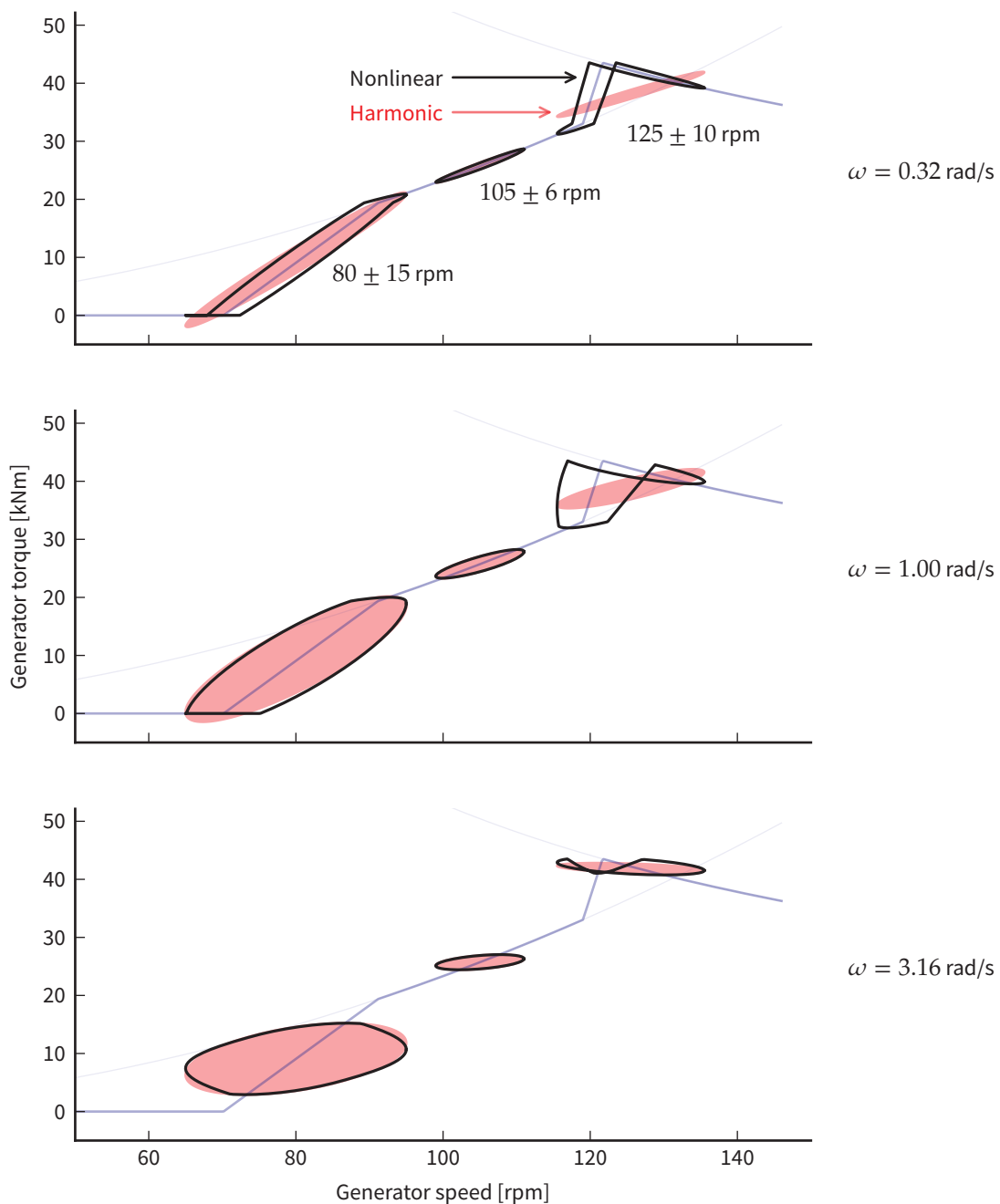


Figure 6.4 – Examples of linearised harmonic generator torque compared to the underlying nonlinear behaviour, for three frequencies. The lines in the background are the same as Figure 6.2. The example at the left is mildly nonlinear at the corners of the torque curve. For the example in the middle the underlying behaviour is quadratic, but over the range shown it is well approximated by the linear solution. The example at the right is highly nonlinear at low frequencies. At high frequencies the filtering of the generator speed measurement reduces the torque variation, improving the accuracy of the harmonic linearisation.

controller and the aerodynamic forces. The rotor speed is required to be harmonic with constant mean:

$$(\dot{\Omega})_0 = 0 \quad (6.12a)$$

$$\overline{\dot{\Omega}} = i\omega\overline{\Omega} \quad (6.12b)$$

The equation of motion of the rotor is

$$Q_a - GQ_g = J\dot{\Omega} \quad (6.13)$$

where  $Q_a$  is the aerodynamic torque,  $Q_g$  is the generator torque,  $G$  is the gear ratio and  $J$  is the rotor rotational inertia. Combining these gives the nonlinear equations to be solved:

$$(Q_a)_0 - G(Q_g)_0 = 0 \quad (6.14a)$$

$$\overline{Q_a} - G\overline{Q_g} = i\omega J\overline{\Omega} \quad (6.14b)$$

The aerodynamic torque and generator torque are both nonlinear functions of the rotor speed, as defined by Equation (5.27) on p 157 and Equation (6.9) respectively. Therefore, Equations (6.14) must be solved numerically, as with the solution of the wake dynamics in the previous chapter (p 161).

### 6.2.3 ABOVE RATED: SOLUTION FOR ROTOR SPEED AND PITCH ANGLE

When the wind speed is higher than the rated wind speed of the turbine, the torque controller switches to constant-power mode and the pitch controller becomes active, as described in Section 6.1. This adds an additional state, the pitch controller integral error  $I_\varepsilon$ , which is defined by Equation (6.4b).

Since a harmonic steady-state solution for the pitch angle is sought, the integral error must have a constant mean value. This implies the mean value of the speed error  $\varepsilon_g$  is zero. The complex amplitude of  $I_\varepsilon$  is determined by Equation (6.4b). Therefore

$$0 = (\Omega_g)_0 - \Omega_{\text{rated}} \quad (6.15a)$$

$$\overline{I_\varepsilon} = \frac{\overline{\Omega_g}}{i\omega} \quad (6.15b)$$

where  $(\Omega_g)_0$  and  $\overline{\Omega_g}$  are given by Equation (6.10).

The non-zero pitch angle must now be taken into account when calculating the aerodynamic torque  $Q_a$ . The pitch angle is calculated from the speed error and integral error as shown by Equation (6.4a), which in the harmonic case becomes

$$\theta_0 = G_K K_I (I_\varepsilon)_0 \quad (6.16a)$$

$$\bar{\theta} = G_K \left[ K_P + \frac{K_I}{i\omega} \right] \overline{\Omega_g} \quad (6.16b)$$

The gain schedule factor  $G_K$  is calculated at the mean pitch angle, on the assumption that it varies slowly relative to the amplitude of the pitch variations. By substituting Equation (6.16a) into (6.5),  $G_K$  may be found as a function of  $I_\varepsilon$  as

$$G_K = \frac{-1 + \sqrt{1 + 4a}}{2a} \quad \text{where } a = K_I I_\varepsilon / \theta_2 \quad (6.17)$$

Given a known harmonic wind speed input, the harmonic rotor speed and pitch angle are found as before using a root-finding algorithm to solve Equations (6.14) and (6.15) for  $(\Omega_g)_0$ ,  $\overline{\Omega_g}$ ,  $(I_\varepsilon)_0$  and  $\bar{I}_\varepsilon$ .

This linearisation does not account for the limits on pitch rate which are implemented in the nonlinear controller. In normal operation the pitch rate limits should not be reached, so this should be acceptable for a first approach to linearising the controller behaviour.

## 6.3 Comparison of linearised and nonlinear results

The harmonic linearisation problem has been solved as described above for harmonic wind speed input at mean wind speeds from  $6 \text{ m s}^{-1}$  to  $15 \text{ m s}^{-1}$ , amplitudes from  $1 \text{ m s}^{-1}$  to  $3 \text{ m s}^{-1}$  and frequencies of  $0.03 \text{ rad s}^{-1}$  to  $3.16 \text{ rad s}^{-1}$ . Since the number of equations to be solved depends on whether the pitch controller is active, for simplicity the pitch controller is assumed to be active only when the mean wind speed is above the nominal rated wind speed of  $11.4 \text{ m s}^{-1}$ . This will cause inaccuracies when the mean wind speed is below rated but part of the harmonic variation rises above

rated; this is visible in the following results.

For comparison, the same conditions were simulated in the time domain using the nonlinear controller implementation described in Section 6.1.

The peak-peak value is a simple but useful measurement of the accuracy of the results, whether extreme or fatigue loads are of interest. Figure 6.5 shows the error in the peak-peak value of the linearised results compared to the nonlinear simulations. The error has been normalised by a representative value of each variable: respectively, the rated rotor torque, rated rotor thrust, rated rotor speed and blade pitch angle at cutout.

In some cases it has not been possible to find a correct harmonic steady-state solution for the rotor speed and pitch angle. These cases are shown by red dots in Figure 6.5. This occurs when the wind speed crosses the rated wind speed of the turbine, meaning that the pitch controller should be active for part of the cycle. For simplicity in these example results the pitch controller has been included only for mean wind speeds above the rated wind speed ( $11.4 \text{ m s}^{-1}$ ). Therefore the correct solution for cases just below the rated wind speed cannot be found. Possible improvements to this approach will be discussed later.

Apart from these areas, in general the errors are fairly small for small variations in wind speed, but increase for larger variations in wind speed. Figures 6.6–6.8 give more detail by plotting the variation with time of the nonlinear and linearised responses, at a low, a medium and a high frequency respectively.

It can be seen in Figure 6.5 that, apart from the cases mentioned above, the rotor speed error is consistently less than the errors in the other variables: this is because above the rated wind speed the objective of the pitch controller is to minimise the rotor speed error. The same effect is visible in Figure 6.8, where although the amplitude of the linearised pitch angle variations is greater than the nonlinear results, the amplitude of the rotor speed variations is similar.

The linearised results in Figures 6.6–6.8 show the best agreement with the nonlinear simulations at mean wind speeds far from the turbine's rated wind speed (left and right columns). When the mean wind speed close to rated (middle columns), the generator torque behaviour is much more nonlinear. This corresponds to operation at the right-hand side of

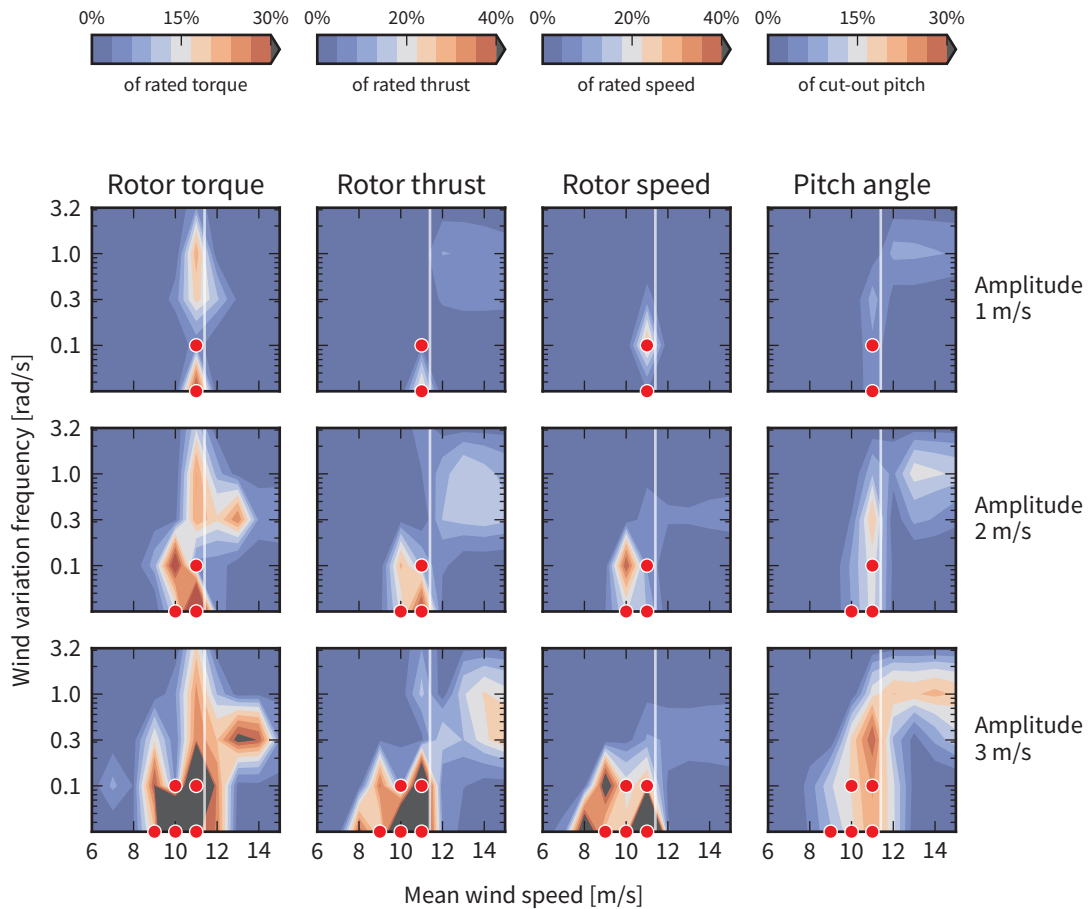


Figure 6.5 – Error in peak-peak value of linearised results compared to nonlinear simulations. In some areas it was not possible to find a harmonic solution; these are shown by the red dots. The colour scale for each column is different, as shown by the scales at the top. In each column the error is normalised by a representative value: the rated rotor torque (4.18 MN m), the rated rotor thrust (721 kN), the rated rotor speed (12.1 rpm) and the maximum operation blade pitch angle (23.2°).

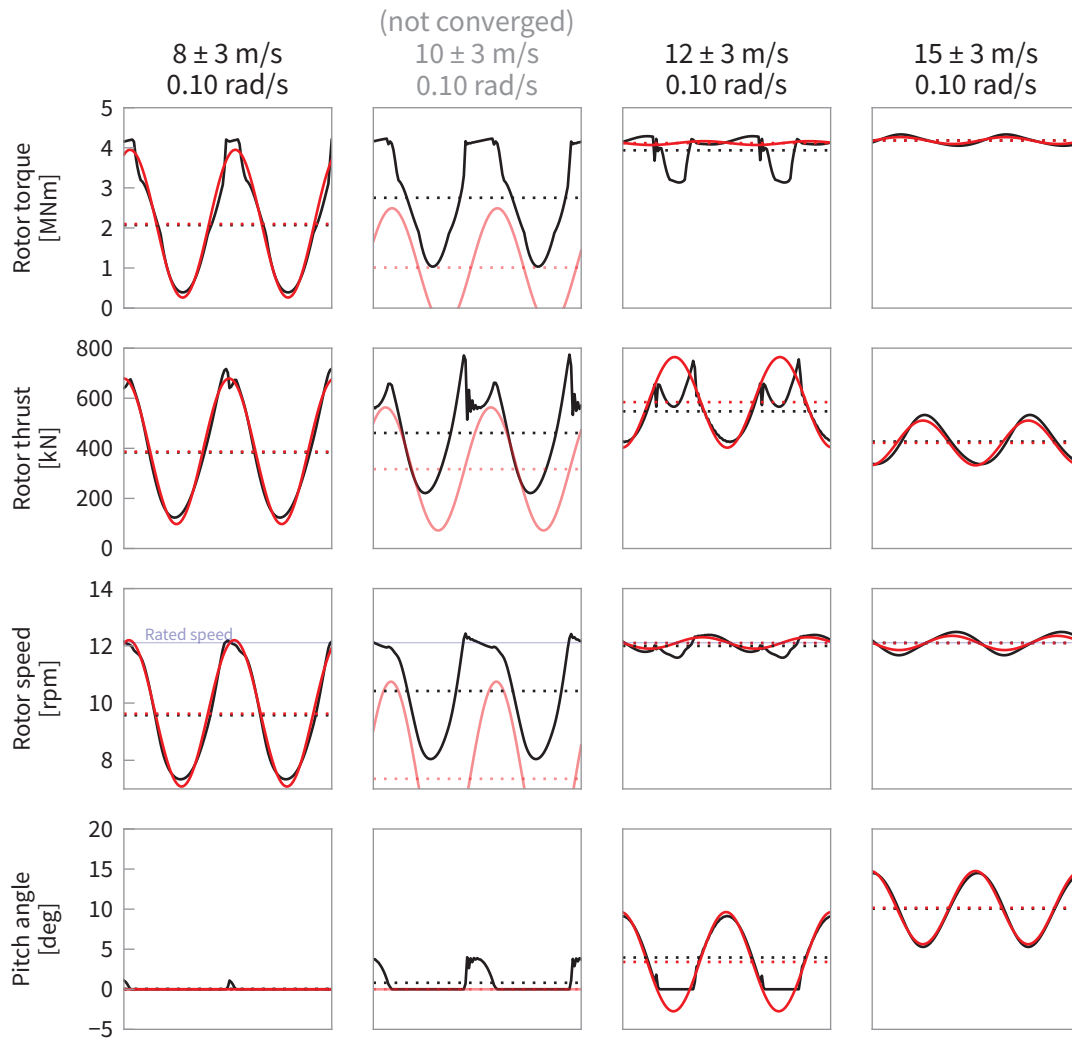


Figure 6.6 – Comparison of linearised and nonlinear results for harmonic wind speed input varying at  $0.10 \text{ rad s}^{-1}$ . Dotted lines show mean values. It was not possible to find a solution with a mean wind speed of  $10 \text{ m s}^{-1}$ ; see text for discussion.

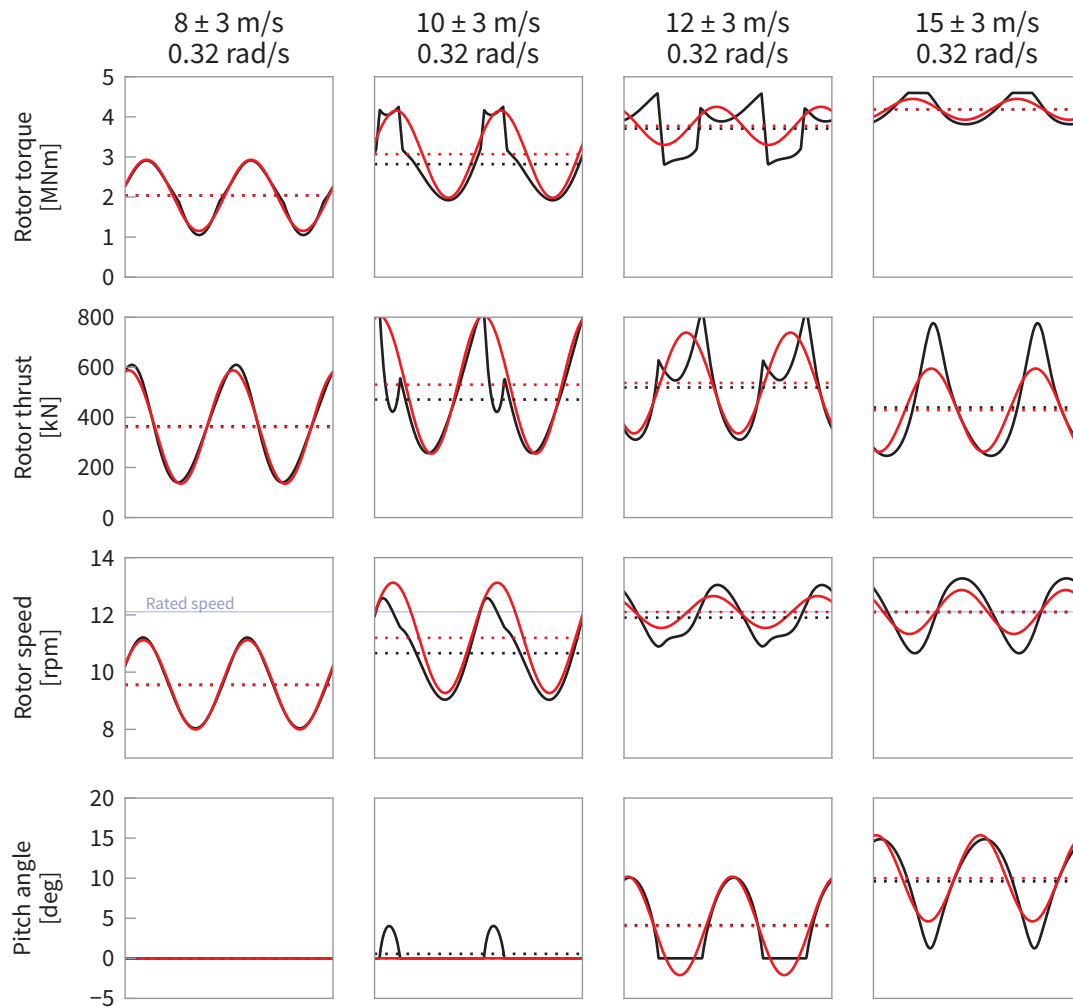


Figure 6.7 – Comparison of linearised and nonlinear results for harmonic wind speed input varying at  $0.32 \text{ rad s}^{-1}$ . Dotted lines show mean values.

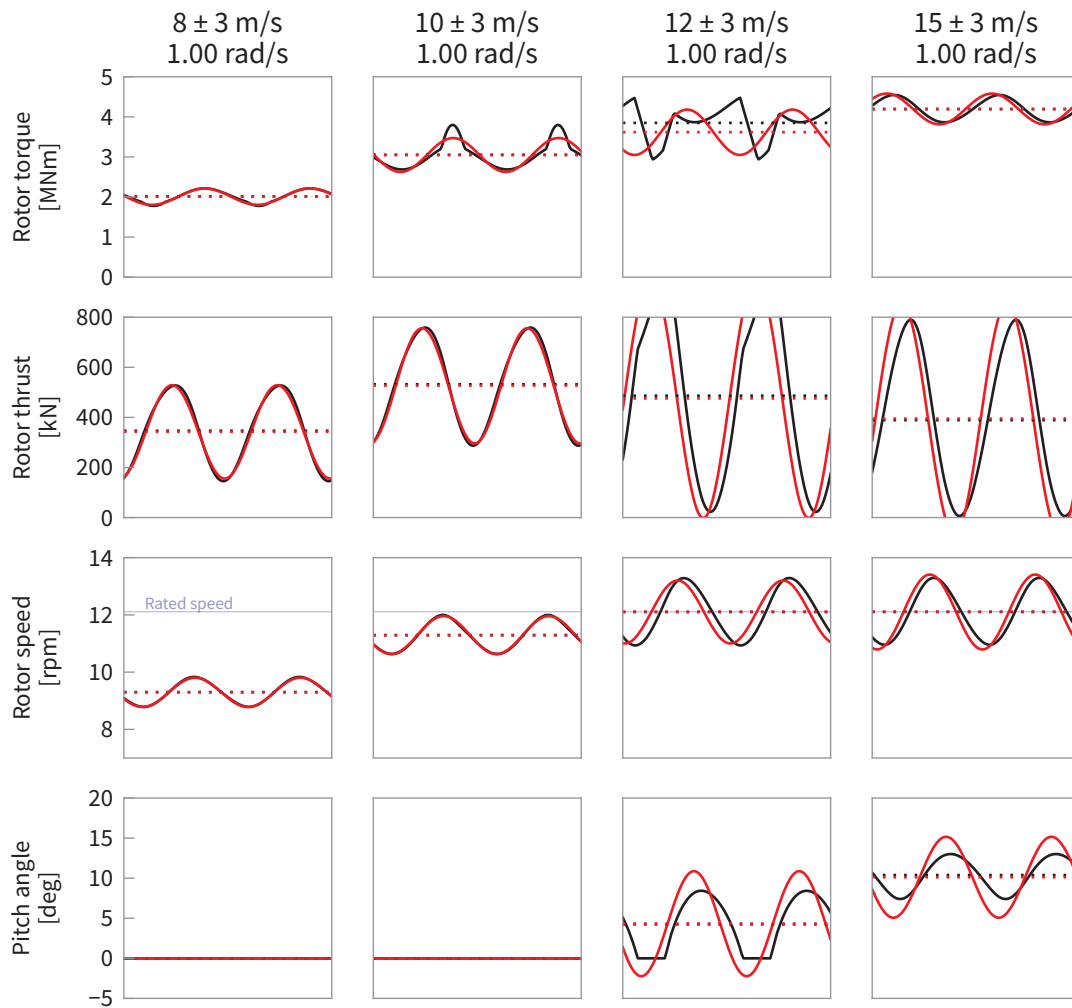


Figure 6.8 – Comparison of linearised and nonlinear results for harmonic wind speed input varying at  $1.00 \text{ rad s}^{-1}$ . Dotted lines show mean values.

Figure 6.2. The pitch angle limits also take effect close to rated, but are not captured by the present linearisation: just below rated, the blades begin to pitch for part of the cycle, and just above rated, the blades may hit the minimum-pitch limit for part of the cycle.

## 6.4 Conclusions

In this chapter, a typical wind turbine control system has been introduced. The torque and pitch controllers have been implemented in nonlinear discrete-time form, and verified against a reference implementation.

A harmonic linearisation of the generator torque and pitch angle controllers has been developed, and the results compared against time-domain simulations of the nonlinear controllers. For these results only two degrees of freedom are considered: the rotor speed and the blade pitch angle.

The linearisation is shown to perform well in conditions far from the rated wind speed of the turbine. Near the rated wind speed, the performance is less good for two reasons: firstly, both the pitch and torque controllers are active and the interactions between them are not fully captured in the present linearisation, and secondly, the underlying torque controller curve is less linear in this region. Possible improvements to the linearisation are discussed in the final chapter.

In this chapter the control system has been considered in isolation. In the next chapter, a final example is presented in which the platform response is solved together with the control system behaviour.



## Chapter 7

### *Linearised modelling of floating turbines*

In the preceding chapters, various aspects of modelling floating wind turbines in the frequency domain have been considered. The use of a linear model of the structural dynamics was found to be reasonable. The aerodynamic loading on the rotor and the control system behaviour are more obviously nonlinear, but harmonic linearisation allows the behaviour to be approximated in a linearised model. In this chapter these sub-problems are brought together to find the overall response of the floating wind turbine with a linearised model.

For this final example, the rigid-body platform motion, the tower and blade flexibility, harmonic wind loading and harmonic wave loading are included. For simplicity the wake dynamics are not included. In Chapter 5 it was found that a typical wake model was only weakly nonlinear, and the linearised model was able to represent the wake dynamics well. Therefore, neglecting the wake dynamics reduces the computational complexity by reducing the number of degrees of freedom of the model, but should not greatly affect the conclusions on the effectiveness of the linearised approach. Similarly, although in practice second-order hydrodynamic forces may be important, simulating the low-frequency second-order response in the time domain would require significant computational effort in order to provide a reference result. In this example, only linear hydrodynamic forces are considered.

Solving for the rotor speed and blade pitch angle by modelling the control system behaviour also adds significant computational effort. In Chapter 6 it was seen that although the linearised control system works well in many conditions, there are also several cases in which the present

implementation is not sufficient. Therefore first a set of results is presented which are calculated for constant rotor speed and blade pitch angle. A second set of results are then presented which include the control system behaviour for a limited set of conditions.

The results in this chapter use the commercial wind turbine simulation code *Bladed* to obtain the nonlinear reference results. This contrasts with the previous chapters, in which the performance of the linearisation was assessed in isolation by comparing the linearised results against the same underlying nonlinear model from which the linearised models were obtained. The intention here is to give more confidence in the practical performance of the linearised approaches by comparing against a recognised reference. Although significant effort has been put into verifying the present nonlinear models against *Bladed*, it should be expected that the errors presented in this chapter will be larger than previous chapters since they will include any remaining differences between the underlying models.

The target accuracy will depend on the application of the linearised analysis. Examples might include parameter optimisation studies, estimating fatigue damage over many conditions, or identifying the critical conditions to focus further simulation effort. There are many ways that accuracy could be measured, but a simple approach which is relevant for both fatigue and extreme loads is the error in the peak-peak range of a response. For the sake of argument, here the accuracy is considered to be good if the error is less than 5 %, and acceptable if under 10 %.

## 7.1 Model configuration with fixed rotor speed and blade pitch angle

Three sets of results are presented in this section: nonlinear simulations run in *Bladed*, harmonic linearisation results, and the simpler tangent linearisation results. In each case results have been found for a similar set of harmonic wind speed inputs as have been used throughout the thesis, listed in Table 7.1. In the interests of limiting computational effort,

Table 7.1 – Input parameters for simulations

Parameter	Symbol	Values
Mean wind speed	$U$	8 and 16 m s <sup>-1</sup>
Wind variation amplitude	$A$	1, 2, 3, 4 and 5 m s <sup>-1</sup>
Wind variation frequency	$\omega$	0.10, 0.32 and 1.00 rad s <sup>-1</sup>
Wave height and period	$H, T$	(1 m, 7 s), (6 m, 10 s), (25 m, 16 s)

and because the aerodynamic loads calculated by the underlying model were found to differ between Bladed and the present code at the highest frequency (Section 5.1.3 on p 147), the lowest and highest frequencies used previously are not repeated here.

The floating platform is also subject to linear wave loading. Wave periods and heights as shown in Table 7.1 were considered. The intention of including two smaller wave heights was to exercise the linearisation of the nonlinear part of the loading: since in the present model the aerodynamic loads are nonlinear while the hydrodynamic loads are linear, it might be expected that the worst case for the linearised model would be the small waves. In practice this is not always the case because it was not possible to limit the hydrodynamic loading in Bladed to a purely linear model, as described below. The large 25 m waves are included to represent an extreme sea state. The wave heights and periods were selected from the typical North Sea scatter table provided by Faltinsen (1993).

#### 7.1.1 MODEL DEFINITION

The floating wind turbine model is the same OC3-Hywind reference floating wind turbine (Jonkman 2010) as used previously (hydrodynamics: p 118; aerodynamics: p 147)

The flexible structure is modelled with five degrees of freedom: one normal mode per blade, two tower fore-aft attachment modes, and three rigid-body platform motions – surge, heave and pitch.

Regular linear waves are assumed, which are aligned with the rotor and the wind direction. The wind speed is assumed to be uniform across the whole rotor, with harmonic variations in wind speed, as in previous

simulations.

The structural system dynamics were obtained by numerical linearisation of the nonlinear multibody dynamics model of the floating wind turbine (Section 2.4). The same multibody model was previously introduced in Section 4.1.2, and is illustrated by Figure 4.1 on p 119. The linearised hydrodynamic mass, damping and stiffness matrices and the mooring stiffness were added to the structural matrices to give the complete system matrices  $M$ ,  $C$  and  $K$ . Because the rotor is rotating, the MBC transformation is applied to the blade degrees of freedom (Section 3.5).

### 7.1.2 AERODYNAMIC LOADS

The aerodynamic thrust and torque are calculated in a similar manner as described in Chapter 5. There, aeroelasticity was included by accounting for the velocity of elastic vibrations of the blade when calculating the aerodynamic loads. Now the velocity due to blade vibration is supplemented by the velocity of the blade due to platform motion. Some approximation is required here, since one of the assumptions of the BEM theory is that the air flow is uniform around each annular ring on the rotor. If the platform is pitching this will not be the case. This situation is very similar to the problem of “yawed flow” in traditional wind turbines, when the wind direction is not aligned with the rotor axis, and various enhanced wake models have been developed which allow for non-uniform flow within an annulus. However, for this study the non-uniform flow is neglected and the aerodynamic loads are calculated based on the average blade motion across the rotor. This amounts to adding the hub velocity to the elastic deformation of each blade, and results in a pure thrust and torque load on the rotor.

A more subtle problem is created by the motion of the rotor through the air as the platform pitches. In the present work, the harmonic wind speed has been defined as a function of time,  $U = A \cos \omega t$ . In Bladed, the wind speed is defined as a spatial field which moves past the rotor at the mean wind speed. As the rotor moves through this field, the wind speed measured at the rotor is no longer purely sinusoidal (Figure 7.1). Additional harmonics are therefore expected in the aerodynamic loads at

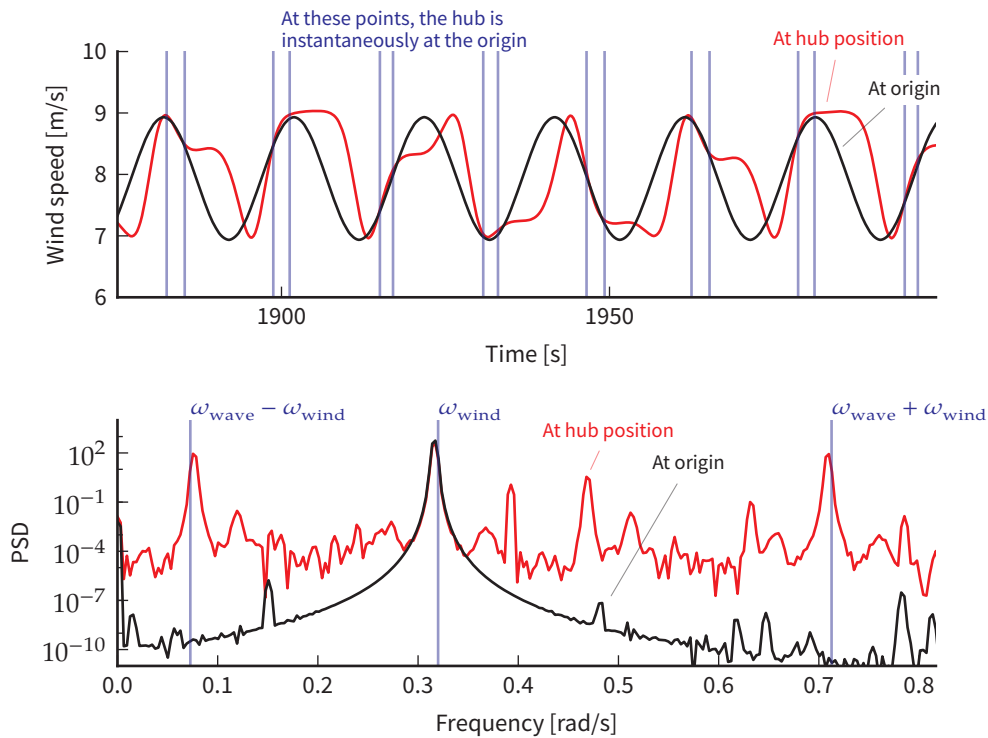


Figure 7.1 – The wind speed in Bladed is defined as a spatial field which moves past the rotor. Top: time series of wind speed measured at the fixed origin and at the rotor hub. As the platform moves, the wind speed measured at the hub is not sinusoidal. Bottom: spectrum of wind speed measurements. Additional harmonics are seen at the sum and difference of the wind and wave frequencies when measured at the moving hub position.

the sum and difference of the wind and wave frequencies, as seen in the figure.

The details of the application of the aerodynamic loads to the rotor have a significant effect on the platform heave response. Here the rotor thrust  $T$  is assumed to act perpendicular to the rotor plane. If the platform pitch angle is  $\varphi$ , there are horizontal and vertical force contributions of

$$F_x = T \cos \varphi \quad \text{and} \quad F_z = -T \sin \varphi \quad (7.1)$$

respectively. It will be seen later that the interaction between the thrust and pitch motion introduces additional harmonics into the response.

### 7.1.3 HYDRODYNAMIC LOADS

In the linearised calculation, the wave loads are applied using only the linear wave excitation coefficients (Chapter 4). Mooring loads are included as stiffness terms in the system matrices.

Since Bladed cannot yet make use of the hydrodynamic added mass, damping and wave excitation matrices (see Section 4.1), the hydrodynamic loads in Bladed are calculated using Morison's equation. This is justified for this model because the diffraction and wave radiation effects are small (Jonkman 2010). Flow separation is likely to occur in large waves over part of the spar, so strictly viscous drag forces should be included (Jonkman 2010). However, for simplicity in this example they have been neglected in both Bladed and the linearised models.

Even without the viscous drag forces, the hydrodynamic loads in Bladed are nonlinear, due to the use of Wheeler stretching to calculate the fluid velocity around the free surface (Garrad Hassan 2011). In regular waves, this introduces an additional mean surge force which is not included in the linear model.

### 7.1.4 LINEARISED HARMONIC SOLUTION

Unlike the previous examples of the harmonic linearisation approach, the floating wind turbine is now subject to both wind and wave loading at different frequencies. Rather than referring to the mean value and complex

amplitude  $q_0$  and  $\bar{q}$ , the mean value and complex amplitudes at  $\omega_1$  and  $\omega_2$  respectively are referred to as  $q_0$ ,  $q_1$  and  $q_2$ . In practical terms, the presence of multiple harmonics makes the numerical calculation of the harmonics less efficient. The harmonics of the nonlinear functions are calculated using a Fast Fourier Transform (FFT). When only the first harmonic at one frequency is required, it can be found efficiently by evaluating the nonlinear function over one period. When two harmonics are included then a finer frequency resolution is needed to capture both correctly, which corresponds to evaluating the nonlinear function over many periods in the time domain.

To find the response, the loads are projected into the generalised coordinates of the system. This can be achieved using the projection matrix  $\mathbf{R}$  defined in Section 2.4 on p 66. The system transfer function is evaluated at the three frequencies:

$$\mathbf{H}_0 = [\mathbf{K}]^{-1} \quad (7.2a)$$

$$\mathbf{H}_1 = [-\omega_1^2 \mathbf{M}(\omega_1) + i\omega_1 \mathbf{C}(\omega_1) + \mathbf{K}]^{-1} \quad (7.2b)$$

$$\mathbf{H}_2 = [-\omega_2^2 \mathbf{M}(\omega_2) + i\omega_2 \mathbf{C}(\omega_2) + \mathbf{K}]^{-1} \quad (7.2c)$$

where  $\mathbf{M}$ ,  $\mathbf{C}$  and  $\mathbf{K}$  are the total linearised system matrices, which are frequency-dependent. The harmonic response is found as

$$\mathbf{q}_j = \mathbf{H}_j \mathbf{Q}_j \quad j = 0, 1, 2 \quad (7.3)$$

where  $\mathbf{Q}_0$  are the mean generalised forces, and  $\mathbf{Q}_1$  and  $\mathbf{Q}_2$  are the components of the generalised forces at  $\omega_1$  and  $\omega_2$ .

Since the generalised forces are nonlinear functions of the response, the solution is found numerically by searching for the solutions of the nonlinear equations

$$\mathbf{0} = \mathbf{q}_j - \mathbf{H}_j \mathbf{Q}_j(\mathbf{q}_0, \mathbf{q}_1, \mathbf{q}_2) \quad j = 0, 1, 2 \quad (7.4)$$

Note that because the nonlinear force is numerically linearised, the 'stiffness' and 'damping' components of the force are not explicitly found. Compare this to the following tangent linearisation, in which the stiffness and damping components are identified.

## 7.1.5 LINEARISED TANGENT SOLUTION

To understand if the extra effort of finding the iterative harmonic linearisation solution is worthwhile, the tangent linearisation solution was also found. This is calculated in a similar way to the harmonic linearised solution: the structural model and wave loads are identical. The difference is in the linearisation of the aerodynamic loads, which are found by perturbing the wind speed and platform motion about the mean operating point.

Because here the main source of nonlinearity is the aerodynamic loading, the difference between the harmonic and the tangent linearisation is expected to be similar to the differences found in Chapter 5, where the harmonic and tangent linearisations of the aerodynamic loading were compared (see Figure 5.7 on p 158).

The solution of the tangent linearisation response is not iterative. The solution is found by solving for the mean value and the amplitudes of the two harmonics,

$$q_j = H_j \left[ Q_j^{\text{wave}} + (\mathbf{K}_U + i\omega_j \mathbf{C}_U) U_j \right] \quad j = 0, 1, 2 \quad (7.5)$$

with

$$H_0 = [\mathbf{K}]^{-1} \quad (7.6a)$$

$$H_1 = \left[ -\omega_1^2 \mathbf{M}(\omega_1) + i\omega_1 (\mathbf{C}(\omega_1) + \mathbf{C}_q) + (\mathbf{K} + \mathbf{K}_q) \right]^{-1} \quad (7.6b)$$

$$H_2 = \left[ -\omega_2^2 \mathbf{M}(\omega_2) + i\omega_2 (\mathbf{C}(\omega_2) + \mathbf{C}_q) + (\mathbf{K} + \mathbf{K}_q) \right]^{-1} \quad (7.6c)$$

Here  $\mathbf{M}$ ,  $\mathbf{C}$  and  $\mathbf{K}$  are the same system matrices which appear in Equation (7.2).  $\mathbf{C}_U$  and  $\mathbf{K}_U$  are the parts of the linearised aerodynamic force which depend on the wind speed.  $\mathbf{C}_q$  and  $\mathbf{K}_q$  are the parts of the linearised aerodynamic force which depend on the platform motion and blade vibration, thereby accounting approximately for aeroelastic effects. Unlike in the harmonic solution, these stiffness and damping matrices are identified explicitly and included in the transfer function matrices.

### 7.1.6 BLADED SIMULATIONS

Simulations in Bladed were run for 2000 s to ensure that transient platform motions have decayed.

For practical reasons, more degrees of freedom were included in the simulations than in the linearised model, but this does not affect the results: because in Bladed modes must be included in sequence, to reach the tower fore-aft rotation attachment mode, the side-side and torsion tower modes were also included. Also, it is not possible to exclude the platform sway, roll and yaw degrees of freedom, but no significant response was found in these directions.

Bladed has the capability to model individual mooring lines with non-linear characteristics, but for comparison with the linearised results, a simple linear stiffness matrix was applied at the platform origin to represent the mooring lines. Mooring line damping was applied to represent the additional linear damping defined by OC3.

## 7.2 Results with fixed rotor speed and blade pitch angle

An overall view of the nonlinear Bladed simulation results is given in Figure 7.2, which shows the peak-peak range of the platform response and tower and blade deflections. The sea state with 25 m waves gives large responses. In particular, the large maximum peak-peak blade deflections of 13 m are likely to lead to differences in blade response between the linear and nonlinear models.

Due to the number of combinations of wave period and height, mean wind speed, wind speed variation amplitude and variation frequency, detailed results from every case are not given here. The agreement between the linearised and nonlinear results is first summarised by the error in the peak-peak range for five variables: the platform surge, heave and pitch, the tower translational deflection, and the blade tip deflection. The peak-peak error is a simple measurement, but is relevant whether extreme or fatigue loads are of interest. Because the structural model is linear, the error in the deflections is also indicative of the error in the structural bending moments

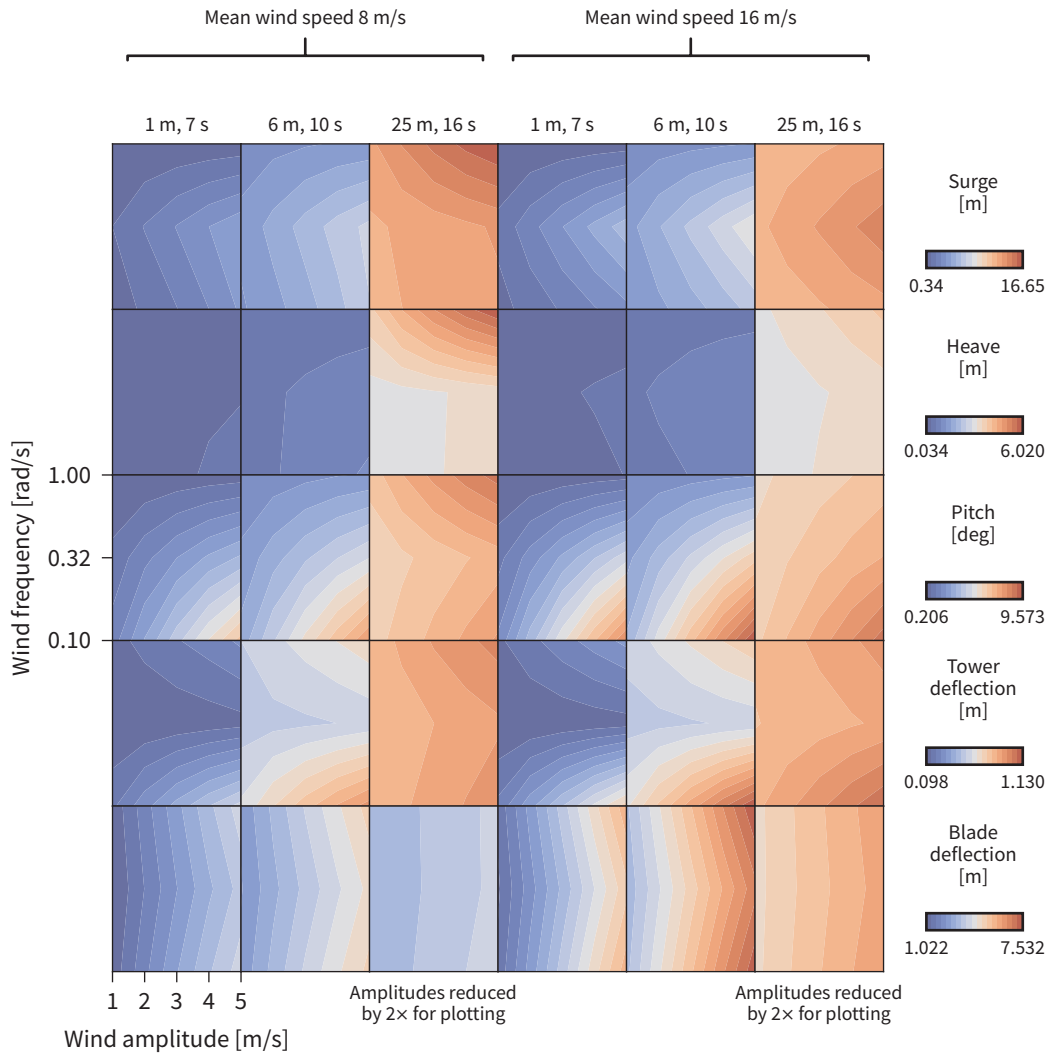


Figure 7.2 – Peak-peak range of nonlinear Bladed simulation results. Each row shows one response, with the peak-peak range shown by the colour bar at the right. The columns show different sea states and mean wind speeds. Each small contour plot shows the response for different amplitudes and frequencies of variation in the wind speed. Note that since the responses for 25 m waves are much larger, they are plotted at a smaller scale.

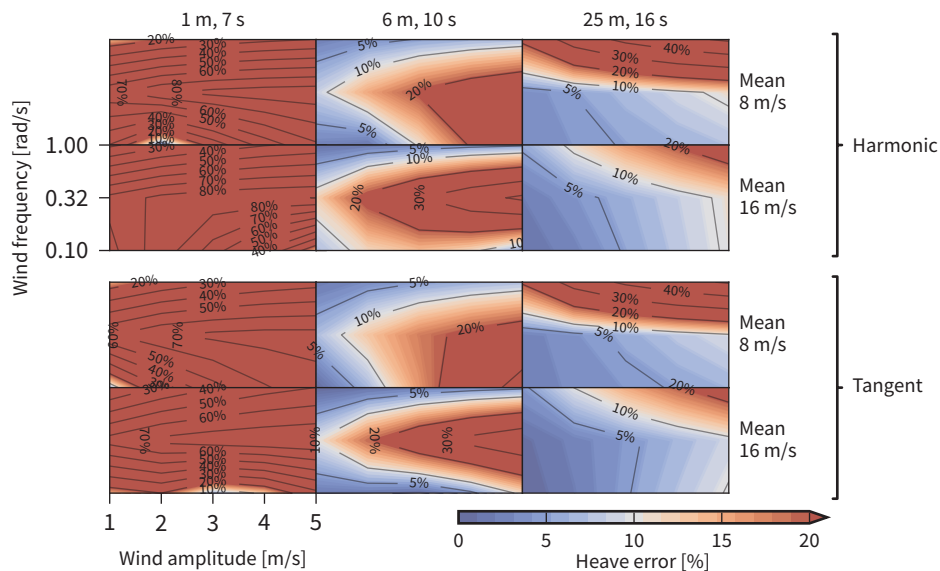


Figure 7.3 – Normalised peak-peak error between nonlinear (Bladed) and harmonic solutions in heave response.

and forces. Detailed results for selected cases are given subsequently.

The peak-peak error, normalised by the peak-peak amplitude of the nonlinear Bladed results, is plotted for the full range of conditions in Figures 7.3, 7.7, 7.8, 7.10 and 7.12. Each figure contains 12 contour plots, each showing the dependence of the error on the amplitude and frequency of the wind speed variations. The contour plots are arranged into columns corresponding to the three sea states, and rows corresponding to the two mean wind speeds. The results for both the harmonic and tangent linearisations are given in each figure. For ease of comparison, a consistent colour scale is used in each figure showing errors from 0% to 20%. Larger errors are shown by additional contour lines. Each response will now be discussed in turn, starting with the heave response.

The heave response (Figure 7.3) shows very large relative errors. In some cases this is due to the small peak-peak range of the reference nonlinear heave motion used to calculate the relative error (1 m and 6 m waves, at the higher two frequencies; see Figure 7.2). In other cases the error is significant, such as the case with 1 m waves and wind at  $0.1 \text{ rad s}^{-1}$ ; the responses for this case are shown in detail in Figure 7.4. The reason for the heave error is the vertical component of the aerodynamic thrust which

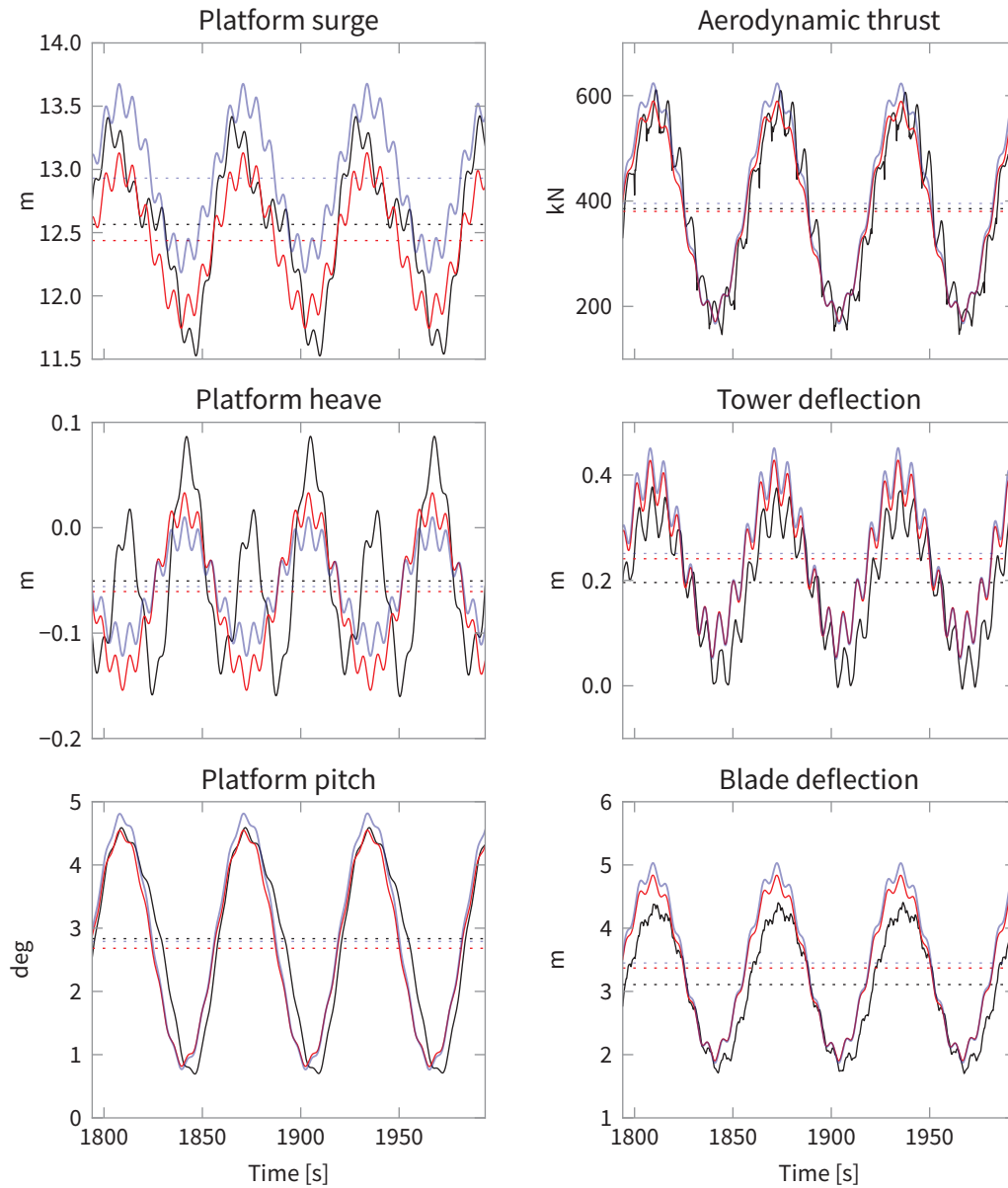


Figure 7.4 – Response with 1 m, 7 s waves, wind speed  $8 \pm 3 \text{ m s}^{-1}$  at  $0.1 \text{ rad s}^{-1}$ . Black: nonlinear (Bladed); red: harmonic; blue: tangent. The low-frequency variation is at  $\omega_{\text{wind}}$  and the high-frequency oscillation is at  $\omega_{\text{wave}}$ . The heave motion occurs at  $2\omega_{\text{wind}}$ , which is not captured by the linearised models (see text and Figure 7.5). The surge motion occurs mostly at  $\omega_{\text{wind}}$ , but the linearised results are missing a component at  $2\omega_{\text{wind}}$  (see text and Figure 7.9).

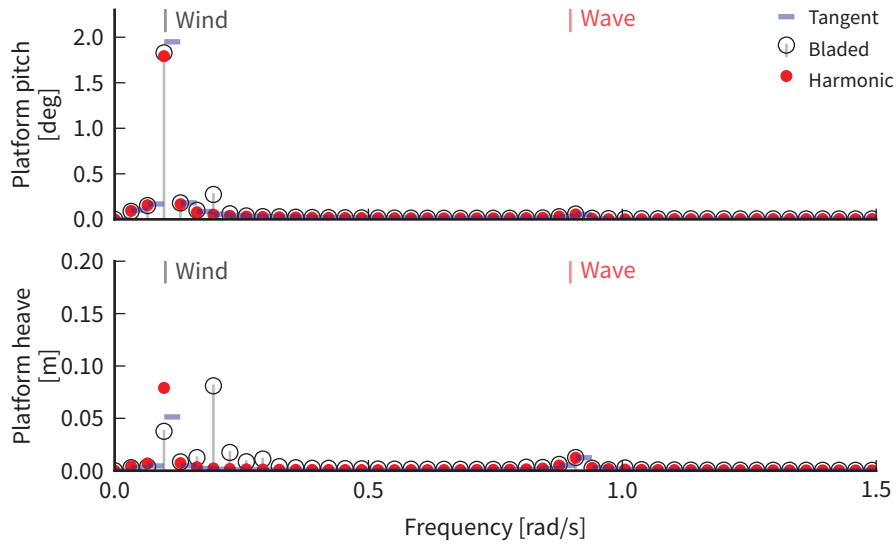


Figure 7.5 – Spectrum of heave response with 1 m, 7 s waves, wind speed  $8\pm 3 \text{ m s}^{-1}$  at  $0.1 \text{ rad s}^{-1}$ . The platform pitching motion at the wind frequency combines with the aerodynamic thrust to produce a heave motion at twice the wind frequency, which is not included in the linearised models.

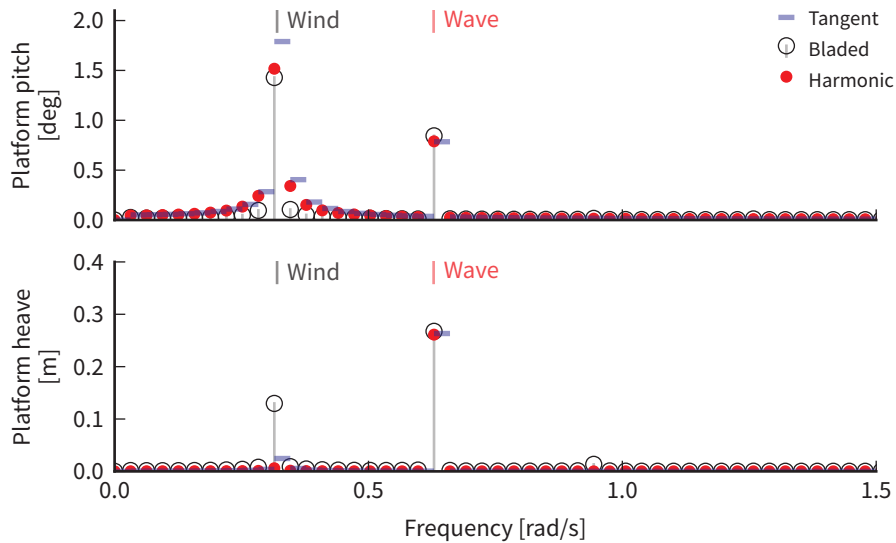


Figure 7.6 – Spectrum of heave response with 6 m, 10 s waves, wind speed  $8\pm 5 \text{ m s}^{-1}$  at  $0.32 \text{ rad s}^{-1}$ . The missing harmonic is at  $\omega_{\text{wave}} - \omega_{\text{wind}}$ ; by coincidence, the difference is close to the wind frequency.

varies as the platform rotates: from Equation (7.1), the vertical force has components at the sum and difference of the wind and pitching frequencies. Since the pitching motion in this case is mostly occurring at the wind frequency, the wind-induced heave motion occurs at twice the wind frequency (Figure 7.5). It is not possible to represent this motion with the two available components of the harmonic solution<sup>1</sup>.

In the larger waves (6 m and 25 m), the error is reduced because the heave response is caused to a greater extent by the linear wave excitation. As the wind variation increases the error increases because the nonlinear excitation discussed above again becomes important. For example, Figure 7.6 shows the spectrum of the platform pitch and heave responses with 6 m waves and a wind frequency of  $0.32 \text{ rad s}^{-1}$ . Although it appears that a component at the wind frequency is missing in the linearised results, in fact the missing harmonic is at  $\omega_{\text{wave}} - \omega_{\text{wind}}$ ; by coincidence, the difference frequency is close to the wind frequency for this case. The large errors in the remaining cases in Figure 7.3 are likewise caused by missing harmonics in the linearised response.

The errors in the surge and pitch responses are shown in Figures 7.7 and 7.8. The behaviour of these two responses is broadly similar. Good accuracy is achieved for small variations in wind speed, with increasing peak-peak error for larger variations. Slightly better accuracy is achieved with the mean wind speed of  $16 \text{ m s}^{-1}$ ; this is the same result seen in Chapter 5, where it was attributed to the weaker nonlinearity in the aerodynamic forces.

One case with a large error in surge is 1 m waves with a wind frequency of  $0.1 \text{ rad s}^{-1}$ . This is the case which was shown in Figure 7.4 on the previous page. Here the main component of the surge response at  $\omega_{\text{wind}}$  is approximately correct. An additional component at  $2\omega_{\text{wind}}$ , which causes the larger dips in the nonlinear response, is missing from the linearised results. This is shown more clearly by the spectrum in Figure 7.9. Errors in the surge and pitch responses for the remaining conditions are due similarly to additional harmonics missing from the linearised results.

Although the mean value of the nonlinear surge response in Figure 7.4

1. It is not included in the harmonic solution *as currently implemented*, but it would be possible to extend the solution to include this harmonic; this will be discussed later.

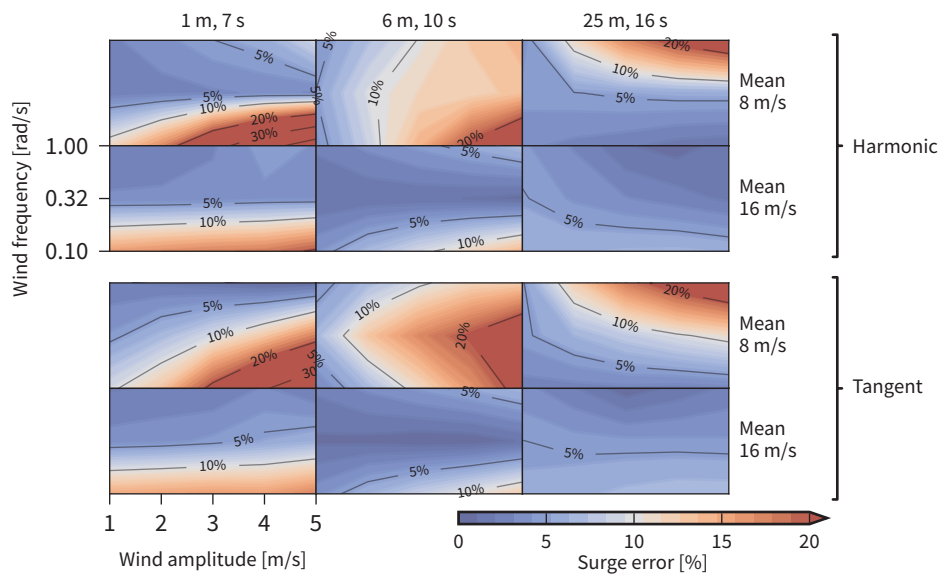


Figure 7.7 – Normalised peak-peak error between nonlinear (Bladed) and harmonic solutions in surge response.

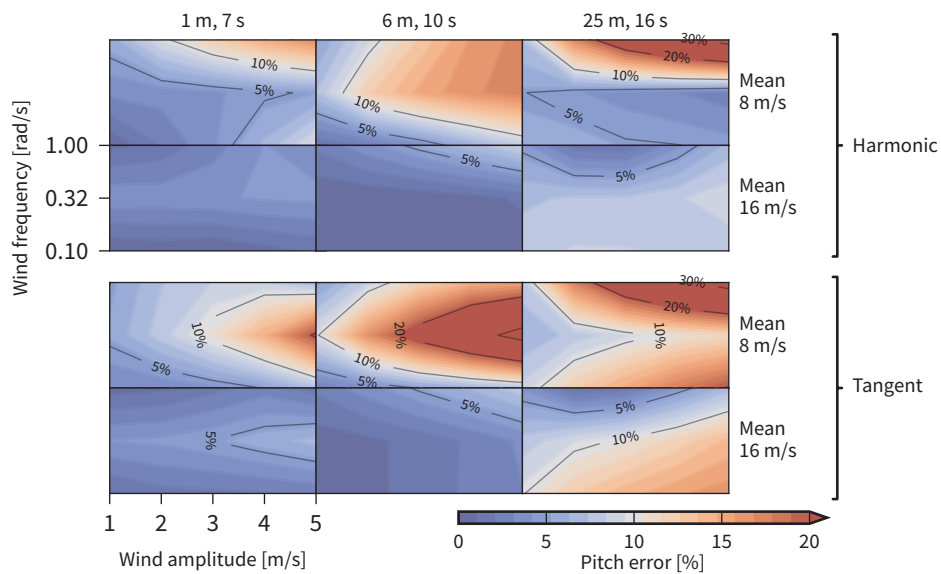


Figure 7.8 – Normalised peak-peak error between nonlinear (Bladed) and harmonic solutions in pitch response.

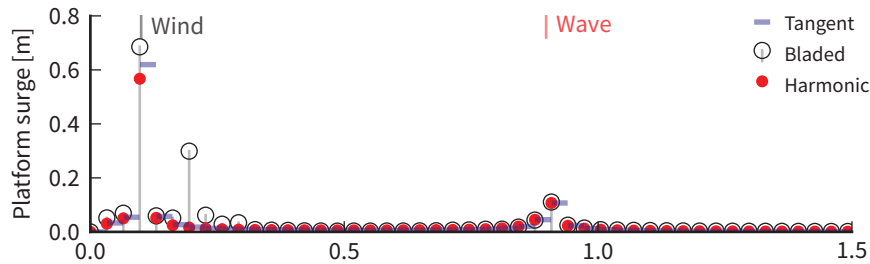


Figure 7.9 – Spectrum of surge response with 1 m, 7 s waves, wind speed  $8\pm 3 \text{ m s}^{-1}$  at  $0.1 \text{ rad s}^{-1}$ . The nonlinear response contains a significant harmonic at  $2\omega_{\text{wind}}$  which is not included in the linear response.

agrees well with the harmonic linearisation results, the tangent linearisation has a mean value about 4 % higher. This is due to the aerodynamic thrust, and the same difference can be seen in the plot of thrust in Figure 7.4. The reason is the better representation of aerodynamic stall in the harmonic linearisation, as seen previously in Figure 5.7 on p 158.

The error in the tower deflection response (Figure 7.10) is mostly acceptable. With 1 m waves, the relative error is greater than 10 %, but the response is also small here. The larger error with 25 m waves is due to additional low-frequency aerodynamic loading in the nonlinear results (Figure 7.11). The amplitudes of the harmonics which are present in the linearised results agree well.

The blade deflection error is shown in Figure 7.12. As discussed in Section 7.1.2 on p 188, the linearised solutions provide the average response over the three blades. In the nonlinear simulation, the response is different between the three blades, due to the varying relative wind speed across the rotor. In the results presented here, the nonlinear blade responses are averaged for comparison with the linearised results.

The error is acceptable for the smaller waves and smaller variations in wind speed, but exceeds 20 % for the 25 m waves. Example results for this case are shown in Figures 7.13 and 7.14, for amplitudes of  $1 \text{ m s}^{-1}$  and  $5 \text{ m s}^{-1}$  respectively. In the first case, there is an error in the amplitude of the blade deflection variations, but the general behaviour is in agreement. As seen before, the harmonic linearisation is better than the tangent linearisation for the aerodynamic thrust and blade deflection, which is due to the better representation of the nonlinear aerodynamic forces. In the second case, for

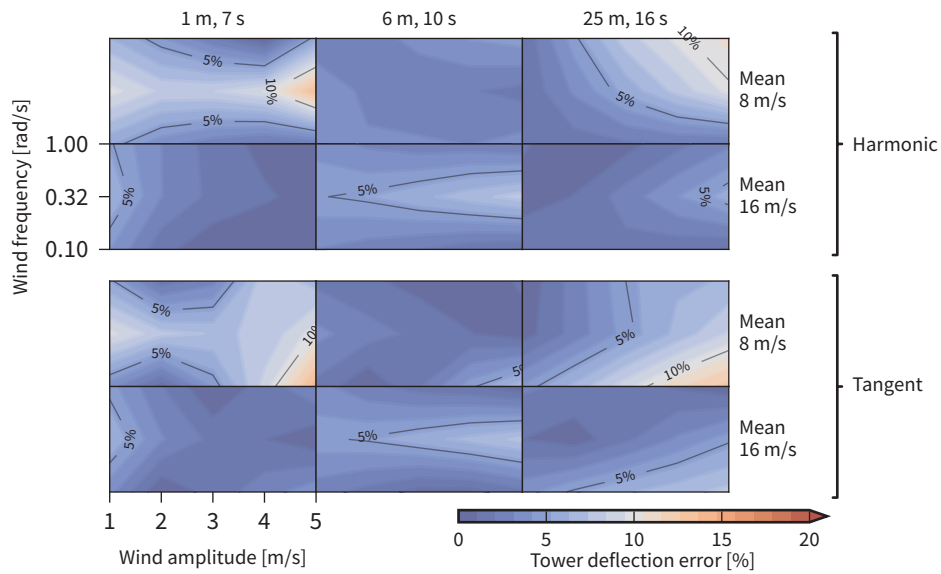


Figure 7.10 – Normalised peak-peak error between nonlinear (Bladed) and harmonic solutions in tower deflection response.

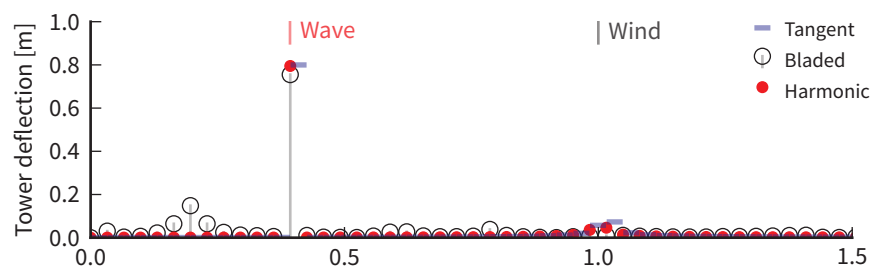


Figure 7.11 – Spectrum of tower deflection response with 25 m, 16 s waves, wind speed  $8\pm 5 \text{ m s}^{-1}$  at  $1.0 \text{ rad s}^{-1}$ . The nonlinear response contains additional low-frequency harmonics which cause the error in the linearised response.

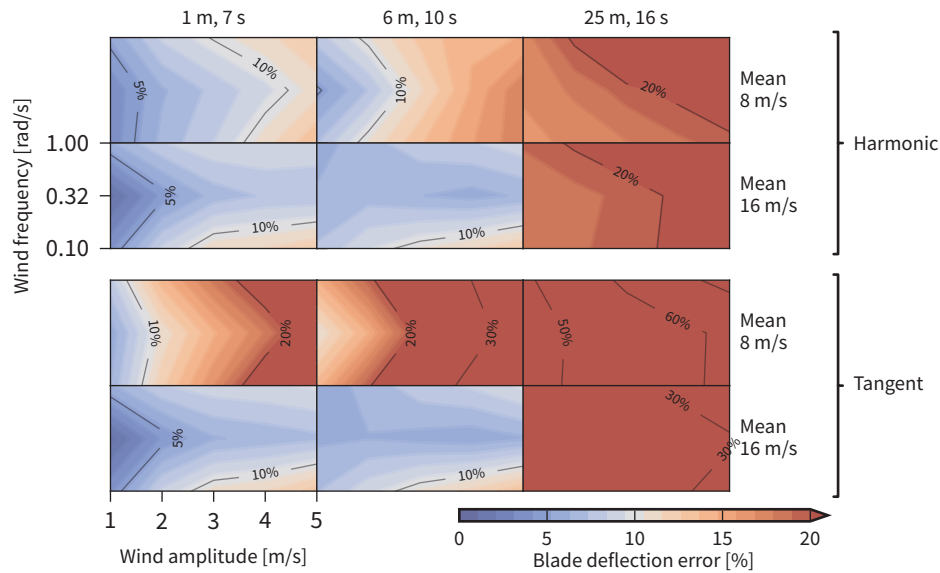


Figure 7.12 – Normalised peak-peak error between nonlinear (Bladed) and harmonic solutions in blade deflection response.

wind speed variations of  $5 \text{ m s}^{-1}$ , the agreement is worse and additional harmonics are present.

This can be seen more clearly in the spectrum, which is shown in Figure 7.15 for the same cases. For the smaller variations in wind speed, the correct harmonics are included but the amplitudes do not exactly match. Note that the harmonic linearisation gives much better results than the tangent linearisation in this case, due to the better representation of the nonlinear aerodynamic forces. The error can be traced directly to the aerodynamic thrust, which is also shown in Figure 7.15. At larger amplitudes, the component of the thrust at the difference frequency  $\omega_{\text{wave}} - \omega_{\text{wind}}$  is increased. This component is due to the fact that Bladed is using a spatial wind field, as shown in Figure 7.1.

### 7.2.1 COMPARISON OF TANGENT AND HARMONIC LINEARISATIONS

Comparing the two linearisation techniques gives mixed results. Figure 7.16 plots the ratio of the tangent and harmonic errors for each mean wind speed and sea state.

Most often the harmonics linearisation gives a lower peak-peak error

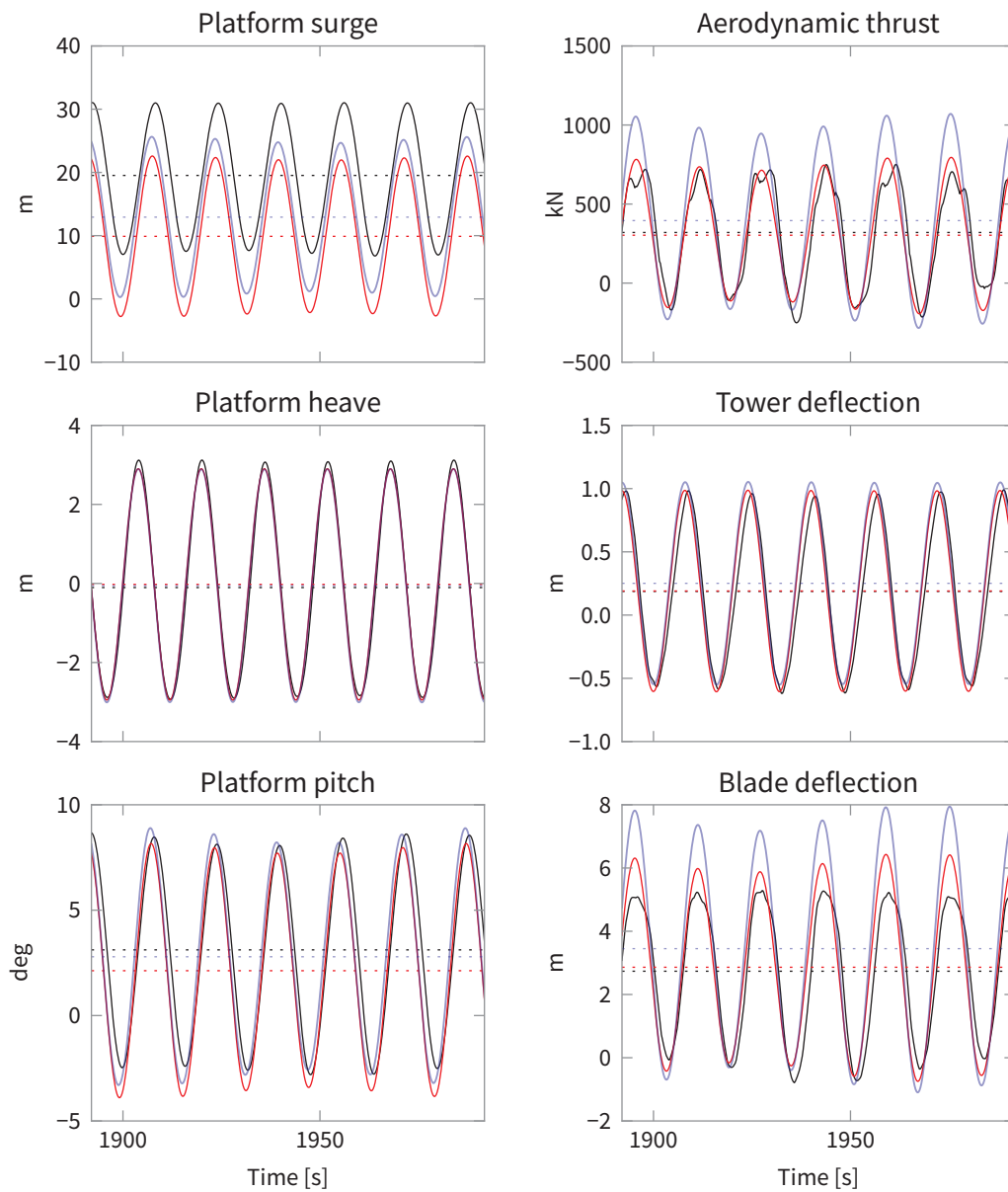


Figure 7.13 – Response with 25 m, 16 s waves, wind speed  $8 \pm 1 \text{ m s}^{-1}$  at  $0.32 \text{ rad s}^{-1}$ . Black: nonlinear (Bladed); red: harmonic; blue: tangent. Dotted lines show the mean value. The difference between the mean values of the nonlinear and linearised results is greater here than in previous examples; the nonlinear wave loading in Bladed has a greater effect in large waves (see p 190).

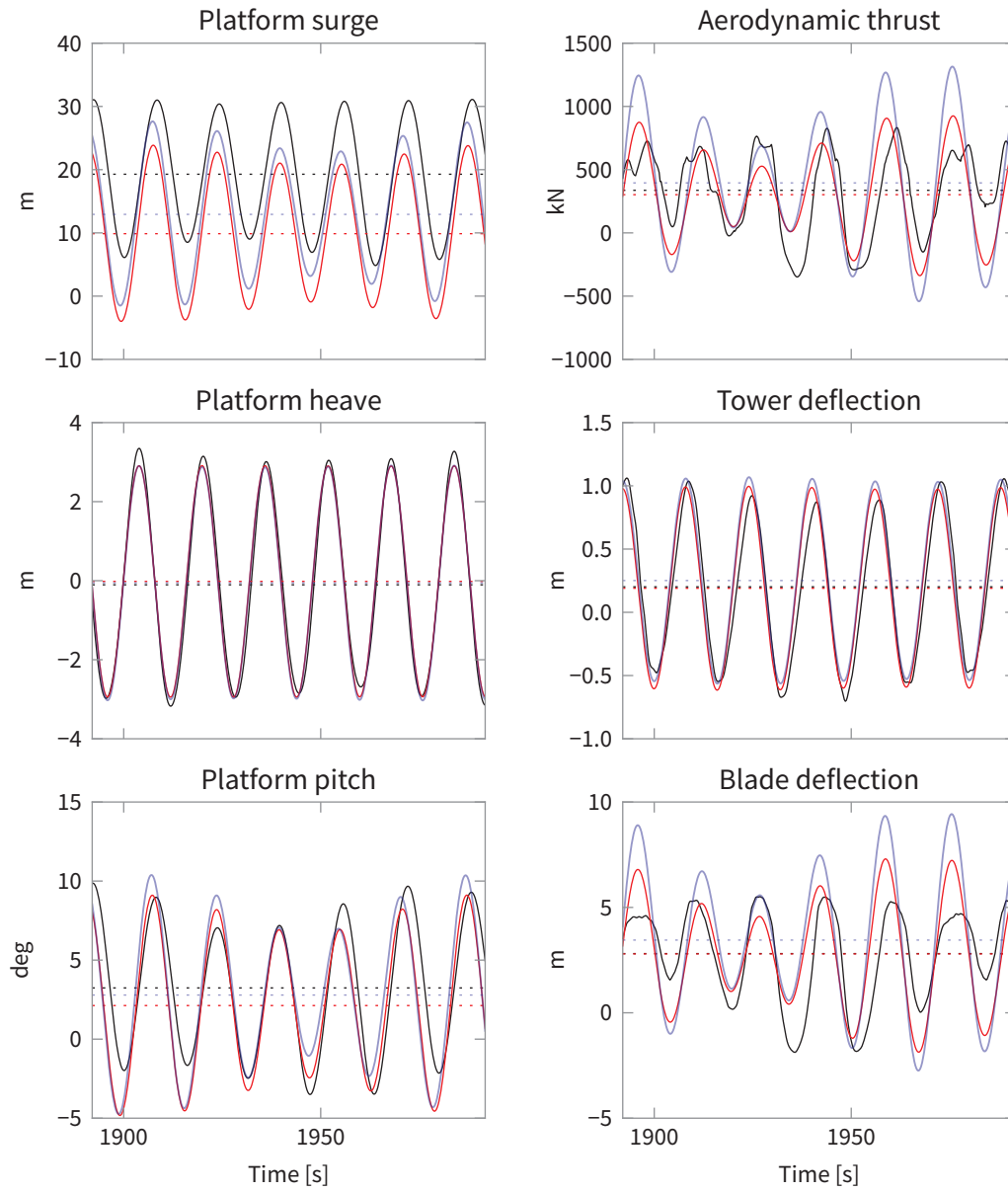


Figure 7.14 – Detailed results: same as previous figure but for larger variations in wind speed of  $8 \pm 5 \text{ m s}^{-1}$ .

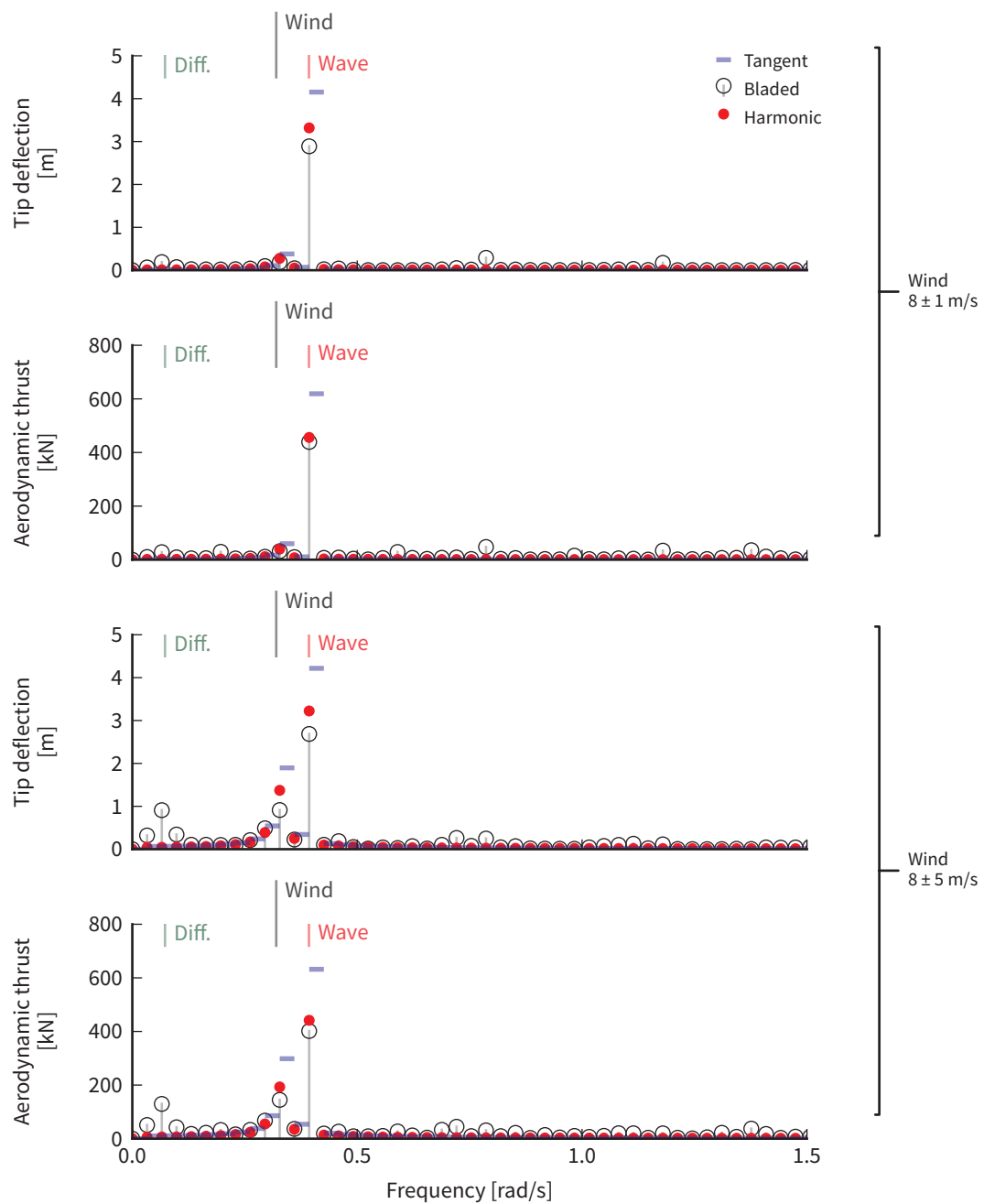


Figure 7.15 – Top two plots: spectrum of blade deflection response and aerodynamic thrust with 25 m, 16 s waves, wind speed  $8 \pm 1 \text{ m s}^{-1}$  at  $0.32 \text{ rad s}^{-1}$ . Bottom two plots: as above but for  $8 \pm 5 \text{ m s}^{-1}$  wind. For small variations in wind speed (top) the error is due to the amplitude of the linearised response. When the wind speed variations are large (bottom), there is also some nonlinear response at  $\omega_{\text{wave}} - \omega_{\text{wind}}$ . The blade deflection is closely linked to the thrust.

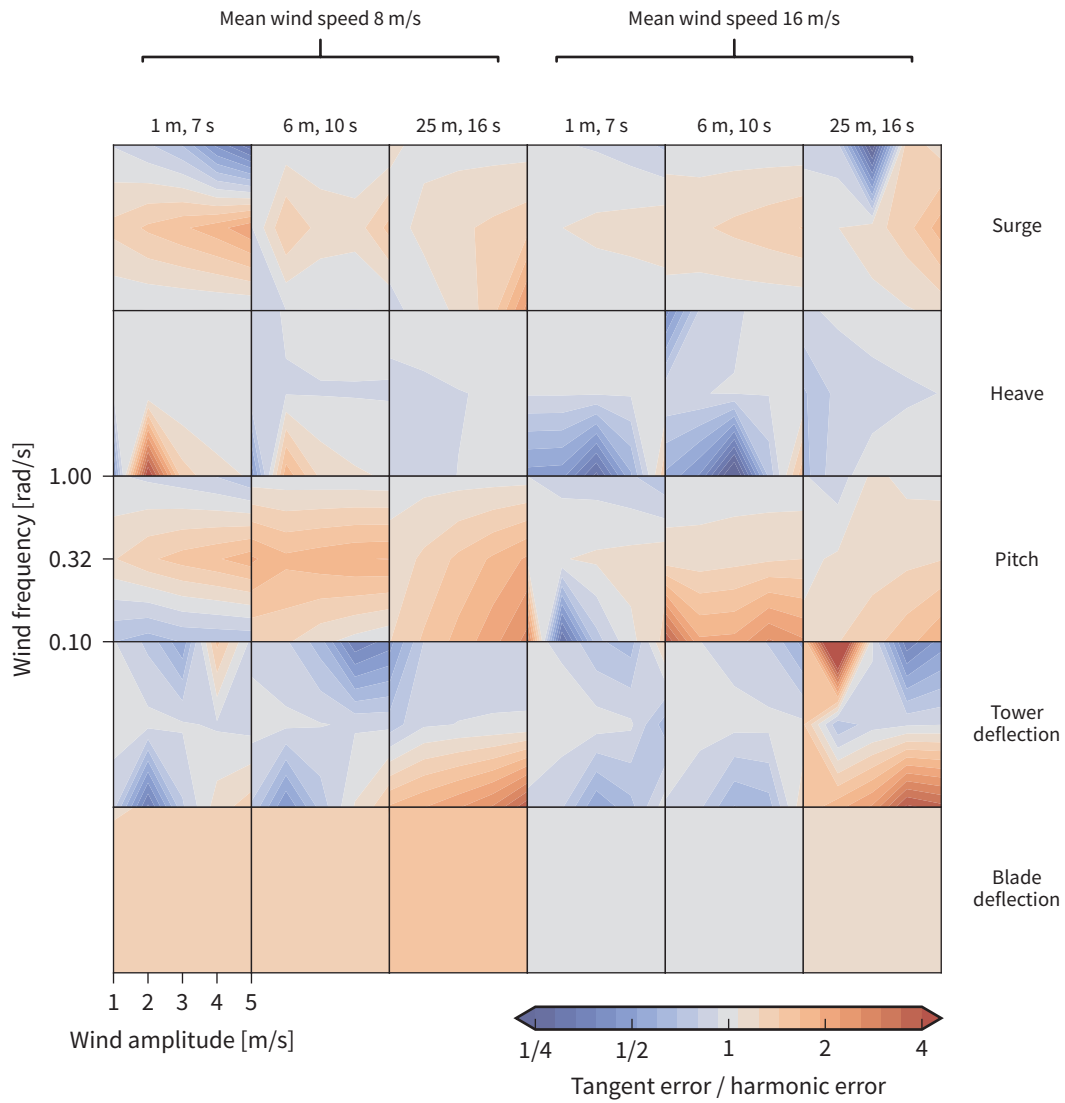


Figure 7.16 – Error in tangent linearisation compared to harmonic linearisation. Each column relates to particular mean wind speed and sea state. Each subplot has the same axes as the error plots in Figures 7.7–7.12 above.

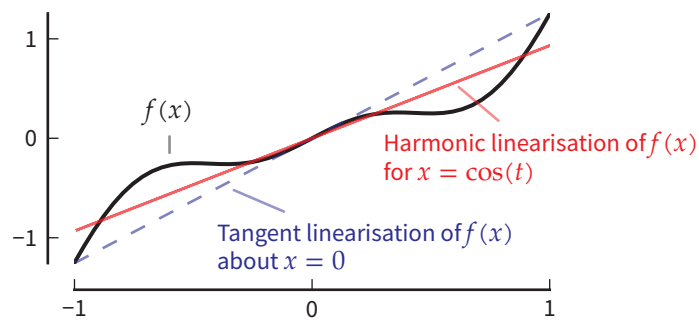


Figure 7.17 – A contrived example to show that while the harmonic linearisation minimises the mean-squared error, it does not necessarily minimise the peak-peak error.

than the tangent linearisation. The gains are most consistent in the blade deflection, which is consistent with the better performance of the harmonic linearisation seen in Chapter 5 when dealing with the aerodynamic forces. The surge and pitch responses also benefit from the harmonic linearisation, although there are some cases where the tangent linearisation error is smaller. On the other hand, the tower deflection error is generally slightly better with the tangent rather than harmonic linearisation, but the errors are relatively small in these cases. The heave response error is mostly unaffected by the linearisation method; this is because the heave error is due to effects which apply to both methods, as discussed above.

Given that the harmonic linearisation approach is based on the minimisation of the mean-squared error between the nonlinear and linear functions, it may seem strange that in some cases the tangent linearisation gives a smaller error. This is because the results in this chapter (including Figure 7.16) are based on the peak-peak error, and minimising the mean-squared error does not necessarily minimise the peak-peak error. Figure 7.17 presents a contrived example which demonstrates this. However, when the tangent linearisation gives a lower peak-peak error it is only through good luck, and the harmonic linearisation should be more robust in the face of a variable level of nonlinearity.

Although the harmonic linearisation method has clear advantages in some situations, whether its complexity is worthwhile over the tangent linearisation depends on the relative computational expense, which is presented below.

## 7.3 Solution including control system behaviour

Now the control system is reintroduced into the simulations. Selected results are given for one set of wave conditions ( $T = 10$  s,  $H = 6$  m) and for harmonic wind with a frequency of  $\omega = 0.32$  rad s<sup>-1</sup> only. Again, the harmonic linearisation will be compared to the nonlinear Bladed simulation results. It is not possible to extend the tangent linearisation results from the previous section to include the control system, since by definition the tangent linearisation is evaluated at the mean rotor speed and mean pitch angle.

### 7.3.1 BLADED SIMULATIONS

The only change from the Bladed simulations described in Section 7.1.6 is that the controller is enabled. In Chapter 6 the standard controller defined for the NREL 5 MW turbine was used (Jonkman, Butterfield, et al. 2009), but when this turbine is mounted on a floating platform it has been found to be unstable and to develop platform-pitch limit cycle oscillations. A modified version of the controller has been developed for the OC3 project (Jonkman 2010). The modified version has lower gains in the pitch controller and does not use constant-power torque control above rated, which avoids the instability.

### 7.3.2 LINEARISED HARMONIC SOLUTION

In the linearised model, harmonic solutions are sought for the rotor speed and pitch angle, in addition to solutions for the three platform motions, two tower modes and one blade mode found previously. All the harmonic solutions consist of a mean value and the two complex amplitudes at the wind and at the wave forcing frequencies, denoted by the subscripts 0, 1 and 2 respectively.

The solution is found by combining the nonlinear equations for the platform response from Section 7.1.4 with the nonlinear equations for the

rotor speed and pitch angle from Section 6.2:

$$0 = (Q_a)_0 - G(Q_g)_0 \quad (7.7a)$$

$$(\Omega)_1 = [(Q_a)_1 - G(Q_g)_1] / Ji\omega_1 \quad (7.7b)$$

$$(\Omega)_2 = [(Q_a)_2 - G(Q_g)_2] / Ji\omega_2 \quad (7.7c)$$

and

$$0 = (\Omega_g)_0 - \Omega_{\text{rated}} \quad (7.8a)$$

$$(I_\varepsilon)_1 = [(\Omega_g)_1] / i\omega_1 \quad (7.8b)$$

$$(I_\varepsilon)_2 = [(\Omega_g)_2] / i\omega_2 \quad (7.8c)$$

where  $Q_a$  and  $Q_g$  are the aerodynamic torque and the generator torque,  $J$  is the rotor inertia,  $\Omega$  is the rotor speed, and  $\Omega_g$  is the filtered generator speed signal defined on p 174.

Below the rated wind speed, when the pitch controller is not active, Equations (7.4) and Equations (7.7) are solved simultaneously. Above the rated wind speed, Equations (7.8) are solved in addition.

The same modifications which were applied to the controller in Bladed to avoid instability were also applied to the underlying nonlinear controller used to obtain the linearised harmonic solution.

### 7.3.3 RESULTS

Figures 7.18–7.19 compare the linearised and the nonlinear results for two different mean wind speeds. The previous results from Section 7.2 are also shown by the faint lines. In the first case, for mean wind speed  $8 \text{ m s}^{-1}$ , the presence of the controller increases the variation in the aerodynamic thrust. In the second case, for mean wind speed  $16 \text{ m s}^{-1}$ , the controller acts to reduce the variations in thrust. This can also be seen in the spectrum (Figure 7.20). The change in aerodynamic thrust carries through to similar changes in the blade deflection and platform surge responses.

The mean values of the platform responses have also changed; this is because the mean blade pitch angle with the controller active differs from the nominal constant pitch angle used previously.

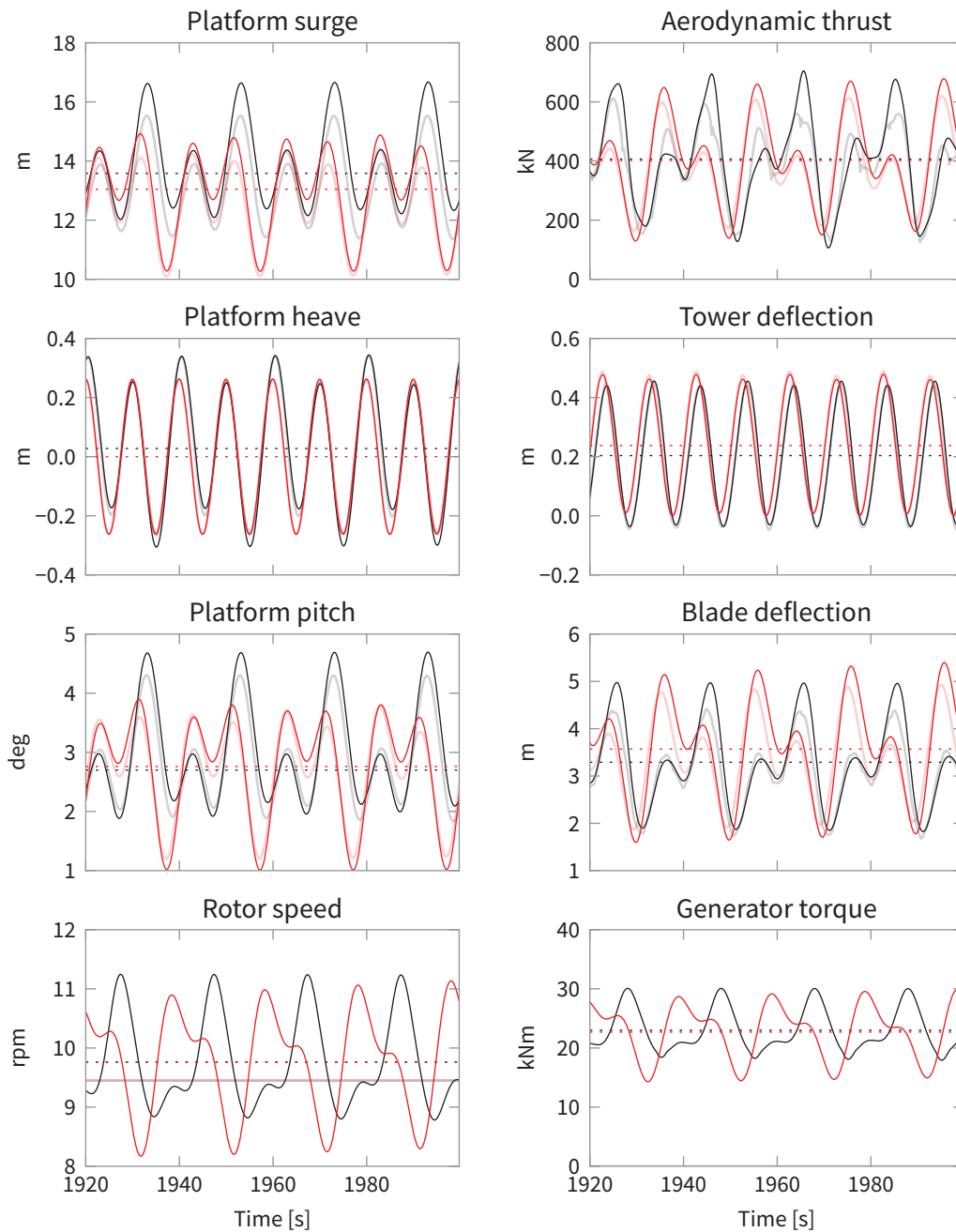


Figure 7.18 – Results including control system behaviour for mean wind speed  $8 \text{ m s}^{-1}$ . The wave height and period are 6 m and 10 s, and the wind speed varies by  $2 \text{ m s}^{-1}$   $0.32 \text{ rad s}^{-1}$ . The dotted lines show the mean value. The faint lines show the previous non-control results. Black: nonlinear (Bladed) results. Red: harmonic linearisation.

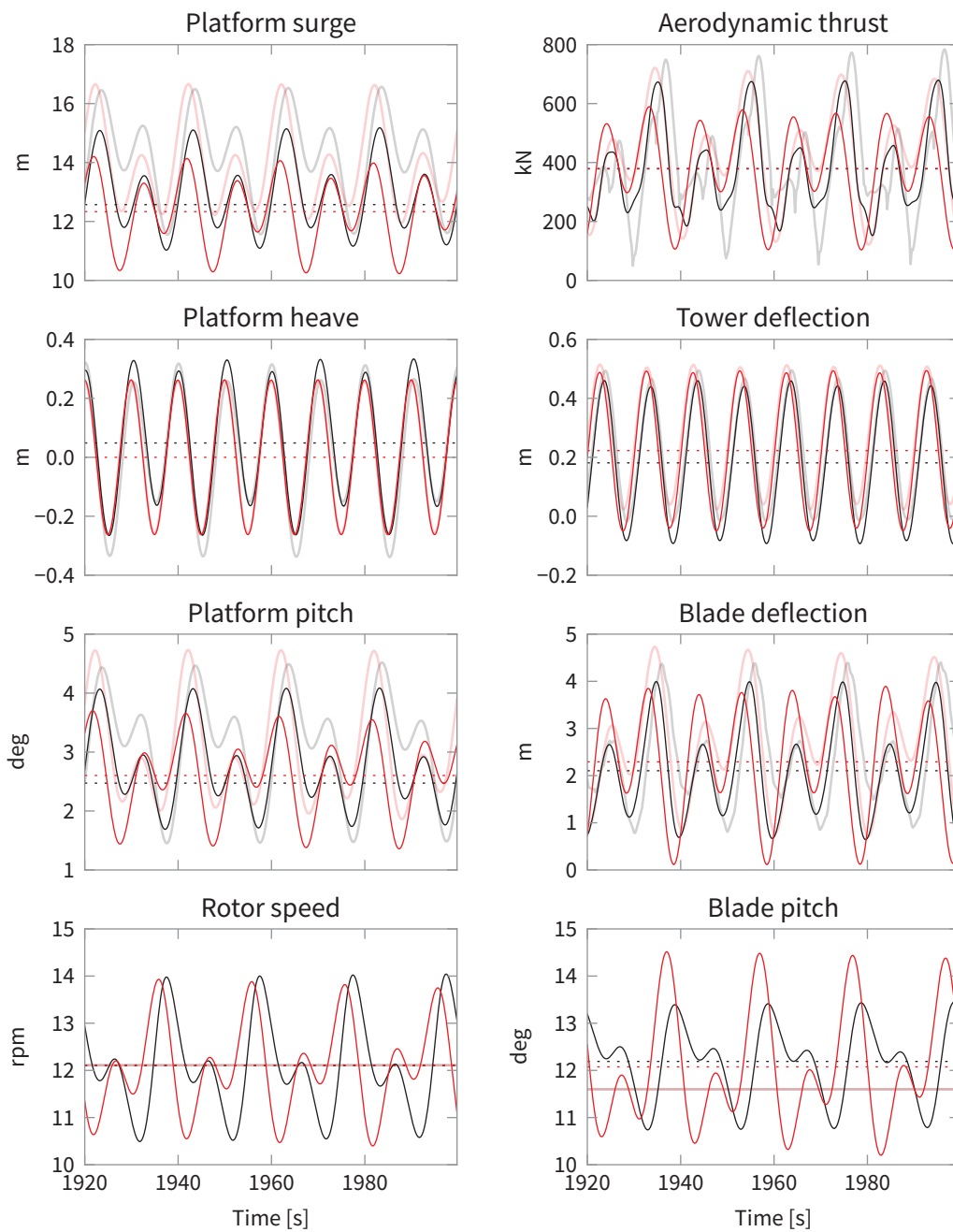


Figure 7.19 – Results including control system behaviour for mean wind speed  $16 \text{ m s}^{-1}$ . See previous caption for details.

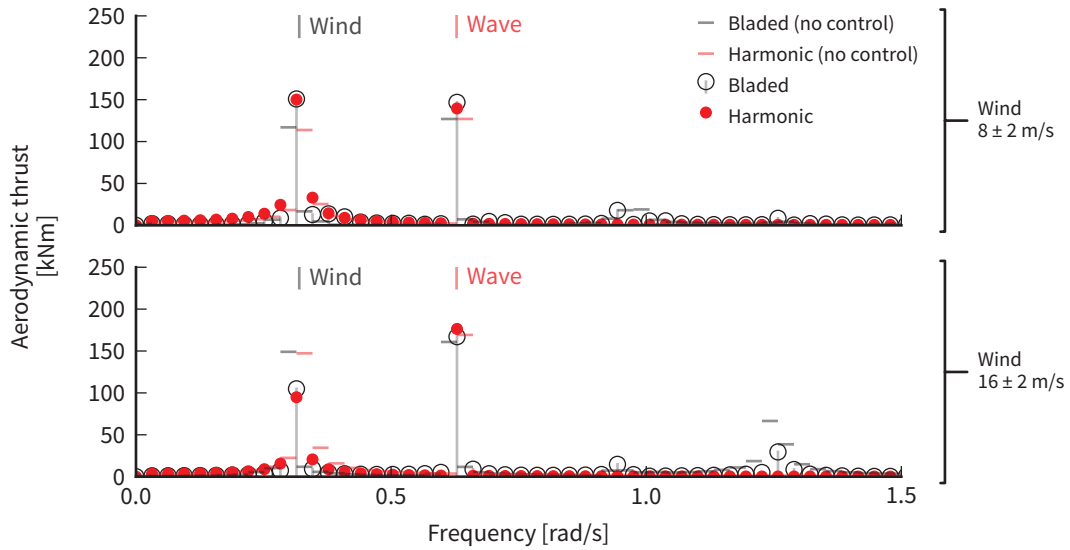


Figure 7.20 – Spectrum of aerodynamic thrust with control system, at two mean wind speeds. At  $8 \text{ m s}^{-1}$ , adding the control system increases the thrust variation, while at  $16 \text{ m s}^{-1}$  the variation is reduced. These changes are also seen in the linearised results.

Figure 7.21 shows the peak-peak error between the harmonic linearisation and the nonlinear Bladed simulations for the remaining cases which have been run with the control system active. Generally by adding the control system the errors have increased by up to 15%. Part of this change is due to the change in the nonlinear response described above, which tends to increase the relative error for the mean wind speed of  $16 \text{ m s}^{-1}$ , and tends to decrease the error for the mean of  $8 \text{ m s}^{-1}$ . Although the error in the control variables is large, especially the blade pitch angle, this does not carry through into equally large errors in the overall response. Suggestions are made later on how the pitch controller would be improved.

Overall, the change in response due to adding the control system is large compared to the errors, and the linearised system is successful in representing this.

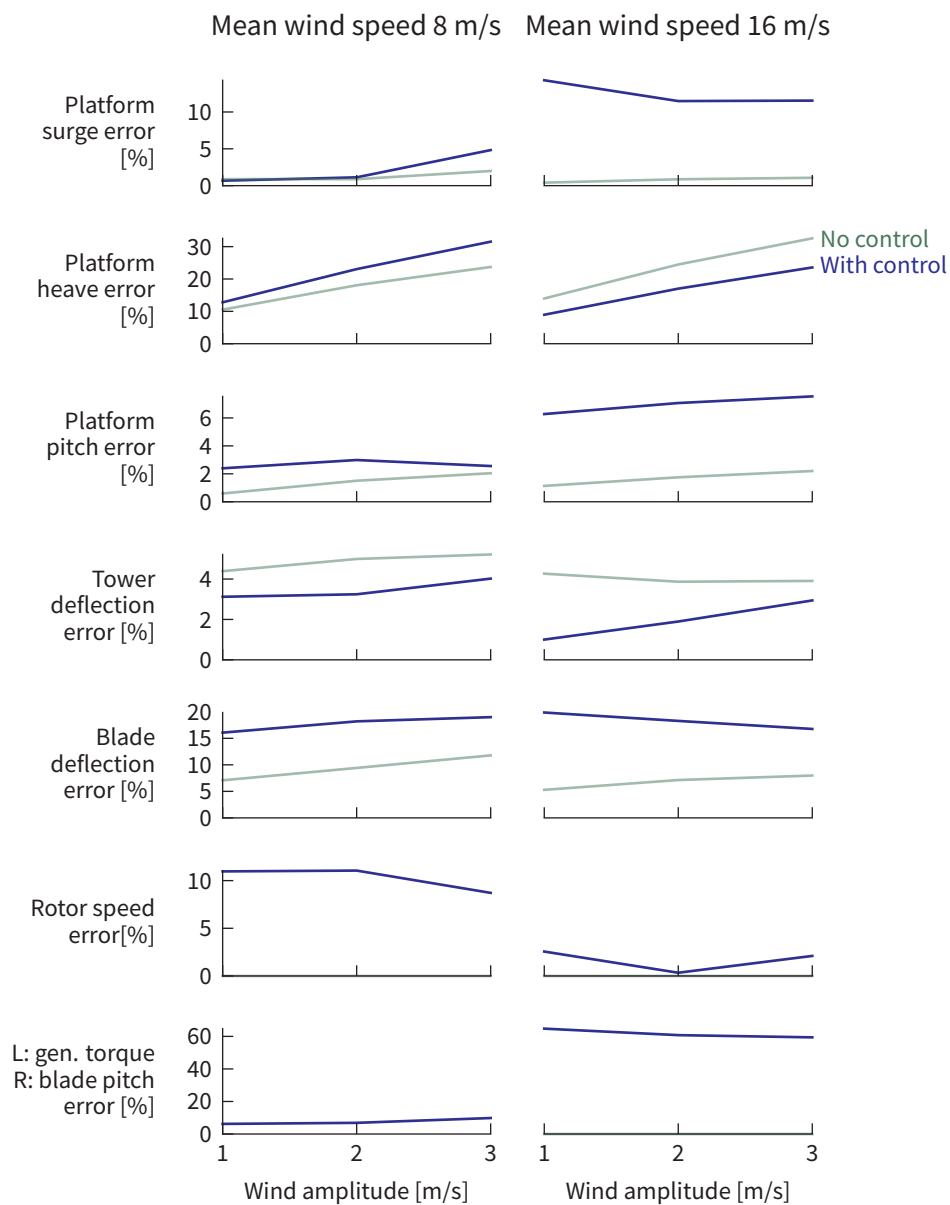


Figure 7.21 – Peak-peak error in results including control system, compared to previous results with no control.

## 7.4 Computational time comparison

All calculations were run on an Intel Core i7-2600 3.4 GHz processor. The Bladed simulations of the floating wind turbine without the control system were consistent across all cases, taking 900 s to 1000 s to run. The tangent linearisation calculation was also consistent across all the cases, taking 27 s to 29 s to run. The harmonic linearisation, on the other hand, was much more dependent on the wind and wave frequencies involved in the calculation, as shown in Table 7.2. Calculation times varied between about 70 s to 1750 s.

Firstly, it is important to note that the linearised results were calculated entirely in Python, an interpreted programming language, while Bladed is a compiled and optimised commercial code which is expected to run faster. To estimate how much of the difference in calculation time is due to this, a time-domain integration was performed using the same underlying Python code as used for the integration. While this does not represent a full nonlinear time-domain simulation tool, which would require significantly more work to implement, it approximates the calculations which would be performed. The difference between the run-times of this Python code and Bladed represents the differences due to implementation, rather than the difference between the linearised and nonlinear approaches. From this the present implementation is estimated to be 38 times slower than Bladed.

Using this factor to compensate for the slower implementation of the linearised models, the harmonic solution is estimated to be 20–500 times faster than the time domain solution. In the same way, the tangent solution is estimated to be 1200 times faster.

There are two main reasons for the variability of the harmonic linearisation calculations: evaluating the harmonics of the nonlinear functions, and solving the nonlinear equations. The harmonics of the nonlinear functions are calculated using a FFT approach described previously, but the efficiency of this is dependent on the relative frequencies of the harmonics involved: if the frequencies of the harmonics are close in the frequency domain, the nonlinear function is evaluated over a long sample in the time domain. Solving the nonlinear algebraic equations is achieved using a standard

Table 7.2 – Calculation time relative to Bladed for linearised solutions. There is little dependence on the mean wind speed, wind variation amplitude and wave height; the mean value over all these variables has been taken. The harmonic solution time with control is normalised against the Bladed solution time with control.

$\omega$	$T$	No control		With control
		Harmonic	Tangent	Harmonic
0.10	7	42 %	2.9 %	
0.10	10	30 %	2.8 %	
0.10	13	21 %	2.7 %	
0.32	7	14 %	2.9 %	
0.32	10	175 %	2.7 %	63 %
0.32	13	7 %	2.7 %	
1.00	7	13 %	2.8 %	
1.00	10	7 %	2.7 %	
1.00	13	36 %	2.7 %	

multidimensional root-finding algorithm<sup>2</sup>. The efficiency of this algorithm determines the number of times the nonlinear functions must be evaluated, and therefore directly influences the total calculation time. Although it is difficult to quantify the possible improvements, little work has been put into improving the efficiency of these algorithms, so it seems likely that improvements could be made.

Adding the control system dynamics into the model increases the duration of both the Bladed simulations and the harmonic linearisation calculation. The harmonic linearisation time has been increased by a factor of 3 and the Bladed simulations times are increased by a factor of 6 on average.

2. a Powell hybrid method (Jones, Oliphant and Peterson 2001)



## *Conclusions and future work*

### 8.1 Conclusions

1. *A linear structural model of a floating wind turbine is sufficient for approximate analysis.*

While strictly the structural dynamics of a floating wind turbine are nonlinear, for realistic conditions the effects were found to be small (Section 3.3.5 on p 105). This simplifies the analysis of floating wind turbines in the frequency domain, because a linear structural model can be used.

Specifically, the blade response was linear even for large platform motions as long as the rotor speed is below 20 rpm and the frequency of platform motion is below  $1.2 \text{ rad s}^{-1}$ . These are reasonable limits: for the NREL reference turbine used here, the rated rotor speed is 12 rpm, and the platform natural frequencies are from  $0.05 \text{ rad s}^{-1}$  to  $0.76 \text{ rad s}^{-1}$ .

This conclusion assumes that the aim of the analysis is to estimate the overall response of the floating turbine, including an estimate of the blade response. The linear model neglects coupling between the blade deflection and inertial loading which can be important for the detailed blade response. If necessary, the detailed blade response may be calculated afterwards in the time domain.

Model-scale testing is an important part of the design process of floating wind turbines. It was shown that if the blade properties are scaled properly then the same dynamic behaviour should be observed in model tests as at

full scale (Section 3.4 on p 107). Due to the practicalities of constructing small-scale blades, in testing to date, the model blades have been too stiff and the blade dynamics have not been considered. If model-scale measurements of the blade dynamics are undertaken, the nonlinear parts of the response will be underestimated unless the blade stiffness is reduced to the correct level.

2. *Harmonic linearisation improves the approximation of the nonlinear aerodynamic loads on a wind turbine by a factor of up to 4 over straightforward tangent linearisation.*

The tangent linearisation overestimates the forces when stall occurs; the harmonic linearisation can capture this better, reducing the error (Section 5.3 on p 155). These results are based on a specific wind turbine blade design and aerofoils, but are expected to be broadly representative of large wind turbine blades.

Although the dynamics of the rotor wake are nonlinear, it was demonstrated that a similar linearisation can capture the dynamic behaviour well (Section 5.4 on p 161).

3. *The wind turbine control system can be approximated using the harmonic linearisation method.*

This avoids the need to specify the rotor speed and pitch angle in advance, and accounts for variations in rotor speed and pitch angle in response to the wind and wave loading. The linearisation works well when the wind speed is not close to the rated wind speed, with errors in the rotor torque and thrust loads less than 10 % of the rated torque and thrust (Section 6.3 on p 177).

Close to the rated wind speed, the control behaviour is less linear and the two controllers interact, leading to larger errors. In some cases this is due to the underlying nonlinear behaviour, causing the rotor torque and thrust errors to increase up to 40 %. In other cases, limitations of the harmonic linearisation implementation mean the interaction between the controllers

is not fully captured. Here the errors are even larger, but improvements should be possible.

While the controller used here is realistic, it is unlikely to have been subject to the same level of refinement as real wind turbine controller. The same discontinuities in the control system which cause difficulties for the linearisation are also demanding for the wind turbine drive train, pitch system and blade loading. A real wind turbine controller design will consider these areas, so if anything smoother behaviour could be expected which will improve the linearisation.

4. *The linearised frequency-domain approach is suitable for fast, approximate modelling of the overall response of floating wind turbines.*

This has been demonstrated by the application of this approach to a floating wind turbine model, including much more detail than previous work has achieved: a flexible structure, aeroelastic rotor loads and the effect of the control system. Although the results are approximate, it seems that reasonable accuracy is achievable (Section 7.2 on p 193).

A caveat to these conclusions is that the examples and numerical results in this thesis are based entirely on the OC3-Hywind floating wind turbine. This is a spar-buoy type platform which is relatively effective at controlling platform motions. Although the methods developed and applied in the previous chapters are independent of the type of platform, it may be found that the linearisation performs less well for other platform types which show a larger dynamic response.

5. *Fast calculation times are possible, but were not achieved in every case.*

The calculation time of the linearised methods is important, since it is a key advantage over other methods. As implemented, the tangent linearisation approach is about 35 times faster than the nonlinear simulations. The harmonic linearisation approach was more variable, running between 14 times faster and 2 times slower than the nonlinear simulations (Section 7.4 on p 214).

Little effort has been put into optimising the linearised calculation, which are written entirely in an interpreted programming language. It is estimated that the implemented code is 38 times slower than the reference nonlinear code Bladed; there is therefore potential for significant improvements in speed, which would make the linearisation methods appear more advantageous. Compared to Bladed, the potential calculation time reduction is estimated at 20–500 times for the harmonic linearisation, and 1200 times for the tangent linearisation.

It may be worth considering whether the harmonic approach is justified over the rather simpler and faster tangent linearisation approach. The iterative harmonic linearisation approach increases the accuracy and the robustness of the linearised results, when compared to the tangent linearisation, at the expense of greater computational complexity. Although the absolute improvement in accuracy in many cases was found to be small, the additional confidence given by knowing that the linearisation is minimising the error between the linear and nonlinear functions may be valuable. Indeed, the error can be calculated while finding the linearisation, and used to check the suitability of the linearised approach to any given situation. In any case, the harmonic approach is necessary if the control system behaviour is to be included in the response.

6. *Slow drift motion of floating cylinders was shown to decrease with the size of the cylinder (for realistic floating wind turbine platform sizes).*

While this is an idealised result, the practical implication is that since floating wind turbines are relatively small floating structures, their slow drift motions should also be relatively small (Section 4.2 on p 124).

For traditional floating structures, the slow drift motion can be very large and influences the solution of the response: in the time domain, very long simulations are required to capture the statistics of the low-frequency response; in the frequency domain, because the low-frequency force is non-Gaussian, it is more difficult to find the statistics of the combined first- and second-order response. If the slow drift motion is relatively small, simpler analysis is possible, such as by approximating the force distribution as

Gaussian in the frequency-domain approach.

Comparisons of the idealised result against limited numerical results showed the results are conservative by a large margin. More data is needed to verify the result for other platforms.

7. *A nonlinear flexible multibody dynamics code has been developed.*

The code has been verified against Bladed and other tests, and used to provide reference nonlinear results throughout this thesis (Chapter 2 on p 37). It is freely available and not specific to modelling floating wind turbines, so it is hoped it may be useful to other researchers.

## 8.2 Future work

For practical application, more work is needed in some areas. Various aspects of the floating wind turbine have been discussed but not included in the final example, in order to achieve a reasonable complexity for this preliminary study. This includes the second-order wave forces, viscous drag, and wake dynamics. Other areas which may be important in practice, such as nonlinear mooring line dynamics, should also be considered. These are discussed below.

### 8.2.1 STOCHASTIC INPUTS

In reality, the wind and waves are best described in a stochastic manner, rather than the deterministic harmonic approach used here. The extension of the harmonic linearisation method to random variables should be fairly straightforward: instead of minimising the mean squared error over one cycle of the harmonic input, instead the expectation of the squared error is minimised (see for example Roberts and Spanos 1990, chapter 6). This is known as ‘stochastic linearisation’.

Allowing for simultaneous random and deterministic inputs is more complicated. This can be viewed as the extension of the stochastic linearisa-

tion to accept non-stationary stochastic inputs, with harmonically varying mean. In this case the nonlinear equations to be solved are ordinary differential equations rather than algebraic equations (Roberts and Spanos 1990, chapter 7).

### 8.2.2 ADDING ADDITIONAL HARMONICS TO THE SOLUTION

Returning to the harmonic linearisation, the linearised solutions in the final chapter included two harmonics, at the frequencies of the wind and wave forcing, but in principle more harmonics could be added. This increases the number of nonlinear equations to be solved, so harmonics should only be added if justified by the increase in accuracy.

Examples of this were seen in the platform heave response, which contains a harmonic at twice the wind frequency, and in the nonlinear aerodynamic force, which contains components at the sum and difference of the wind and wave frequencies.

In general, forces in a wind turbine are also expected at multiples of the rotor speed. Specifically, loads are expected on the blades at multiples of the rotor speed  $\Omega$ , and on the support structure at multiples of  $3\Omega$ . This was not observed here because the loading was always identical on the three blades. If this is no longer the case, due to wind shear, wind misalignment or platform motion, it may be helpful to include these harmonics in the linearisation.

### 8.2.3 SPATIAL VARIATION OF TURBULENCE

Only spatially uniform variations in wind speed have been considered here, but in practice turbulence does vary in space. The effect of this was seen in Chapter 7, where the motion of the rotor through the wind field caused additional harmonics in the aerodynamic forces. More generally, spatial turbulence should be considered where the wind speed can vary across the rotor.

#### 8.2.4 IMPROVED IMPLEMENTATION

There is room for improvement in the speed of the harmonic linearisation implementation. The current version is written in Python, and significant speed improvements should come from implementing the key parts in a faster, compiled language. It may be possible to evaluate the harmonics of the nonlinear functions more efficiently. Further gains should be possible by improvements to the root-finding algorithm to account for the specific characteristics of the problem: for example, improving the initial guess of the result, or making use of additional knowledge about the derivatives of the nonlinear function to estimate the Jacobian.

#### 8.2.5 APPLICATION TO OTHER PLATFORMS

So far this approach has been demonstrated with only one floating wind turbine model, the OC3-Hywind platform. Although there is nothing in the method which is specific to this platform, other platforms and turbines will have different response characteristics which may affect the performance of the linearised calculation.

In Chapter 3 it was found that the blade bending response could be excited by harmonics at various combinations of the frequency of platform motion and the rotor speed. Although this was not found to be a problem in practice for a typical large offshore wind turbine, this may not be true for future designs with higher rotor speeds or more flexible blades, and these effects could be investigated further.

#### 8.2.6 HYDRODYNAMICS AND MOORING LINES

The results for the scaling of the slow drift motion developed in Chapter 4 depend on various approximations and assumptions. More tests against numerical calculations are needed to determine to what extent this result is useful.

One assumption is that the platform is cylindrical. While this is true for some platforms, it is common to have a platform consisting of multiple columns. In this case the mean drift force can be sharply peaked at some

frequencies corresponding to the spacing between the columns. It would be interesting to determine if similar results can be found for this case.

In the final chapter, the mooring system is represented by a simple linear stiffness matrix. In reality the mooring force is often significantly nonlinear over the range of motion of the platform, especially considering the mean offset and slow drift motion. A harmonic linearisation method could be applied to the mooring characteristics to address this. Alternatively hybrid time-/frequency-domain methods exist, in which the nonlinear low-frequency slow drift motion and mooring line behaviour is modelled in the time domain, with the higher-frequency part of the response solved in the frequency domain (Low 2006).

### 8.2.7 AERODYNAMICS

The standard BEM model used to calculate the aerodynamic loads assumes that the air flow is uniform through each annular ring of the rotor. This will not strictly be the case when the platform pitches for two reasons: firstly because a steady pitch angle leads to steady misaligned flow, and secondly because the velocity of the rotor caused by the platform pitching motion is greater at the top of the rotor than the bottom. The first situation is analogous to the problem of a fixed-bottom turbine misaligned with the wind direction, which is a situation also likely to occur for a floating wind turbine. Various approaches have been developed to model this (Burton et al. 2011). The second reason has no analogue for a fixed-bottom wind turbine, but is unlikely to be very important due to the low frequencies of pitching motions.

### 8.2.8 CONTROL SYSTEM

A significant limitation of the way the linearised control system was implemented is that the pitch controller is only active when the mean wind speed is above the rated wind speed of the turbine. This means the behaviour is poor when the wind speed passes from below to above rated transiently, since the nonlinear controller starts to pitch the blades but the linearised controller does not. Improving this should address the issues found in

Chapter 6 where solutions could not be found for wind speeds below rated.

The nonlinearities in the pitch control system were also not fully captured, because the harmonic pitch angle was solved based on the theoretical PID controller equation rather than the actual nonlinear control output. Calculating the pitch angle numerically in a similar way to the calculation of the linearised generator torque may give better results.



## Appendix A

### *Further details of the multibody code*

#### A.1 Matrix form of cross product

A useful notation is the matrix form of the cross product (G eradin and Cardona 2001):

$$\mathbf{a} \times \mathbf{b} = \tilde{\mathbf{a}}\mathbf{b} \quad (\text{A.1})$$

where the tilde denotes the skew-symmetric matrix corresponding to the vector,

$$\tilde{\mathbf{a}} \equiv \begin{bmatrix} 0 & -a_3 & a_2 \\ a_3 & 0 & -a_1 \\ -a_2 & a_1 & 0 \end{bmatrix} \quad (\text{A.2})$$

The matrix cross product has the following properties:

$$\tilde{\mathbf{a}}^\top = -\tilde{\mathbf{a}} \quad (\text{A.3})$$

$$\tilde{\mathbf{a}}\mathbf{b} = -\tilde{\mathbf{b}}\mathbf{a} \quad (\text{A.4})$$

$$\tilde{\mathbf{a}}\tilde{\mathbf{b}} = \mathbf{b}\mathbf{a}^\top - (\mathbf{a}^\top\mathbf{b})\mathbf{I} \quad (\text{A.5})$$

$$\tilde{\mathbf{a}}\tilde{\mathbf{b}} = \tilde{\mathbf{b}}\tilde{\mathbf{a}} + \mathbf{b}\mathbf{a}^\top - \mathbf{a}\mathbf{b}^\top \quad (\text{A.6})$$

The first follows from the matrix definition, Equation (A.2). The second represents the anti-symmetric property of the cross product,  $\mathbf{a} \times \mathbf{b} = -\mathbf{b} \times \mathbf{a}$ . The third is derived by G eradin and Cardona (2001) from the double vector product, and the fourth follows from that.

When deriving the motion of points in a moving reference frame, a

useful property is

$$\dot{R}X = \tilde{\omega}RX \quad (\text{A.7})$$

$$= -R\tilde{X}R^\top \omega \quad (\text{A.8})$$

$$= -\tilde{x}\omega \quad (\text{A.9})$$

where  $\omega$  is the angular velocity of  $R$  in the global frame, and  $x = RX$ .

The order of cross products which appear in the centrifugal moment can be exchanged as follows:

$$\begin{aligned} \tilde{x}\tilde{\omega}\tilde{\omega}x &= (\tilde{\omega}\tilde{x} + \omega x^\top - x\omega^\top) \tilde{\omega}x && \text{using (A.6)} \\ &= -\tilde{\omega}\tilde{x}\tilde{x}\omega - \omega x^\top \tilde{x}\omega - x\omega^\top \tilde{\omega}x && \text{using (A.4)} \\ &= -\tilde{\omega}\tilde{x}\tilde{x}\omega && \begin{array}{l} \text{since } x^\top \tilde{x} = x \times x = 0 \\ \text{and } \omega^\top \tilde{\omega} = \omega \times \omega = 0 \end{array} \end{aligned} \quad (\text{A.10})$$

## A.2 Derivation of beam element mass matrix

The mass matrix of the flexible beam element described in Section 2.3.6 consists of submatrices defined by Equation (2.67). In this section these submatrices are derived from Equation (2.65).

The first part is simply a diagonal matrix consisting of the total mass of the body:

$$M_{rr} = \sum_j \int I \, dm^j = m \quad (\text{A.11})$$

The part which couples rigid-body translation and rotation of the element is

$$M_{r\omega} = - \sum_j \int \tilde{X}^j \, dm^j = -\tilde{Y} \quad (\text{A.12})$$

where  $Y = S q_n$ , and  $S$  is the first shape function integral:

$$S = \sum_j \int N^j \, dm^j \quad (\text{A.13})$$

$S$  depends on the form of the finite element model but does not change with time.

The part which couples rigid-body translation and elastic deformation of the element is

$$\mathbf{M}_{rf} = \left[ \sum_j \int N^j dm^j \right] \mathbf{B}_2 = \mathbf{S} \mathbf{B}_2 \quad (\text{A.14})$$

The part relating to rotation of the element is

$$\mathbf{M}_{\omega\omega} = - \sum_j \int \tilde{\mathbf{X}}^j \tilde{\mathbf{X}}^j dm^j = \mathbf{J} \quad (\text{A.15})$$

where  $\mathbf{J}$  is the inertia matrix in local coordinates. By substituting Equation (2.60),  $\mathbf{J}$  can be written in terms of the second shape function integrals  $S_{kl}$  as the symmetric matrix

$$\mathbf{J} = \begin{bmatrix} \mathbf{q}_n^\top (S_{22} + S_{33}) \mathbf{q}_n & -\mathbf{q}_n^\top S_{21} \mathbf{q}_n & -\mathbf{q}_n^\top S_{31} \mathbf{q}_n \\ \cdot & \mathbf{q}_n^\top (S_{33} + S_{11}) \mathbf{q}_n & -\mathbf{q}_n^\top S_{32} \mathbf{q}_n \\ \cdot & \cdot & \mathbf{q}_n^\top (S_{11} + S_{22}) \mathbf{q}_n \end{bmatrix} \quad (\text{A.16})$$

where

$$S_{kl} = \sum_j \int N_k^{j\top} N_l^j dm^j \quad (\text{A.17})$$

in which  $N_k^j$  is the  $k$ th row of the shape functions of the  $j$ th finite element.

The part which couples rigid-body rotation and elastic deformation of the element is

$$\mathbf{M}_{\omega f} = \left[ \sum_j \int \tilde{\mathbf{X}}^j N^j dm^j \right] \mathbf{B}_2 = \mathbf{I}_{\Omega f} \mathbf{B}_2 \quad (\text{A.18})$$

where

$$\begin{aligned}
 I_{\Omega f} &= \sum_j \int \tilde{\mathbf{X}}^j \mathbf{N}^j dm^j \\
 &= \sum_j \int \begin{bmatrix} X_2^j N_3^j - X_3^j N_2^j \\ X_3^j N_1^j - X_1^j N_3^j \\ X_1^j N_2^j - X_2^j N_1^j \end{bmatrix} dm^j \\
 &= \begin{bmatrix} \mathbf{q}_n^\top (\mathbf{S}_{23} - \mathbf{S}_{23}^\top) \\ \mathbf{q}_n^\top (\mathbf{S}_{31} - \mathbf{S}_{31}^\top) \\ \mathbf{q}_n^\top (\mathbf{S}_{12} - \mathbf{S}_{12}^\top) \end{bmatrix} \quad (\text{A.19})
 \end{aligned}$$

in which  $N_k^j$  and  $X_k^j$  are the  $k$ th row of  $N^j$  and the  $k$ th element of  $\mathbf{X}^j$  respectively.

Finally, the part relating to the elastic deformations is

$$\begin{aligned}
 \mathbf{M}_{ff} &= \mathbf{B}_2^\top \left[ \sum_j \int \mathbf{N}^{j\top} \mathbf{N}^j dm^j \right] \mathbf{B}_2^\top \\
 &= \mathbf{B}_2^\top (\mathbf{S}_{11} + \mathbf{S}_{22} + \mathbf{S}_{33}) \mathbf{B}_2^\top \quad (\text{A.20})
 \end{aligned}$$

These expressions are all identical to those given by Shabana (2013).

### A.3 Derivation of beam element velocity-dependent forces

The vector of velocity-dependent forces for the flexible beam element described in Section 2.3.6 consists of submatrices defined by Equation (2.69). These submatrices are derived in this section.

The forces are

$$\begin{aligned}
 \mathbf{g}_r &= \sum_j \left[ \tilde{\boldsymbol{\Omega}} \tilde{\boldsymbol{\Omega}} \left( \int \mathbf{X}^j dm^j \right) + 2\tilde{\boldsymbol{\Omega}} \left( \int \mathbf{N}^j dm^j \right) \mathbf{B}_2 \dot{\mathbf{q}}_f \right] \\
 &= \tilde{\boldsymbol{\Omega}} \left( \tilde{\boldsymbol{\Omega}} \mathbf{Y} + 2\mathbf{S} \mathbf{B}_2 \dot{\mathbf{q}}_f \right) \quad (\text{A.21})
 \end{aligned}$$

where  $\mathbf{Y}$  and  $\mathbf{S}$  are the same matrices as appear in Equation (A.12).

The first term of  $\mathbf{g}_\omega$  is the moment due to centrifugal loading on the element and is similar to the equivalent term for the rigid body element in Equation (2.56); the difference is that the inertia matrix now depends on

the current deformation of the body, as described by Equation (A.16) above. The order of cross products can be exchanged as shown by Equation (A.10). The second term of  $\mathbf{g}_\omega$  represents the Coriolis moment. The total moment is

$$\begin{aligned}\mathbf{g}_\omega &= \sum_j \left[ -\tilde{\Omega} \left( \int \tilde{\mathbf{X}}^j \tilde{\mathbf{X}}^j dm^j \right) \Omega + 2 \left( \int \tilde{\mathbf{X}}^j \tilde{\Omega} \mathbf{N}^j dm^j \right) \mathbf{B}_2 \dot{\mathbf{q}}_f \right] \\ &= \tilde{\Omega} \mathbf{J} \Omega + 2 \mathbf{I}'_{\Omega f} \mathbf{B}_2 \dot{\mathbf{q}}_f\end{aligned}\quad (\text{A.22})$$

where

$$\begin{aligned}\mathbf{I}'_{\Omega f} &= \sum_j \int \tilde{\mathbf{X}}^j \tilde{\Omega} \mathbf{N}^j dm^j \\ &= \begin{bmatrix} \mathbf{q}_n^\top (\Omega_1 (\mathbf{S}_{22} + \mathbf{S}_{33}) - \Omega_2 \mathbf{S}_{21} - \Omega_3 \mathbf{S}_{31}) \\ \mathbf{q}_n^\top (\Omega_1 (\mathbf{S}_{33} + \mathbf{S}_{11}) - \Omega_2 \mathbf{S}_{32} - \Omega_3 \mathbf{S}_{12}) \\ \mathbf{q}_n^\top (\Omega_1 (\mathbf{S}_{11} + \mathbf{S}_{22}) - \Omega_2 \mathbf{S}_{13} - \Omega_3 \mathbf{S}_{23}) \end{bmatrix}\end{aligned}\quad (\text{A.23})$$

To evaluate  $\mathbf{g}_f$ , apply Equation (A.4) to give

$$\begin{aligned}\mathbf{g}_f &= \sum_j \left[ -\mathbf{B}_2^\top \left( \int \mathbf{N}^{j\top} \tilde{\Omega} \tilde{\mathbf{X}} dm^j \right) \Omega + 2 \mathbf{B}_2^\top \left( \int \mathbf{N}^{j\top} \tilde{\Omega} \mathbf{N}^j dm^j \right) \mathbf{B}_2 \dot{\mathbf{q}}_f \right] \\ &= -\mathbf{B}_2^\top \mathbf{I}'_{\Omega f} \Omega - 2 \mathbf{B}_2^\top \mathbf{I}_{ff} \mathbf{B}_2 \dot{\mathbf{q}}_f\end{aligned}\quad (\text{A.24})$$

where  $\mathbf{I}'_{\Omega f}$  is defined in Equation (A.23) and

$$\begin{aligned}\mathbf{I}_{ff} &= - \sum_j \int \mathbf{N}^{j\top} \tilde{\Omega} \mathbf{N}^j dm^j \\ &= - \sum_j \int \mathbf{N}^{j\top} \begin{bmatrix} \Omega_2 \mathbf{N}_3^j - \Omega_3 \mathbf{N}_2^j \\ \Omega_3 \mathbf{N}_1^j - \Omega_1 \mathbf{N}_3^j \\ \Omega_1 \mathbf{N}_2^j - \Omega_2 \mathbf{N}_1^j \end{bmatrix} \\ &= \Omega_1 (\mathbf{S}_{23} - \mathbf{S}_{23}^\top) + \Omega_2 (\mathbf{S}_{31} - \mathbf{S}_{31}^\top) + \Omega_3 (\mathbf{S}_{12} - \mathbf{S}_{12}^\top)\end{aligned}\quad (\text{A.25})$$

## A.4 Derivation of beam element applied forces

The generalised forces corresponding to applied distributed forces on the flexible beam element described in Section 2.3.6 consists of submatrices defined by Equation (2.72). These submatrices are derived in this section.

The translational generalised force is  $Q_r = \bar{S}F_n$ , where

$$\bar{S} = \sum_j \int \bar{N}^j dx^j \quad (\text{A.26})$$

$\bar{S}$  is analagous to  $S$  which appears in Equation (A.13), but involves the applied load shape functions  $\bar{N}$  and integration of length, rather than the deformation shape functions  $N$  and integration of mass.

The rotational generalised force is  $Q_\omega = I_{\Omega F}F_n$ , where  $I_{\Omega F}$  is analagous to  $I_{\Omega f}$  of Equation (A.19):

$$I_{\Omega F} = \begin{bmatrix} \mathbf{q}_n^\top (\bar{S}_{23} - \bar{S}_{23}^\top) \\ \mathbf{q}_n^\top (\bar{S}_{31} - \bar{S}_{31}^\top) \\ \mathbf{q}_n^\top (\bar{S}_{12} - \bar{S}_{12}^\top) \end{bmatrix} \quad (\text{A.27})$$

$$\bar{S}_{kl} = \sum_j \int N_k^{j\top} \bar{N}_l^j dx^j \quad (\text{A.28})$$

The generalised stress is  $Q_f = \mathbf{B}_2^\top (\bar{S}_{11} + \bar{S}_{22} + \bar{S}_{33}) F_n$ .

## Appendix B

### *Further details of flapped-blade equations of motion*

#### B.1 Kinematics for platform pitching motion

Although in practice the equations of motion were derived for general platform motion using a computer algebra system, the resulting equations are rather long and difficult to understand. Rather than presenting the general equations, here the simpler case of platform pitching motion is used to illustrate the procedure.

##### B.1.1 COORDINATE SYSTEMS

The model, shown in Figure B.1, is described by several coordinate systems, which in this case are related as follows:

1. A fixed coordinate system  $IJK$ .
2. Rotation of  $IJK$  through an angle  $\varphi$  about the  $J$  axis gives the platform coordinate system  $ijk$ .
3. Rotation of  $ijk$  through an angle  $\theta$  about the  $i$  axis gives the blade root coordinate system  $abc$ . The rotor axis is located at a height  $h$ .
4. For flapwise and edgewise deflections respectively:
  - (a) Rotation of  $abc$  through an angle  $\alpha$  about the  $b$  axis gives the blade-fixed coordinate system  $mnp$ , where  $n = b$ . This rotation represents the blade flexibility in the flapwise direction.
  - (b) Rotation of  $abc$  through an angle  $\beta$  about the  $a$  axis gives the blade-fixed coordinate system  $mnp$ , where  $m = a$ . This rotation represents

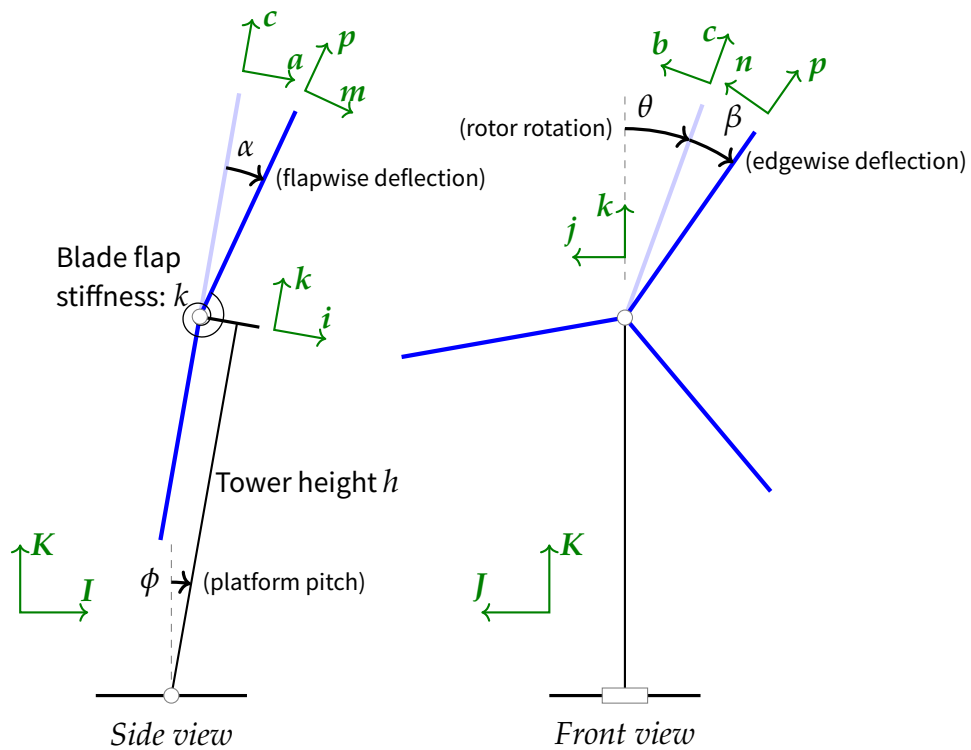


Figure B.1 – Reproduction of Figure 3.2: the simplified model of a floating wind turbine showing the flapwise blade response to platform pitching motion. The coordinates are the platform pitch angle  $\phi$ , the rotor azimuth angle  $\theta$ , the blade flapwise deflection  $\alpha$  and the blade edgewise deflection  $\beta$ .

the blade flexibility in the edgewise direction.

The turbine unit vectors and their derivatives are related to the fixed unit vectors as follows:

$$\mathbf{i} = I \cos \varphi - K \sin \varphi \quad \dot{\mathbf{i}} = -\dot{\varphi} \mathbf{k} \quad (\text{B.1a})$$

$$\mathbf{j} = J \quad \dot{\mathbf{j}} = 0 \quad (\text{B.1b})$$

$$\mathbf{k} = K \cos \varphi + I \sin \varphi \quad \dot{\mathbf{k}} = \dot{\varphi} \mathbf{i} \quad (\text{B.1c})$$

The rotor unit vectors and their derivatives are related to the turbine unit vectors as follows:

$$\mathbf{a} = \mathbf{i} \quad \dot{\mathbf{a}} = -\dot{\varphi} \mathbf{k} \quad (\text{B.2a})$$

$$\mathbf{b} = \mathbf{j} \cos \theta + \mathbf{k} \sin \theta \quad \dot{\mathbf{b}} = \dot{\theta} \mathbf{c} + \dot{\varphi} \sin \theta \mathbf{i} \quad (\text{B.2b})$$

$$\mathbf{c} = -\mathbf{j} \sin \theta + \mathbf{k} \cos \theta \quad \dot{\mathbf{c}} = -\dot{\theta} \mathbf{b} + \dot{\varphi} \cos \theta \mathbf{i} \quad (\text{B.2c})$$

For flapwise deflections, the blade unit vectors are related to the rotor unit vectors as follows:

$$\mathbf{m} = -\mathbf{c} \sin \alpha + \mathbf{a} \cos \alpha \quad \dot{\mathbf{m}} = -\dot{\alpha} \mathbf{p} - \dot{\varphi} \cos \alpha \mathbf{k} \quad (\text{B.3a})$$

$$+ \sin \alpha (\dot{\theta} \mathbf{b} - \dot{\varphi} \cos \theta \mathbf{i})$$

$$\mathbf{n} = \mathbf{b} \quad \dot{\mathbf{n}} = \dot{\theta} \mathbf{c} + \dot{\varphi} \sin \theta \mathbf{i} \quad (\text{B.3b})$$

$$\mathbf{p} = \mathbf{c} \cos \alpha + \mathbf{a} \sin \alpha \quad \dot{\mathbf{p}} = \dot{\alpha} \mathbf{m} - \dot{\varphi} \sin \alpha \mathbf{k} \quad (\text{B.3c})$$

$$- \cos \alpha (\dot{\theta} \mathbf{b} - \dot{\varphi} \cos \theta \mathbf{i})$$

while for edgewise deflections,

$$\mathbf{m} = \mathbf{a} \quad \dot{\mathbf{m}} = -\dot{\varphi} \mathbf{k} \quad (\text{B.4a})$$

$$\mathbf{n} = \mathbf{b} \cos \beta + \mathbf{c} \sin \beta \quad \dot{\mathbf{n}} = \dot{\beta} \mathbf{p} + \cos \beta (\dot{\theta} \mathbf{c} + \dot{\varphi} \sin \theta \mathbf{i}) \quad (\text{B.4b})$$

$$+ \sin \beta (-\dot{\theta} \mathbf{b} + \dot{\varphi} \cos \theta \mathbf{i})$$

$$\mathbf{p} = \mathbf{c} \cos \beta - \mathbf{b} \sin \beta \quad \dot{\mathbf{p}} = -\dot{\beta} \mathbf{n} + \cos \beta (-\dot{\theta} \mathbf{b} + \dot{\varphi} \cos \theta \mathbf{i}) \quad (\text{B.4c})$$

$$+ \sin \beta (\dot{\theta} \mathbf{c} + \dot{\varphi} \sin \theta \mathbf{i})$$

### B.1.2 BLADE KINEMATICS

The position of an arbitrary point on the blade (at radius  $r$ ) is

$$\mathbf{r} = h\mathbf{k} + r\mathbf{p} \quad (\text{B.5})$$

By differentiating this, and using the coordinate system relationships above, the velocity is found to be

$$\dot{\mathbf{r}} = \dot{\varphi} (h + r \cos \alpha \cos \theta) \mathbf{i} - r\dot{\varphi} \sin \alpha \mathbf{k} - r\dot{\theta} \cos \alpha \mathbf{b} + r\dot{\alpha} \mathbf{m} \quad (\text{B.6a})$$

for flapwise deflections, and

$$\dot{\mathbf{r}} = \dot{\varphi} (h + r \cos \beta \cos \theta - r \sin \beta \sin \theta) \mathbf{i} - r (\dot{\theta} + \dot{\beta}) \mathbf{n} \quad (\text{B.6b})$$

for edgewise deflections. To find the kinetic energy, the speed is needed. The relevant dot products to evaluate  $\dot{\mathbf{r}} \cdot \dot{\mathbf{r}}$  can be found from equations (B.1)–(B.4). For flapwise deflections, the only non-zero products are

$$\mathbf{i} \cdot \mathbf{m} = \cos \alpha \quad \mathbf{k} \cdot \mathbf{m} = -\sin \alpha \cos \theta \quad \mathbf{k} \cdot \mathbf{b} = \sin \theta \quad (\text{B.7})$$

while for edgewise deflections,  $\mathbf{i} \cdot \mathbf{n} = 0$ . The speed squared is therefore

$$\begin{aligned} \dot{\mathbf{r}} \cdot \dot{\mathbf{r}} = & [(h + r \cos \alpha \cos \theta)^2 + (r \sin \alpha)^2] \dot{\varphi}^2 + (r \cos \alpha)^2 \dot{\theta}^2 + r^2 \dot{\alpha}^2 \\ & + 2r\dot{\alpha}\dot{\varphi} (h \cos \alpha + r \cos \theta) + r^2 \dot{\varphi}\dot{\theta} \sin 2\alpha \sin \theta \end{aligned} \quad (\text{B.8a})$$

for flapwise deflections, and

$$\dot{\mathbf{r}} \cdot \dot{\mathbf{r}} = (h + r \cos \beta \cos \theta - r \sin \beta \sin \theta)^2 \dot{\varphi}^2 + r^2 (\dot{\theta} + \dot{\beta})^2 \quad (\text{B.8b})$$

for edgewise deflections.

To find the potential energy, the height of an arbitrary point on the blade is also needed. From Equation (B.5),

$$H = \mathbf{r} \cdot \mathbf{K} = h \cos \varphi + r (\cos \alpha \cos \theta \cos \varphi - \sin \alpha \sin \theta) \quad (\text{B.9a})$$

for flapwise deflections, and

$$H = \mathbf{r} \cdot \mathbf{K} = h \cos \varphi + r \cos \varphi (\cos \beta \cos \theta - \sin \beta \sin \theta) \quad (\text{B.9b})$$

for edgewise deflections.

## B.2 Equation of motion for response to pitching motion

### B.2.1 KINETIC AND POTENTIAL ENERGY

The kinetic energy of the blade is given by

$$T = \frac{1}{2} \int (\mathbf{r} \cdot \mathbf{r}) dm \quad (\text{B.10})$$

Substituting the expressions for the speed at radius  $r$  from Equations (B.8) gives

$$\begin{aligned} 2T = & [Mh^2 + 2hI_1 \cos \alpha \cos \theta + I_2 \cos^2 \alpha \cos^2 \theta + I_2 \sin^2 \alpha] \dot{\varphi}^2 \\ & + I_2 \cos^2 \alpha \dot{\theta}^2 + I_2 \dot{\alpha}^2 + 2\dot{\alpha}\dot{\varphi} (hI_1 \cos \alpha + I_2 \cos \theta) + I_2 \dot{\varphi}\dot{\theta} \sin 2\alpha \sin \theta \end{aligned} \quad (\text{B.11a})$$

for flapwise deflections, and

$$\begin{aligned} 2T = & [Mh^2 + 2hI_1 (\cos \beta \cos \theta - \sin \beta \sin \theta) \\ & + I_2 (\cos \beta \cos \theta - \sin \beta \sin \theta)^2] \dot{\varphi}^2 + I_2 [\dot{\theta} + \dot{\beta}]^2 \end{aligned} \quad (\text{B.11b})$$

for edgewise deflections, where  $M$  is the blade's mass, and  $I_1$  and  $I_2$  are its first and second moments of mass, defined as

$$M = \int dm \quad (\text{B.12a})$$

$$I_1 = \int r dm \quad (\text{B.12b})$$

$$I_2 = \int r^2 dm \quad (\text{B.12c})$$

The potential energy is

$$V = \frac{1}{2} k_f \alpha^2 + Mgh \cos \varphi + I_1 g (\cos \alpha \cos \varphi \cos \theta - \sin \alpha \sin \varphi) \quad (\text{B.13a})$$

for flapwise deflections, and

$$V = \frac{1}{2} k_e \beta^2 + Mgh \cos \varphi + I_1 g \cos \varphi (\cos \beta \cos \theta - \sin \beta \sin \theta) \quad (\text{B.13b})$$

for edgewise deflections, and the stiffness of the blade hinge is  $k_f$  and  $k_e$  in the flapwise and edgewise directions respectively.

### B.2.2 FULL EQUATION OF MOTION

The kinetic and potential energies lead to the equation of motion through Lagrange's equation:

$$\frac{d}{dt} \left[ \frac{\partial T}{\partial \dot{\alpha}} \right] - \frac{\partial T}{\partial \alpha} + \frac{\partial V}{\partial \alpha} = Q_\alpha \quad (\text{B.14})$$

For the blade flapwise response to platform pitch motion, these terms are:

$$\frac{\partial T}{\partial \dot{\alpha}} = I_2 \dot{\alpha} + \dot{\varphi} (I_1 h \cos \alpha + I_2 \cos \theta) \quad (\text{B.15a})$$

$$\frac{d}{dt} \left[ \frac{\partial T}{\partial \dot{\alpha}} \right] = I_2 \ddot{\alpha} + \ddot{\varphi} (I_1 h \cos \alpha + I_2 \cos \theta) - \dot{\varphi} (I_1 h \dot{\alpha} \sin \alpha + I_2 \dot{\theta} \sin \theta) \quad (\text{B.15b})$$

$$\begin{aligned} \frac{\partial T}{\partial \alpha} = & \dot{\varphi}^2 (I_2 \cos \alpha (1 - \cos^2 \theta) - I_1 h \cos \theta) \sin \alpha \\ & + \dot{\varphi} (I_2 \dot{\theta} \sin \theta \cos 2\alpha - I_1 h \dot{\alpha} \sin \alpha) - I_2 \dot{\theta}^2 \sin \alpha \cos \alpha \end{aligned} \quad (\text{B.15c})$$

$$\frac{\partial V}{\partial \alpha} = k\alpha - I_1 g (\sin \alpha \cos \varphi \cos \theta + \cos \alpha \sin \varphi) \quad (\text{B.15d})$$

$$Q = 0 \quad (\text{B.15e})$$

Substituting these into Equation (B.14) leads directly to the equation of motion. The equation of motion for the edgewise response is derived in exactly the same way, but for brevity is not written in full. All the equations of motion, assuming harmonic motion of the platform, are given starting on p 83.

### B.2.3 SMALL-ANGLE EQUATION OF MOTION

Some simplifications can be introduced to allow for further analysis. The rotor speed is assumed constant with  $\Omega = \dot{\theta}$ . The flap angle will be assumed to be small, such that  $\sin \alpha \approx \alpha$  and  $\cos \alpha \approx 1$ . This is reasonable because the flap angle is a simplified model of the blade's flexibility which is only realistic for small deflections. The potential energy (B.13) contains the terms  $\sin \varphi$  and  $\cos \varphi$ , but the platform motion  $\varphi$  is assumed to be small, so  $\sin \varphi \approx \varphi$  and  $\cos \varphi \approx 1$ . Finally, a factor of  $I_2$  is removed and the ratio  $\lambda = I_1/I_2$  is introduced. With these simplifications, the terms in (B.15)

become

$$\frac{d}{dt} \left[ \frac{\partial T}{\partial \dot{\alpha}} \right] = \ddot{\alpha} + \ddot{\varphi} (\lambda h + \cos \theta) - \dot{\varphi} (\lambda h \dot{\alpha} + \Omega \sin \theta) \quad (\text{B.16a})$$

$$\frac{\partial T}{\partial \alpha} = (\dot{\varphi}^2 (1 - \cos^2 \theta - \lambda h \cos \theta) - \lambda h \dot{\varphi} \dot{\alpha} - \Omega^2) \alpha + \dot{\varphi} \Omega \sin \theta \quad (\text{B.16b})$$

$$\frac{\partial V}{\partial \alpha} = \omega_f^2 \alpha - \lambda g (\alpha \cos \theta + \varphi) \quad (\text{B.16c})$$

where  $\omega_f^2 = k/I_2$  is the natural frequency of the blade. Substituting into Equation (B.14) shows the simplified equation of motion for the blade flap motion to be

$$\ddot{\alpha} + \left[ \omega_f^2 + \Omega^2 + \dot{\varphi}^2 \left( \lambda h \cos \theta + \frac{1}{2} \cos 2\theta - \frac{1}{2} \right) - \lambda g \cos \theta \right] \alpha = \lambda g \varphi + 2\dot{\varphi} \Omega \sin \theta - \ddot{\varphi} (\lambda h + \cos \theta) \quad (\text{B.17})$$

All the simplified equations of motion are given starting on p 86.



## Bibliography

- Aranha, JAP and AC Fernades (1995). "On the second-order slow drift force spectrum". In: *Applied Ocean Research* 17, pp. 311–313.
- Bachynski, EE and T Moan (2012). "Design considerations for tension leg platform wind turbines". In: *Marine Structures* 29.1, pp. 89–114. DOI: 10.1016/j.marstruc.2012.09.001.
- Bae, YH and MH Kim (2013). "Rotor-floater-tether coupled dynamics including second-order sum-frequency wave loads for a mono-column-TLP-type FOWT (floating offshore wind turbine)". In: *Ocean Engineering* 61, pp. 109–122. DOI: 10.1016/j.oceaneng.2013.01.010.
- (2014). "Aero-Elastic-Control-Floater-Mooring Coupled Dynamic Analysis of Floating Offshore Wind Turbine in Maximum Operation and Survival Conditions". In: *Journal of Offshore Mechanics and Arctic Engineering* 136.2. DOI: 10.1115/1.4025029.
- Bae, YH, MH Kim, et al. (2011). "Aero-elastic-control-floater-mooring coupled dynamic analysis of floating offshore wind turbines". In: *Proceedings of the 21st International Offshore and Polar Engineering Conference*. Maui, Hawaii, pp. 429–435.
- Bayati, I et al. (2014). "The effects of second-order hydrodynamics on a semisubmersible floating offshore wind turbine". In: *Journal of Physics: Conference Series* 524, p. 012094. DOI: 10.1088/1742-6596/524/1/012094.
- Bland, DR (1960). *The theory of linear viscoelasticity*. Pergamon Press.
- Blue H (2014). *Blue H*. URL: <http://www.bluehgroup.com> (visited on 10/09/2014).
- BP (2014). *Statistical Review of World Energy 2014*. Tech. rep. URL: <http://www.bp.com/en/global/corporate/about-bp/energy-economics/statistical-review-of-world-energy.html>.
- Brommundt, M et al. (2012). "Mooring System Optimization for Floating Wind Turbines using Frequency Domain Analysis". In: *Energy Procedia* 24. January, pp. 289–296. DOI: 10.1016/j.egypro.2012.06.111.

- Burton, T et al. (2011). *Wind Energy Handbook*. John Wiley & Sons.
- Casale, C et al. (2010). "Preliminary design of a floating wind turbine support structure and relevant system cost assessment". In: *Wind Engineering* 34.1, pp. 29–50.
- Cermelli, CA, DG Roddier and A Aubault (2009). "Windfloat: A floating foundation for offshore wind turbines Part II: Hydrodynamics analysis". In: *Proceedings of the 28th International Conference on Offshore Mechanics and Arctic Engineering*. Honolulu, Hawaii, pp. 135–143.
- Chakrabarti, SK (2005). *Handbook of offshore engineering*. Elsevier.
- Cook, RD, DS Malkus and ME Plesha (1989). *Concepts and applications of finite element analysis*. John Wiley & Sons.
- Cordle, A (2010). *State-of-the-art in design tools for floating offshore wind turbines*. Tech. rep. Upwind.
- Coulling, AJ et al. (2013). "Importance of Second-Order Difference-Frequency Wave-Diffraction Forces in the Validation of a FAST Semi-Submersible Floating Wind Turbine Model". In: *Proceedings of the ASME 2013 32nd International Conference on Ocean, Offshore and Arctic Engineering*. Nantes, France: ASME, V008T09A019. DOI: 10.1115/OMAE2013-10308.
- Craig, RR and MC Bampton (1968). "Coupling of Substructures for Dynamic Analysis". In: *AIAA Journal* 6.7, pp. 1313–1319.
- Cunff, CL et al. (2013). "Fully-coupled floating wind turbine simulator based on nonlinear finite element method - Part I: Methodology". In: *Proceedings of the ASME 2013 32nd International Conference on Ocean, Offshore and Arctic Engineering*. Nantes, France.
- Drake, KR (2011). "An analytical approximation for the horizontal drift force acting on a deep draught spar in regular waves". In: *Ocean Engineering* 38.5-6, pp. 810–814. DOI: 10.1016/j.oceaneng.2011.02.003.
- DTU Wind Energy. *HAWC2*. URL: <http://www.hawc2.dk>.
- Duarte, T, AJNA Sarmiento and J Jonkman (2014). "Effects of Second-Order Hydrodynamic Forces on Floating Offshore Wind Turbines". In: *AIAA SciTech*. April. National Harbour, Maryland.
- Eatock Taylor, R, CS Hu and FG Nielsen (1990). "Mean drift forces on a slowly advancing vertical cylinder in long waves". In: *Applied Ocean Research* 12.3, pp. 141–152.
- Engelen, TG van and H Braam (2004). *TURBU Offshore, computer program for frequency-domain analysis of horizontal-axis offshore wind turbines - Implementation*. Tech. rep. September. ECN.

- EWEA (2014a). *The European offshore wind industry - key trends and statistics 2013*. Tech. rep.
- (2014b). *Wind in power: 2013 European statistics*. Tech. rep. February. European Wind Energy Association.
- Faltinsen, OM (1993). *Sea Loads on Ships and Offshore Structures*. Cambridge University Press.
- Fujiwara, H, T Tsubogo and Y Nihei (2011). "Gyro Effect of Rotating Blades on the Floating Wind Turbine Platform in Waves". In: *Proceedings of the International Offshore and Polar Engineering Conference 8*, pp. 399–406.
- Fulton, GR et al. (2007). *Semi-Submersible Platform and Anchor Foundation Systems for Wind Turbine Support*. Tech. rep. December. NREL.
- Fylling, I and PA Berthelsen (2011). "WINDOPT: An Optimization Tool for Floating Support Structures for Deep Water Wind Turbines". In: *OMAE 2011*. Asme. DOI: 10.1115/OMAE2011-49985.
- Garrad Hassan (2011). *Bladed Theory Manual*. Tech. rep.
- Gérardin, M and A Cardona (2001). *Flexible multibody dynamics : a finite element approach*. Chichester: Wiley.
- Goupee, AJ et al. (2012). "Experimental comparison of three floating wind turbine concepts". In: *Proceedings of the 31st International Conference on Offshore Mechanics and Arctic Engineering*. Rio de Janeiro, Brazil: ASME.
- Gueydon, S, K Lindenburg and F Savenije (2013). "Coupling of Two Tools for the Simulation of Floating Wind Turbines". In: *Proceedings of the ASME 2013 32nd International Conference on Ocean, Offshore and Arctic Engineering*. ASME. DOI: 10.1115/OMAE2013-11174.
- Hairer, E, SP Norsett and G Wanner (1993). *Solving Ordinary Differential Equations: i. Nonstiff Problems*. Springer-Verlag.
- Halfpenny, A (1998). "Dynamic Analysis of Both On and Offshore Wind Turbines in the Frequency Domain". PhD thesis. University College London.
- Hall, M, B Buckham and C Crawford (2013). "Evaluating the importance of mooring line model fidelity in floating offshore wind turbine simulations". In: *Wind Energy*. DOI: 10.1002/we.
- (2014). "Hydrodynamics-based floating wind turbine support platform optimization: A basis function approach". In: *Renewable Energy* 66, pp. 559–569. DOI: 10.1016/j.renene.2013.12.035.
- Hansen, MH (2004). "Aeroelastic stability analysis of wind turbines using an eigenvalue approach". In: *Wind Energy* 7.2, pp. 133–143. DOI: 10.1002/we.116.

- Hansen, MH (2007). "Aeroelastic Instability Problems for Wind Turbines". In: *Wind Energy* 10.6, pp. 551–577. DOI: 10.1002/we.
- Henderson, AR, K Argyriadis, et al. (2010). "Offshore wind turbines on TLPs – assessment of floating support structures for offshore wind farms in German waters". In: *10th German Wind Energy Conference*. November. Bremen, Germany.
- Henderson, AR and D Witcher (2010). "Floating Offshore Wind Energy-A Review of the Current Status and an Assessment of the Prospects". In: *Wind Engineering* 34.1, pp. 1–16.
- Henderson, AR, MB Zaaijer, et al. (2004). "Floating windfarms for shallow offshore sites". In: *Proceedings of the 14th International Offshore and Polar Engineering Conference*. Toulon, France, pp. 120–127.
- International Electrotechnical Commission (2005). *Wind turbines - Part 1: Design requirements (edition 3)*.
- Jalón, JG de and E Bayo (1994). *Kinematic and Dynamic Simulation of Multibody Systems*. Springer-Verlag.
- Jones, E, T Oliphant, P Peterson, et al. (2001). *SciPy: Open source scientific tools for Python*. URL: <http://www.scipy.org/>.
- Jonkman, J (2007). *Dynamics Modeling and Loads Analysis of an Offshore Floating Wind Turbine*. Tech. rep. NREL/TP-500-41958. Golden, USA: National Renewable Energy Laboratory.
- (2009). "Dynamics of offshore floating wind turbines-model development and verification". In: *Wind Energy* 12.5, pp. 459–492. DOI: 10.1002/we.347.
- (2010). *Definition of the Floating System for Phase IV of OC3*. Tech. rep. NREL/TP-500-47535. Golden, USA: National Renewable Energy Laboratory.
- Jonkman, J and MLJ Buhl (2005). *FAST Users' Guide*. Tech. rep. NREL.
- Jonkman, J, S Butterfield, et al. (2009). *Definition of a 5-MW Reference Wind Turbine for Offshore System Development*. Tech. rep. February. Golden, USA: National Renewable Energy Laboratory.
- Jonkman, J and D Matha (2009). *A Quantitative Comparison of the Responses of Three Floating Platforms*. Tech. rep. NREL/CP-46726. Golden, USA: National Renewable Energy Laboratory.
- Kallesøe, BS and AM Hansen (2011). "Dynamic mooring line modeling in hydro-aero-elastic wind turbine simulations". In: *Proceedings of the International Offshore and Polar Engineering Conference*. 21st International Offshore and Polar Engineering Conference, ISOPE-2011. RisøNational

- Laboratory, Technical University of Denmark, Roskilde, Denmark, pp. 375–382.
- Karimirad, M (2013). “Modeling aspects of a floating wind turbine for coupled wave–wind-induced dynamic analyses”. In: *Renewable Energy* 53, pp. 299–305. DOI: 10.1016/j.renene.2012.12.006.
- Karimirad, M and T Moan (2012a). “A simplified method for coupled analysis of floating offshore wind turbines”. In: *Marine Structures*. DOI: 10.1016/j.marstruc.2012.03.003.
- (2012b). “Stochastic dynamic response analysis of a tension leg spar-type offshore wind turbine”. In: *Wind Energy* 16, pp. 953–973. DOI: 10.1002/we.
- (2012c). “Wave-and Wind-Induced Dynamic Response of a Spar-Type Offshore Wind Turbine”. In: *Journal of Waterway, Port, Coastal, and Ocean Engineering* 138.1, pp. 9–20. DOI: 10.1061/(ASCE)WW.1943-5460.
- Lackner, MA and MA Rotea (2011). “Passive structural control of offshore wind turbines”. In: *Wind Energy* 14, pp. 373–388. DOI: 10.1002/we.
- Langley, RS (1984). “The linearisation of three dimensional drag force in random seas with current”. In: *Applied Ocean Research* 6.3, pp. 126–131.
- (1987). “Second order frequency domain analysis of moored vessels”. In: *Applied Ocean Research* 9.1, pp. 7–18.
- (1988). “Harmonic linearisation of geometrically non-linear finite element models”. In: *Computers & Structures* 28.2, pp. 165–172. DOI: 10.1016/0045-7949(88)90036-3.
- Larsen, TJ and TD Hanson (2007). “A method to avoid negative damped low frequent tower vibrations for a floating, pitch controlled wind turbine”. In: *Journal of Physics: Conference Series* 75, p. 012073. DOI: 10.1088/1742-6596/75/1/012073.
- Larsen, TJ, BS Kallešøe and HF Hansen (2011). “Dynamics of a floating wave energy platform with three wind turbines operating”. In: *Proceedings of the 21st International Offshore and Polar Engineering Conference*. Maui, Hawaii, pp. 391–398.
- Lee, KH (2005). “Responses of Floating Wind Turbines to Wind and Wave Excitation”. PhD thesis. MIT.
- Lin, YK (1976). *Probabilistic theory of structural dynamics*.
- Low, YM (2006). “Efficient methods for the dynamic analysis of deepwater offshore production systems”. PhD thesis. University of Cambridge.
- Lucas, J (2011). *Upwind project: comparison of first and second hydrodynamic-results for floating offshore wind structures*. Tech. rep. Garrad Hassan.

- Lupton, R (2014a). *beamfe: simple beam finite element model in Python*. URL: <https://github.com/ricklupton/beamfe>.
- (2014b). *mbwind: flexible multibody dynamics in Python*. URL: <https://github.com/ricklupton/mbwind>.
- (2014c). *py-bem: Blade Element Momentum implementation in Python*. URL: <https://github.com/ricklupton/py-bem>.
- Martin, HR et al. (2014). “Methodology for Wind/Wave Basin Testing of Floating Offshore Wind Turbines”. In: *Journal of Offshore Mechanics and Arctic Engineering* 136.2, p. 021902. DOI: 10.1115/1.4025030.
- Matha, D (2009). “Model Development and Loads Analysis of an Offshore Wind Turbine on a Tension Leg Platform, with a Comparison to Other Floating Turbine Concepts”. PhD thesis. Boulder, USA: University of Colorado.
- Matha, D, T Fischer, et al. (2009). “Model Development and Loads Analysis of a Wind Turbine on a Floating Offshore Tension Leg Platform”. In: *European Offshore Wind Conference*. Stockholm, Sweden.
- Matha, D, F Sandner and D Schlipf (2012). “Efficient critical design load case identification for floating offshore wind turbines with a reduced nonlinear model”. In: *The Science of Making Torque from Wind*.
- Matha, D, M Schlipf, et al. (2011). “Challenges in simulation of aerodynamics, hydrodynamics, and mooring-line dynamics of floating offshore wind turbines”. In: *Proceedings of the 21st International Offshore and Polar Engineering Conference*. Maui, Hawaii, pp. 421–428.
- Meijaard, JP (2005). *A proposal for the application of multibody dynamics to the simulation of wind turbines*. Tech. rep. Garrad Hassan.
- Muliawan, MJ et al. (2013). “Extreme responses of a combined spar-type floating wind turbine and floating wave energy converter (STC) system with survival modes”. In: *Ocean Engineering* 65, pp. 71–82. DOI: 10.1016/j.oceaneng.2013.03.002.
- Myhr, A, C Bjerkseter, et al. (2014). “Levelised cost of energy for offshore floating wind turbines in a life cycle perspective”. In: *Renewable Energy* 66, pp. 714–728. DOI: 10.1016/j.renene.2014.01.017.
- Myhr, A, KJ Maus and TA Nygaard (2011). “Experimental and computational comparisons of the OC3-HYWIND and Tension-Leg-Buoy (TLB) floating wind turbine conceptual designs”. In: *Proceedings of the 21st International Offshore and Polar Engineering Conference*. Maui, Hawaii, pp. 353–360.
- Nielsen, FG, TD Hanson and B Skaare (2006). “Integrated Dynamic Analysis of Floating Offshore Wind Turbines”. In: *Proceedings of the 25th International*

- Conference on Offshore Mechanics and Arctic Engineering*. Hydro Oil & Energy. Hamburg, Germany. DOI: 10.1115/OMAE2006-92291.
- Ormberg, H, E Passano and N Luxcey (2011). "Global Analysis of a Floating Wind Turbine Using an Aero-Hydro-Elastic Model: Part 1—Code Development and Case Study". In: *OMAE 2011*. Asme. DOI: 10.1115/OMAE2011-50114.
- Philippe, M, A Babarit and P Ferrant (2011). "Comparison of time and frequency domain simulations of an offshore floating wind turbine". In: *OMAE 2011*.
- (2012). "Modes of response of an offshore wind turbine with directional wind and waves". In: *Renewable Energy*. DOI: 10.1016/j.renene.2012.01.042.
- (2014). "Aero-Hydro-Elastic Simulation of a Semi-Submersible Floating Wind Turbine". In: *Journal of Offshore Mechanics and Arctic Engineering* 136.2, p. 021905. DOI: 10.1115/1.4025031.
- Pinkster, J (1980). *Low frequency second order wave exciting forces on floating structures*. Tech. rep. Wageningen, The Netherlands: Netherlands Ship Model Basin.
- Pitt, DM and DA Peters (1981). "Theoretical prediction of dynamic-inflow derivatives". In: *Vertica* 5.1, pp. 21–34.
- Ramachandran, GKV (2012). "A numerical model for a floating TLP wind turbine". PhD thesis. Technical University of Denmark.
- Ramachandran, GKV et al. (2014). "Fully Coupled Three-Dimensional Dynamic Response of a Tension-Leg Platform Floating Wind Turbine in Waves and Wind". In: *Journal of Offshore Mechanics and Arctic Engineering* 136.2, p. 021103. DOI: 10.1115/1.4025599.
- Reddy, J (1993). *Introduction to the Finite Element Method*.
- Roald, L et al. (2013). "The effect of second-order hydrodynamics on floating offshore wind turbines". In: *Energy Procedia*. Vol. 00. Trondheim: Elsevier.
- Roberts, JB and PD Spanos (1990). *Random vibration and statistical linearization*. John Wiley & Sons.
- Robertson, AN and J Jonkman (2011). "Loads analysis of several offshore floating wind turbine concepts". In: *Proceedings of the 21st International Offshore and Polar Engineering Conference*. Maui, Hawaii, pp. 443–450.
- Roddier, DG et al. (2010). "WindFloat: A floating foundation for offshore wind turbines". In: *Journal of Renewable and Sustainable Energy* 2.3, p. 033104. DOI: 10.1063/1.3435339.
- Sandner, F et al. (2012). "Reduced nonlinear model of a spar-mounted floating wind turbine". In: *DEWEK*.

- Sebastian, T and MA Lackner (2013). "Characterization of the unsteady aerodynamics of offshore floating wind turbines". In: *Wind Energy* 16, pp. 339–352. DOI: 10.1002/we.545.
- Shabana, AA (2012). *Computational continuum mechanics*. Cambridge University Press.
- (2013). *Dynamics of multibody systems*. 4th ed. Cambridge University Press.
- Si, Y, HR Karimi and H Gao (2014). "Modelling and optimization of a passive structural control design for a spar-type floating wind turbine". In: *Engineering Structures* 69, pp. 168–182. DOI: 10.1016/j.engstruct.2014.03.011.
- Skaare, B, TD Hanson, et al. (2006). "Integrated dynamic analysis of floating offshore wind turbines". Hydro Oil and Energy, Research Centre Bergen.
- Skaare, B, FG Nielsen and TD Hanson (2014). "Analysis of measurements and simulations from the Hywind Demo floating wind turbine". In: *Wind Energy*. DOI: 10.1002/we.
- Skjoldan, PF and MH Hansen (2010). "Implicit Floquet analysis of wind turbines using tangent matrices of a non-linear aeroelastic code". In: *Wind Energy*.
- Snel, H and JG Schepers (1995). *Joint investigation of dynamic inflow effects and implementation of an engineering method*. Tech. rep.
- Stoker, JJ (1950). *Nonlinear Vibrations*. New York: Interscience Publishers Ltd.
- Stol, K, M Balas and G Bir (2002). "Floquet Modal Analysis of a Teetered-Rotor Wind Turbine". In: *Journal of Solar Energy Engineering* 124.4, pp. 364–371. DOI: 10.1115/1.1504846.
- Sultania, A and L Manuel (2011). "Long-term reliability analysis of a spar buoy-supported floating wind turbine". In: *OMAE 2011*. ii.
- Sway (2014). *Sway*. URL: <http://www.sway.no> (visited on 10/09/2014).
- SymPy Development Team (2012). *SymPy: Python library for symbolic mathematics*. URL: <http://www.sympy.org>.
- Tracy, C (2007). "Parametric Design of Floating Wind Turbines". PhD thesis. Massachusetts Institute of Technology.
- Vaal, JB de, MOL Hansen and T Moan (2014). "Effect of wind turbine surge motion on rotor thrust and induced velocity". In: *Wind Energy* 17.1, pp. 105–121. DOI: 10.1002/we.1562.
- Vidyasagar, M (1993). *Nonlinear systems analysis*. 2nd ed. Prentice Hall.
- Viselli, AM, AJ Goupee and HJ Dagher (2014). "Model test of a 1:8 scale floating wind turbine offshore in the Gulf of Maine". In: *Proceedings of the ASME 2014*

- 33rd International Conference on Ocean, Offshore and Arctic Engineering. San Francisco, USA.
- Wamit Inc (2002). *WAMIT User Manual, Version 6.4*. Tech. rep.
- Wang, L and B Sweetman (2012). "Simulation of large-amplitude motion of floating wind turbines using conservation of momentum". In: *Ocean Engineering* 42, pp. 155–164. DOI: 10.1016/j.oceaneng.2011.12.004.
- Wayman, EN et al. (2006). "Coupled Dynamic Modeling of Floating Wind Turbine Systems". In: *Offshore Technology Conference*. Houston, USA.
- Withee, JE (2004). "Fully Coupled Dynamic Analysis of a Floating Wind Turbine System". PhD thesis. MIT.
- Zhang, R et al. (2013). "Dynamic response in frequency and time domains of a floating foundation for offshore wind turbines". In: *Ocean Engineering* 60, pp. 115–123. DOI: 10.1016/j.oceaneng.2012.12.015.
- Zhang, Y (2010). "Response Statistics of a Floating Vessel in Spreading Seas". PhD thesis. University of Cambridge.